The Sedimentology, Mineralogy and Geochemistry of the ~1.4 Ga Roper Superbasin Northern Australia

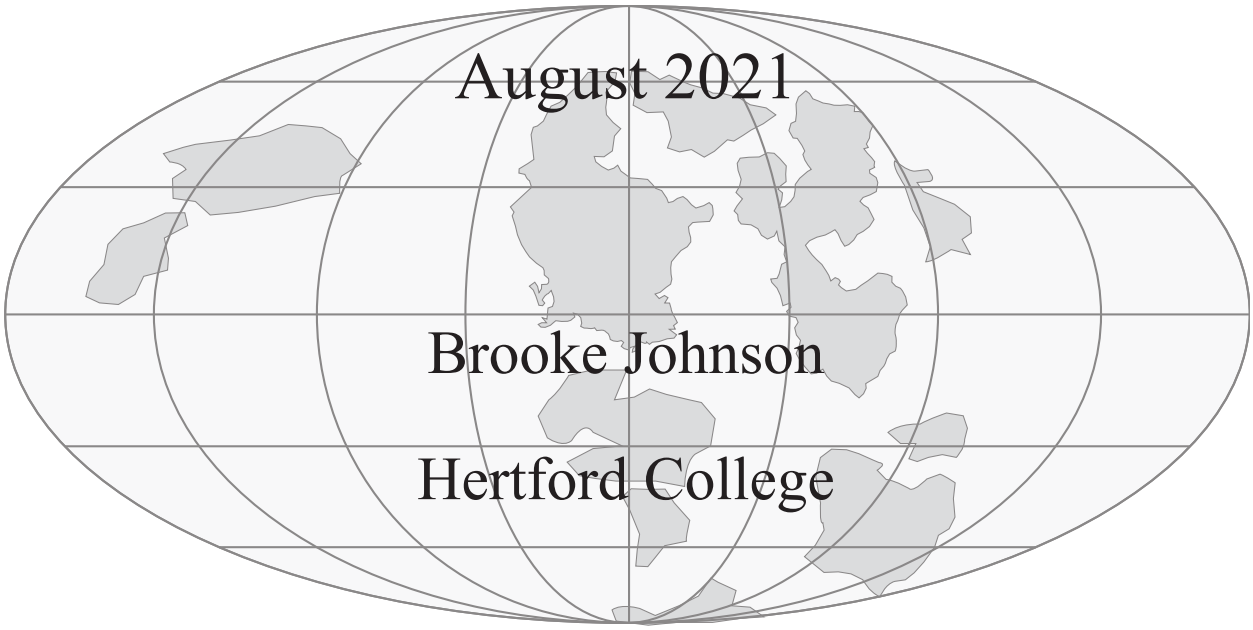

August 2021

Brooke Johnson

Hertford College

Supervisors: Dr Nick Tosca, Dr Rosalie Tostevin,

Dr Stuart Robinson

Table of Contents

Abstract **1**

1. Introduction **2**

1.1 Why Did Life Take So Long To Get Interesting?. 2

1.2 Background 6

1.3 Middle Proterozoic Eukaryotic Biological Records. 14

1.4 The Geological History of The North Australian Craton 21

1.5 Research Questions 28

1.6 Thesis Outline. 29

1.7 References 32

2. Sedimentology and Sequence Stratigraphy of the Roper Superbasin **37**

2.1 Introduction. 38

2.2 Geological Setting 40

2.3 Materials and Methods 41

2.4 Results. 42

2.5 Discussion. 86

2.6 Conclusion 102

2.7 References 103

3. Phosphorus Burial in Ferrguinous SiO_2-rich Mesoproterozoic Sediments **107**

3.1 Introduction. 107

3.2 Geological Background and Methods 108

3.3 Results. 109

3.4 Discussion. 116

3.5 Conclusion 119

3.6 Sherwin Chapter Appendix 120

3.7 References 122

4. Unravelling Sedimentary Redox Dynamics within the Mesoproterzoic Velkerri Formation **125**

4.1 Introduction. 125

4.2 Methods. 128

4.3 Results. 129

4.4 Discussion. 137

4.5 Conclusions 149

4.6 References 150

5. Discussion and Synthesis **156**

5.1 Introduction . . . 156

5.2 A New Environmental and Depositional Model for the Roper Superbasin . . . 164

5.3 Constraints on mid-Proterozoic Marine Redox from the RSB . . . 174

5.4 mid-Proterozoic Marine Phosphate Availability . . . 184

5.5 mid-Proterozoic Paralic and Terrestrial Environments . . . 191

5.6 Implications for the Wider mid-Proterozoic World . . . 193

5.7 Future Work . . . 197

5.8 Conclusions . . . 200

5.9 References . . . 202

6. Core Logs **209**

7. Acknowledgements **226**

8. Honesty Declaration **228**

This work is dedicated to the following individuals who helped in ways they will never know

Elaine “The Kraken” Billingham - *’Ah dunno wor an ooid is, but am glad it makes ye happy’*

Steve “Biff” Black - *‘Tremendous! But you are now officially the biggest nerd I know.’*

Daniel “Pouteeny” Kondla - *‘lol! Bummo!’*.

"I would rather
be a geographer
than study
Precambrian sedimentology"

– Brooke R. Johnson, April 2013.

Abstract Eukaryotic life arose around 1.6 billion years ago, but for much of Earth history has been ecologically and biologically conservative. There is a gap of around a billion years between the first eukaryotic fossils and their rise to ecological prominence around 800 million years ago. The causes of this delay in eukaryote evolution are widely debated, but in recent years the role of oxygen, has been proposed as a major driver in the evolution of complex life. Oxygen drives metabolism for energy intensive organisms like eukaryotes, it is also a key component of eukaryotic biomolecules. Oxygen is also a key player in the cycling of essential bio-limiting nutrients such as phosphorus. Some have hypothesized that in the low oxygen Proterozoic world, phosphorus was scarce and thus limited primary productivity, slowing the oxygenation of the Earth and locking the planet into a billion-year long period of environmental stasis. Additionally, the iron rich oceans are proposed to have sequestered phosphorus in sediments as iron phosphate minerals. To date, neither of these hypotheses have been robustly tested against the sedimentary record.

To test these two hypotheses, I conducted a high-resolution study of exquisitely preserved ~1.4 - 1.3 Ga sedimentary rocks from the Roper Superbasin (RSB), northern Australia. I find no evidence of sedimentary sequestration of phosphorus as Fe-phosphate in the examined sediments. Additionally, I find that sediments were deposited under ferruginous and oxic conditions, contrary to published work. Also, in contrast to previous work, I find that the RSB is a restricted basin and underwent periods of disconnection from the global ocean. As an epicratonic basin enclosed on multiple sides, the RSB is unsuitable for investigating global ocean conditions in the Proterozoic. However, such locations appear to be commonnly preserved in this interval, and may have been important sites for phosphorus deposition. Regardless of ocean connection the RSB, and locations like it, are where we find eukaryote fossils, and so were obviously an important part of eukaryote evolution. The questions raised by this study highlight how much is left to learn about Earths distant past and the organisms that inhabited the planet at that time.

1. Introduction

1.1 Why Did Life Take So Long To Get Interesting

In this thesis, I will use the informal term 'mid-Proterozoic' to describe the interval of 1800 Ma to 800 Ma. This interval is informally known by some as the 'boring billion'. I reject this term because it was coined to describe a stable carbon isotope curve through a section of rock that has since been shown not to span this whole interval. Secondly, the apparently unusual behaviour of the whole Earth system recorded in this interval makes it far from boring in any sense of the word. Thirdly, as recent research is beginning to show (including this thesis), this interval does not appear to be as 'stable' as first believed.

1.1.1 The Gap

On the basis of both fossil and molecular data there is an apparent gap of ~1000 million years (Myrs) between the emergence of the first single-celled eukaryotic organism and their rise to ecological significance (Brocks et al.,2017). Currently, the causes of this delay are unknown, but a number of studies have suggested that sustained low levels of atmospheric oxygen played a major role (Lambert and Donnelly, 1991; Knoll, 1996; Lyons et al., 2014a). In addition to its importance in eukaryotic respiration, oxygen is required for building complex eukaryotic biomolecules and cellular material such as collagen (Towe, 1970; Runnegar, 1991). Oxidative weathering is also responsible for recycling key nutrients such as phosphorus, particularly from uplifted marine sediments and mafic rocks, back into the global ocean (Reinhard et al.,2017).

Modeling studies informed by geochemical evidence from the sedimentary rock record indicate that mid-Proterozoic surface environments were low oxygen, with ventilation restricted to shallow coastal areas and a thin surface layer in the open ocean (Poulton and Canfeld, 2011). In this model, below a thin surface oxygenated layer, the oceans were depleted in O_2 and rich in Fe^{2+} and H_2S, both of which would present difficulties for eukaryotic organisms (Poulton and Canfeld, 2011). For example, H_2S is toxic, even in small doses, due to its interference with respiration processes in eukaryote mitochondria (e.g., Buckler, 2012). Similarly, Fe^{2+} may have played an indirect role in influencing early eukaryotic life through a hypothesised reaction with the key nutrient phosphorus to produce Fe(II)-phosphate minerals such as vivianite (Derry, 2015).

When phosphorus is mineralised in this way, it is buried in marine sediments, and effectively removed from the biologically available P-pool (Derry, 2015). It has been proposed that without enough biologically available P to support their metabolic needs, oxygenic cyanobacteria were

unable to compete with anaerobically photosynthesising organisms and thus, unable to produce enough oxygen to overcome the O_2 sink represented by oxidizable organic matter (Reinhard et al., 2017). In this model, because of this C-P-O_2 interrelationship, the Earth settled into a low-oxygen, low-nutrient feedback loop that lasted ~1200 Ma (Reinhard et al.,2020).

This C-P-O_2 model is based on a number of studies. Firstly, bulk P contents in marine siliciclastic sediments are orders of magnitude lower in the mid-Proterozoic relative to younger sediments (Reinhard et al.,2017). Such compilations filter out chemical sediments, quartz sandstones and sediments with an aluminium content below 1 wt.% (Reinhard et al.,2017). Additionally, these compilations do not include a number of key mid-Proterozoic successions, such as the Roper Superbasin (RSB), further restricting the available sample pool (Reinhard et al.,2017). Thus, such compilations do not show a complete record of P levels in available mid- Proterozoic marine sediments. Even including these uncounted successions is unlikely to give a complete record of Mid-Proterozoic oceans, due to their limited extent and their state of preservation. Secondly, modelling simulations based on the behaviour of P in modern ferruginous sediments suggests P would be limited in dominantly ferruginous oceans (Derry, 2015). However, modern marine sediments have a significantly different chemistry to ancient sediments. For example, dissolved silica and ferrous iron levels were much higher in mid-Proterozoic marine sediments than in modern marine sediments. (März et al.,2018; Johnson et al.,2020). Additionally, the presence of vivianite or other Fe(II)-phosphates has not been widely reported in mid-Proterozoic sediments. The lack of vivianite, or other authigenic Fe(II)-phosphates, suggests that these minerals may not be an important sink for P in mid-Proterozoic oceans. Certainly, vivianite does not appear to be an important sink for P in Phanerozoic and modern typical marine environments. Alternatively, it could be argued that the stability of authigenic Fe(II)-phosphates is unconstrained over geological timescales and these minerals may not survive typical diagenetic processes. Examination of ferruginous, phosphate bearing mid- Proterozoic sediments will help to constrain these uncertainties.

1.1.2 mid- Proterozoic sedimentary rocks

Despite their age, a number of sedimentary successions survive from the mid- Proterozoic interval, providing valuable insight into early eukaryotic ecosystems and their environmental setting. Perhaps the best preserved of these sedimentary sequences and as a consequence, some of the most studied, are the mid- Proterozoic sediments of the McArthur Basin and the overlying Roper Superbasin in northern Australia (Donnelly and Crick, 1988; Munson, 2016). Much of these sediments remain in the subsurface and have only experienced shallow burial and highly localised

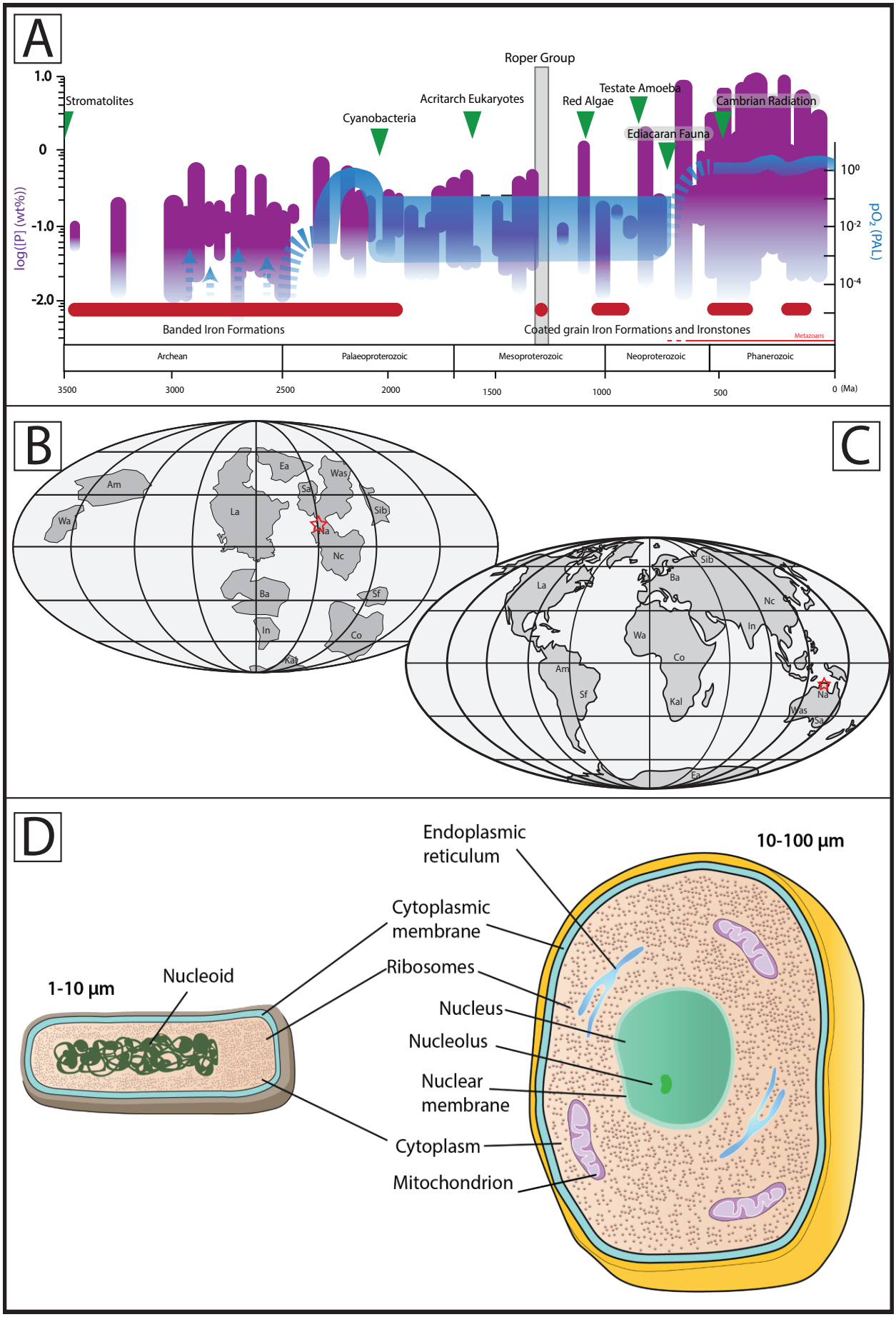
A
Roper Group
1.0
0
-1.0
-2.0
log([P] (wt%))
Stromatolites
Cyanobacteria
Acritarch Eukaryotes
Red Algae
Testate Amoeba
Ediacaran Fauna
Cambrian Radiation
10^0
10^{-2}
10^{-4}
pO_2 (PAL)
Banded Iron Formations
Coated grain Iron Formations and Ironstones
Metazoans
Archean
Palaeoproterozoic
Mesoproterozoic
Neoproterozoic
Phanerozoic
3500
3000
2500
2000
1500
1000
500
0 (Ma)
B
C
Am
Wa
Ea
Was
Sa
La
Sib
Na
Nc
Ba
Sf
In
Co
Kal
D
Endoplasmic reticulum
10-100 µm
Cytoplasmic membrane
Ribosomes
Nucleus
Nucleolus
Nuclear membrane
Cytoplasm
Mitochondrion
1-10 µm
Nucleoid

Fig 1: A) Temporal context of the present study showing major biotic innovations (green arrows), deposition of ferruginous sediments (dark red bars), appearance of metazoans (light red bar), bulk sedimentary P wt% (purple bars and left vertical axis) and atmospheric oxygenation as a percentage of modern atmospheric oxygen levels.(Javaux and Knoll, 2002, Lyons et al, 2008, Reinhard et al, 2017). B) Paleogeographic plate reconstruction ~1400 Ma (Shen et al, 2018) C) Modern locations of cratons in B, red star in both diagrams is the location of the RSB. D) Cartoon of typical bacterial cell (left) and eukaryote cell (right, image supplied by Rosalie Tostevin). Craton name abbreviations: Wa = West Africa, Am = Amazoinia, La = Laurentia, Ba = Baltica, In = India, Ka = Kalahari, Co = Congo, Sf = Sao Francisco, Nc = North China, Sib = Siberia, Na = North Australia, Sa = South Australia, Was = West Australia.

deformation and alteration. Because of this, they are unusually well-preserved, making them ideal candidates for the study of mid- Proterozoic life and environments (Munson, 2016). In addition, abundant core material is available due to mineral and hydrocarbon exploration in northern Australia (Ahmad and Hollis, 2013). The Mesoproterozoic Roper Group, for example, contains abundant hydrocarbons and the world's oldest live oil (Jackson et al.,1986). The excellent preservation and abundance of easily available core material have made the Roper Group in particular an active target for research into mid- Proterozoic life and environments (Javaux and Knoll, 2017).

Much of the data generated from studies of the Roper Group have come from a small number of drill cores (Table 1) and sample the same stratigraphically-equivalent sediments. This means that our understanding of environmental change in the Roper Group is limited by moderate temporal resolution, but at relatively low spatial resolution, given the large area over which these sediments were deposited. Additionally, the majority of previous biogeochemical studies of the RSB have used bulk powder analytical techniques, with little of the published work tying together the sedimentology, petrography, and mineralogy with the bulk geochemistry and wider geological context of the basin (e.g., Shen et al.,2003). Thus, we are left attempting to understand the environment and geochemistry of an entire sedimentary basin, and any global implications, while looking through a metaphorical keyhole.

This thesis attempts to address these problems by placing the Roper Group into wider context, characterising the basinal depositional setting, and tying bulk powder analyses to high-resolution sedimentary, petrographic and mineralogical observations. I include samples from the three most heavily studied cores as well as from four additional cores, three of which have never been formally described or studied outside of initial drill reports (Table 1). Drill cores were selected to provide north-south and east-west transects through the Roper Group, so that coeval proximal, basinal and distal sediments could be compared and, for the first time, placed in their correct stratigraphic and paleogeographic context.

1.2 Background

1.2.1 Eukaryotic Life

All life on Earth falls into three domains: bacteria, archaea, and eukaryotes (Fig 1D). Bacteria and archaea are simple cells in which the contents, DNA etc., float freely within the cell, separated from the outside environment by a cell wall. In the following discussion, "bacteria" will be used to describe both true bacteria, and archaea as it is impossible to differentiate between the two from fossil morphology alone. The oldest accepted bacteria fossils are dated to ~ 2500 Ma, although bacteria undoubtedly arose earlier than that (Knoll, 2015). Bacteria have spread into every available ecological niche and can exploit a bewildering array of metabolic pathways (Knoll, 2015). One of the most significant biological innovations of the bacteria was the development of aerobic oxygenic photosynthesis in the late Archean to early Paleoproterozoic, which led to the accumulation of molecular oxygen in the Earth's atmosphere and oceans (Butterfield, 2015b; Fischer, Hemp and Johnson, 2016; Soo et al.,2017). This oxygenation permanently changed the chemistry of Earth surface environments and is proposed to have paved the way for more complex life to evolve. However, despite their early appearance and colonisation of all available habitats, bacteria have remained small and morphologically simple, never achieving obligate multicellularity.

Eukaryotic cells, in contrast, contain discrete organelles with specific biological functions within a flexible cytoskeletal membrane (Fig 1D, Knoll, 2014). Perhaps most important are the nucleus, which contains the cell's genetic material and directs the cellular function, and the mitochondria, which use oxygenic respiration to convert metabolites into adenosine-triphosphate (ATP) - the energy currency of the eukaryotic cell (Knoll, 2014). This form of metabolism is more efficient than those utilised by bacteria and has a greater energy yield. It is this difference in energy capacity that has allowed eukaryotic cells to grow larger and more complex than their prokaryotic counterparts, and has allowed the development of obligate multicellularity, leading in turn to all modern metazoans: organisms with obligate multicellularity such as plants, fungi and animals (Lane and Martin, 2010).

The oldest accepted eukaryote candidate microfossils occur between 1800 – 1600 Ma, though molecular clocks place eukaryote origins earlier (Javaux et al., 2003; Betts et al.,2018; Javaux and Lepot, 2018). Precambrian eukaryote microfossils can be distinguished from bacterial microfossils using a combination of diagnostic characters unknown (or rare) in any bacterium or Archaean: (i) large size (generally around 100x the size of bacterial cells), (ii) complex wall ultrastructure featuring multiple layers, and (iii) possession of processes (spines) (Javaux et al., 2003). Eukaryote microfossil morphologies range from simple spheres to complex star-like shapes and

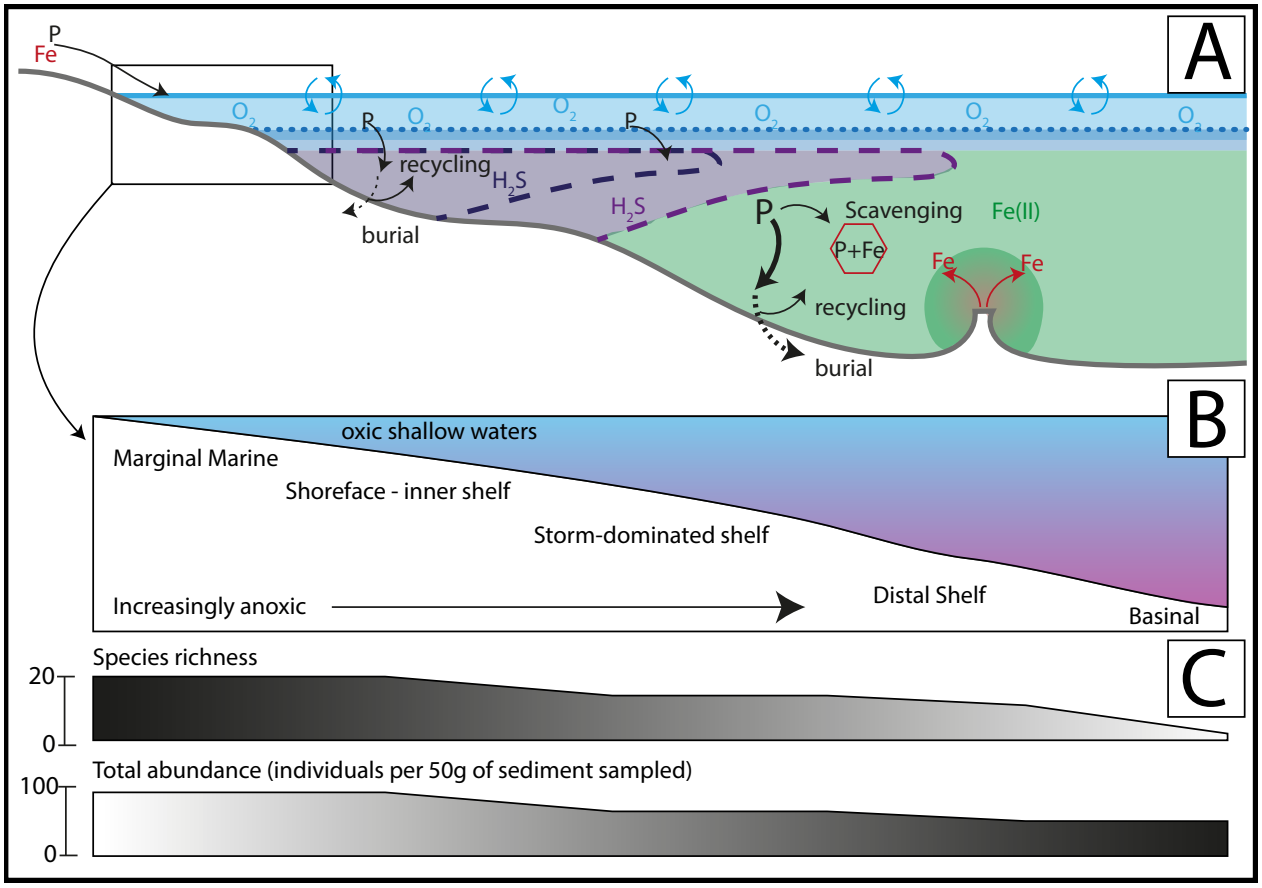

Fig 2: A) Schematic model of the redox structure proposed for Proterozoic oceans and oceanic continental shelves (Poulton and Canfield, 2011). B) Schematic model of the redox structures of cratonic basins such as the RSB (Jackson and Raiswell, 1991). C) Species richness and total abundance for RSB acritarchs as a function of the depositional distance from the paleocoast in B (Javaux and knoll, 2002).

polygons. Eukaryote candidate microfossils may be smooth, reticulate, or ornamented. Together, these features indicate a candidate microfossil represents a single-celled eukaryote-grade organism, if not a direct ancestor of the modern eukaryotic groups (Javaux et al.,2003). Eukaryotic biomarkers remain very low in abundance, in comparison to bacterial biomarkers, until the mid-late Neoproterozoic (Brocks et al.,2017). It is unclear if this biomarker data reflects eukaryote relative abundance as early eukaryotes may have been biochemically indistinguishable from their bacteria ancestors (Brocks et al.,2017; Porter et al., 2018).

Aside from minor changes in surface ornamentation, early eukaryotes underwent very little morphological evolution in the following ~600 Ma after their initial appearance (but see Huntley et al., 2006 for an alternative view). The first unambiguous multi-cellular eukaryotes arose around 1000 Ma in the early Neoproterozoic. The morphology of these organisms shows clear cellular level tissue differentiation and a probable affinity to the Rhodophyta and Chlorophyte algae (Gibson et al.,2018; Tang et al.,2020). Coeval with the appearance of Rhodophytes and Chlorophytes, microfossil eukaryotes appear to increase in abundance, diversity and complexity (Porter, 2004;

but again, see Huntley, Xiao and Kowalewski, 2006 or an alternate view). Scale-like phosphatic microfossils also appear around this time along with vase-shaped organic forms, thought to represent early teste amoeba (Porter and Knoll, 2000; Cohen et al.,2017).

Eukaryote microfossils bearing precise incisions and holes, interpreted as feeding traces, suggest that inter-eukaryote predation may have been a contributing factor driving the increase in diversity during the early Neoproterozoic (Knoll and Lahr, 2016). Likewise, a steady decline in the abundance and diversity of biogenic stromatolites during this interval is attributed to grazing by, and increasing abundance of, heterotrophic eukaryotes (Marais, 1991; Allwood et al.,2009). In the Neoproterozoic, the eukaryotes underwent two major pulses of increased diversity: in the Tonian Period, prior to the first of the global Cryogenian glaciations, and subsequently in the Ediacaran Period following the end of the last global glaciation (Knoll, 2014; Cohen and Macdonald, 2015). It is in this post Cryogenial interval that biomarker evidence suggests that eukaryotes become major primary producers for the first time, and the first biomarkers for the chlorophytes are detectable (Brocks et al.,2017).

1.2.2 Environmental Redox

Redox reactions, or those that transfer electrons between chemical species, are a major energy transfer process in both biotic and abiotic natural systems. Living organisms use redox reactions during respiration because the transfer of electrons between chemical species is linked directly to the Gibbs free energy changes of those reactions. As a consequence, bacteria have developed multiple respiration pathways to utilise energy from naturally occurring chemical species that are in apparent redox disequilibrium. This has allowed them to colonise every suitable habitat on Earth. Aerobic respiration (where O_2 is the terminal electron acceptor) has the largest energy yield of the redox pathways and for this reason it is favoured by eukaryotes and metazoans which have high energy requirements (Lane and Martin, 2010). Because redox reactions are such a central pillar of life, the redox state of an ancient natural environment can indicate which metabolisms were present, or even dominant, in that environment (Froelich et al.,1979). In modern oxygenated aquatic or sedimentary environments, aerobic respiration is usually the dominant metabolic pathway. As the oxygen level decreases, such as in an oceanic oxygen minimum zone, metabolisms favour the reduction of Mn or nitrate for respiration. In oxygen depleted waters, anaerobic respiration becomes dominant. Because of this, the redox state is often used to describe the abundance of dissolved oxygen in pore waters and the overlying water column (Froelich et al.,1979).

The modern atmosphere is ~21% O_2, which is described as 100% of Present Atmospheric

Levels (PAL) when compared to ancient atmospheric O_2 levels (Lyons et al.,2014). Modern fully oxygenated marine waters have a dissolved O_2 content of up to 250 μmol/kg, and waters containing any detectable dissolved O_2 are described as 'oxic' (Matear and Hirst, 2003). In low oxygen and fully anoxic environments, intermediate metabolisms become dominant and support the biogeochemical cycles of N, Mn and Fe. Anoxic waters may support the cycling of S and methane and contain dissolved O_2 concentrations < 0.01 μmol/kg (Froelich et al.,1979; Matear and Hirst, 2003).

The organic matter budget plays an important role in regulating the long-term C cycle. Mineralisation of organic matter also regulates the long-term oxidant balance of the atmosphere and oceans over time. The oxygenation of Earth's atmosphere through the mid- and late- Proterozoic is thought to have occurred, at least in part, because the rate of organic carbon export to the seafloor was able to outpace the supply of oxidants. This allowed excess O_2 to accumulate in the atmosphere, which then infiltrated surface waters. While organic C was not the only sink for O_2 during this interval, it was thought to have been the largest and most efficient when compared to e.g., Fe. Organic C burial is recorded during the mid-Proterozoic as the deposition of black shales, and though these deposits never reach the high TOC levels seen in Phanerozoic deposits, the median TOC is still comparable to younger organic rich sedimentary rocks (Sperling E. A. and Stockey R. G., 2018). During the mid-Proterozoic, oxygenic photosynthesis by cyanobacteria would have been the primary source of O_2. However, it has been proposed that low atmospheric oxygen levels slowed the supply of the bio-limiting nutrient P to the global ocean. This is because oxygenic weathering of continental rocks, particularly uplifted marine shales and basalts, is a major source of P delivered to the oceans by rivers (Laakso and Schrag, 2014; Lyons et al.,2014). It is hypothesised that in a low O_2 world, the rate of continental weathering would be much lower, and hence so would the amount of continentally derived P (Reinhard et al.,2020). In turn, the low oceanic nutrient levels may have limited net primary productivity, decreasing the organic carbon export fluxes to deeper waters.

mid- Proterozoic oceans are thought to have featured a relatively oxygenated surface layer, while microbial consumption of organic carbon with depth produced ferruginous (anoxic and Fe-rich) or euxinic (anoxic and H_2S-rich) deeper waters (Fig 2A). In addition to limited dissolved oxygen, anoxic deep waters may have provided extra challenges for early eukaryotic life. Free sulphide in euxinic waters can be toxic to many modern eukaryotic organisms, even in small concentrations. Modelling studies have also suggested that ferruginous waters would have effectively sequestered phosphorus as Fe(II)-phosphates such as vivianite, a precipitation pathway observed in some modern ferruginous aquatic and sedimentary systems (e.g., Slomp et al., 2013).

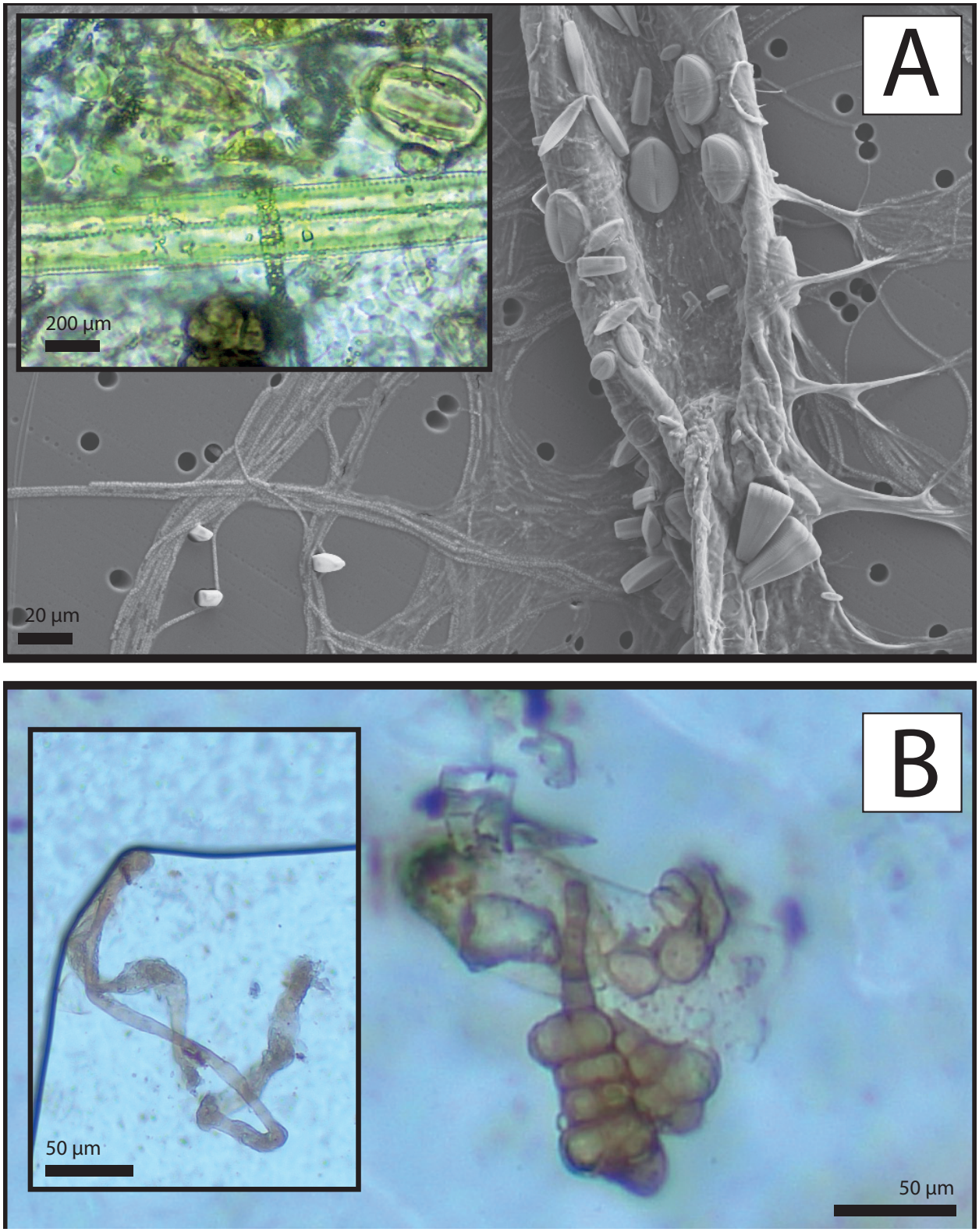

Fig 3: A) SEM Back Scatter image of Typical modern freshwater micro eukaryotic organisms, large central strand is a multicellular algae *cf Cladophora*, wedge, ellipse and lozenge shaped organisms are diatoms, thin strands with whit dots are colonies or sulphur oxidising and reducing bacteria, white dots are granules of elemental sulphur. Inset shows optical microscopy image of the same sample. B) Organic walled microfossils of unknown affinity extracted from a sample of the Velkerri Formation. SEM image by Chrissie Nimms, other images by the author.

These inter-linked redox controlled mechanisms have been proposed by some as the cause of the apparent stasis in eukaryote evolution during the mid-Proterozoic. In this view, eukaryotes would have been restricted to relatively oxygen- and nutrient-rich surface and shallow coastal waters, while bacteria are thought to have dominated offshore oligotrophic, and deep ferruginous and euxinic waters. Additionally, studies of modern oligotrophic and anoxic marine systems have shown that under ferruginous and euxinic conditions, bacteria can use available nutrients, including phosphorus, more efficiently than their eukaryotic counterparts (Cotner and Biddander., 2002, Zubkov., 2014) . Therefore, marine environmental conditions may have favoured bacteria as the dominant primary producers for most of the Proterozoic.

1.2.3 The mid- Proterozoic World

An apparent gap of around 800 million years exists following the appearance of eukaryotic microfossils, ~1600 Ma, and major eukaryotic diversification between ~800 Ma (Cohen and Macdonald, 2015). This mid-Proterozoic interval, from the terminal Paleoproterozoic era to the late Tonian period, is noted for the apparent stability and stasis of the whole Earth system (Cawood and Hawkesworth, 2014, Large, 2014), although this apparent stasis may be an artefact of low preservation potential of rocks from this age (Cawood and Hawkesworth, 2014; Cohen and Macdonald, 2015). During this interval of time, rates of change in everything from plate tectonics, ore deposit generation, climatic upheaval and the evolution of the biosphere are thought to have slowed considerably (Roberts, 2013; Cawood and Hawkesworth, 2014). This period of stability is even more marked when compared with the major events that bookend this period. Prior to the mid-Proterozoic, the Earth experienced a period of major environmental change including widespread glaciation, possibly due to the sudden biogenic removal of carbon dioxide from the atmosphere and the formation of the first supercontinent (Williams and Schmidt, 1997; Gumsley et al.,2017). Likewise, the interval following the mid-Proterozoic saw the breakup of a long-lived supercontinent, at least two widespread glaciations, and major upheavals in the biosphere (Rooney et al.,2015; Alexander et al.,2018).

1.2.4 Paleogeography

Evidence for a mid-Proterozoic stall in plate tectonics derives from the relative paucity of orogenic and subduction-related ore deposits during this interval (Cawood and Hawkesworth, 2014; Liu et al.,2019). These deposits are typically generated by the intrusion of hydrous magmatic bodies during orogenesis and their associated metalliferous hydrothermal fluids (Yuan et al.,2019). Conversely, rift and oceanic ridge related deposits, such as volcanogenic massive sulphides, are relatively more abundant and larger in average size during this interval (Cawood and Hawkesworth, 2014; Pehrsson et al.,2016). This suggests that subduction related tectonic processes played a relatively minor role in global tectonics at this time, or perhaps involved a significantly different geochemistry than younger subduction processes (Cawood and Hawkesworth, 2014).

The ore-based evidence for an unusual global tectonic regime is consistent with other geologic data. The supercontinent Nuna is thought to have formed near the start of the mid-Proterozoic with a suite of orogenic events which began ~2000 Ma and had concluded by ~1600 Ma (Pisarevsky et al.,2014). By the end of the mid-Proterozoic, the Grenville suite of orogenic belts from ~1100 to 850 Ma record the dominant phases of amalgamation of the supercontinent Rodinia (Panzik et al.,2016). However, between these major orogenic episodes, there appears to have been no large-scale breakup and reorganisation of the Nuna supercontinent. Rather than the standard Wilson Cycle (e.g., as proposed for the formation and break-up of Pangea), available data have led to the generation of a model whereby the outer regions of Nuna underwent rifting and then rotated and reorganised around a stable nucleus formed by Laurentia and parts of what would become western Gondwana (Cawood and Hawkesworth, 2014; Li et al.,2019).

1.2.4 Climate in the mid- Proterozoic

Sedimentary evidence from paralic and terrestrial environments suggests that the mid-Proterozoic climate was persistently warm and with humidity/aridity levels that varied with the paleolatitude of the preserved sediments. For example, laterites of the Mapedi Red Beds of South Africa, deposited when the Kalahari Craton was in southern temperate regions, indicate a warm, wet climate (Rasmussen et al.,2020). Similarly, the Torridonian sediments of Scotland indicates a hot arid environment and were deposited when the region was in the northern sub-tropics (Williams, 1968). The lack of large $\delta^{13}C$ or $\delta^{18}O$ excursions relative the rest of isotope record, is used in particular to suggest climatic stability with no periods of extreme cooling or glaciation (Brasier and Lindsay, 1998). There is also no surviving evidence for persistent sea ice or sea level glaciation at the poles during the mid-Proterozoic.

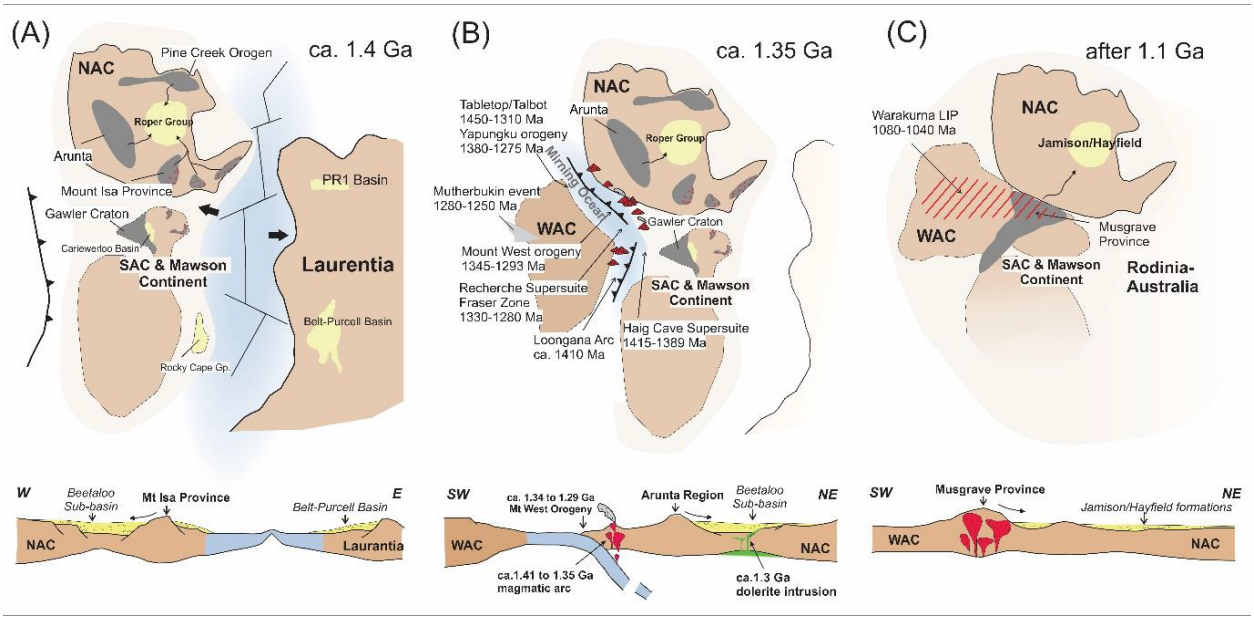

Fig 4: The tectonic evolution of the Northern Australian Craton during deposition of the Roper Group. A) Onset of Velkerri Formation deposition. B) Onset of Moroak Sandstone deposition. C) Post Roper Group erosion and deposition (Yang et al 2018).

The tectonic model described in the previous section may help to explain the long-term climatic stability (e.g., Roberts, 2013). For example, subduction zones are an important carbon sink on geological timescales. Likewise, the chemical weathering of silicates in orogenic uplift removes CO_2 from the atmosphere. On a planet with reduced levels of both subduction and orogenic removal of carbon, it is conceivable that the sedimentary burial of carbon, including organic carbon, would become the primary carbon sink. The steady burial of carbon in sediments, especially those in geologically stable epicratonic basins, could have been buffered by outgassing from ridge and rift related volcanism and LIP eruptions – both apparently abundant through the mid-Proterozoic (Ernst et al.,2008; Zhang et al.,2017). This tectonic mechanism may have created a balance between the sources and sinks of the long-term C cycle, resulting in the climatic stability characteristic of this interval. Many of the nascent rift basins created during this interval formed within intracratonic regions (Abbott and Sweet, 2000). An epicratonic position would support a stable sedimentary basin, and any buried carbon, over geologically significant intervals (i.e., tens of millions of years), effectively removing the buried carbon from the global pool.

1.3 Middle Proterozoic Eukaryotic Biological Records

1.3.1 Molecular Clocks and Biomarkers

Molecular clocks provide a hypothesis for evolutionary history that can be tested with geological/fossil evidence. The most recent clocks place the origin of stem eukaryotes as early as the Archaean, with crown eukaryotes emerging much later (1850 – 1200 Ma, Betts et al.,2018). In contrast, biomarker evidence that eukaryote biomass contributed to sedimentary organic matter is at least equivocal until Tonian time (Brocks et al*.,* 2017). Archaean and early Paleoproterozoic eukaryote biomarkers are unreliable, as they are likely to have been contaminated by fluids derived from younger rocks and preparation processes (Brocks et al.,2008, Rasmussen et al.,2008). Although several studies have claimed to find eukaryote biomarkers in early-Proterozoic-aged sediments, consistent with molecular clock estimates for eukaryote antiquity (Betts et al*.,*2018), subsequent studies have failed to reproduce these results. Consequently, the view now is that the earliest reliable biomarker evidence for eukaryotes is from the Tonian (Brocks et al.,2017, Jarrett et al., 2019, Nyugen et al.,2019).

Brocks et al. (2017) argue that this disconnect reflects ecological change over the Proterozoic Eon, with eukaryotes evolving in Paleoproterozoic time but remaining marginal. Only in the Tonian Period did they achieve ecological prominence and begin to make a detectable contribution to the sedimentary record of organic matter. An alternative explanation, however, is that early eukaryotes produced biomarkers similar to prokaryotes because they evolved from them and lived in similar environments (Nyugen et al 2019, Porter et al 2004). Modern eukaryotic biomarkers may not have appeared until the Cryogenian because that is simply when eukaryotes began to adapt to early modern-type environments and to develop the necessary metabolic strategies to exploit these environments (Bouwknegt et al., 2021). Further, recently published biomarker data indicate that eukaryotic red and green algae may have been present and abundant in marine environments from 1400 Ma (Zhang, et al. 2021). However, new data on previously undocumented sterol structures, suggests that eukaryotes may have been more abundant in the pre-Cryogenian oceans than previously thought (Brocks and Nettersheim, 2020).

1.3.2 Microfossil record

Eukaryote biomineralization did not appear until the Cryogenian period (Porter 2004, Cohen et al 2018). In contrast, mid-Proterozoic eukaryote fossils are entirely formed from recalcitrant organic materials (Knoll, 2014). The preservation and final composition of any fossil is entirely dependent on the original composition of the organism and the subsequent taphonomic, as well as

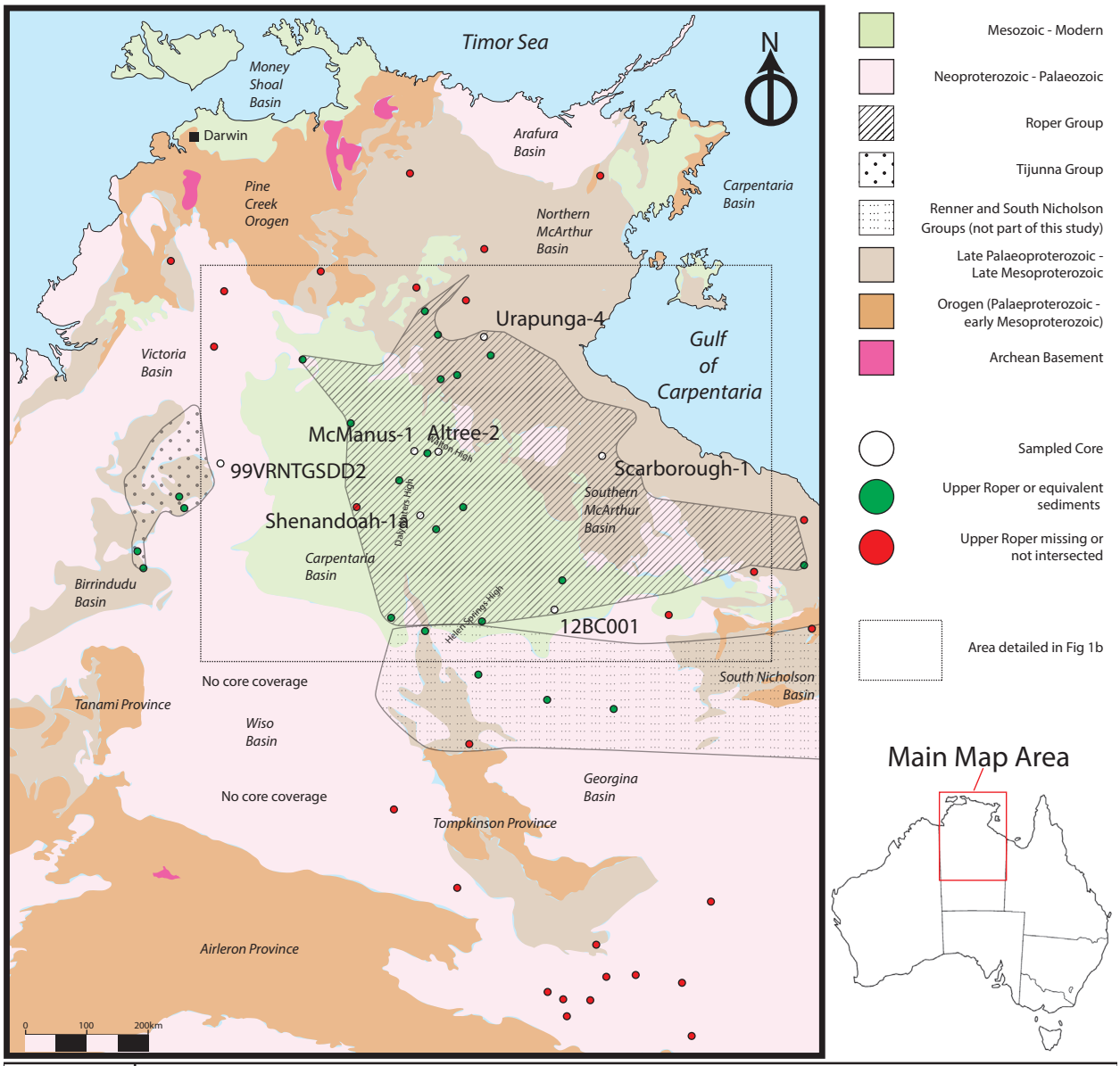

Roper Basin Chronostratigraphy

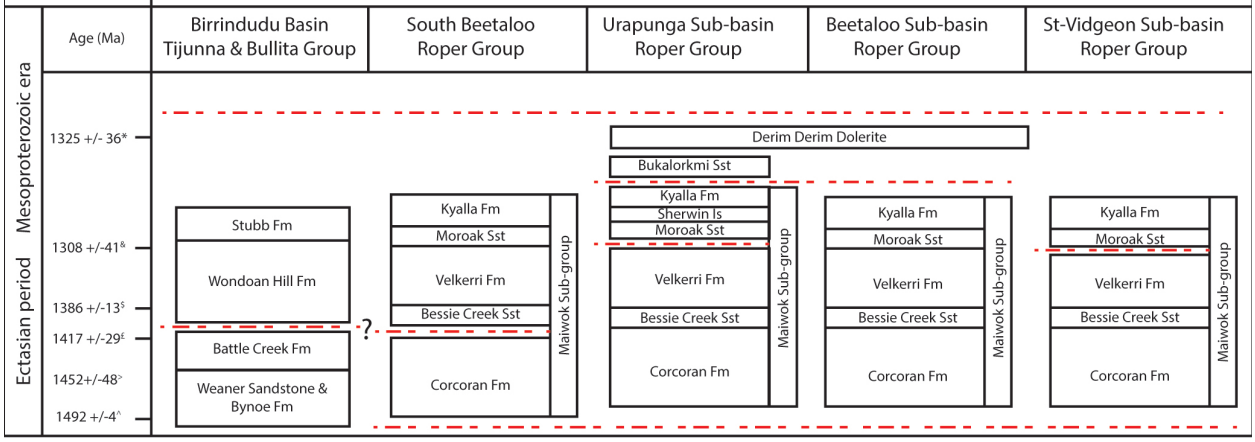

*Dolerite age from SHRIMP and SIMS U-Pb on baddelyite (Abbott et al., 2001) & and $ Upper Velkerri Age from detrital zicron (Yang et al., 2018) £ Base of Velkerri from Re-Os (Munson, 2016)
^ SHRIMP zircon U-Pb age from top of underlying Mainorou Formation (Munson, 2016) >Detrital Zircon in Weaner Sandstone (Kositcin & Carson, 2017)

Fig 5: A) Simplified geological map of the Northern Territory showing major geological packages, the currently known extent of the studied units, and the locations of examined and sampled drill cores, grey box is area shown in Fig 6 (Munson, 2016). B) Current age constraints and stratigraphy for the upper Roper Group and Tijunna Group, red dashed lines represent unconformities, see diagram and main text for references.

the diagenetic and metamorphic processes, to which it is subjected (Javaux et al., 2003). Because mid-Proterozoic microfossils are not mineralised, they are relatively rare. It is essential to establish that putative microfossils are definitively of biological origin (i.e., not contaminants) and are the same age as the host sediment (Javaux, Knoll and Walter, 2003). Observations of biological features that are not replicated by abiotic processes, such as trilaminar walls, complex ultra-structures, spines and processes, are good indicators of the biogenicity of the candidate fossil (Javaux 2004, Javaux 2019). The most common form of preservation for mid-Proterozoic eukaryote micro- and macro- fossils is as bedding parallel carbonaceous impressions in fine grained siliciclastic sediments (Cohen and Macdonald, 2015; Javaux and Lepot, 2018). Fossils may be mineralised during deposition or diagenesis by authigenic and diagenetic minerals, commonly pyrite and phosphate (with 3D preservation) and Fe-oxides replacements have also been recognised (Schiffbauer et al.,2014; Muscente et al., 2015; Javaux and Lepot, 2018).

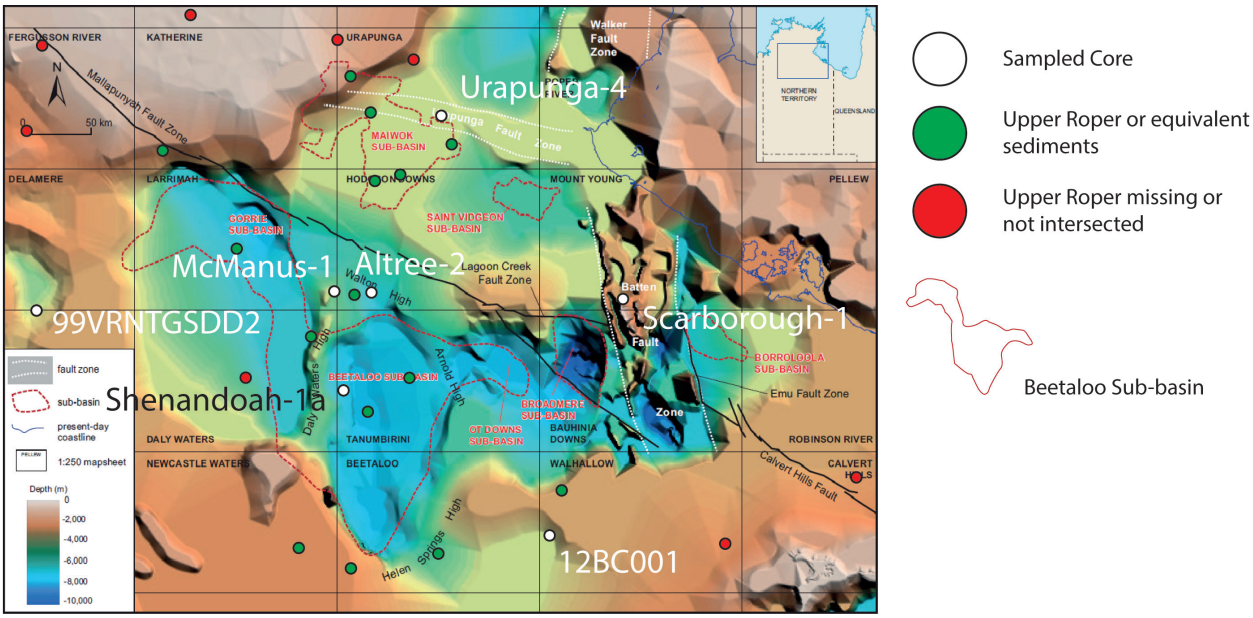

Fig 6: Main structural elements of the study area overlain on a map showing depth to basement, areas of highs are interpreted as being paleotopography.Data from the NTGS SEEBASE tool (Munson, 2016).

1.3.3 The oldest fossil eukaryote

Acritarchs represent the bulk of mid-Proterozoic eukaryote candidate microfossils (Fig 3B, Porter, 2004; Cohen and Macdonald, 2015; Javaux and Lepot, 2018). The term acritarch literally means "uncertain origin" and serves as a catch all clade for large ~30 – >100 µm organic walled fossils found in sediments from the late Archean to the present (Javaux and Lepot 2018, Porter 2004). Most acritarchs are considered to be resting cysts or vegetative stages of unicellular eukaryotes but cannot be assigned more specifically to a clade due to lack of distinguishing features. Some late Proterozoic forms have been suggested to be resting stages of early animals and other metazoans (Cohen et al*.,* 2009; Sergeev, Knoll and Vorob'Eva, 2011; Shang et al*.,* 2019). Some acritarchs represent bacterial colonies but these are distinguished from proposed eukaryote acritarchs by being smaller and simpler. Organic walled microfossils with a sheet or filament morphology are not classed as acritarchs and are considered to be bacterial colonies.

Spherical unornamented acritarchs are often reported as candidate eukaryotes based on their large size alone. Large simple unornamented organic spheres are referred to as *Sphereomorphs* because their morphological simplicity does not even allow general assignment within the acritarch group (Javaux et al*.,*2003). *Sphereomorphs* are often found in early Paleoproterozoic and even Archean rocks, and have been suggested as evidence for the an even earlier origin for eukaryotes (Javaux, Knoll and Walter, 2003). However, prokaryote colonies are capable of forming single walled ~100 µm organic spherical envelopes (Javaux and Lepot, 2018). Examples can be found in the 2100 Ma Franceville Formation, Gabon, the 2100 – 1800 Ma Vempalle Formation, India, and the Kondopgoa Formation, Siberia (Javaux and Lepot, 2018). In all cases preservation is too poor to assign these specimens as anything other than organic walled microfossils (Javaux and Lepot, 2018). The earliest accepted eukaryote candidate acritarch, *Valeria lophostriata,* is found in the ~1650 Ma Changzhougou Formation, China. *Valeria* is also present in the overlying Chuangligyou Formation, and the ~1650 Ma Mallapunyah Formation, Australia, along with *Dictyosphaera* and *Tappania*, two other common and long ranging mid-Proterozoic acritarch genera (Javaux and Lepot, 2018). The oldest acanthomorph acritarchs (those bearing conspicuous spines and processes) are found in the ~1631 Ma Deonar Formation, India, and the ~1611 Ma Baicaoping and Beidajian Formations in the Ruyang Group, China (Butterfield, 2015a). The ~1631 Ma Bahraich and Kheinjah Groups of India also host a modest acritarch assemblage of simple unornamented spheres along with the above-named taxa (Javaux and Lepot, 2018). Between ~1670 and 1500 Ma there is a moderate increase in acritarch diversity.

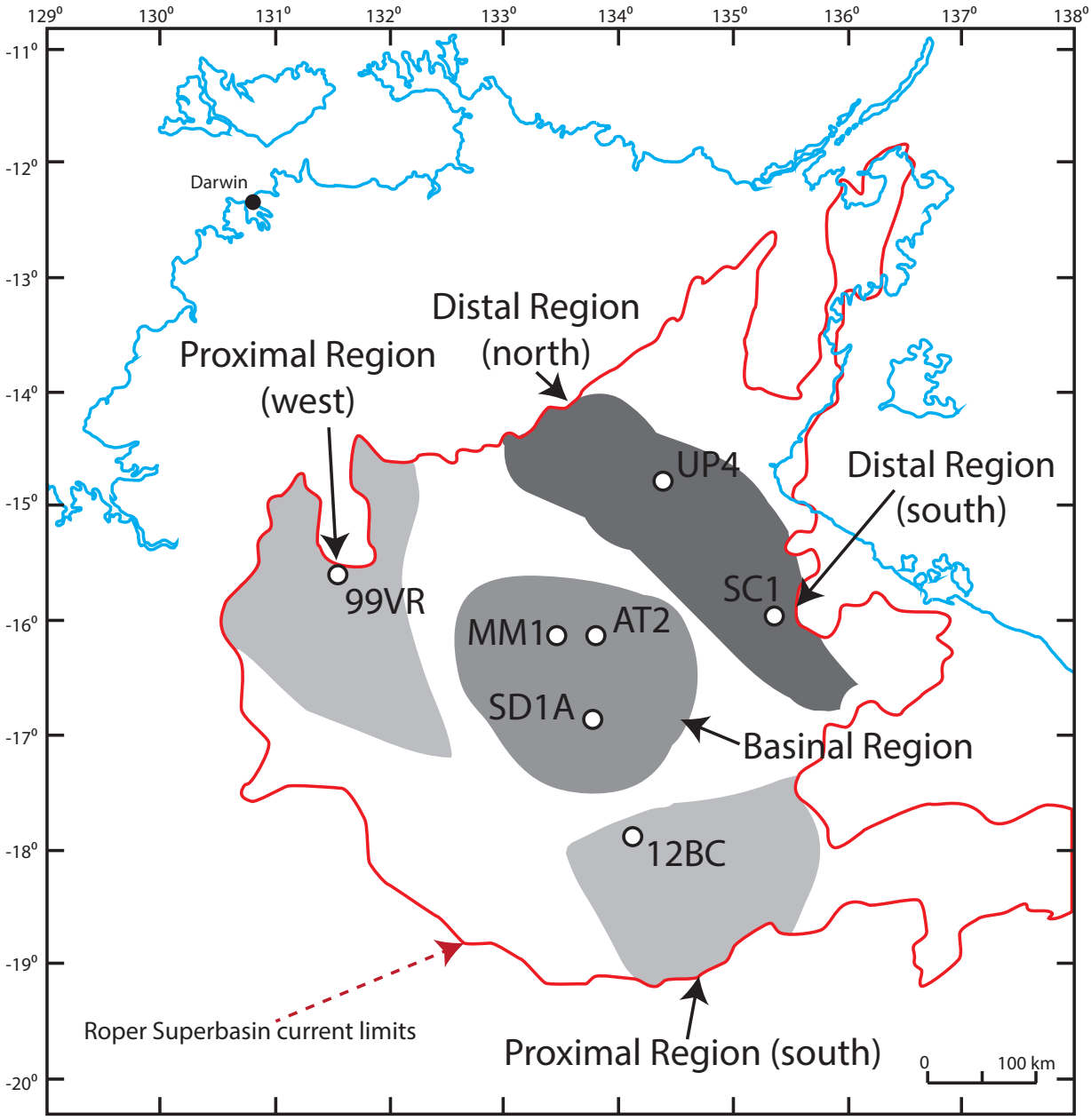

Fig 7: Current known extent of the Roper Superbain and the paleogeographic regions used in this study (Munson, 2016).

Tappania plana, which displays long branching tapering processes and shows evidence of reproductive budding, is found in the ~1400 Ma upper Roper Group alongside *Gigantosphaeridium fibratum*, a very large (~300 µm) taxa that hosts complex spines and processes, and an outer covering of imbricated polygonal organic plates (Javaux et al., 2003; Porter, 2004). These morphological features indicate that the eukaryote cytoskeleton had evolved by Mesoproterozoic time which is required to produce the observed morphological complexity (Javaux 2004, Javuax and Knoll 2017). Yet it is not clear whether Roper Group acritarchs represent stem or crown eukaryotes (Javaux et al., 2003; Porter, 2004; Butterfield, 2015a; Javaux and Knoll, 2017). Both *Tappania* and *Gigantospaeridium* are also found in the equivalently aged Belt Supergroup sediments in

Montana, USA, and in the ~1300 Ma Kamo Group, Siberia (Adam et al.,2017; Javaux and Lepot, 2018). The Kamo Group is thought to record marine shelf deposition on a passive continental margin, but both the Roper Group and Belt Supergroup are interpreted to have accumulated in epicratonic basins. The global occurrence of these taxa suggests that these basins were connected to the open ocean at least briefly during their existence, and that *Tappania* and *Gigantospharidium* had cosmopolitan ecologies (Adam et al.,2017).

Examined cores	Code	Region	Studies
99VRNTGS002	99VR	Proximal (west)	
12BundaraCreek	12BC	Proximal (south)	
Altree-2	AT2	Basinal	Ngyuen *et al* 2018, Jarrett *et al* 2019, Cox *et al* 2016,
Shenandoah-1a	SD1	Basinal	
McMannus-1a	MM1	Basinal	
Urapunga-4	UP4	Distal (North)	Jackson & Raiswell 1991, Shen et al 2003 Abbott & Sweet 2000, Arnold *et al* 2004, Johnston *et al* 2008, Kendall *et al* 2009, Mukherjee & Large 2016, 2018
Scarborough-1	SC1	Distal (south)	Munson & Revie

Other cores	Studies
Urapunga-3	Donnelly & Crick 1988 Johnston et al 2008
Broadmere-1	Jackson & Raiswell 1991 Abbott & Sweet 2000
Goldengrove-1	Abbott & Sweet 2000 Shen et al 2003
Amoco-82/1	Jackson & Raiswell 1991
Amoco-82/3	Shen et al 2003

Table 1: Left – Cores sampled in this study and previous studies. Right – Cores sampled in previous studies.

1.3.4 Multicellular eukaryotes

While unicellular eukaryotes are common in Mesoproterozoic rocks, multicellular forms are rare and their phylogenetic affinities (even to eukaryotes) are ambiguous. Qu et al.,(2018) found macroscopic carbonaceous impressions in shales of the ~1630 Ma Tuanshanzi Formation of northern China. The complex branching forms were interpreted as photosynthetic macroscopic algae living in a supratidal or lagoonal setting. These fossils are also similar to those found in the ~1560 Ma Gaoyuzhuang Formation (Qu et al.,2018). *Grypania spiralis* is a filamentous spiral shaped carbonaceous compression that is commonly several centimeters long. It is found in sediments worldwide, ranging from ~2300 – 600 Ma in age (Porter, 2004). A possible multicellular eukaryote affinity has been proposed on the basis of its large size, but specimens generally do not show any other morphological features, and geochemical analysis has been inconclusive, beyond confirming a biological origin (Porter, 2004; Knoll, 2014). Other interpretations include bacterial colonies and even a single giant bacterium (Samuelsson and Butterfield, 2001; Porter, 2004). However, Knoll et al.,(2006) suggest that the features that are visible indicate that the fossils represent single organisms, not colonial organisms. Additionally, examples of similar fossils found in the ~1450 Ma upper Vindyhan Supergroup (India) are larger and display septation and possible tissue

differentiation and are more convincingly eukaryotic in appearance (Sharma and Shukla, 2009; Sharma et al.,2009).

Sharma et al (2009) conducted a morphometric and biomarker reassessment of various coiled filamentous Proterozoic macrofossils, including *Grypania spiralis*, and concluded that some were probably cyanobacteria colonies while others were shreds of microbial mat and too degraded to identify further. A small subset of the examined fossils contained aliphatic organic material, which may indicate a macroalgal origin, though de Leeuw, Versteegh and van Bergen, (2005) suggest that aliphatics are too broad a group to be taxon specific and could be a diagenetic product of prokaryote biomarkers (but see also Briggs and Summons, 2014). If *Grypania spiralis* is indeed a macroscopic multicellular photosynthetic algae, it would mean the eukaryotic clades would have diverged as early as the Palaeoproterozoic because plants acquired plastids *after* divergence from other eukaryotic clades. Currently the origin and affinities of *Grypania spiralis* remain uncertain and highly contested. *Horodyskia moniliformis* is a proposed multicellular eukaryote originally identified in the ~1500 Ma Appekuny Formation, Montana but has also been identified in upper Ediacaran rocks in China (Porter, 2004; Dong et al.,2008). *Horodyskia* is preserved in siltstones as small rounded mounds up to 3 mm in diameter, which are connected to the substrate by holdfasts and to each other with a subsurface tube. *Horodyskia moniliformis* has been variously interpreted as a fungi, a colonial foraminifera or alga (Fedonkin, 2003; Dong et al.,2008; Retallack et al., 2013). However, others have proposed an abiotic origin for *Horodyskia moniliformis*, such as capture of clay flocs in benthic microbial mats that are common in the same beds as *Horodyskia* fossils (Rule and Pratt, 2019). The poor preservation, lack of morphological detail and lack of associated organic matter or biomarkers makes assigning *Horodyskia moniliformis* as biological, let alone a metazoan eukaryote, extremely difficult and origins and affinities of *Horodyskia* remain unresolved. More convincing multicellular eukaryotes are phosphatised fossils from the ~1600 Chitrakoot Formation, India (Bengtson et al.,2017). These have been argued to be red algae and share morphological and preservational characteristics with younger Ediacaran fossils (Xiao et al.,2004). However, the purported red algal affinity is not without controversy, so too is the age of these rocks (Ray, 2006; Gibson et al.,2018).

As demonstrated above, the eukaryotic 'body' fossil record prior to 1000 Ma is far from certain. Lack of distinct morphological features hamper efforts to assign candidate eukaryotes to particular clades, so molecular clock dates for the divergence of the major groups cannot be calibrated (Porter, 2004). What is certain is that a major step change in the complexity of life took place around 1600 Ma, and it is around this interval when molecular clocks suggest that eukaryogenesis

occurred (Porter, 2020). This change is signalled by the appearance of organic walled organisms with a relative size range and level of structural complexity an order of magnitude greater than that of contemporaneous bacterial fossils (Javaux et al., 2003). These features suggest that, even if not the direct ancestors of later eukaryotes, these organisms were at least probably comparable in complexity and environmental requirements to single celled eukaryotic organisms (Javaux et al.,2002.; Porter, 2020). However, until new fossils are discovered that provide more morphological detail, or there are new ways to interrogate the existing Proterozoic fossil record, these enigmatic fossils are our best direct evidence of the early stages of the emergence and evolution of eukaryotic life on Earth.

1.4 The Geological History of The North Australian Craton

By the late Archean, the cores of the major tectonic blocks of Protoaustralia had already formed. The collision and assembly of these separate blocks began across the Archean – Proterozoic boundary (Ahmad and Hollis, 2013; Munson, 2016). The central portion of the North Australian Craton (NAC) formed within the Neoarchean between ~2670 and 2500 Ma, based on the ages and probable protoliths of the metamorphic rocks that form the cratonic core (e.g., those exposed in the Rum Jungle Complex). These basement rocks are overlain by early Paleoproterozoic metasediments dated to ~2030 – 2000 Ma and deformed ~ 1870 – 1830 Ma in the Pine Creek Orogeny (Ahmad and Hollis, 2013; Munson, 2016). The first major collisional events occurred ~1870 – 1845 Ma as the Kimberly Craton approached from the west. This event was marked by arc magmatism in the Kimberly region and early deformation and metamorphism in the Halls Creek region of the Northern Territory and is associated with the Halls Creek, Tanami and Pine Creek orogens (Ahmad and Hollis, 2013; Munson, 2016). The eastern and south-eastern flank of the central NAC underwent felsic volcanism and uplift as arcs on the north-western edge of the Gawler-Adelie (GAC) craton began to accrete against the NAC. The uplift along margins of the NAC lead to the first episodes of sedimentation in the central region of the NAC, which would become the McArthur Basin (Ahmad and Hollis, 2013; Munson, 2016).

Between ~1840 and 1800 Ma, volcanism and uplift occurred on the south-west margin of the NAC as the small arc terranes to the north of the West Australian Craton (WAC) made initial contact and began to subduct (Ahmad and Hollis, 2013; Munson, 2016). This interval is recorded by the initial formation of the Aileron Province on the southern margin of the NAC. Final accretion of the Kimberly Craton occurred ~1835 – 1810 Ma and produced sedimentation across the eastern and central NAC. Oceanic crustal collision between WAC and NAC occurred at ~1800 –

1770 Ma, causing the Yambah uplift event on the southern NAC margin (Ahmad and Hollis, 2013; Munson, 2016). At around the same time the GAC rotated around the eastern margin of the NAC causing extension and related volcanism, and sedimentation along the eastern margin of the NAC. Following the Yambah event, the WAC rotated eastward around the south-western margin of the NAC from ~1770 – 1730 Ma. This movement caused subduction of WAC oceanic crust beneath the southern NAC margin, and initiated the main phase of uplift and metamorphism in the Aileron Province (Ahmad and Hollis, 2013; Munson, 2016).

Following a hiatus in tectonic events and sedimentation between ~1730 – 1699 Ma, the continent-continent phase of the WAC-NAC collision began. On the south-eastern NAC margin, the GAC transitioned from rotational to compressional movement (Ahmad and Hollis, 2013; Munson, 2016). The tectonic regime change inverted the previously extended rift basins and initiated the earliest stages of the Isa Orogen. On the eastern margin of the GAC, collision with arcs on the outer margin of Laurentia caused rifting and related magmatism (Ahmad and Hollis, 2013; Munson, 2016). In the interval ~1690 – 1650 Ma, slab roll back of minor oceanic crustal plates produced arc magmatism and the accretion of small arc terranes along the southern margin of the NAC. The resulting collisions caused the Warrumpi Orogen, producing further uplift and metamorphism of the Aileron Province (Ahmad and Hollis, 2013; Munson, 2016). Following a period of erosion and sedimentation across the central NAC, a major episode of slab rollback on the southern NAC margin caused the formation and accretion of the Musgrave Province between ~1640 – 1600 Ma. This event caused further deformation and metamorphism of the Warrumpi and Aileron Provinces (Ahmad and Hollis, 2013; Munson, 2016). Associated uplift produced sedimentation across most of the NAC and GAC. Oceanic subduction beneath the Musgrove Province and produced uplift in the Aileron Province and into the north-west of the NAC from ~1600 – 1580 Ma (Ahmad and Hollis, 2013; Munson, 2016). The uplift caused extensive erosion and sedimentation across most of the craton. During the same interval, the Coompania-Tazmania terrane accreted to the southern margin of GAC, completing the South Australian Craton (Ahmad and Hollis, 2013; Munson, 2016).

1.4.1 Proterozoic Basins of the central NAC

The McArthur Basin formed during the final phases of the assembly of Northern Australia ~1850 Ma (Rawlings et al.,2002; Dutkiewicz et al.,2007). Initial basin formation occurred through compressional movements during the Yambah event (~1800 – 1700Ma), followed by extension associated with thermal sag and the emplacement of anorogenic granites from ~1700 – 1580 (Scott et al.,2000). The McArthur Basin developed further during flexural loading following erosion of

uplifted Yambah rocks and transtensional wrenching during the later phases of the Isan Orogeny from 1580 – 1480 Ma (Lindsay and Brasier, 2000; Scott et al.,2000). In general, sedimentation progressed from fluvio-terrestrial in the oldest units moving toward a shallow marine depositional regime in the youngest. However, sedimentation was highly variable on a local scale due to the development of discrete topographic highs and lows that resulted in kilometer-scale lenses of alternating carbonates and evaporites, and siliciclastic sedimentation (Munson and Revie, 2018). The development of these shallow water carbonate and evaporite lenses indicates that the McArthur Basin underwent frequent periods of disconnection from the global ocean. A shallow angular unconformity between McArthur Basin and Roper Superbasin rocks followed a minor period of uplift and subaerial erosion (Ahmad and Hollis, 2013; Munson and Revie, 2018).

1.4.2 Geological History of The Roper Superbasin: Paleo- to early Mesoproterozoic

Formation of the Roper Superbasin began with folding and deformation of pre-Roper sediments and basement during the ~1620 Ma – 1500 Ma phase of the Isa Orogeny to the east and the ~1590 Ma – 1560 Ma phase of the Chewings Orogeny to the south. These events created the Batten and Walker fault zones, which accommodated east – west shortening with oblique transpressional movements. The reactivation of pre-existing faults as reverse-oblique movements accommodated northwest – southeast and additional east – west shortening. Folding and down warping during this time led to the formation of initial accommodation for Roper sedimentation and created the angular unconformity at the top of the McArthur Basin succession (Munson, 2016).

On the western side of the Roper Superbasin, compressional east - west movements related to the Isan and Chewings orogenic events produced the Daly Waters arch. The Daly Waters arch was a major long-lived structural feature that may have been emergent in regressive phases of Roper Group sedimentation (Munson, 2016). Pre-Roper rocks to the west of the Daly Waters arch were tilted to the west, creating a shallow angular unconformity and accommodation space on the eastern edge of the Birrindudu Basin (Munson, 2016). The Isan and Chewings compressional movements also produced minor folding and uplift in the Birrindudu area, which remained a relatively shallow depocenter throughout deposition of Roper Superbasin sediments (Munson, 2016). The formation of a minor depocentre by downward tilting from the Daly Waters arch may explain why Birrindudu sediments are much more locally heterogeneous than other Roper Superbasin sediments (Munson, 2016). Following cessation of Nathan Group deposition, there is an estimated hiatus of ~80 – 90 million years (Munson, 2016). This timing places the onset of lowermost Roper Group sedimentation between ~1500 – 1325 Ma (Munson, 2016).

In contrast to the highly variable localised sedimentation styles seen in the underlying McArthur Basin, sediments of the Roper Superbasin display continuous deposition over several separate sedimentary basins. The distinct and widespread sedimentation style, a change to siliciclastic-dominated sediments and the unconformable contact with McArthur Sediments, prompted the name "Roper Superbasin" to describe the entire sequence (Jackson et al.,1999; Jackson, Scott and Rawlings, 2000; Southgate et al.,2000). The term Wilton Package was proposed as a non-genetic classification by Rawlings, (1999), who divided the entire northern Australian sedimentary sequence into five basinwide disconformity or unconformity bound packages. Rawling (1999) assigned rocks to a particular package on the basis of similar ages, stratigraphic position, lithofacies composition, style and composition of volcanism, and basin-fill geometry.

Both approaches fit the superbasin concept, first proposed by Walter et al.,(1995) of large-scale deposition of discrete sedimentary packages that were continuous or contiguous with other, geographically separated but roughly coeval depocenters. The cyclicity of these packages is hypothesised to have been controlled to the third order by episodic tectonism (Abbott and Sweet, 2000). In this work, the 'Superbasin' scheme of Walter et al (1995) is used as it more accurately reflects the widespread deposition of related sedimentary rocks as observed in this study.

Formation of the Beetaloo Sub-Basin in an aulacogen occurred between 1480 and 1280 Ma, along with localised minor tectonic movements associated with craton reorganisation as fragments of Nuna amalgamated to Rodinia (Donnelly and Crick, 1988; Scott et al.,2000). The whole Superbasin underwent mild inversion in the latest Mesoproterozoic – earliest Neoproterozoic (Rawlings, 1999; Dutkiewicz et al.,2007), which resulted in a regional unconformity between the earlier Mesoproterozoic, and latest Mesoproterozoic and Neoproterozoic sedimentary rocks (Rawlings, 1999; Scott et al.,2000). The mid--to-late Neoproterozoic sedimentary rocks are unconformably overlain by Cambrian to Cretaceous rocks (Munson, 2016).

1.4.3 Geological History of The Roper Superbasin: middle Meso- to early Neoproterozoic

The Bukalorkmi Sandstone and the Chambers River Formation represent the last episodes of Roper Superbasin deposition. Both units are absent from the Beetaloo area and are found only in the sub-surface. These sedimentary rocks continue the regressive-transgressive cyclicity found in older Roper Group sediments, though the finer grained Chambers River Formation never achieves the thickness, or clay to sand ratio, of the underlying Velkerri or Kyalla Formations. These units record a drop in relative sea-level, possibly as basinal subsidence slowed or ceased. The Chambers River Formation also never attains the level of organic enrichment identified in the Velkerri or

Kyalla Formations (Munson, 2016). Another episode of erosion took place between the deposition of the Chambers River Formation and deposition of the overlying Jameson Sandstone and Hayfield Mudstone which are not considered part of the Roper Group and are currently classified as "Ungrouped Units" in the regional stratigraphy (Munson, 2016). Recent work by Yang et al (2019) has constrained the lower Jameson Sandstone to a Stennian age (~ 1092 Ma), and the upper Jameson Sandstone to a Tonian age of ~959 Ma (and, by extension, the conformably overlying Hayfield Mudstone). These data place a conservative gap of ~200 million years between the end of Roper Group deposition and the start of Jameson Sandstone deposition. The upper Roper Group is intruded by a suite of dolerite dykes and sills dated from 1327.5 ± 0.6 Ma to 1312.9 ± 0.7 which are believed to be part of a wider regional suite of intraplate magmatic rock that intruded from ~1330–1300 Ma , helping to further constrain the end of Roper Group deposition (Bororkos, et al., 2021, Collins et al., 2018, Yang, et al (2020). Cryogenian and Ediacaran sediments and volcanics are currently only known from the west of the Roper Superbasin e.g. the Auvergne Group (Munson, 2016).

1.4.4 Post Roper erosion, deformation and Phanerozoic cover

Much of the erosion of Mesoproterozoic and Neoproterozoic sediments probably occurred in the latest Ediacaran during uplift and mild inversion of the Roper Superbasin during the Peterman Orogeny. Following this, there was a major episode of Cambrian carbonate deposition with interspersed siliciclastic sedimentation. These units were then overlain and intruded by the late Cambrian Kalkarindji large igneous province (Munson, 2016). Between the Ordovician and Devonian, much of the NAC was flooded and deposition alternated between shallow carbonates and paralic to near shore siliciclastic deposits during cyclic sea-level changes. Another large unconformity exists between the late Devonian and middle Cretaceous, probably related to sea-level fall and subsequent erosion during the Permo-Carboniferous ice age. From the mid Permian to the mid Cretaceous, much of the central NAC is thought to have been fully terrestrial. It is during this period that erosion and exposure of the Palaeozoic and younger Neoproterozoic sediments occurred (Munson, 2016). From the mid Cretaceous to the mid Palaeocene, the NAC was flooded by a shallow seaway, which was part of the more extensive Eromanga Seaway. The Cretaceous to Paleocene flooding produced a veener of carbonate sedimentation across the NAC (Munson, 2016). However, following a final lowering of sea level in the mid Palaeocene, there has been little subsequent deposition. During the Pleistocene and early Holocene, hot and seasonally wet and dry conditions have produced an intense weathering profile across the NAC. As a consequence,

lateritic soils, karsts, duricrust, silcrete and caliche surfaces are common across the present-day NAC (Munson, 2016).

1.4.5 Present Day Sedimentary Rock Distribution within The Roper Superbasin

I have divided the Roper Superbasin into three distinct regions to aid description and interpretation. The regions are divided on the basis of sedimentary thicknesses, lithology, and the paleogeographic proximity to the ancient landmass that provided the detrital component of the sedimentation (Fig 5, and Table 1).

The Proximal Regions are found in the western and southern areas of the Roper Superbasin and host relatively thin sedimentary successions compared to the Basinal or Distal Regions, e.g. ~400 m in the southern Proximal Region compared to ~1000 m+ in the Basinal Region (Fig 2,).

The Basinal Region is divided into a series of depositional centres, the largest of which is the Beetaloo Sub-basin. The Beetaloo contains the thickest sequence of Roper Group sediments at around ~3km and covers an area of around 15,000 km^2. The extent of the Beetaloo sub-basin has been defined by extensive geophysical data and is supported by both wire line logs and drill cores. A number of smaller sub-basins are found around the Beetaloo but have essentially the same configuration and sediment fill (see Fig 2 and Table 2 for details).

The Distal Region forms a broad shelf that arcs around the Basinal Region from the north to the east. In the east, the Distal Region onlaps the Murphy Inlier, a flat-topped ridge of Archean to Paleoproterozoic-aged crystalline basement that probably represented antecedent topography during Roper Group deposition. In the main Roper Superbasin, the Distal Region is separated from the Basinal Region by the Urapunga, Batten and Walker fault zones. Moving north and east of the fault zone Roper Group sediments are erosionally truncated and older sediments are brought to the surface.

1.4.6 Sedimentology and Stratigraphy of The Roper Superbasin

Sediments of the Roper Group are divided into the lower Corralla Subgroup and the upper Maiwok Subgroup (Fig 6, Munson, 2016). This study focuses on sediments from the upper most Maiwok Subgroup. These sediments represent two cycles of transgression and regression (Abbott and Sweet, 2000, Munson, 2016). Deposition of Maiwok sediments is proposed to have taken place on a broad flat ramp with a shallow seaward dip (to the presentday north), and with the overlying waters in direct communication with the global ocean (Jackson and Raiswell, 1991; Abbott and Sweet, 2000). Highest relative sea levels are represented in the studied succession

by the Velkerri Formation and the Kyalla Formation, both of which are dominantly fine grained and relatively organic-rich siliciclastic units. Both units are found across the Roper Superbasin with their maximum thicknesses (reaching ~900 m for the Velkerri and ~800 m for the Kyalla) in the central Beetaloo sub-basin (Munson 2016). Lowest relative sea level is recorded by the Moroak Sandstone which records deposition in a variety of shallow water settings ranging from near shore to intertidal. The thickness of Maiwok sub-group units varies across the basin but generally thins away from the Beetaloo sub-basin. Locally restricted lithologies in the Maiwok include thin thrombolitic carbonates found in the Proximal Region, and microbial and oolitic ironstones found in the Distal Region (Jackson and Raiswell, 1991; Abbott and Sweet, 2000).

The Wondoan Hill and Stubb Formations of the Tijunna Group and the Battle Creek, Weaner Sandstone, and Bynoe Formations of the Bullita Group, also represent two transgression and regression cycles of a relative sealevel change (Munson, 2016). Deposition of Tijunna and Bullita Group sediments took place in environments ranging from fluvio-terrestrial, sabkha and lagoonal, to upper shore face and carbonate platform. Lowest relative sea levels are recorded by evaporitic sandstones at the base of the Bynoe Formation, and well developed paleosols and fluvial sandstones in the lower to middle Wondoan Hill Formation (Munson, 2016). Locally restricted stromatolitic and thrombolitic carbonates are found in the upper Battle Creek Formation. The Battle Creek carbonates are the thickest and most significant carbonate sediments in the Roper Superbasin. Unusual clastic oncoids are found in the Wondoan Hill Formation and represent a unique environment not seen elsewhere in the Roper Superbasin (Munson, 2016).

1.5 Research Questions

Q: What is the wider depositional context of the RSB?

Given the uncertainty around the correct depositional setting of the wider RSB, and its importance for the broader environmental interpretation, the first goal of this project is to ascertain whether the RSB was a ramp-style shelf in communication with the open ocean, or a different basin geometry with limited oceanic connection. This will help us understand how directly the waters of the RSB mixed with the global and what RSB sediments can tell us, if anything, about mid-Proterozoic oceans.

Q: How heterogenous were depositional environments across the RSB?

Previous work has proposed that sediment deposition and hence the depositional environment was homogenous across the RSB in space and time. I will test this model by examining distantly located core material from the wider RSB and comparing it with previously studied core material. I will use high resolution graphic logging, petrography and geochemistry to correlate units across the RSB. Using the new core material, I will build spatial transects across the basin and describe coeval environmental conditions and changes through proximal, basinal and distal environments during deposition of the Roper Group and explore the significance of our data in the context of early eukaryote and Earth surface evolution.

Q: Was the RSB fully marine and do contemporaneous paralic and terrestrial environments survive?

Previous work has suggested that no demonstratable contemporaneous marine, paralic or terrestrial sediments have survived to the present, and thus have relied on stratigraphically adjacent units to describe environmental change. Previous studies have used these stratigraphically adjacent sedimentary rocks to infer the environmental preferences of early eukaryotes. I will test this model by examining core material selected from areas that are candidates for non-marine deposition on the basis of published tectonic and geophysical studies of the RSB. This will allow me to further test if stratigraphically adjacent environments can be used as a proxy for laterally adjacent environments. This is particularly important where sedimentary rocks from laterally adjacent environments are not available, e.g., they were not preserved, or did not survive to the present day.

Q: Do bulk powder studies accurately capture environmental redox conditions within the RSB?

Bulk powder Fe-speciation and isotope studies of pyrite have formed the core of previous environmental interpretations of the RSB. These studies have assumed that the analysed mineralogy is primary and does not reflect later episodes of diagenesis and alteration. Using petrography, I will examine how well primary sedimentary textures and minerals support this interpretation of published bulk powder data for the studied rocks. Additionally, this will also allow us to investigate the role of diagenesis and alteration in skewing our view of ancient environmental conditions recorded in sedimentary rocks.

Q: Do Ferruginous waters create an Fe(II)-phosphate sink?

Derry (2015) has proposed that Fe-phosphates such as vivianite may have been a major sink for marine P during the Mesoproterozoic, and thus limited primary production by oxygen producing cyanobacteria. However, while vivianite is known as a sedimentary sink for P in modern restricted marine environments and some meromictic lakes, this hypothesis has not been tested against Mesoproterozoic sediments until now. The hypothesis of Derry (2015) will be tested by examining ferruginous sediments using optical petrography, SEM-EDS and bulk powder XRD to identify the variety and quantity of various phosphate minerals.

By answering these questions, I will be able to use my new understanding as a lens to hold against our keyhole into ancient environments of the RSB. I will be able to assess just how accurately we have been viewing the ancient RSB, and if we really can make global interpretations from such relatively small sample sets.

1.6 Methods

1.6.1 Sample and Data Collection

Five drill cores were selected and sampled for this study by me and Rosalie Tostevin. Cores were chosen to provide a north-south and east west transect of the Roper Superbasin (Fig 1). Sampling was conducted at the Northern Territory Geological Survey, Darwin, Australia, and at Geoscience Australia, Canberra, Australia. Each core was selected to provide a representative section through the sedimentary succession in different areas of the Roper Superbasin. Cores were graphically logged at the centimeter scale by me and sampled with a minimum resolution of every 10 m (or greater where complex lithologies was encountered). The core Shenandoah-1a could only be

sampled every 100 m due to limited core availability and no log could be produced directly from the core. A proxy log was produced using wire line data from the drill report and compared with the available core sections and chips.

Where necessary, core sections were trimmed to size on site using a standard industrial diamond tipped saw with water coolant. Material from an additional core, Altree-2 was sampled and provided by Dr Amber Jarrett (Geoscience Australia). Altree-2 was sampled every 10 – 20 m by Dr Jarrett and as I was not present to inspect the core, no graphic log was produced directly from the core. Instead, a log was constructed using high-resolution core scans from the GSA Hylogger system which were compared with published data and samples provided by Dr Jarrett. Altree-2 is also held at the NTGS Darwin facility. Outcrop samples of the Sherwin Ironstone were provided by Grant Cox (University of Adelaide). Physical samples were complimented with digital core images and geochemical data from the NTGS virtual core library called Auscope. Images and geochemical data are provided using the HyLogger system which collects high resolution photographs of cores and infra-red mineral spectra. Using these data, a further 30 cores where incorporated into the current study.

1.6.2 Sample Preparation

Two hundred and ten thin sections were produced by me and technician Jon Wells at the University of Oxford, by Pam Frail at Acadia University, Canada, and Spectra Petrographic, USA. Thin sections were studied using optical microscopy and scanning electron microscopy-energy dispersive X-ray spectroscopy (SEM-EDS) using a FEI Quanta 650 FEG SEM.

Rock powders were prepared from each core sample by powdering in a TEEMA swing mill in a tungsten carbide collar pestle for 30 seconds at 950 rpm. The process was repeated until the produced powder could pass through a 50 μm sieve. For XRD analysis a small quantity of powder was mixed with ethanol and spread on a wafer composed of a single silicon crystal. All samples were analysed for bulk and clay-specific mineralogy at the University of Oxford using a Panalytical Empyrean Series 2 X-ray diffractometer (XRD) equipped with a Co Kα source at 40 kV and 40 mA (Fig 7).

1.7 Thesis Outline

Chapter 2 – Sedimentology and Sequence Stratigraphy of the Roper Superbasin.

In this chapter, previously understudied core material from the Roper Superbasin is described for the first time in detail and interpreted as near shore and terrestrial deposits. Facies analysis is used to build a sequence stratigraphic framework for the studied succession. These new data are compared and correlated to well-studied core material from offshore settings. Current environmental interpretations of the Roper Superbasin are examined in the context of these new data. A new paleogeographic model is proposed for the Roper Superbasin and is discussed in the wider context of Mesoproterozoic environments.

To be submitted to *Australian Journal of Geoscience, McArthur Basin Special Edition* as *Brooke R. Johnson., Rosalie Tostevin., Bruce K. Levell., Peir K. Pufahl., Stuart A. Robinson., and Nicholas J. Tosca., A sedimentological re-evaluation of paleoenvironments in the Mesoproterozoic Roper Superbasin.*

Chapter 3 - Phosphorus burial in ferruginous SiO_2-rich Mesoproterozoic sediments.

This chapter discusses the hypothesis that ferruginous waters sequestered phosphorus as Fe(II)-phosphates. I examine the sedimentology, mineralogy and geochemistry of ferruginous sediments from across the Roper Superbasin. These data are discussed in the context of previous works, which proposed that Proterozoic oceans were deficient in phosphorus relative to the Phanerozoic. The implications of Proterozoic paleogeography on nutrient cycling is also discussed.

Published in *Geology*, January 2020 as *Brooke R. Johnson, Rosalie Tostevin, Philip Gopon, Jon Wells, Stuart A. Robinson, Nicholas J. Tosca. Phosphorus burial in ferruginous SiO_2-rich Mesoproterozoic sediments* Geology (2020) 48 (1): 92–96. https://doi.org/10.1130/G46824.1

Chapter 4 – Unravelling sedimentary redox dynamics within the Velkerri Formation

This chapter re-evaluates the hypothesis that offshore and deep waters (e.g., below storm wave base) were dominantly ferruginous but with periods of water column euxinia during the Mesoproterozoic. These new data are placed in the wider context of the Mesoproterozoic world and biosphere, and the implications for the early evolution of eukaryotes are discussed. The importance of comparing petrographic observations with bulk geochemical analysis is also examined.

To be submitted to Precambrian Research as *Brooke R. Johnson., Rosalie Tostevin., Philip Gopon., Camille Lecouche., Jon Wells., Amber Jarrett., Stuart A. Robinson., and Nicholas J. Tosca., Mineralogical and micro-textural constraints on sedimentary redox: The Mesoproterozoic Velkerri Formation, Roper Superbasin, Northern Australia*

Chapter 5 – Synthesis and discussion of the above work. Results are compared to previous studies and the wider Mesoproterozoic world. Conclusions and ideas for future work are also discussed.

Appendix – detailed graphic logs, acknowledgements, and honesty declaration.

1.7 References

Abbott, S. T. and Sweet, I. P. (2000) "Tectonic control on third-order sequences in a siliciclastic ramp-style basin: An example from the Roper Superbasin (Mesoproterozoic), northern Australia," Australian Journal of Earth Sciences, 47(3), pp. 637–657. doi: 10.1046/j.1440-0952.2000.00795.x.

Adam, Z. R. et al. (2017) "A Laurentian record of the earliest fossil eukaryotes," Geology, 45(5), pp. 387–390. doi: 10.1130/G38749.1.

Ahmad, M. and Hollis, J. A. (2013) "Geology and mineral resources of the Northern Territory," Geology and mineral resources of the Northern Territory, (June).

Alexander, M. et al. (2018) "Cryogenian iron formations in the glaciogenic Kingston Peak Formation , California CA," Precambrian Research, 310(April), pp. 443–462. doi: 10.1016/j.precamres.2018.04.003.

Allwood, A. C. et al. (2009) "Controls on development and diversity of Early Archean stromatolites," Proceedings of the National Academy of Sciences of the United States of America. National Academy of Sciences, pp. 9548–9555. doi: 10.1073/pnas.0903323106.

Bengtson, S. et al. (2017) "Three-dimensional preservation of cellular and subcellular structures suggests 1.6 billion-year-old crown-group red algae," PLOS Biology. Edited by D. Penny, 15(3), p. e2000735. doi: 10.1371/journal.pbio.2000735.

Betts, H. C. et al. (2018) "Integrated genomic and fossil evidence illuminates life's early evolution and eukaryote origin," Nature Ecology and Evolution, 2(10), pp. 1556–1562. doi: 10.1038/s41559-018-0644-x.

Brasier, M. D. and Lindsay, J. F. (1998) "A billion years of environmental stability and the emergence of eukaryotes: new data from northern Australia," Geology, 26(6), pp. 555–558. doi: 10.1130/0091-7613(1998)026<0555:ABYOES>2.3.CO;2.

Briggs, D. E. G. G. and Summons, R. E. (2014) "Ancient biomolecules: Their origins, fossilization, and role in revealing the history of life," BioEssays, 36(5), pp. 482–490. doi: 10.1002/bies.201400010.

Brocks, J. J. et al. (2017) "The rise of algae in Cryogenian oceans and the emergence of animals," Nature, 548(7669), pp. 578–581. doi: 10.1038/nature23457.

Brocks, J.J., Nettersheim, B.J., 2020. Lost world of complex life: Molecular traces of our deep eukaryotic ancestors [WWW Document]. URL https://goldschmidtabstracts.info/abstracts/abstractView?doi=10.46427/gold2020.263 (accessed 7.15.21).

Bouwknegt, J., Wiersma, S.J., Ortiz-Merino, R.A., Doornenbal, E.S.R., Buitenhuis, P., Giera, M., Müller, C., Pronk, J.T., 2021. A squalene-hopene cyclase in Schizosaccharomyces japonicus represents a eukaryotic adaptation to sterol-independent anaerobic growth. bioRxiv 2021.03.17.435848. https://doi.org/10.1101/2021.03.17.435848

Buckler, K. J. (2012) "Effects of exogenous hydrogen sulphide on calcium signalling, background (TASK) K channel activity and mitochondrial function in chemoreceptor cells," Pflugers Archiv European Journal of Physiology, 463(5), pp. 743–754. doi: 10.1007/s00424-012-1089-8.

Butterfield, N. J. (2015a) "Early evolution of the Eukaryota," Palaeontology, 58(1), pp. 5–17. doi: 10.1111/pala.12139.

Butterfield, N. J. (2015b) "Proterozoic photosynthesis - a critical review," Palaeontology, 58(6), pp. 953–972. doi: 10.1111/pala.12211.

Cawood, P. A. and Hawkesworth, C. J. (2014) "Earth's middle age," Geology, 42(6), pp. 503–506. doi: 10.1130/G35402.1.

Cohen, P. A. et al. (2017) "Controlled hydroxyapatite biomineralization in an ~810 million-year-old unicellular eukaryote," Science Advances, 3(6), pp. 1–9. doi: 10.1126/sciadv.1700095.

Cohen, P. A., Knoll, A. H. and Kodner, R. B. (2009) "Large spinose microfossils in Ediacaran rocks as resting stages of early animals," Proceedings of the National Academy of Sciences of the United States of America, 106(16), pp. 6519–6524. doi: 10.1073/pnas.0902322106.

Cohen, P. A. and Macdonald, F. A. (2015) "The Proterozoic Record of Eukaryotes," Paleobiology, 41(4), pp. 610–632. doi: 10.1017/pab.2015.25.
Derry, L. A. (2015) "Causes and consequences of mid-Proterozoic anoxia," Geophysical Research Letters, 42(20), pp. 8538–8546. doi: 10.1002/2015GL065333.
Dong, L. et al. (2008) "Silicified Horodyskia and Palaeopascichnus from upper Ediacaran cherts in South China: Tentative phylogenetic interpretation and implications for evolutionary stasis," Journal of the Geological Society, 165(1), pp. 367–378. doi: 10.1144/0016-76492007-074.
Donnelly, T. H. and Crick, I. H. (1988) "Depositional environment of the middle proterozoic velkerri formation in Northern Australia: Geochemical evidence," Precambrian Research, 42(1–2), pp. 165–172. doi: 10.1016/0301-9268(88)90015-0.
Dutkiewicz, A. et al. (2007) "Precambrian inclusion oils in the Roper Group: A review," In: Proceedings of the Central Australian Basins Symposium (CABS), Alice Springs, Northern Territory, 16–18 August, 2005, (eds. T.J. Munson and G.J. Ambrose), Northern Territory Geological Survey, Special Publication, 2(July 2007), pp. 326–348.
Ernst, R. E. et al. (2008) "Global record of 1600-700 Ma Large Igneous Provinces (LIPs): Implications for the reconstruction of the proposed Nuna (Columbia) and Rodinia supercontinents," Precambrian Research, 160(1–2), pp. 159–178. doi: 10.1016/j.precamres.2007.04.019.
Fedonkin, M. A. (2003) "The origin of the Metazoa in the light of the Proterozoic fossil record," Paleontological Research, 7(1), pp. 9–41. doi: 10.2517/prpsj.7.9.
Fischer, W. W., Hemp, J. and Johnson, J. E. (2016) "Evolution of Oxygenic Photosynthesis," Annual Review of Earth and Planetary Sciences, 44(1), pp. 647–683. doi: 10.1146/annurev-earth-060313-054810.
Froelich, P.N., Klinkhammer, G.P., Bender, M.L., Luedtke, N.A., Heath, G.R., Cullen, D., Dauphin, P., Blaynehartman, D.Hammond., 1979. Early oxidation of organic matter in pelagic sediments of the eastern equatorial Atlantic: suhoxic diagenesis 16.
Gibson, T. M. et al. (2018) "Precise age of Bangiomorpha pubescens dates the origin of eukaryotic photosynthesis," 46(2), pp. 6–9.
Gumsley, A. P. et al. (2017) "Timing and tempo of the great oxidation event," Proceedings of the National Academy of Sciences of the United States of America, 114(8), pp. 1811–1816. doi: 10.1073/pnas.1608824114.
Huntley, J. W., Xiao, S. and Kowalewski, M. (2006) "1.3 Billion years of acritarch history: An empirical morphospace approach," Precambrian Research, 144(1–2), pp. 52–68. doi: 10.1016/j.precamres.2005.11.003.
Jackson, M. J. et al. (1986) "Hydrocarbon shows and petroleum source rocks in sediments as old as 1.7 × 109 years," Nature, 322(6081), pp. 727–729. doi: 10.1038/322727a0.
Jackson, M. J. et al. (1999) "The South Nicholson and Roper Groups: evidence for the early Mesoproterozoic Roper Superbasin," Integrated Basin Analysis of the Isa Superbasin using Seismic, Well-log, and Geopotential Data: An Evaluation of the Economic Potential of the Northern Lawn Hill Platform: Canberra, Australia, Australian Geological Survey Organisation Record, 19.
Jackson, M. J. J. and Raiswell, R. (1991) "Sedimentology and carbon-sulphur geochemistry of the Velkerri Formation, a mid-Proterozoic potential oil source in northern Australia," Precambrian Research, 54(1), pp. 81–108. doi: 10.1016/0301-9268(91)90070-Q.
Jackson, M. J., Scott, D. L. and Rawlings, D. J. (2000) "Stratigraphic framework for the Leichhardt and Calvert superbasins: Review and correlations of the pre-1700 Ma successions between Mt Isa and McArthur River," Australian Journal of Earth Sciences. Taylor & Francis Group , pp. 381–403. doi: 10.1046/j.1440-0952.2000.00789.x.
Javaux, E. J. and Knoll, A. H. (2017) "Micropaleontology of the lower Mesoproterozoic Roper Group, Australia, and implications for early eukaryotic evolution," Journal of Paleontology, 91(2), pp. 199–229. doi: 10.1017/jpa.2016.124.
Javaux, E. J., Knoll, A. H. and Walter, M. (2003) "Recognizing and Interpreting the Fossils of," Origins of Life and Evolution of the Biosphere, (April 2002), pp. 75–94.
Javaux, E. J. and Lepot, K. (2018) "The Paleoproterozoic fossil record: Implications for the evolution of the biosphere during Earth's middle-age," Earth-Science Reviews, 176(September 2017), pp. 68–86. doi: 10.1016/j.earscirev.2017.10.001.
Johnson, B. R. et al. (2020) "Phosphorus burial in ferruginous SiO2-rich Mesoproterozoic sediments," Geology, 48(1), pp. 92–96. doi: 10.1130/G46824.1.
Knoll, A. H. (1996) "Breathing room for early animals," Nature, 382(6587), pp. 111–112. doi: 10.1038/382111a0.

Knoll, A. H. et al. (2006) "Eukaryotic organisms in Proterozoic oceans," Philosophical Transactions of the Royal Society B: Biological Sciences, 361(1470), pp. 1023–1038. doi: 10.1098/rstb.2006.1843.
Knoll, A. H. (2014) "Paleobiological perspectives on early eukaryotic evolution," Cold Spring Harbor Perspectives in Biology, 6(1), p. a016121. doi: 10.1101/cshperspect.a016121.
Knoll, A. H. (2015) "Paleobiological perspectives on early microbial evolution," Cold Spring Harbor Perspectives in Biology, 7(7), pp. 1–17. doi: 10.1101/cshperspect.a018093.
Knoll, A. H. and Lahr, D. (2016) "Fossils, Feeding, and the Evolution of Complex Multicellularity," in Multicellularity. The MIT Press. doi: 10.7551/mitpress/10525.003.0006.
Laakso, T.A., Schrag, D.P., 2014. Regulation of atmospheric oxygen during the Proterozoic. Earth Planet. Sci. Lett. 388, 81–91. https://doi.org/10.1016/j.epsl.2013.11.049
Lambert, I. B. and Donnelly, T. H. (1991) "Atmospheric oxygen levels in the precambrian: a review of isotopic and geological evidence," Global and Planetary Change, 5(1–2), pp. 83–91. doi: 10.1016/0921-8181(91)90129-K.
Lane, N. and Martin, W. (2010) "The energetics of genome complexity," Nature, 467(7318), pp. 929–934. doi: 10.1038/nature09486.
Large, R., 2014. The boring billion. Australas. Sci. 35, 22–25. https://doi.org/10.3316/ielapa.520236687944675
de Leeuw, J. W., Versteegh, G. J. M. and van Bergen, P. F. (2005) "Biomacromolecules of algae and plants and their fossil analogues," in Plants and Climate Change. Springer Netherlands, pp. 209–233. doi: 10.1007/978-1-4020-4443-4_14.
Li, S. et al. (2019) "Global Meso-Neoproterozoic plate reconstruction and formation mechanism for Precambrian basins: Constraints from three cratons in China," Earth-Science Reviews, 198, p. 102946. doi: 10.1016/J.EARSCIREV.2019.102946.
Lindsay, J. F. and Brasier, M. D. (2000) "A carbon isotope reference curve for ca. 1700-1575 Ma, McArthur and Mount Isa Basins, northern Australia," Precambrian Research, 99(3–4), pp. 271–308. doi: 10.1016/S0301-9268(99)00062-5.
Liu, C. et al. (2019) "The same and not the same: Ore geology, mineralogy and geochemistry of Rodinia assembly versus other supercontinents," Earth-Science Reviews, 196(October 2018), p. 102860. doi: 10.1016/j.earscirev.2019.05.004.
Lyons, T. W., Reinhard, C. T. and Planavsky, N. J. (2014) "The rise of oxygen in Earth's early ocean and atmosphere," Nature, 506(7488), pp. 307–315. doi: 10.1038/nature13068.
Marais, D. J. Des (1991) "Microbial mats, stromatolites and the rise of oxygen in the Precambrian atmosphere," Palaeogeography, Palaeoclimatology, Palaeoecology, 97, pp. 93–96.
März, C. et al. (2018) "Phosphorus dynamics around the sulphate-methane transition in continental margin sediments : Authigenic apatite and Fe (II) phosphates," Marine Geology, 404(July), pp. 84–96. doi: 10.1016/j.margeo.2018.07.010.
Matear, R.J., Hirst, A.C., 2003. Long-term changes in dissolved oxygen concentrations in the ocean caused by protracted global warming. Glob. Biogeochem. Cycles 17, n/a-n/a. https://doi.org/10.1029/2002GB001997
Munson, T. J. (2016) NO RTH E R N TE R R ITO RY G EO LOG I CA L SURV E Y NTGS RECORD 2016-003 Sedimentary characterisation of the Wilton package , greater McArthur Basin , Northern Territory.
Munson, T. J. and Revie, D. J. (2018) NO RTH E R N TE R R ITO RY G EO LOG I CA L SURV E Y NTGS RECORD 2018-006 Stratigraphic subdivision of the Velkerri Formation , Roper Group , McArthur Basin , Northern Territory.
Muscente, A. D., Hawkins, A. D. and Xiao, S. (2015) "Fossil preservation through phosphatization and silicification in the Ediacaran Doushantuo Formation (South China): A comparative synthesis," Palaeogeography, Palaeoclimatology, Palaeoecology, 434, pp. 46–62. doi: 10.1016/j.palaeo.2014.10.013.
Panzik, J. E. et al. (2016) "Using palaeomagnetism to determine late Mesoproterozoic palaeogeographic history and tectonic relations of the Sinclair terrane, Namaqua orogen, Namibia," Geological Society Special Publication, 424(1), pp. 119–143. doi: 10.1144/SP424.10.
Pehrsson, S. J. et al. (2016) "Metallogeny and its link to orogenic style during the Nuna supercontinent cycle," Geological Society, London, Special Publications, 424(1), pp. 83–94. doi: 10.1144/SP424.5.
Pisarevsky, S. A. et al. (2014) "Mesoproterozoic paleogeography: Supercontinent and beyond," Precambrian Research, 244(1), pp. 207–225. doi: 10.1016/j.precamres.2013.05.014.
Porter, S. M. (2004) "The fossil record of early eukaryotic diversification," Paleontological Society Papers, 10(December), pp. 35–50. doi: 10.1017/s1089332600002321.

Porter, S.M., 2020. Insights into eukaryogenesis from the fossil record. Interface Focus 10, 20190105. https://doi.org/10.1098/rsfs.2019.0105

Porter, S. M., Agić, H. and Riedman, L. A. (2018) "Anoxic ecosystems and early eukaryotes," Emerging Topics in Life Sciences, (July), p. ETLS20170162. doi: 10.1042/ETLS20170162.

Porter, S. M. and Knoll, A. H. (2000) "Testate amoebae in the Neoproterozoic Era: evidence from vase-shaped microfossils in the Chuar Group, Grand Canyon," Paleobiology. 2016/02/08, 26(3), pp. 360–385. doi: DOI: 10.1666/0094-8373(2000)026<0360:TAITNE>2.0.CO;2.

Poulton, S. W. and Canfeld, D. E. (2011) "Ferruginous conditions: A dominant feature of the ocean through Earth's history," Elements, 7(2), pp. 107–112. doi: 10.2113/gselements.7.2.107.

Qu, Y. et al. (2018) "Carbonaceous biosignatures of the earliest putative macroscopic multicellular eukaryotes from 1630 Ma Tuanshanzi Formation, north China," Precambrian Research, 304(November 2017), pp. 99–109. doi: 10.1016/j.precamres.2017.11.004.

Rasmussen, B. et al. (2020) "A 1.25 ga depositional age for the 'Paleoproterozoic' mapedi red beds, kalahari manganese field, South africa: New constraints on the timing of oxidative weathering and hematite mineralization," Geology, 48(1), pp. 44–48. doi: 10.1130/G46707.1.

Rawlings, D. J. (1999) "Stratigraphic resolution of a multiphase intracratonic basin system: The McArthur Basin, northern Australia," Australian Journal of Earth Sciences, 46(5), pp. 703–723. doi: 10.1046/j.1440-0952.1999.00739.x.

Rawlings, D. J. et al. (2002) "The 2002 Southern McArthur I N F O R M AT I O N The 2002 Southern McArthur Basin Seismic Reflection Survey The 2002 Southern McArthur Basin Seismic Reflection Survey."

Ray, J. S. (2006) "Age of the Vindhyan Supergroup: A review of recent findings," Journal of Earth System Science. Springer, pp. 149–160. doi: 10.1007/BF02703031.

Reinhard, C. T. et al. (2017) "Evolution of the global phosphorus cycle," Nature, 541(7637), pp. 386–389. doi: 10.1038/nature20772.

Reinhard, C. T. et al. (2020) "The impact of marine nutrient abundance on early eukaryotic ecosystems," Geobiology, (November 2019), p. gbi.12384. doi: 10.1111/gbi.12384.

Retallack, G. J., Dunn, K. L. and Saxby, J. (2013) "Problematic Mesoproterozoic fossil Horodyskia from Glacier National Park, Montana, USA," Precambrian Research, 226, pp. 125–142. doi: 10.1016/j.precamres.2012.12.005.

Roberts, N. M. W. (2013) "The boring billion? - Lid tectonics, continental growth and environmental change associated with the Columbia supercontinent," Geoscience Frontiers, 4(6), pp. 681–691. doi: 10.1016/j.gsf.2013.05.004.

Rooney, A. D. et al. (2015) "A Cryogenian chronology: Two long-lasting synchronous neoproterozoic glaciations," Geology, 43(5), pp. 459–462. doi: 10.1130/G36511.1.

Rule, R. G. and Pratt, B. R. (2019) "The pseudofossil Horodyskia: Flocs and flakes on microbial mats in a shallow Mesoproterozoic sea (Appekunny Formation, Belt Supergroup, western North America)," Precambrian Research, 333, p. 105439. doi: 10.1016/j.precamres.2019.105439.

Runnegar, B. (1991) "Precambrian oxygen levels estimated from the biochemistry and physiology of early eukaryotes," Global and Planetary Change, 5(1–2), pp. 97–111. doi: 10.1016/0921-8181(91)90131-F.

Samuelsson, J. and Butterfield, N. J. (2001) "Neoproterozoic fossils from the Franklin Mountains, northwestern Canada: Stratigraphic and palaeobiological implications," Precambrian Research, 107(3–4), pp. 235–251. doi: 10.1016/S0301-9268(00)00142-X.

Schiffbauer, J. D. et al. (2014) "A unifying model for Neoproterozoic-Palaeozoic exceptional fossil preservation through pyritization and carbonaceous compression," Nature Communications, 5(1), pp. 1–12. doi: 10.1038/ncomms6754.

Scott, D. L. et al. (2000) "Basement framework and geodynamic evolution of the Palaeoproterozoic superbasins of north-central Australia: An integrated review of geochemical, geochronological and geophysical data," Australian Journal of Earth Sciences. Taylor & Francis Group , pp. 341–380. doi: 10.1046/j.1440-0952.2000.00793.x.

Sergeev, V. N., Knoll, A. H. and Vorob'Eva, N. G. (2011) "Ediacaran Microfossils from the Ura Formation, Baikal-Patom Uplift, Siberia: Taxonomy and Biostratigraphic Significance," Journal of Paleontology, 85(5), pp. 987–1011. doi: 10.1666/11-022.1.

Shang, X., Liu, P. and Moczydłowska, M. (2019) "Acritarchs from the Doushantuo Formation at Liujing section in Songlin area of Guizhou Province, South China: Implications for early–middle Ediacaran biostratigraphy," Precambrian Research, 334, p. 105453. doi: 10.1016/j.precamres.2019.105453.

Sharma, M. et al. (2009) “On the affinity of Chuaria-Tawuia complex: A multidisciplinary study,” Precambrian Research, 173(1–4), pp. 123–136. doi: 10.1016/j.precamres.2009.04.003.
Sharma, M. and Shukla, Y. (2009) “Taxonomy and affinity of Early Mesoproterozoic megascopic helically coiled and related fossils from the Rohtas Formation, the Vindhyan Supergroup, India,” Precambrian Research, 173(1–4), pp. 105–122. doi: 10.1016/j.precamres.2009.05.002.
Shen, Y., Knoll, A. H. and Walter, M. R. (2003) “Evidence for low sulphate and anoxia in a mid-Proterozoic marine basin,” Nature, 423(6940), pp. 632–635. doi: 10.1038/nature01651.
Slomp, C.P., Mort, H.P., Jilbert, T., Reed, D.C., Gustafsson, B.G., Wolthers, M., 2013. Coupled Dynamics of Iron and Phosphorus in Sediments of an Oligotrophic Coastal Basin and the Im-pact of Anaerobic Oxidation of Methane. PLoS ONE 8, e62386. https://doi.org/10.1371/journal.pone.0062386
Soo, R. M. et al. (2017) “On the origins of oxygenic photosynthesis and aerobic respiration in Cyanobacteria,” Science, 355(6332), pp. 1436–1440. doi: 10.1126/science.aal3794.
Southgate, P. N. et al. (2000) “Chronostratigraphic basin framework for Palaeoproterozoic rocks (1730-1575 Ma) in northern Australia and implications for base-metal mineralisation,” Australian Journal of Earth Sciences, 47(3), pp. 461–483. doi: 10.1046/j.1440-0952.2000.00787.x.
Tang, Q. et al. (2020) “A one-billion-year-old multicellular chlorophyte,” Nature Ecology and Evolution, 4(4), pp. 543–549. doi: 10.1038/s41559-020-1122-9.
Towe, K. M. (1970) “1970_Towe_-_Oxygen-collagen priority and the early metazoan fossil record.pdf,” 65(4), pp. 781–788.
Walter, M. R. et al. (1995) “Neoproterozoic stratigraphy of the Centralian Superbasin, Australia,” Precambrian Research, 73(1–4), pp. 173–195. doi: 10.1016/0301-9268(94)00077-5.
Williams, G. E. (1968) “Torridonian weathering, and its bearing on Torridonian palaeoclimate and source,” Scottish Journal of Geology, 4(2), pp. 164–184. doi: 10.1144/sjg04020164.
Williams, G. E. and Schmidt, P. W. (1997) “Paleomagnetism of the Paleoproterozoic Gowganda and Lorrain formations, Ontario: Low paleolatitude for Huronian glaciation,” Earth and Planetary Science Letters, 153(3–4), pp. 157–169. doi: 10.1016/s0012-821x(97)00181-7.
Xiao, S. et al. (2004) “Phosphatized multicellular algae in the Neoproterozoic Doushantuo Formation, China, and the early evolution of florideophyte red algae,” American Journal of Botany, 91(2), pp. 214–227. doi: 10.3732/ajb.91.2.214.
Yuan, Y. et al. (2019) “Implication of Mesoproterozoic (□ 1 . 4 Ga) magmatism within microcontinents along the southern Central Asian Orogenic Belt,” Precambrian Research, 327(March), pp. 314–326. doi: 10.1016/j.precamres.2019.03.014.
Zhang, S. H. et al. (2017) “The 1.33–1.30 Ga Yanliao large igneous province in the North China Craton: Implications for reconstruction of the Nuna (Columbia) supercontinent, and specifically with the North Australian Craton,” Earth and Planetary Science Letters, 465, pp. 112–125. doi: 10.1016/j.epsl.2017.02.034.

2. Sedimentology and Sequence stratigraphy of the Roper Superbasin

Abstract The apparent delay in the initial evolution of eukaryotic organisms and their first morphological diversification, is still a topic of much debate. One hypothesis states that low atmospheric pO_2 lead to a scarcity of bioavailable limiting nutrients such as P. As a result of this limitation early eukaryotes could not ecologically compete with prokaryotes. Thus, eukaryotes remained of minor ecological importance until the late Proterozoic. This hypothesis of "permissive evolution" is seemingly supported by geochemical, palaeontological and geobiological evidence obtained from the Proterozoic sedimentary record. However, many of these data come from bulk sediment sampling where limited sample material prevented these data from being placed within their full paleoenvironmental and paleogeographic context. The ~1.4-1.3 Ga Roper Superbasin (RSB), Northern Territory, Australia, is one of the best preserved and most studied Mesoproterozoic sedimentary successions and so provides an ideal opportunity to test the permissive evolution hypothesis. However, existing paleoenvironmental and paleogeographic reconstructions of the RSB were created when only limited core and outcrop material were available and so questions remain as to the environmental context of data generated from these sediments. In order to address this problem, I conducted a high-resolution sampling, core logging, petrographic, and XRD study of seven drill cores which intersect the upper Roper and Tijunna groups in the upper part of the RSB succession. This data set was combined with a meta-study of publicly available photographic, geochemical, and wireline data from an additional 13 cores provided by the Northern Territory Geological Survey and Geoscience Australia. These data sets were synthesised with published data on the regional geology in order to provide a wider regional context. In agreement with published work, my data indicates that deposition of upper RSB sediments took place during a 3rd order transgressive-regressive cycle. This was probably a result of sedimentary loading of the basinal depocenter as a consequence of uplift in the hinterlands. The 3rd order cycle is overprinted by several 4th order cycles whose magnitude and presentation style varies across the basin. These 4th order cycles may have been controlled by local tectonics and regional rifting, however the current data set lacks the spatial and temporal resolution to confirm this. Using the core SD1 as a centerpoint Sequence stratigraphic analysis shows that transgressive facies advance from the present day north to south, with the thickest packages of sediment found in the Beetaloo region, and relatively proximal to the paleo coast. Sedimentary and petrographic data show that fine grained sediment transport was driven by storm generated wave enhanced sediment gravity flows in addition to hyperpycnal deposition, indicating that the seabed was mostly within storm wave base throughout the transgression. During regressive stages, paralic and terrestrial facies prograde from the west, south-southeast, and from the north-northeast. These data suggest that a) the dip of the RSB was probably shallow and in the order of 0.1-0.001º with a rapidly subsiding proximal fore-deep, b) the seafloor in distal areas of the basin was relatively shallow and was emergent during regression, and c) rather than a simple ramp geometry dipping to the north into open ocean, the RSB was probably a large, restricted embayment or seaway. In this regard, the RSB is analogous to more recent cratonic basins such as those in the Cretaceous Western Interior Seaway of North America. Thus, the RSB was probably subject to strong local geochemical signatures which may have overprinted any influence from the global ocean. Additionally, geographically and geometrically comparable cratonic basins from the Phanerozoic were prone to episodes of localised marine anoxia, even under atmospheric pO_2 levels comparable to the modern day. In light of this, evidence for anoxic sediments and waters within the RSB does not necessarily imply globally widespread marine anoxia and by extension, a low oxygen atmosphere. Finally, as cratonic basins such as the RSB form a significant part of the Proterozoic sedimentary archive, it is likely that our view of Proterozoic life and environments has been skewed by this preservational bias which may have made mid-Proterozoic epicratonic basins appear bathymetrically deeper and more anoxic that they probably were.

2.1. Introduction

The timing and tempo of the early eukaryote evolution is thought to be closely tied to the oxygenation of the Earth's surface (Javaux et al., 2003; Porter, 2020; Porter et al., 2018). One interpretation of this "permissive evolution" hypothesises is that low atmospheric pO_2 levels greatly reduced the rate of continental weathering, and hence the input of limiting nutrients such as P into the global ocean (Laakso and Schrag, 2019, 2018, 2014). Limiting the bioavailable P pool would have reduced primary productivity by oxygenic phototrophs, and as a consequence limited O_2 production and carbon burial, producing a low O_2 feedback cycle. Additionally, largely anoxic Fe-rich (ferruginous) oceans are also thought to have been a consequence of low atmospheric and dissolved pO_2 (Poulton and Canfield, 2011). It has been proposed that widespread ferruginous conditions would sequester P in sediments as Fe(II)-phosphates such as vivianite, further reducing the pool of bioavailable P (Derry, 2015). The P limitation hypothesis is seemingly supported by geochemical data obtained from Proterozoic sedimentary rocks which show a significant increase in sedimentary P contents during the mid-Neoproterozoic and Phanerozoic, relative to the Proterozoic and Archean (Reinhard et al., 2017). In oligotrophic conditions such as those described here, anoxygenic phototrophic prokaryotes are able to out-compete both oxygenic phototrophic prokaryotes and eukaryotes (Reinhard et al., 2020). Subsequently early eukaryotes may to have been restricted to shallow coastal areas which are thought to have been relatively richer in dissolved O_2 and P, an inference seemingly supported by palaeontological data (Javaux and Knoll, 2017).

Geochemical data are central to our understanding of the environments occupied by early eukaryotic life (e.g., Johnston et al., 2008). Bulk powder sampling and analytical methods in particular allow the production of large data sets that span multimillion year intervals within a given sedimentary succession. Just as it is necessary to characterise and understand metamorphism and weathering affecting samples of such great age (e.g., Johnson et al., 2020), it is also necessary to have a sound understanding of the wider sequence stratigraphic and depositional context to extract the most information from geochemical data sets. However, this latter point may not be possible due to the limitations posed by lack of available material.

To investigate how sequence stratigraphic and sedimentological data may change our interpretations of the ~1.4 – 1.3 Ga Roper Superbasin (RSB), Northern Territory, Australia, I conducted a high-resolution sampling, graphic logging, sedimentological, petrographic and X-ray diffraction (XRD) study. The RSB is a key archive in the study of the Mesoproterozoic evolution of early eukaryotes and Earth surface environments (Cox et al., 2016; Jarrett et al., 2019; Javaux and Knoll, 2017; Munson, 2016). While outcrop is geographically limited, and has been subject to intense

lateritic weathering, a 30+ year mineral and hydrocarbon exploration program has resulted in abundant drill core and associated data. Additionally, the sedimentary rocks of the RSB are some of the most well studied, and so there is a large library of data for comparison.

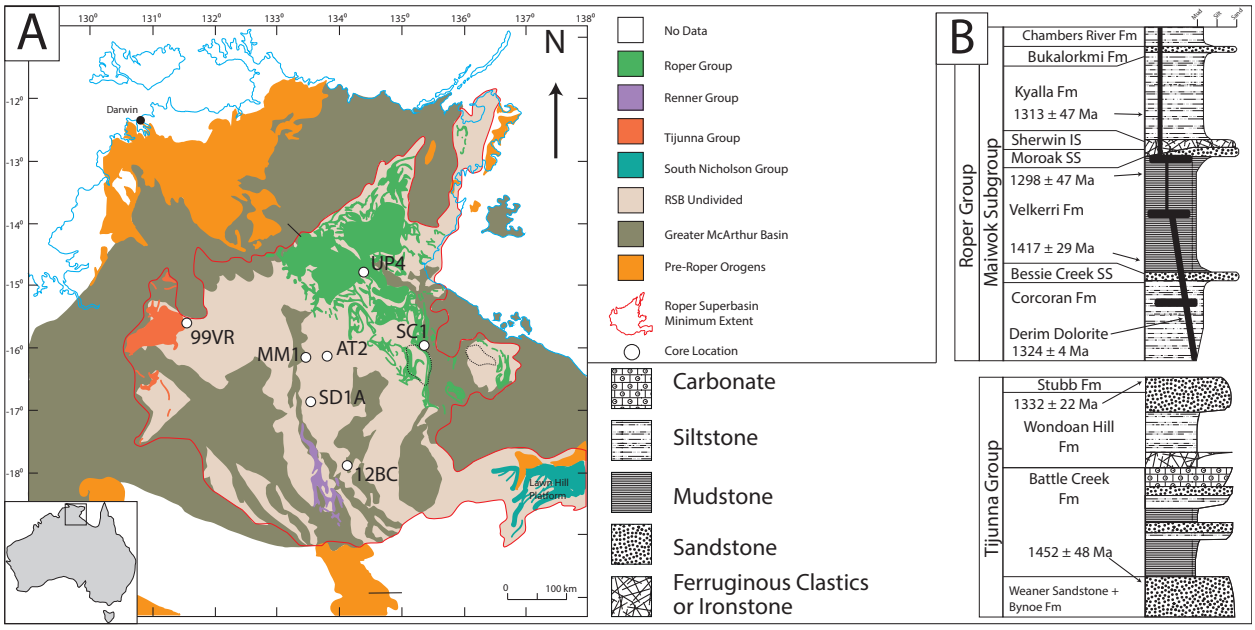

Figure 1: A) Simplified geological map of the study area showing the core locations. B) Simplified stratigraphy of the upper Roper and Tijunna Groups (Yang et al, 2018, Munson, 2016).

Abbott and Sweet, (2000), was the most recent work to place the RSB succession into a sequence stratigraphic framework, but was limited to a small number of cores and outcrop in the east-north east of the RSB. Abbott and Sweet, (2000) concluded that accommodation within the RSB was controlled by 3rd order relative sea level changes resulting from subsidence driven by sediment loading from erosion in the uplifted hinterlands. Supported by earlier work on the same suite of cores by Jackson and Raiswell, (1991), recent geochemical studies have suggested deposition of RSB sediments took place in an anoxic basin, perhaps as deep as 100+ m, and in communication with the global ocean (though see Donnelly and Crick, 1988 for an alternative view). Subsequently, the studies of Abbott and Sweet (2000) and Jackson and Raiswell (1991) have been used as the basis for depositional and environmental interpretations of geochemical data from the RSB over the last twenty years e.g., Johnston et al., 2008; Kendall et al., 2009; Shen, 2002. Another consequence of using geographically close material is that lateral variation in depositional environment must be inferred from stratigraphic successions using Walther's Law. This means that paleoenvironmental change within the RSB has high temporal but low lateral resolution. Therefore, the second aim of this study is to test existing models of lateral variation within the RSB.

2.2. Geological Setting

The Roper Superbasin is a series of contemporaneous epicratonic basins located across northern Australia in (from east to west) Queensland, the northernmost Northern Territory, and north eastern Western Australia (Munson, 2016). The area experienced deposition of dominantly siliciclastic sediments between ~1600 – 1300 Ma. The RSB is the youngest of four unconformity-bound sedimentary packages of the greater McArthur Basin (Munson, 2016). Formation of the RSB began ~1600 Ma with subsidence and reactivation of normal faults in the underlying Isa Superbasin (Munson, 2016). Sedimentation began ~1500 Ma, following uplift on the western and southern margins of the RSB during the later stages of the assembly of Protoaustralia (Munson, 2016). Sedimentation in the RSB continued with few geologically significant gaps until at least ~1300 Ma (Munson, 2016; Yang et al., 2019).

Despite their age, Roper Superbasin sediments have undergone only negligible deformation and limited, highly localised, low-grade contact metamorphism (Munson, 2016). Sediment fill is packaged into six transgressive sequences of basinal shales and proximal sands, bound by surfaces interpreted by Abbott and Sweet (2000) as intra-cycle erosional surfaces. These 3rd order stratigraphic patterns have been interpreted to reflect the influence of local flexural tectonics on both relative sea level and sedimentation whereby deposition of material eroded from actively uplifting hinterlands caused subsidence in the depocenter (Abbott and Sweet, Munson, 2016). The large areal extent, excellent preservation and range of related coeval depositional settings establish the RSB sediments as rare windows offering detailed glimpses into mid-Proterozoic palaeoenvironments.

The stratigraphy and correlation of the upper Roper and Tijunna Groups is well constrained, the details of which can be found in Munson (2016, see also; Bodorkos et al., 2021; Sweet, 1977; Sweet et al., 1974; Yang et al., 2019). In brief, age constraints are based on stratigraphic relationships, detrital zircon, baddeleyite and glauconite dating. Lateral correlations are based on core, wireline and seismic data, and correlation of high TOC intrvals in the Velkerri Formation. The Tijunna Group is correlated with the upper Roper Group on the basis of detrital zircon ages and lithostratigraphy (Munson, 2018; Yang et al., 2019). Observations in this study also support a lithostratigraphic correlation for the upper Roper Group and Tijunna Group. The Battle Hill Formation, Weaner Sandstone and Bynoe Formation form the upper part of the Bullita Group which unconformably underlies the Tijunna Group and has been tentatively correlated with the Nathan Group which underlies the Roper Group. This correlation is based on lithostratigraphy, primarily the presence of dolostones and microbial carbonates, and ages and Hf isotopes from two detrital

zircons collected from the Weaner Sandstone and Bynoe Formation (Kositcin and Carson, 2019).

However, a number of observations suggest that it maybe be appropriate to place the Battle Creek Formation, Weaner Sandstone and Bynoe Formation within the Tijunna Group. Firstly a) the zircon ages and Hf isotopes also overlap with those of the Tijunna Group and Roper Group and the low number of zircons is not a robust data set (Carson, 2013), b) 'dolostones' is a generic term from NTGS field geologist shorthand that is applied to any rock that "looks carbonate but does not fizz in contact with acid or appear to obviously be a limestone" (Amber Jarrett, personal comms, 2021). The "dolostones" of the Battle Creek Formation are mudstones and muddy cherts as shown in this study (see below). Additionally, the microbial carbonates in the Battle Creek Formation do not match published descriptions of lithology and mineralogy, of microbial carbonates from the Nathan Group, e.g. the Karns Dolomite (Jackson et al., 1987; Lindsay and Brasier, 2000). These observations call into question the lithostratigraphic correlation between the Battle Creek Formation and microbialites of the Nathan Group. Additionally, reworked clasts of the Battle Creek Formation in the Base of the Wondoan Hill Formation appear to have undergone ductile deformation and erosion and deformation indicating a relatively short period of time between the end of Battle Creek deposition and the start of Wondoan Hill Deposition. This style of erosional contact is more indicative of a short-term erosional feature such as a ravinement surface and it is therefore unlikely to be an unconformity which represents a geologically significant period of missing time. On the basis of these observations the Battle Creek Formation, Weaner Sandstone and Bynoe Formation have been tentatively included as part of the Tijunna Group in this study.

2.3. Methods and Materials

This study focuses on the sediments of the upper Roper Group which are found basin wide, and the contemporaneous Tijunna Group which is only found in the far west of the RSB. The upper Roper Group was intercepted in the cores Altree-2 (AT2), McMannus-1a (MM1), Shenandoah-1a (SD1), Urapunga-4 (UP4), Scarbrough-1 (SC1), 12-Bundara Creek (12BC). The core 99-Victoria River NTGS 002 (99VR) intercepts the Tijunna Group. These cores were selected in order to provide a north-south and east-west transect across the central RSB, and to include both well studied, and previously unstudied and understudied material. Stratigraphy, including age constraints, the geographic extent of the succession, and the location of the sampled cores are shown in Fig 1.

Each core was graphically logged at centimeter scale to capture the full range of lithologies, grain sizes and grain size changes, bed thicknesses and contacts, and sedimentary structures. Samples were taken at 10-meter intervals to capture the character of each core. Where unusual or

important changes occurred e.g., the contact between two formations, sampling was conducted at higher resolution to capture the full nature of such transitions. The core AT2 was pre-sampled by Dr Amber Jarrett and so the graphic log was constructed using hand samples, high resolution core photos, core drill reports, previous geochemistry and XRD data generated in this study. The core SD1 consisted of limited core material from the middle Velkerri Formation and powders from the full stratigraphy. SD1 powders were sampled at 100m intervals, and the available core was sampled as a continuous section. The graphic log of SD1 was created using a combination of sample material, XRD data, and gamma-ray logs and descriptions from the original drill reports.

A portion of each sample was powdered for bulk powder XRD analysis in a TEEMA swing mill at 950 RPM in a tungsten carbide collar pestle and mortar. All samples were analysed for bulk and clay-specific mineralogy at the University of Oxford using a Panalytical Empyrean Series 2 X-ray diffractometer (XRD) equipped with a Co Kα source at 40 kV and 40 mA. 210 thin sections where produced at the University of Oxford, Acadia University (Nova Scotia), and Spectra Petrographic (Vancouver, USA). Thin sections were studied using optical microscopy and scanning electron microscopy-energy dispersive X-ray spectroscopy (SEM-EDS) using a FEI Quanta 650 FEG SEM.

An additional 13 cores were studied using high resolution photographs to observe sedimentary structure and lithology, and infra-red spectroscopy to examine bulk mineralogy using the data available through Northern Territory Geological Survey Gemis and AuScope Discovery Portal databases. Additional seismic and wireline data were also obtained through the NTGS Gemis website.

2.4. Results

2.4.1. Facies analysis

Facies and Facies Associations are summarised in Table 1 and Fig 2. Facies were assigned based on similarities in lithology, grain size and changes in grain size, bed thickness and contacts, sedimentary structures and the inferred depositional processes and environment. Genetically related facies were grouped into facies associations, and both were used as the basis of correlations between cores (Fig 3).

Facies Association	Log code	Facies	Typical features	Processes	Interpretation of Depositional environment	Log code
1 - Paralic to Fluvio-terrestrial	**FA1**	*i) Cross-bedded sandstones and mudstones*	Medium to coarse sandstone in erosively based, decimeter to meter scale beds, in meter scale coarsening up cycles. Bidirectional, trough, and swaley cross bedding are common, inclined laminated and massive beds are found at the top of coarsening up cycles, convolute bedding is common in the lower part of cycles, locally evaportic.	Wave, tidal, current, and storm	Sub-tidal through intertidal to supra-tidal shore face setting.	*fi*
		ii) Laminated sandstones and mudstones	Medium sandstone in erosively based, decimeter to meter scale beds with decimeter mudstone beds, in meter scale coarsening up cycles. Unidirectional and trough cross bedding, inclined laminated, and massive beds in the upper part of coarsening up cycles, locally evaporitic. Mudstones are wrinkly laminated to rubbly.	Wave, current, pedogenic and fluvial	Supra-tidal to back beach and mud flat or coastal flood plain setting.	*fii*
		iii) Regolith and massive to laminated claystones	Variably silt rich and poor claystone in meter scale, undulose to erosively based, wrinkly laminated to massive beds, with rare unidirectional cross bedding.	Pedogenic and fluvial	Low lying coastal or fluvial flood plain setting.	*fiii*
		iv) Interbedded sandstones and gravels	Coarse to granular sandstone with rip up clasts in thin erosively based beds. Unidirectional cross bedding, convolute bedding and clast imbrication are common.	Fluvial	Fluvial channel or flood events on a low lying coastal or fluvial flood plain setting.	*fiv*
2 - Ferruginous Marine	**FA2**	*v) Coated grain sandstones*	Medium to coarse sandstone, cemented by green clay, in decimeter to meter scale erosively based beds, with green clay coated grains. Unidirectional, trough, and swaley cross bedding are common.	Wave, tidal, current, and storm	Shallow marine shoaling, or sub-tidal to inter tidal shore face setting proximal to source of sedimentary Fe.	*fv*
		vi) Green cemented sandstone	Medium to coarse sandstone, cemented by green claystone in decimeter to meter scale erosivaly based beds. Bidirectional, trough, and swaley cross bedding, and convoluted bedding are common.	Wave, tidal, current, and storm	Shallow marine shoaling, or sub-tidal to inter tidal shore face setting proximal to source of sedimentary Fe.	*fvi*
		vii) Green mudstone	Variably silt rich and poor claystone in decimeter to meter scale meter scale undulose based beds. Wrinkly to horizontal and inclined planar laminations common. Unidirectional, trough, convoluted, and domal stromatolitic laminations are locally common.	Laminar flow and wave	Shallow marine shoaling, or sub-tidal shore face or mud flat setting proximal to source of sedimentary Fe.	*fvii*
3 - Marine	**FA3**	*viii) Interbedded sandstone and mudstone*	Interbedded fine to medium sandstone, and variably silty mudstone, in decimeter to meter scale undolose, erosively based beds in meter scale coarsening up cycles. Unidirectional, trough, hummocky and convoluted bedding are common. Syn-sedimentary faulting, dewatering structures, ptygmoidal mud cracks, and cryptomicrobial textures are locally common. Mudstone beds feature wrinkly to inclined and horizontal planar laminations. Locally rich in organic matter.	Wave, current, and storm	Shallow marine lower-most shore face to inner shelf setting proximal to a source of terrestrial clastic input and experiencing periods of increased primary productivity.	*fviii*
		ix) Interlaminated siltstone and mudstone	Interbedded siltstone and variably silty mudstone in decimeter to meter scale, undolose erosively based beds in meter scale coarsening up cycles. Rare thin erosively based fine sand beds. Other features are the same as as *Facies viii.*	Wave, current, and storm	Shallow marine inner shelf setting medial to a source of terrestrial clastic input and experiencing periods of increased primary productivity.	*fix*
		x) Laminated and massive claystone	Variably silty claystone in decimeter to meter scale undolose erosively based beds. Thin erosively based siltstone beds may be locally common. Rare unidirectional cross bedding is localy present, wrinkly to inclined and horizontal planar lamination is locally common. Crypto microbial textures, ptygmoidal mudcracks, intraclastic breccias and granular claystone horizons locally common. Locally rich in organic matter.	Wave, current, laminar flow and storm	Shallow marine outer shelf setting distal to a source of terrestrial clastic input and experiencing periods of very low sedimentation, seafloor cementation, and increased primary productivity.	*fx*
		xi) Microbial Limestone	Stromatolitic, thrombolitic and fenestral limestones interbedded and interlaminated with variably silty mudstone. Common erosive upper contacts with desication cracks and rare evaporite pseudomorphs.	Wave, tidal, current, and storm	Shallow marine lagoonal, reef or intertidal platform setting.	*fxi*

Table 1: Description of each facies association, and facies with colour codes as used throughout this thesis in figures 2, 3, and 4.

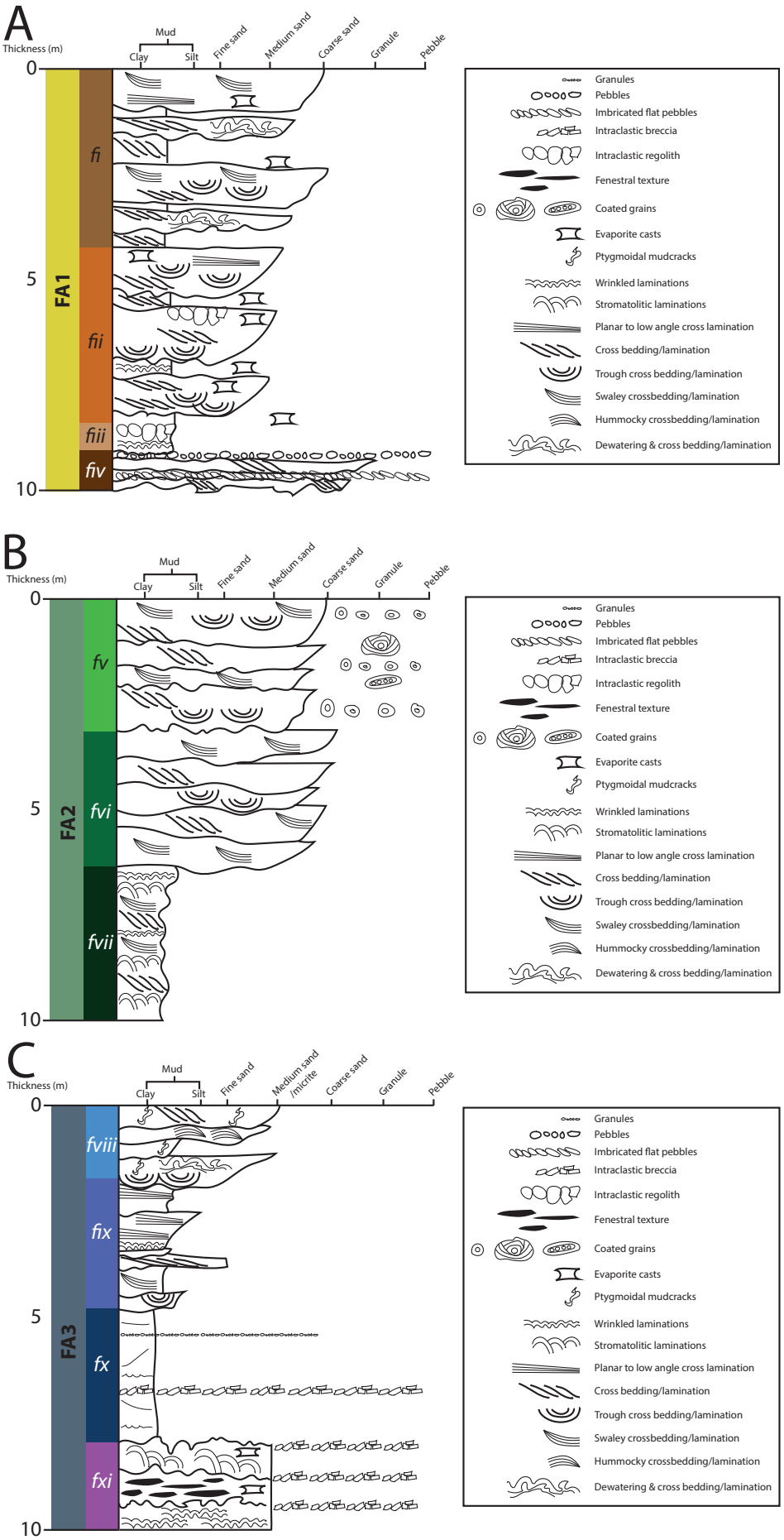

Figure 2: Simplified graphic logs showing the typical features of each facies association, and facies discussed in the main text, see Table 1 for descriptions and colour codes. A) FA1 Paralic to fluvio-terrestrial, B) FA2 Ferruginous Marine, C) FA3 Marine

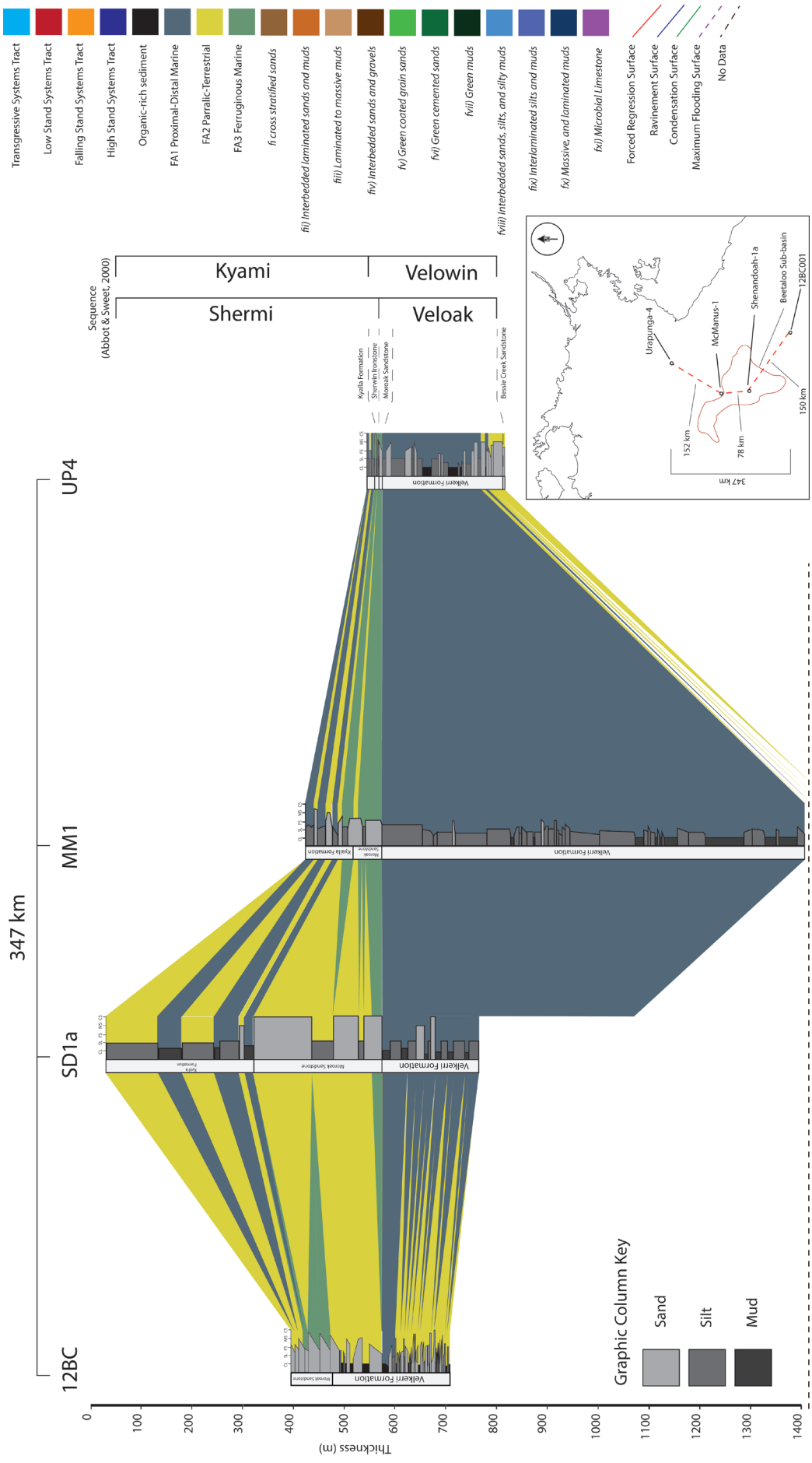

Figure 3: North-south and east-west transects of the study area with simplified graphic logs represented the sampled cores. A) Facies associations on the north-south transect.

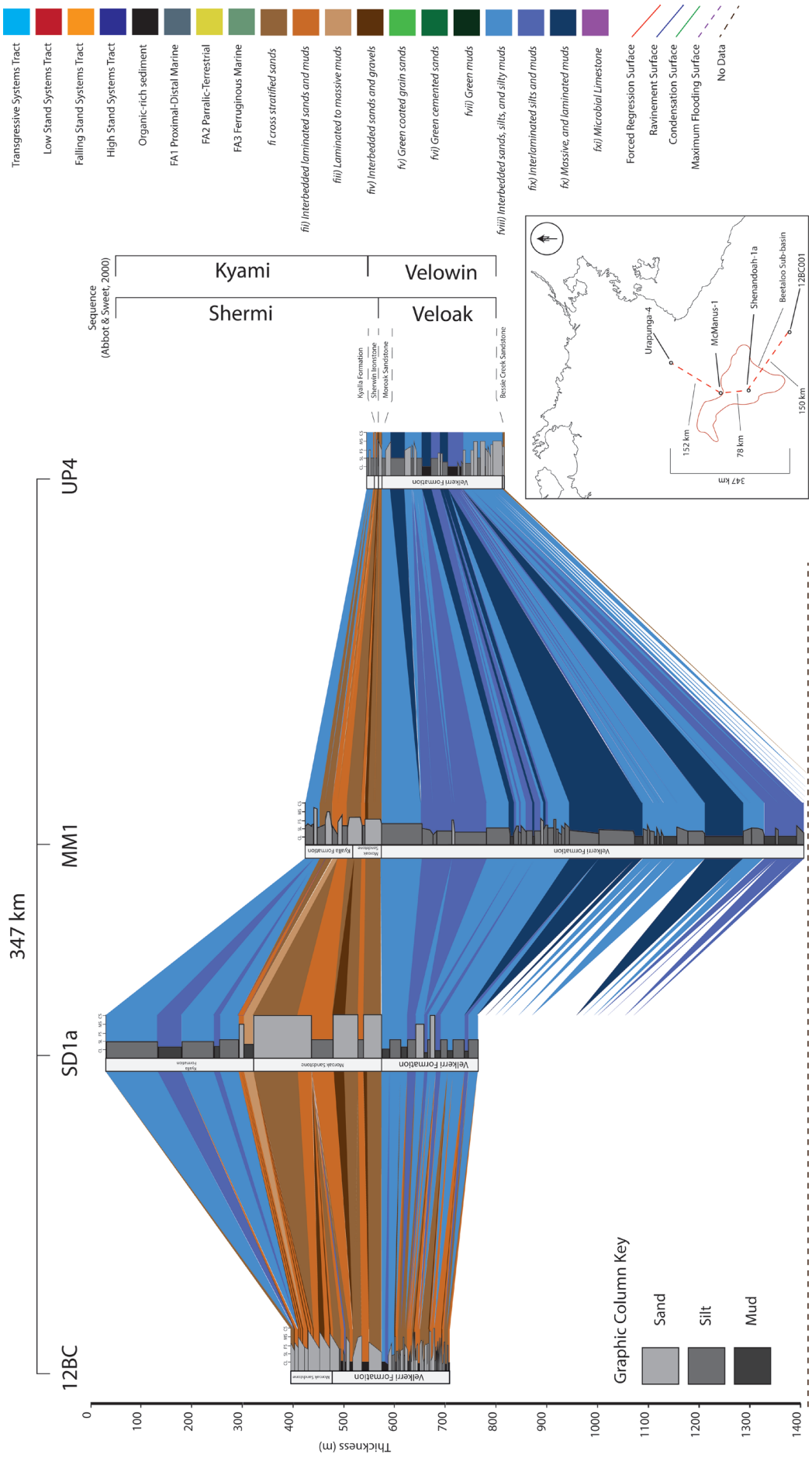

Figure 3: North-south and east-west transects of the study area with simplified graphic logs represented the sampled cores. B) facies on the north-south transect.

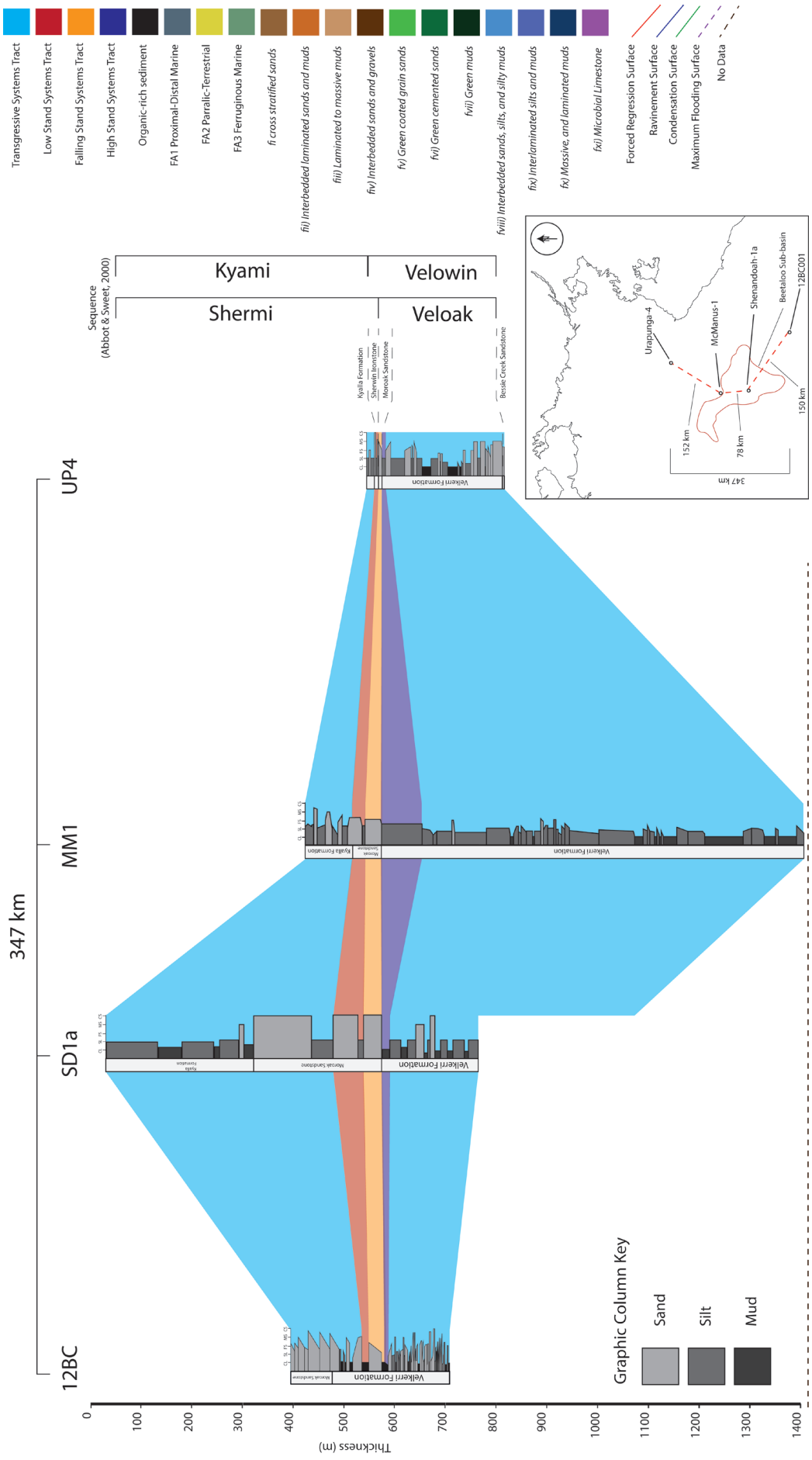

Figure 3: North-south and east-west transects of the study area with simplified graphic logs represented the sampled cores. C) 3rd order sequence stratigraphy on the north-south transect.

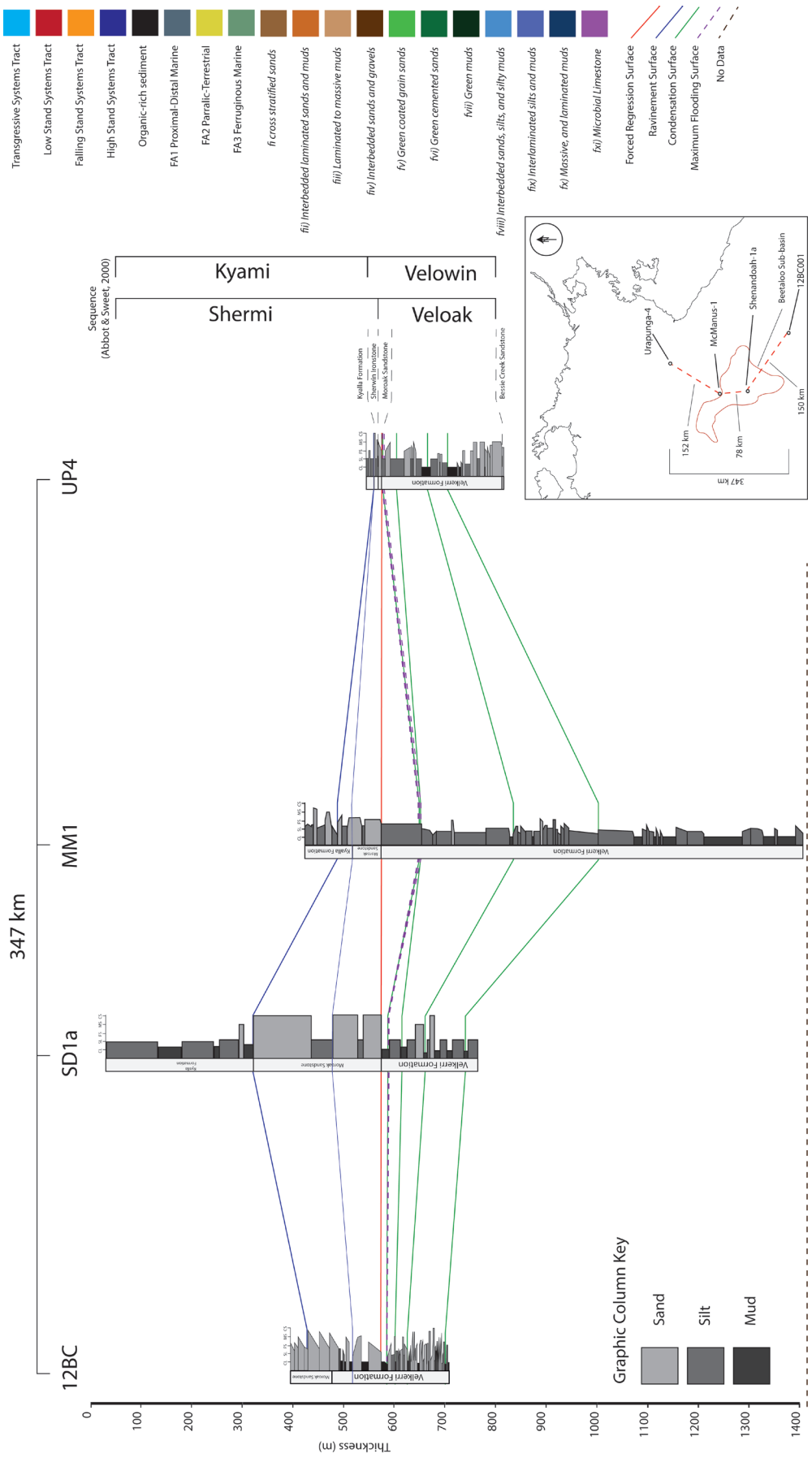

Figure 3: North-south and east-west transects of the study area with simplified graphic logs represented the sampled cores. D) Sequence stratigraphic surfaces on the north-south transect.

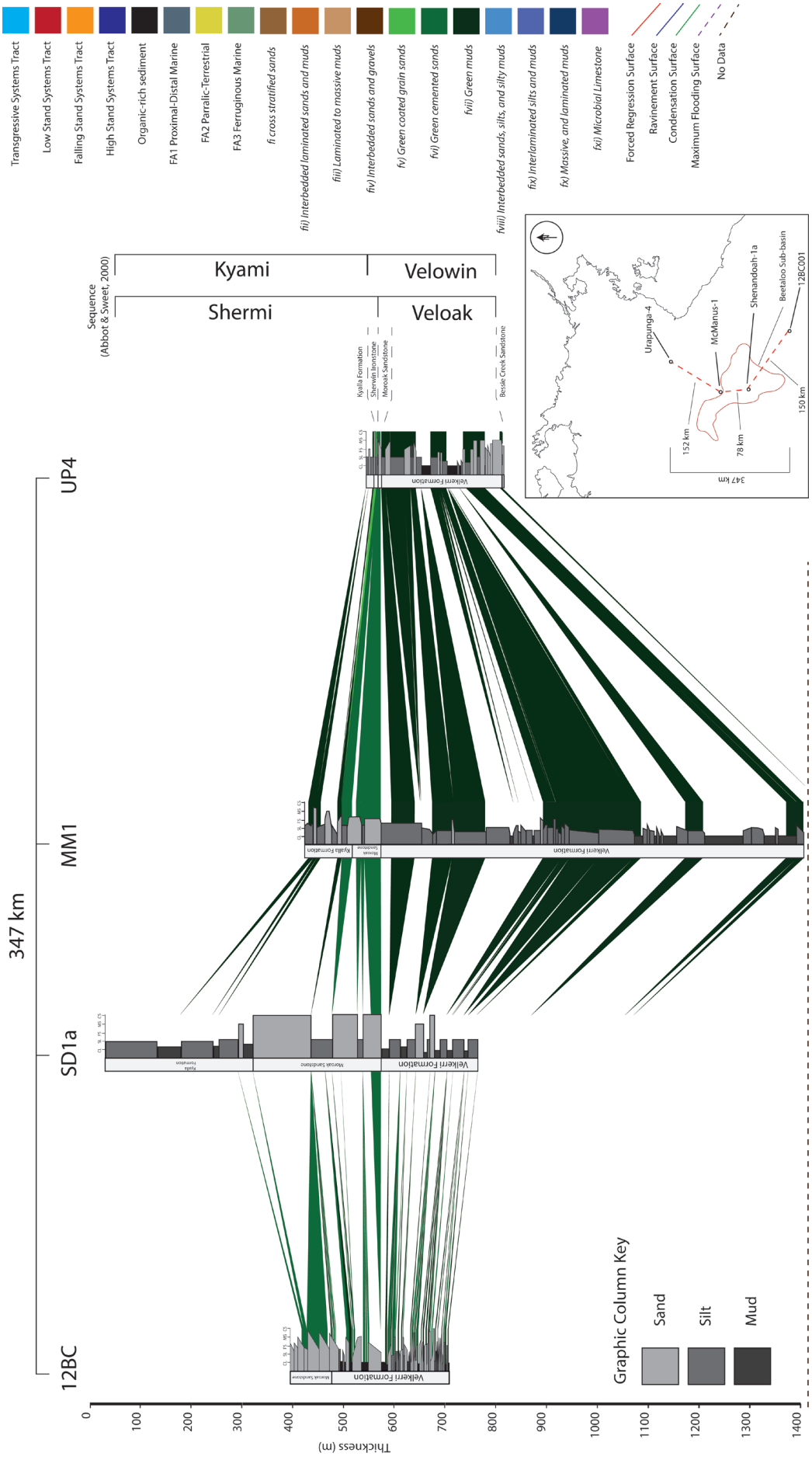

Figure 3: North-south and east-west transects of the study area with simplified graphic logs represented the sampled cores. E) Ferruginous facies on the north-south transect.

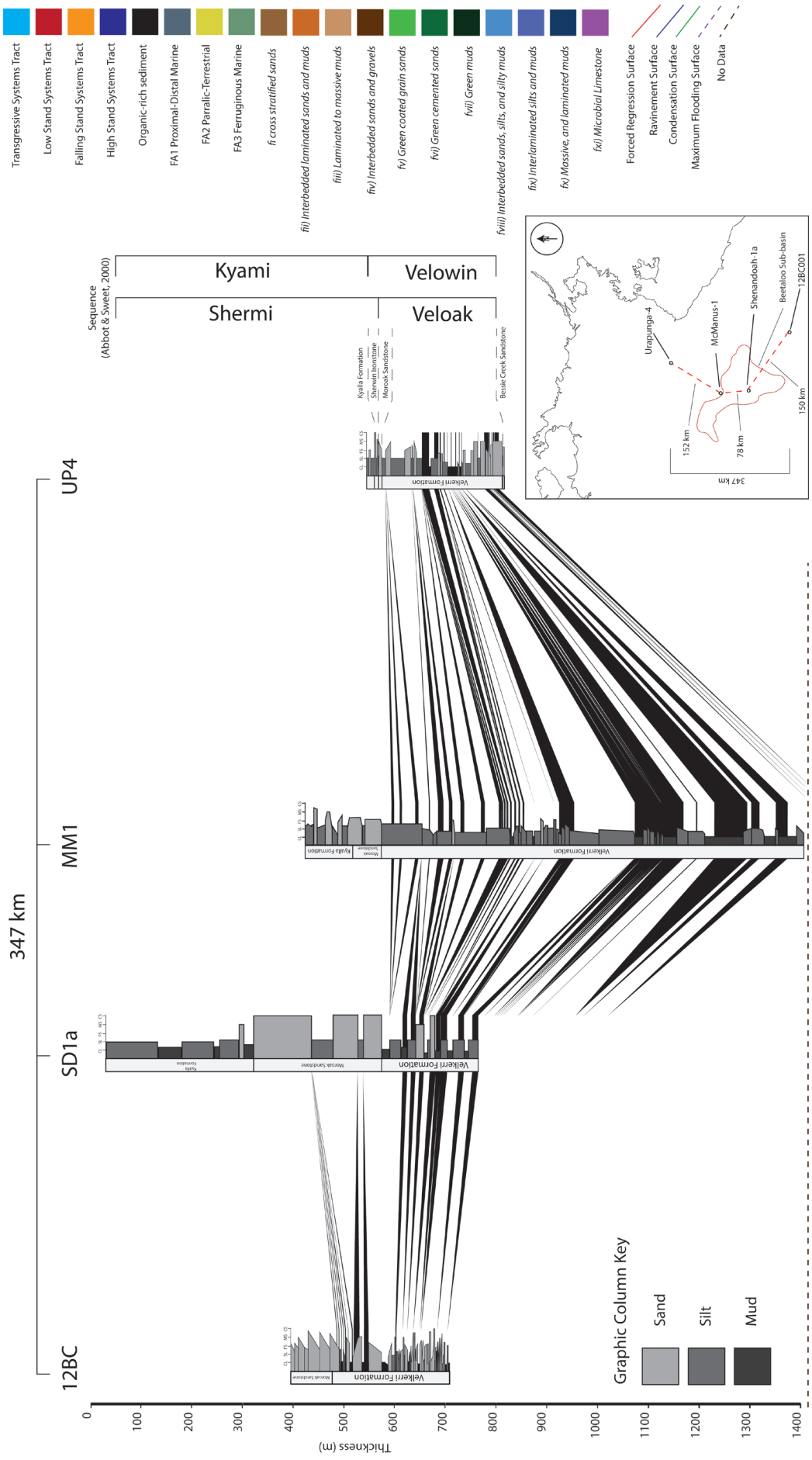

Figure 3: North-south and east-west transects of the study area with simplified graphic logs represented the sampled cores. F) Organic-rich intervals on the north-south transect.

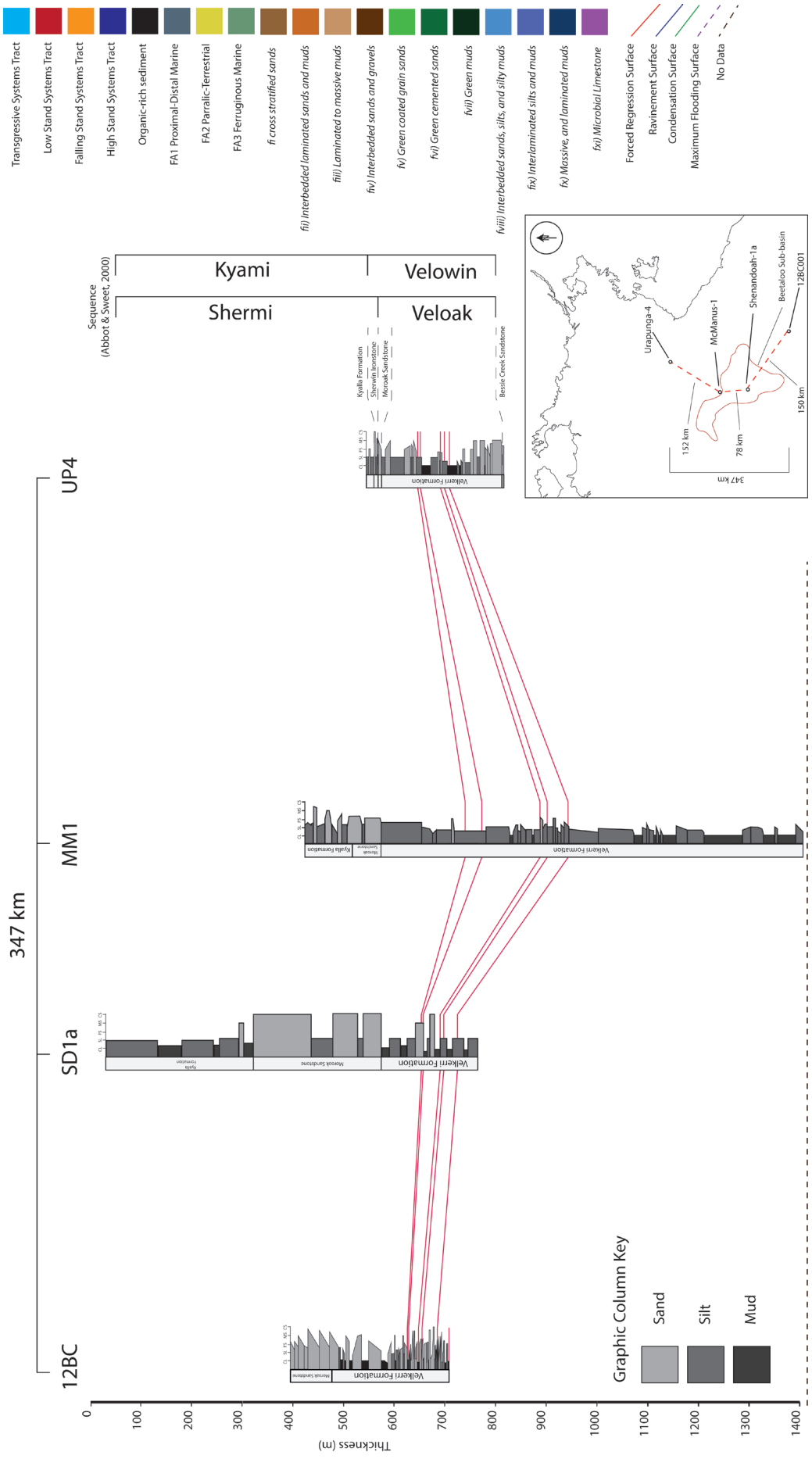

Figure 3: North-south and east-west transects of the study area with simplified graphic logs represented the sampled cores. G) Possible volcanogenic horizonson the north-south transect.

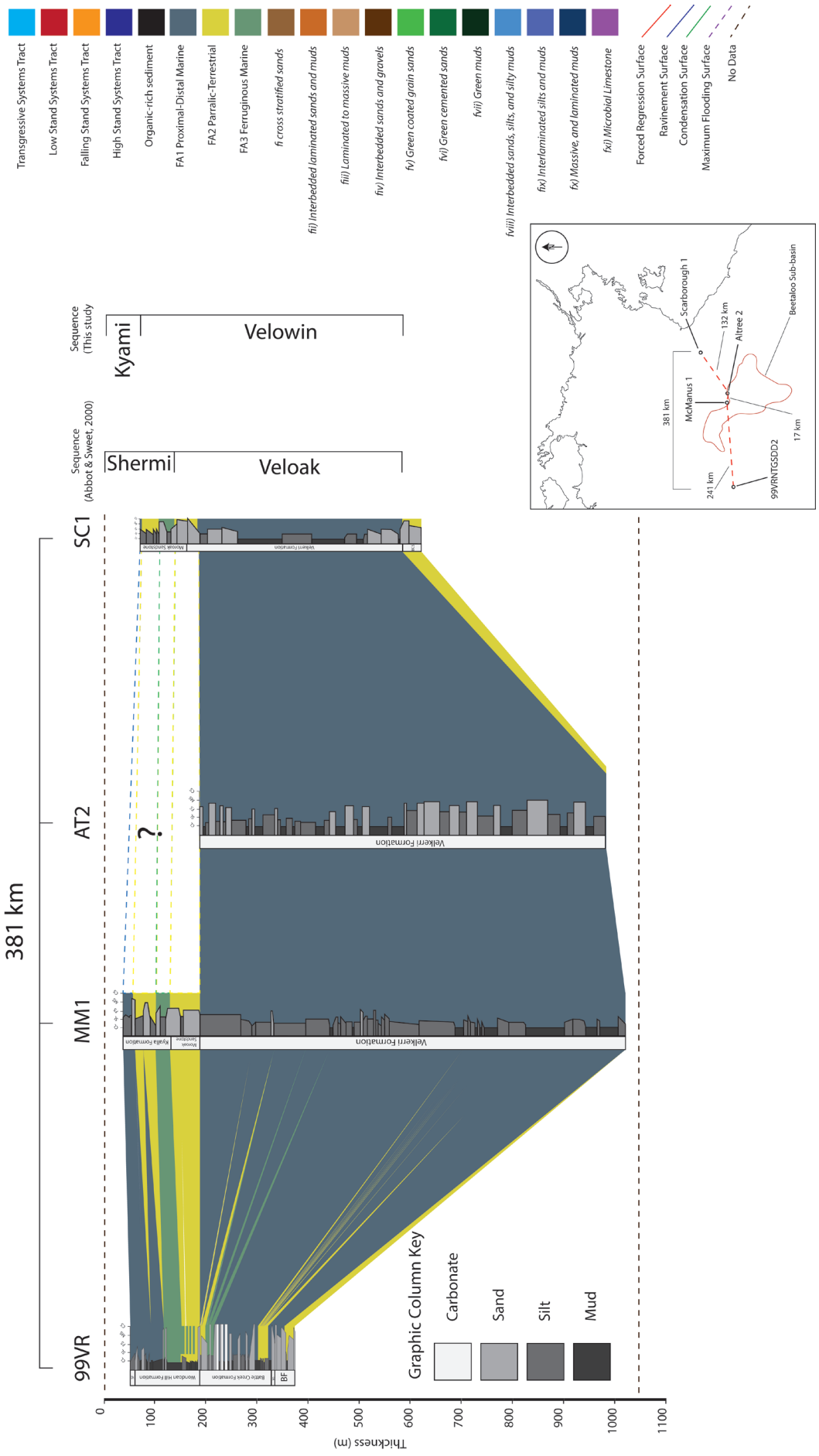

Figure 3: North-south and east-west transects of the study area with simplified graphic logs represented the sampled cores. H) facies associations on the east west transect

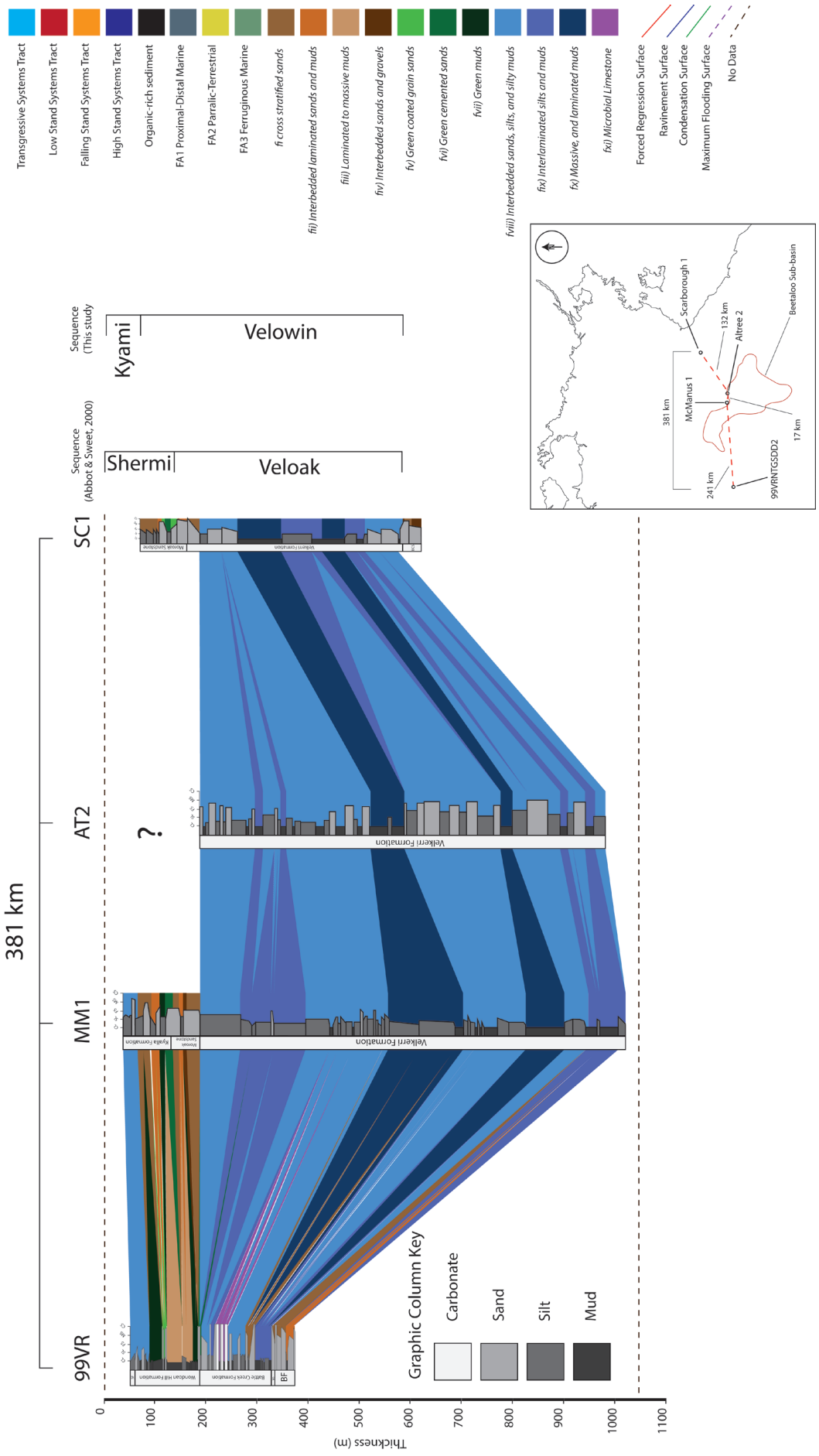

Figure 3: North-south and east-west transects of the study area with simplified graphic logs represented the sampled cores. I) Facies on the east west transect.

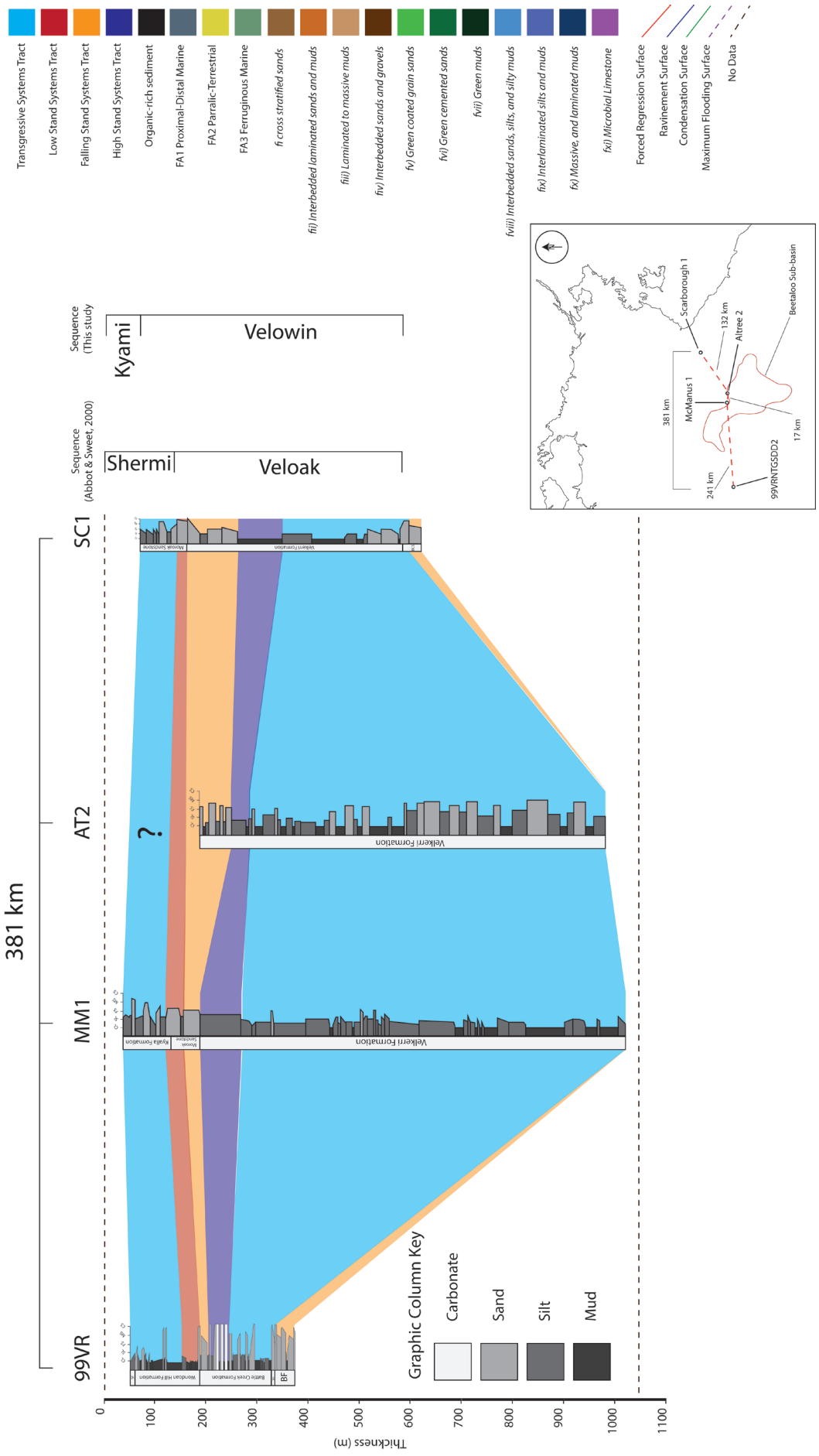

Figure 3: North-south and east-west transects of the study area with simplified graphic logs represented the sampled cores. J) 3rd order sequence stratigraphy on the east west transect.

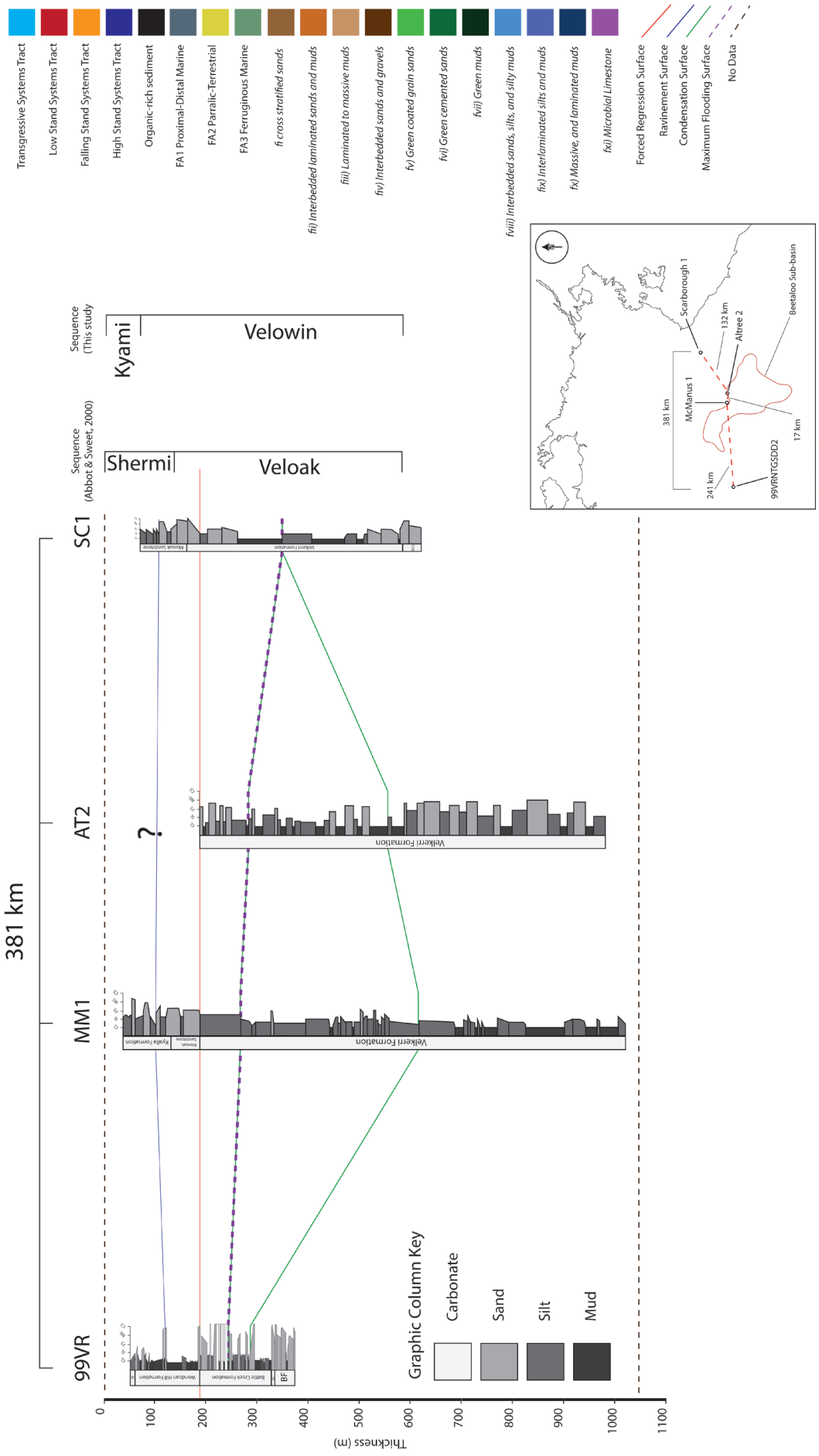

Figure 3: North-south and east-west transects of the study area with simplified graphic logs represented the sampled cores. K) Sequence stratigraphic surfaces on the east west transect.

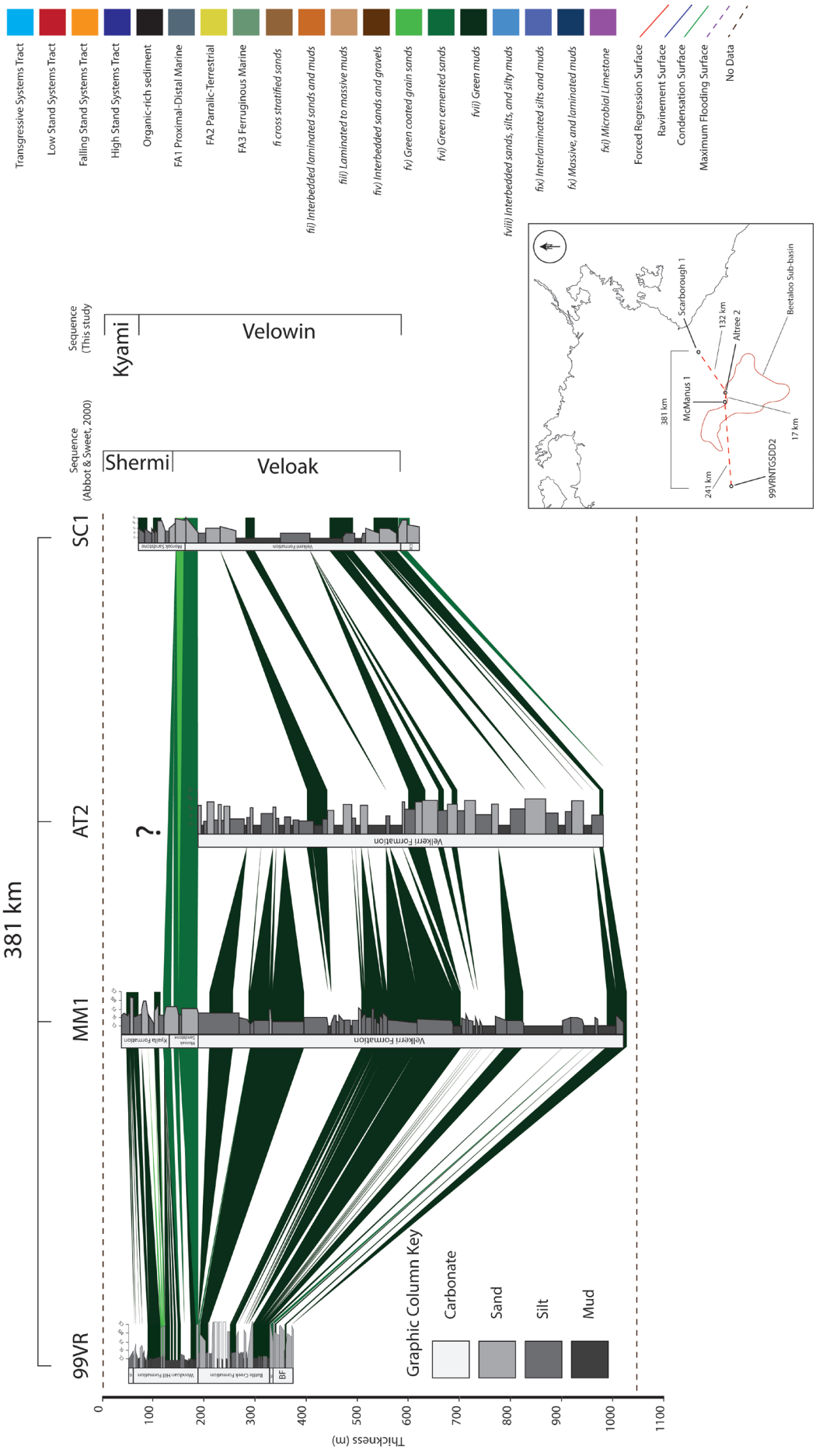

Figure 3: North-south and east-west transects of the study area with simplified graphic logs represented the sampled cores. L) Ferruginous facies on the east west transect.

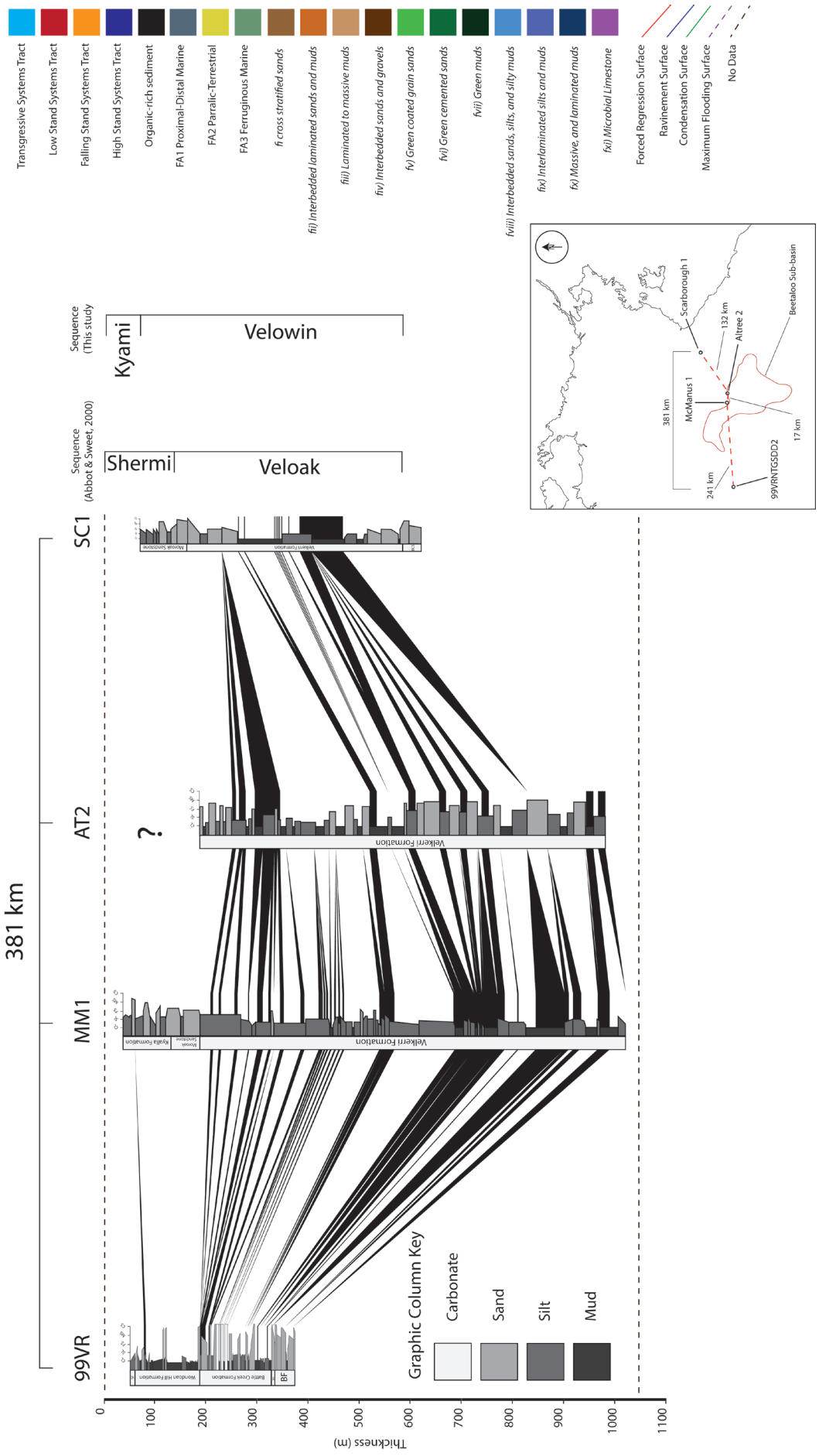

Figure 3: North-south and east-west transects of the study area with simplified graphic logs represented the sampled cores. M) Organic-rich intervals on the east west transect.

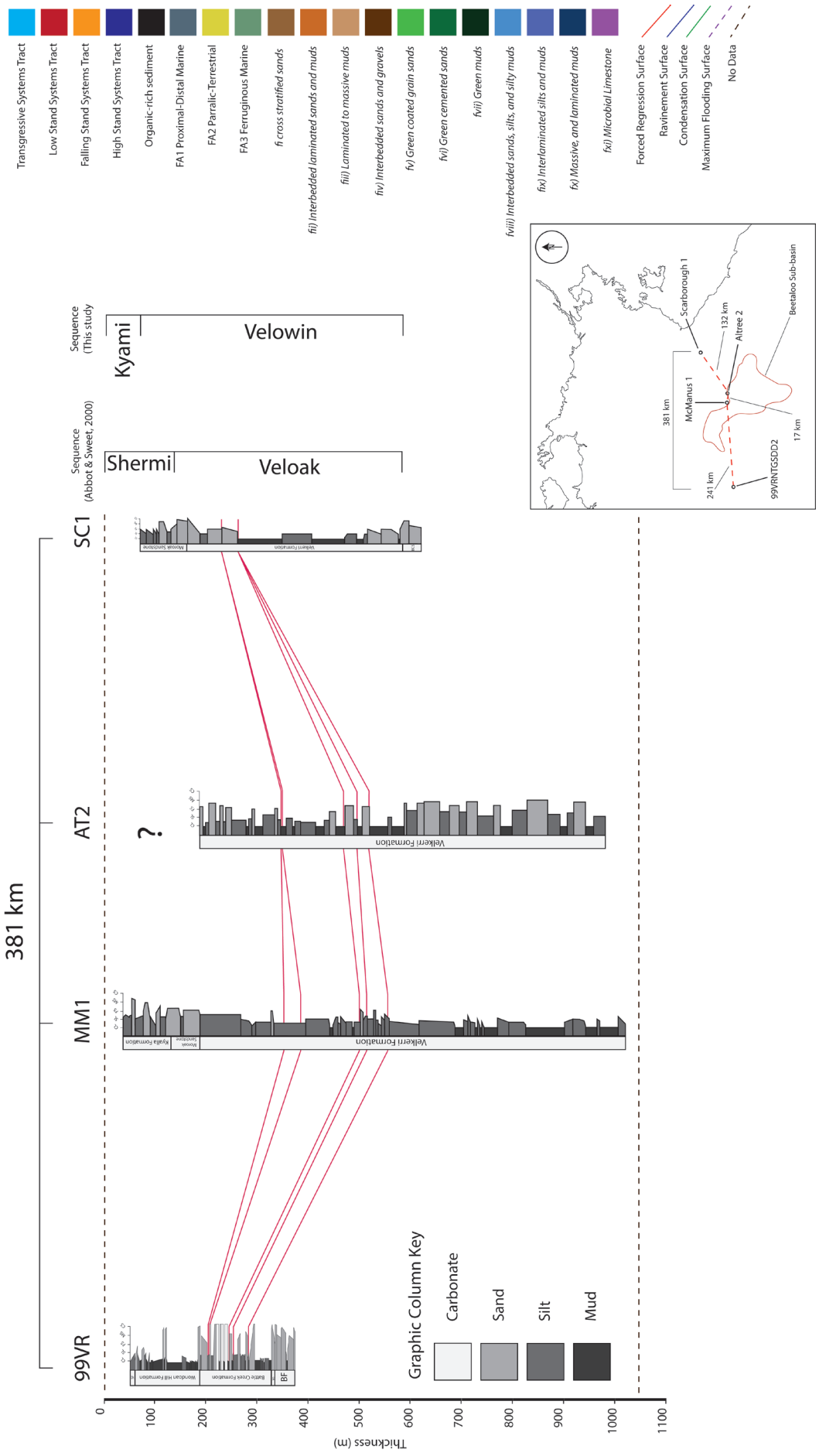

Figure 3: North-south and east-west transects of the study area with simplified graphic logs represented the sampled cores. N) Possible volcanogenic horizons on the east west transect.

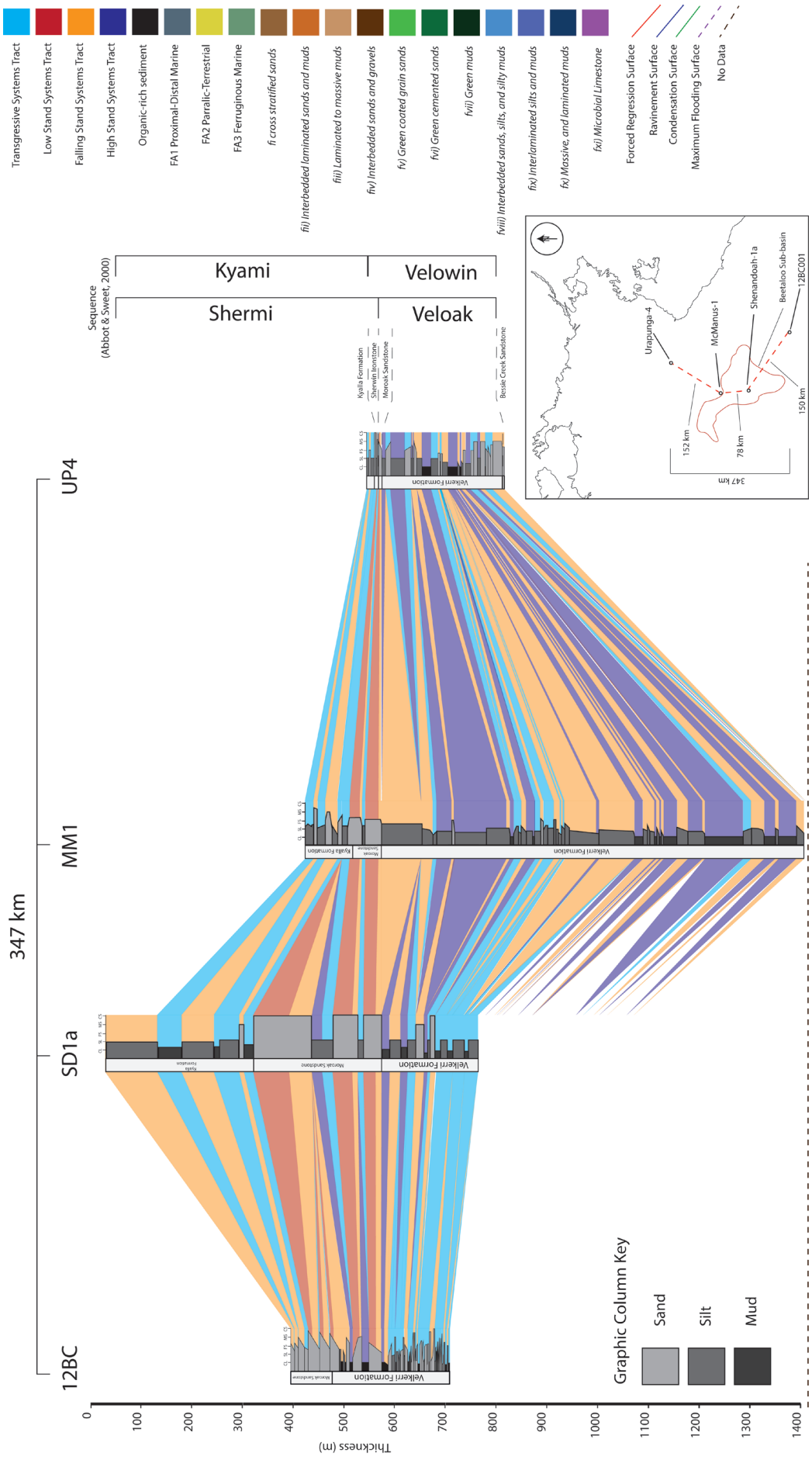

Figure 3: North-south and east-west transects of the study area with simplified graphic logs represented the sampled cores. O) 4th order sequence stratigraphy on the north-south transect.

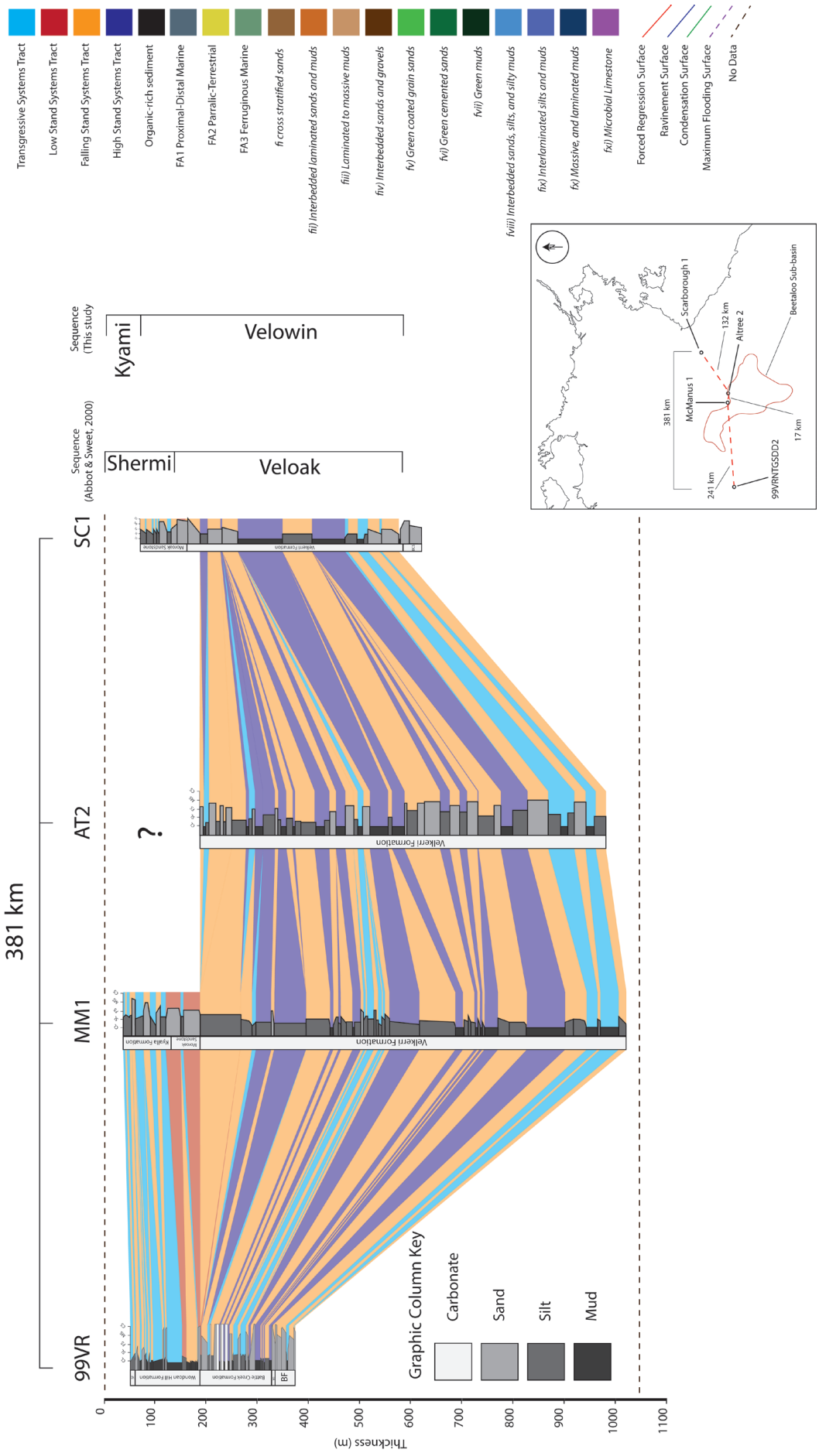

Figure 3: North-south and east-west transects of the study area with simplified graphic logs represented the sampled cores. P) 4th order sequence stratigraphy on the east_west transect.

Facies Association 1 - Paralic to fluvio-terrestrial

Description Facies Association 1 (FA1) consists of fine to medium cross-stratified sandstones with rare thin poorly sorted granular beds at the top of coarsening up cycles and rare flat mud small pebble beds at the base of coarsening up cycles (Fig 2A, Fig3C, D, & H). Sand texture is moderately- to well-sorted and grains are rounded. Sand composition is sub-arenite and is mature, though locally it may be immature. Sedimentary structures consist of parallel planar inclined laminations, unidirectional cross laminations, trough cross bedding and lamination and small scale hummocky cross bedding (Fig 5A, B, & F). Convolute bedding is locally common and hosts dewatering structures. Beds range from ~10+ cm in the finer grained intervals up to several meters in the coarser intervals (Fig 2A). Mud is present as < 5 cm laminations of massive to laminated green clay that drapes the surfaces of sedimentary structures, bed contacts and erosive surfaces (Fig 2A, Fig 5B & I). Mud is also present at the top of coarsening upwards cycles as < 5 cm red clay rich beds formed of centimeter sized chunks of clay with slicken sides, separated by vertical cracks commonly filled with sand and/or a mix of wispy carbonates, silica and green clay (Fig 2A, Fig 5E, J & K). Clay rich beds are also present as meter scale beds of white to cream hard clay with red staining and conchoidal fracture. Bed contacts are sharp throughout and commonly undulose with synoptic relief averaging 2-3 cm. Erosive contacts and surfaces are common, between and within beds. Interbed contacts may be sharply incised up to several cm (Fig 2A). Cuboidal, tabular and lenticular cm scale green ferrous-clay clasts are locally common at the top of coarsening up cycles and on some erosive surfaces often in association with desiccation cracks (Fig 2A Fig 5G). The medium to course sandstones are silica cemented while the finer grained sandstones host green or white clay cements.

Processes and Interpretation The combination of grain size, stratification and lamination described above suggests deposition in a range of environments from a shallow body of water within fair-weather wave base, subject to frequent storms and with varying levels of flow energy. The presence of convolute bedding with dewatering structures indicates occasional rapid influxes of sediment which may indicates close proximity to a clastic sediment source with a variable sediment load such as a fluvial system with seasonal flooding. Alternatively, the convoluted bedding could be the result of storms resuspending and then dumping seabed sediment. Petrographic relationships between the clay laminations and cements, and detrital grains in the finer sandstones indicates a synsedimentary origin for the clay cement. This indicates the laminated clays and clay cemented sandstones were deposited under a variable flow energy regime where cross bedded and laminated sands were deposited during higher energy periods, and clays could precipitate in pore

space or settle from suspension in lower energy periods. The ferrous-clay clasts closely resemble evaporite forms such as hopper crystals and lenticular gypsum. Therefore, the ferrous-clay clasts are most likely replacement moulds of evaporite minerals, and in combination with the presence of desiccation cracks, this suggests formation in very shallow water with some sub-aerial exposure under intense evaporative conditions. The laminated internal texture of the evaporite moulds suggests that the ferrous clay progressively filled the empty space in stages as the original evaporite mineral underwent dissolution. The red clay beds indicate sub-aerial exposure for prolonged periods of time and *in situ* chemical weathering of pre-existing rock. The slickensides and cracks indicate expansion and contraction of clay peds during alternate wet and drying, while the carbonates indicate intense evaporation and the green clays indicate reducing conditions. Therefore, the red clay beds represent the formation of regolith horizons similar to latosols. Likewise, the hard white clay beds represent prolonged periods of *in situ* chemical weathering of pre-existing rock, combined with leaching from groundwater flow which left the clay enriched in Al and Si. The silica cemented sandstones indicate persistent current working that has removed finer sands and clays, and the granular beds at the top of coarsening cycles indicate periods of sustained current action and winnowing. The flat pebble beds indicate episodes of increased flow energy and the erosion and reworking of local substrates in high energy events.

On the basis of the stratigraphic position of this facies association and the features described above, deposition most likely occurred in a range of adjacent depositional environments. Sandstones and mudstones with features indicating deposition in shallow water via wave and storm processes are grouped as *facies i: Cross-bedded sandstones and mudstones* and were deposited in a storm dominated shallow marine shelf to lower shore face setting. Sandstones and mudstones with features indicating oscillating flow energy, common erosive events and occasional high energy deposition and reworking, are grouped together as *facies ii: Laminated sandstones and mudstones* and were deposited in a tidally dominated upper shore face to tidal flat setting. The red clay regolith and white claystone are grouped together as *facies iii: Regolith and massive claystones* and represent deposition in a coastal plain setting. Medium to coarse silica cemented sandstones with granule and pebble beds are here grouped as *facies iv: Interbedded sandstones and gravels* and were deposited in fluvial environments ranging from overbank deposition (massive to laminated sandstones), active channel deposition (cross bedded sandstones) and high energy flooding events (granular and pebble beds).

Facies Association 2: Ferruginous Marine

Description Facies association 2 (FA2) consist of medium to coarse grained sandstone with well sorted and rounded to well-rounded grains and with a sub-arenite composition, that is cemented by, and interbedded with, green claystone (Fig 6A, B C & D). Sandstone beds feature unidirectional, trough and hummocky cross bedding on scales ranging from centimeter to decimeter scale (Fig 6C & D). Beds are between 20 cm and 2 m meters thick, and contacts are sharp and undulose or incised and are usually erosive (Fig 2B, Fig 6B &I). Both bed contacts and the common intra-bed erosion surfaces are coated with green clay, which may be laminated or pustular and stromatolitic. Claystone beds are thin and range from a minimum of ~15 cm up to ~2 m and are planar, inclined planar, undulose and wrinkly laminated and may feature unidirectional and trough cross laminations (Fig 6E, F, G, H, & J). Claystone beds also contain pustular and stromatolitic features that show evidence of synsedimentary erosion and regrowth. The most striking feature of FA2 is the abundant coated grains which have a number of distinct morphologies and structures (Fig 2B, Fig 6A, B & K). The most common are elliptical spheroids between 0.5 and 1 cm in length at the long axis, and which superficially resemble carbonate ooids in structure with a nucleus of green clay or a detrital grain, and a cortex of hundreds of tangential green clay laminations. The next most common coated grains are 0.5 - 2cm and either long rod-shaped with rounded ends, or ovoid-shaped with blunt ends. The internal structure of these grains consists of a nucleus 'string' of detrital grains or green clay fragments, and an outer cortex of tangential to internally truncated green clay laminations. The least common types of coated grains are superficially similar to carbonate oncoids and feature either green clay lamination in discontinuous truncated parallel to intersecting laminations around a core of detrital gains and broken examples of the ooid-like grains. Some of the oncoidal type appear to have settled on the sediment surface and grown into small stromatolites with several mm of synoptic relief. A fourth type of coated grain is found only in one bed of the Wondoan Hill Formation in the west of the basin (Fig 6K). The structure of the Wondoan Hill coated grains consists of fine to medium clastic sand grains adhered to laminae of intergrown organic matter and green clay. The outer structure of these grains is superficially oncoidal, but the central nucleus consists of detrital grains adhered to a green clay-organic lamina and folded into spirals, or other complex patterns. These coated grains, and the bed that hosts them are also unusually rich in heavy detrital minerals.

Processes and Interpretation The combination of grain sizes and sedimentary structures in the sandstone beds indicates deposition in a shallow body of water close to a source of clastic grains. The size of the cross beds and abundance of erosional surfaces indicates deposition above

Surface Type	Proximal Character	Distal Character	Example
Subaerial Unconformity	erosional truncation of underlying unit, intraclasts, conglomerates, palaeokarst, parakarst, palaeoweathering, regolith		*The contact at the base on the Moroak Sandstone*
Correlative Conformity		Shallow water debris in coarse beds	*Erosive courser grained beds in the distal Velkerri Formation*
Transgressive Surface	Sharp based shoreface facies eroding into more distal facies	Sharp based crossed bedded sands eroding into distal muds	*Erosive sand beds and reworking of muds in the Velkerri Formation*
Maxium Regressive Surface	Gravel or regolith beds at the top of coarsening up cycles, or the base of fining up cycles	Parralic to fluvio terrestrial facies eroding into distal and muds	*Granular and intraclastic conglomerate at the base of the Moroak Sandstone*
Maximum Flooding Surface	Condensed or organic rich muds draping coarser proximal sands	Condensed organic rich muds, chemical sediments, early cementation, glauconite and heavy detrital lags	*Glauconitic lag in the upper Velkerri Formation that is correlatable across the transect*
Ravinement Surface	Finer distal facies draping erosively topped coarser proximal facies	Finer distal facies draping erosively topped coarser proximal facies	*Fine sands and muds draping erosively topped sand beds in the Velkerri Formation*
Condensation Surface	Regolith, palaeoweathering, paleokast, parakarst, leached sediments, lags, insitu breccia	Condensed organic rich muds, chemical sediments, early cementation, glauconite and heavy detrital lags, insitu breccia	*Localised glauconite and heavy detrital rich beds in the Velkerri Formation*

Table 2: Sequence stratigraphic surfaces, definitions and examples for the studied sections.

fair-weather wave base in a relatively high energy environment with frequent reworking of the sediment surface by currents. Hummocky cross beds indicate frequent action by storm waves. However, the abundance of green clay as cements and laminations on sandstone cross beds indicates that the flow velocity was variable and included periods of quiescence when clay and silt could settle from suspension and grow in pore space undisturbed. Subsequently this variability in lateral flow velocity indicates a tidal component that was normally overprinted by wave, current and storm action. The coated grain beds formed in the same environments, however, the coated grains themselves formed *within* the sediments via the process of *redox aggradation* (Pufahl and Grimm, 2003), unlike carbonate ooids which form via physical working. During redox aggradation, the Fe^{3+}-Fe^{2+} redox boundary migrates vertically through the upper sediment in response to increasing or decreasing oxygen levels (Fig 2 *in* Pufahl and Grimm, 2003). With each migration, a new layer of the corresponding ferrous clay is precipitated around the nucleus of the coated grains (Fig 2 *in* Pufahl and Grimm, 2003). As this process takes place within the top 5 – 20 cm of the sediment, coated grains maybe subject to physical reworking which can produce *unconformity bound* and composite grains (Fig 2 *in* Pufahl and Grimm, 2003). Oxygen fluctuations within the sediment may be driven by natural variation in dissolved oxygen content, or by biological oxygen demand as a response to increased organic matter export to the sediment (Fig 2 *in* Pufahl and Grimm, 2003). However, the presence of broken green clay coated grains and composite coated grains supports the extensive erosion and reworking of the seabed. In contrast, the coated grains found in

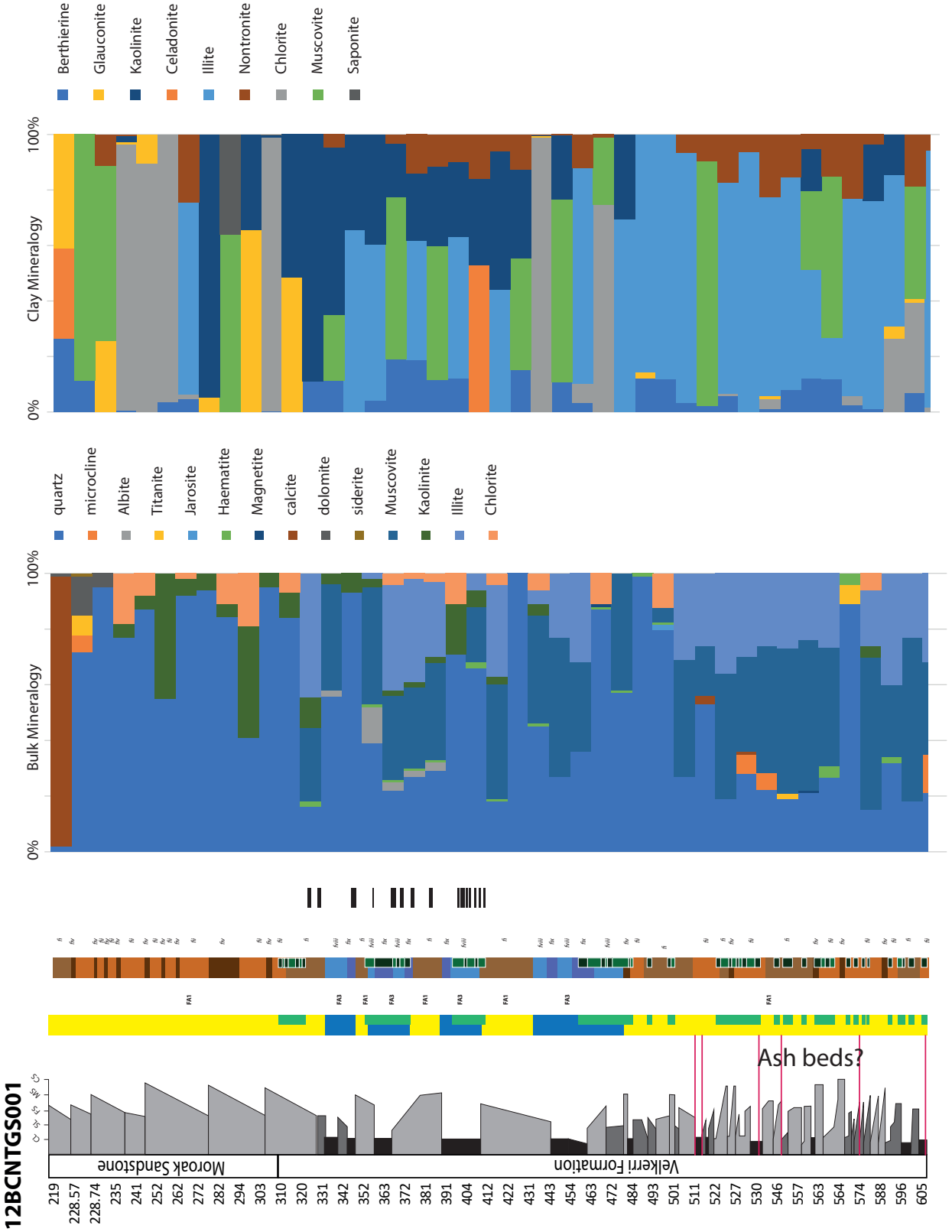

Figure 4: XRD for bulk and clay specific mineralogy for each core 12BC, graphic log key, facies numbering, and colour codes are the same as Figure 2 and 3. A = Facies Association, B = Facies, C = Organic rich intervals, pink horizontal bars represent possible volcanic ash beds.

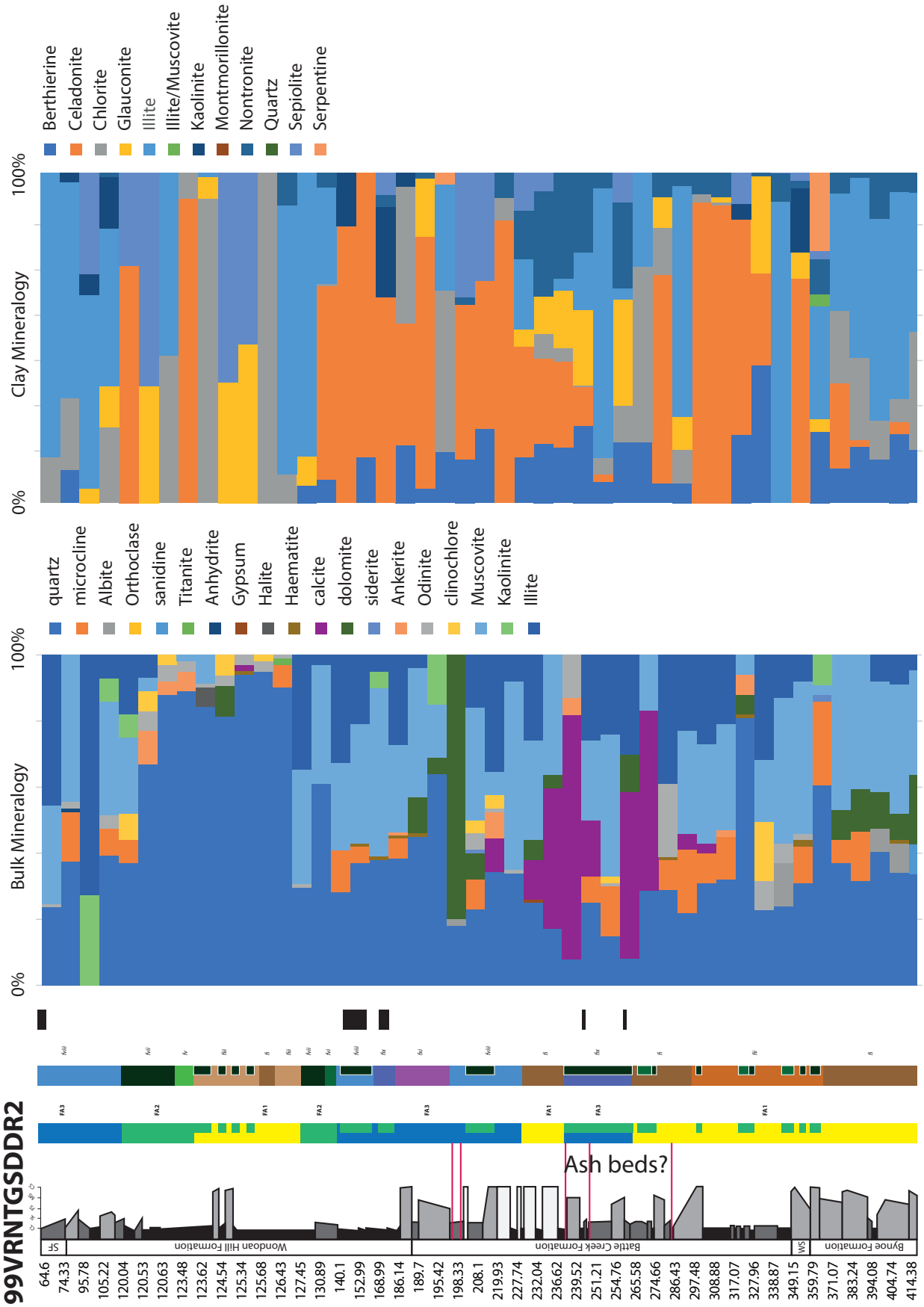

Figure 4: XRD for bulk and clay specific mineralogy for each core 99VR, graphic log key, facies numbering, and colour codes are the same as Figure 2 and 3. A = Facies Association, B = Facies, C = Organic rich intervals, pink horizontal bars represent possible volcanic ash beds.

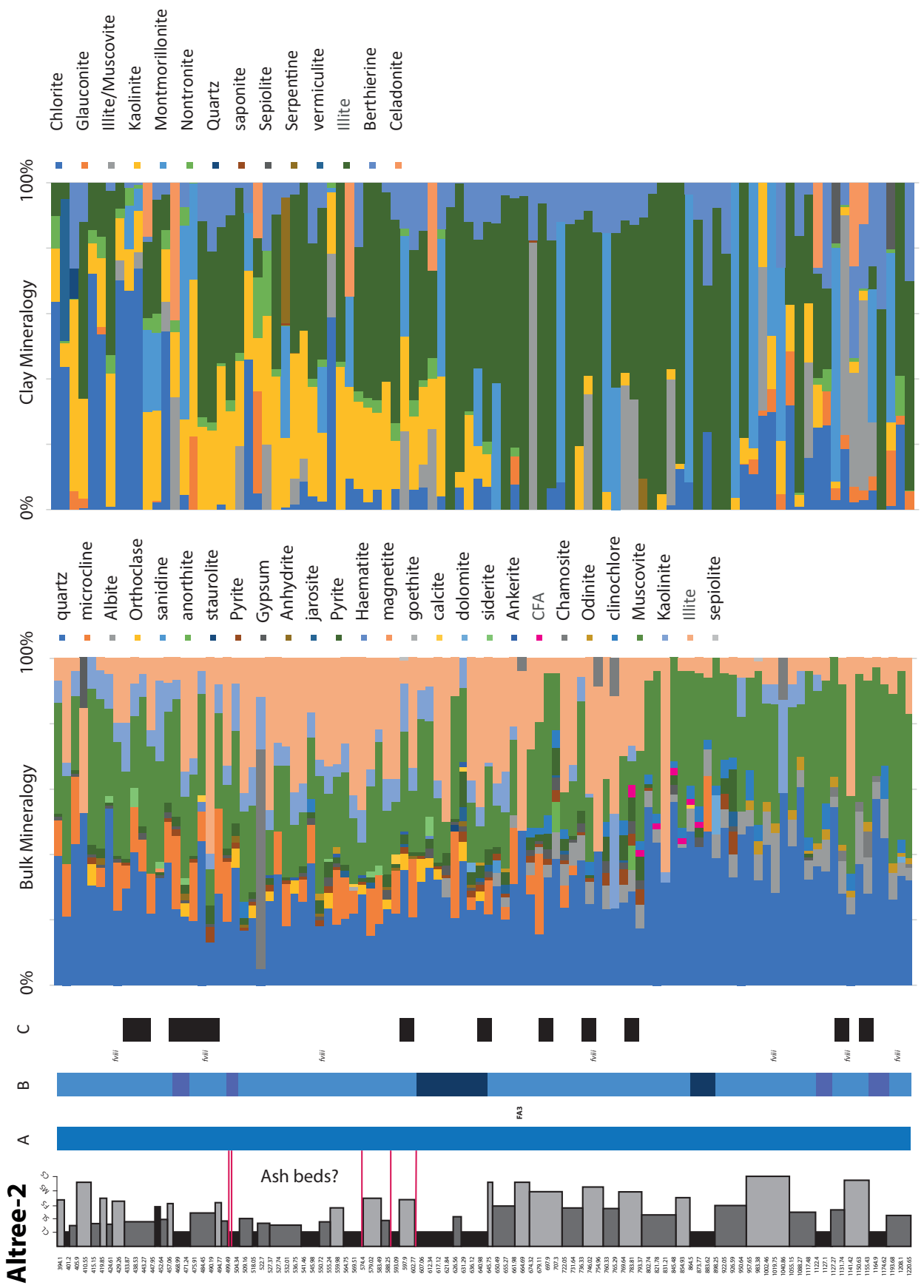

Figure 4: XRD for bulk and clay specific mineralogy for each core AT2, graphic log key, facies numbering, and colour codes are the same as Figure 2 and 3. A = Facies Association, B = Facies, C = Organic rich intervals, pink horizontal bars represent possible volcanic ash beds.

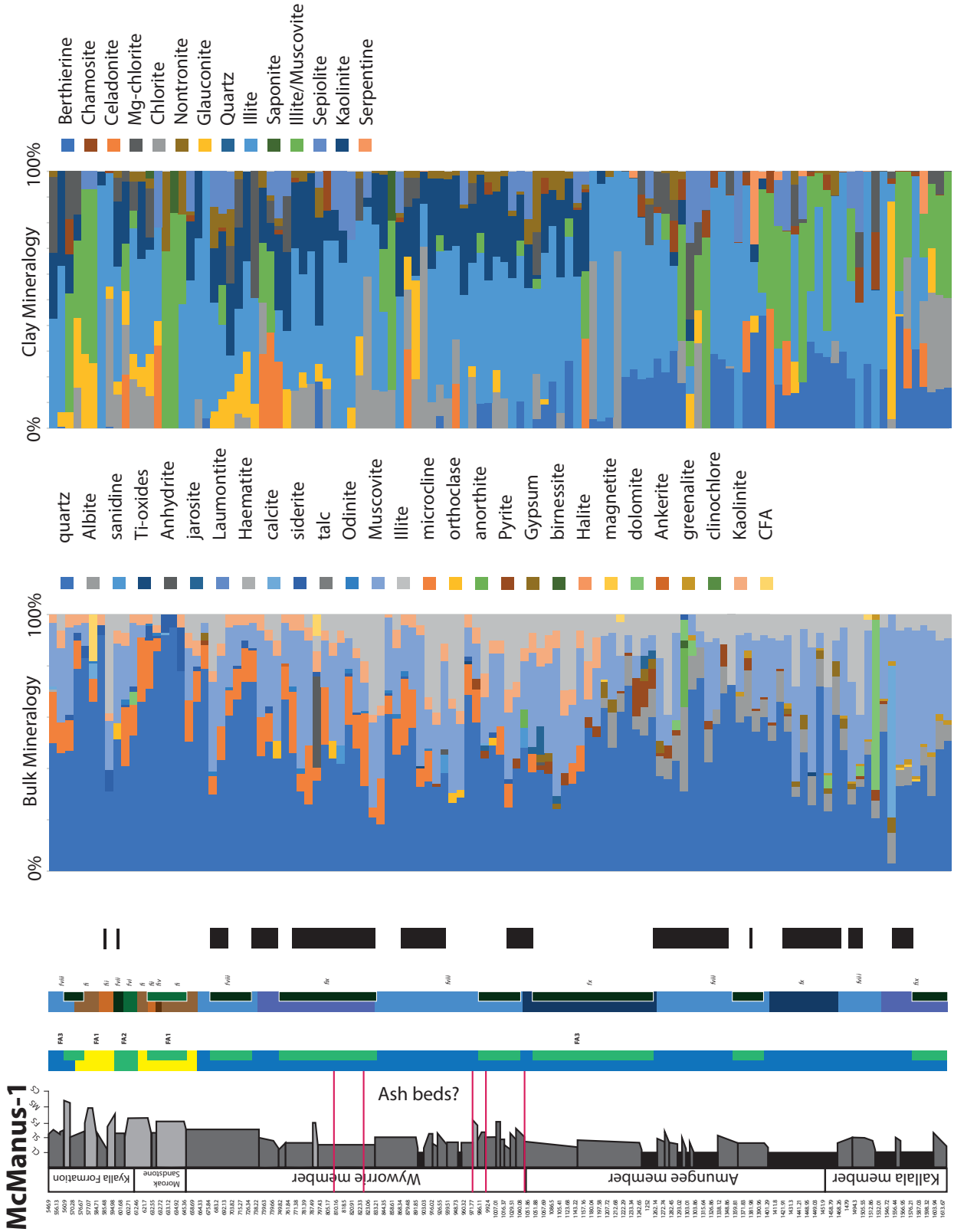

Figure 4: XRD for bulk and clay specific mineralogy for each core MM1, graphic log key, facies numbering, and colour codes are the same as Figure 2 and 3. A = Facies Association, B = Facies, C = Organic rich intervals, pink horizontal bars represent possible volcanic ash beds.

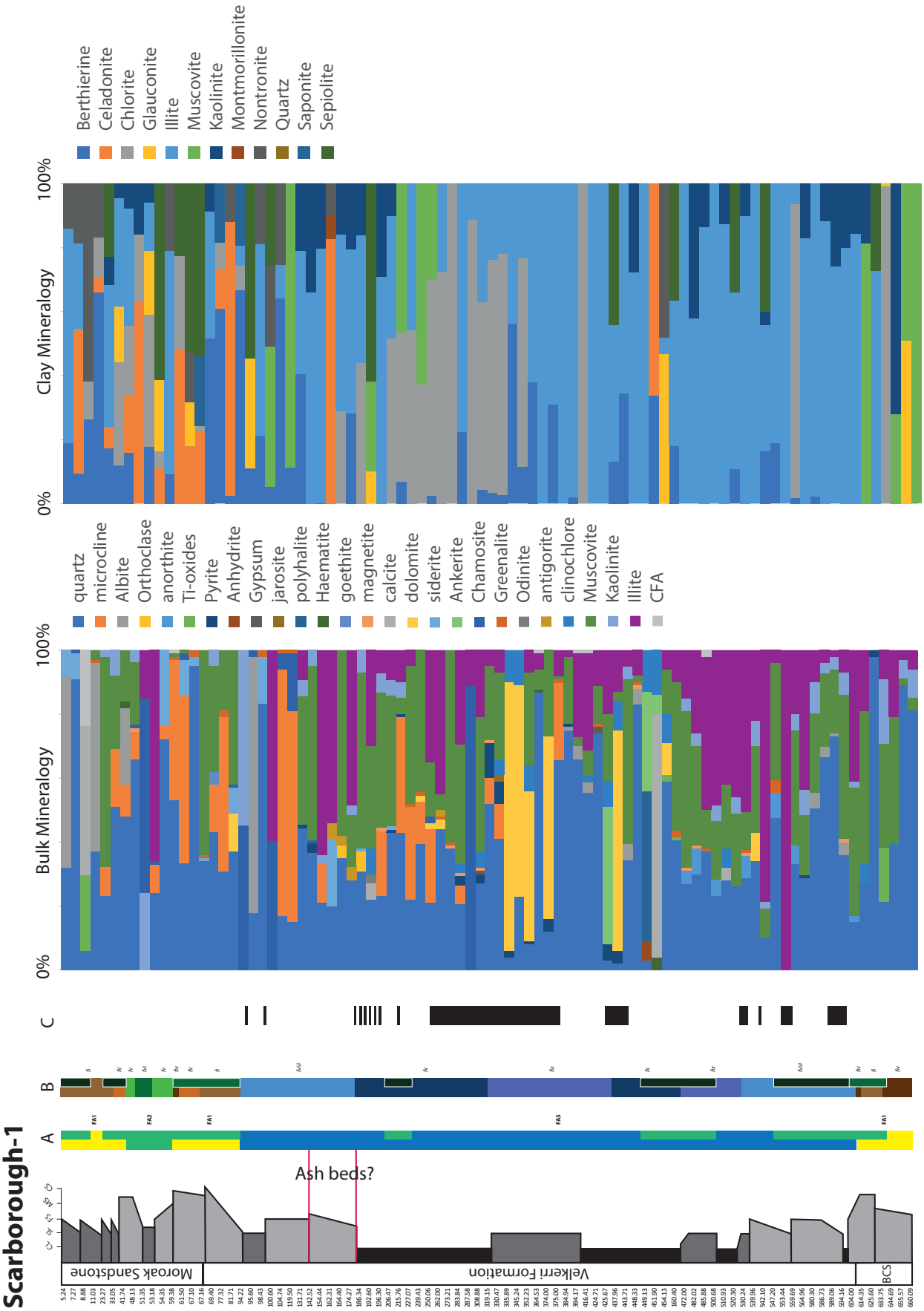

Figure 4: XRD for bulk and clay specific mineralogy for each core MM1, graphic log key, facies numbering, and colour codes are the same as Figure 2 and 3.

the Wondoan Hill Formation must have formed with some physical working in order to account for the coiled and folded inner structure and laminations packed with detrital grains. The relative abundance of heavy detrital minerals associated with the Wondoan Hill coated grains indicates formation of these coated grains took place during a period of sedimentary condensation. Claystone beds represent periods of prolonged lower energy conditions where authigenic green clays could precipitate on the seabed and form beds with microbial textures. However, the claystone beds also contain inclined planar, unidirectional and trough cross laminations, and silt-rich laminations, indicating that while lower in flow energy than the sandstones, persistent current energy was still interacting with seafloor sediments and forming ripples.

On the basis of the features described above and the stratigraphic position of the components of this facies, it was most likely deposited in a range of chemically related, but not necessarily laterally connected environments. Sandstones containing the coated grains are grouped as *facies v: Coated grain sandstones* and were deposited in a shallow high energy environment subject to frequent reworking by waves and storms. The abundance of green clay requires a relatively low sedimentation rate and continuous supply of dissolved sedimentary Fe. Shoreface settings or shoals at the front of a large river delta during the early stages of a transgression, would provide a high energy environment with low clastic sedimentation rates and high rates of fluvial Fe input. Similarly, the Fe could be delivered by coastal upwelling of deep oceanic waters, also during the early stages of the transgression. The stratigraphic position of this facies and data from Johnson *et al* (2020) support deposition of the coated grains during early stages of a transgression. Sandstones rich in green clay but without coated grains are grouped together as *facies vi: Green cemented sands* and were deposited in the same setting as the facies *v*. Johnson *et al* (2020) observed more abundant phosphate grains, and organic matter in the coated grain facies than the green cemented sands facies. Therefore, frequent intense pore water redox fluctuations due to the breakdown of organic matter as a consequence of higher primary productivity, is one explanation for the presence of coated grains in facies v, but not facies vi. Green claystone and mudstone are grouped together as *facies vii: Green muds* and were deposited in a moderate to low energy prodelta setting between lower fair weather wave base and storm wave base.

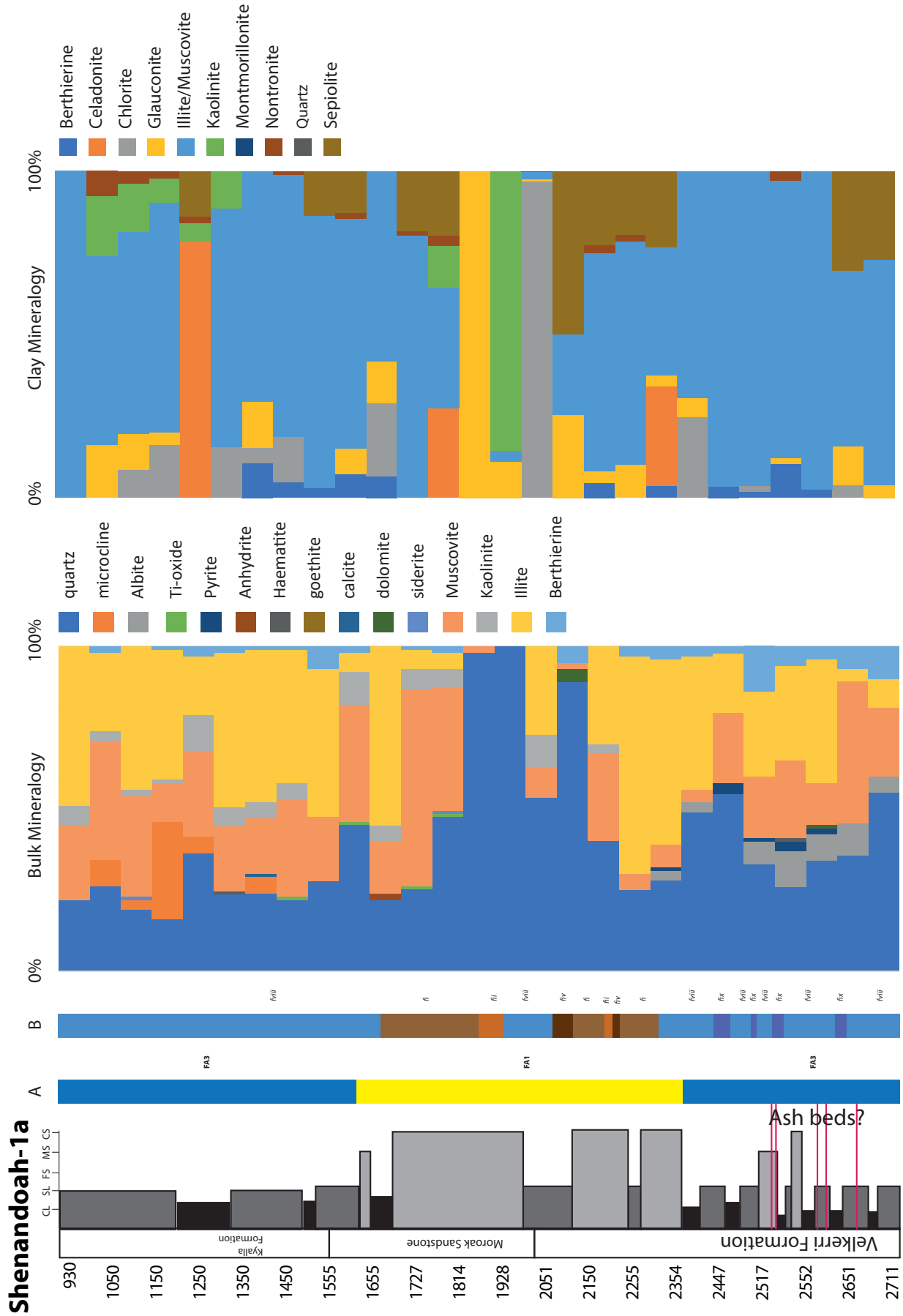

Figure 4: XRD for bulk and clay specific mineralogy for core SD1.

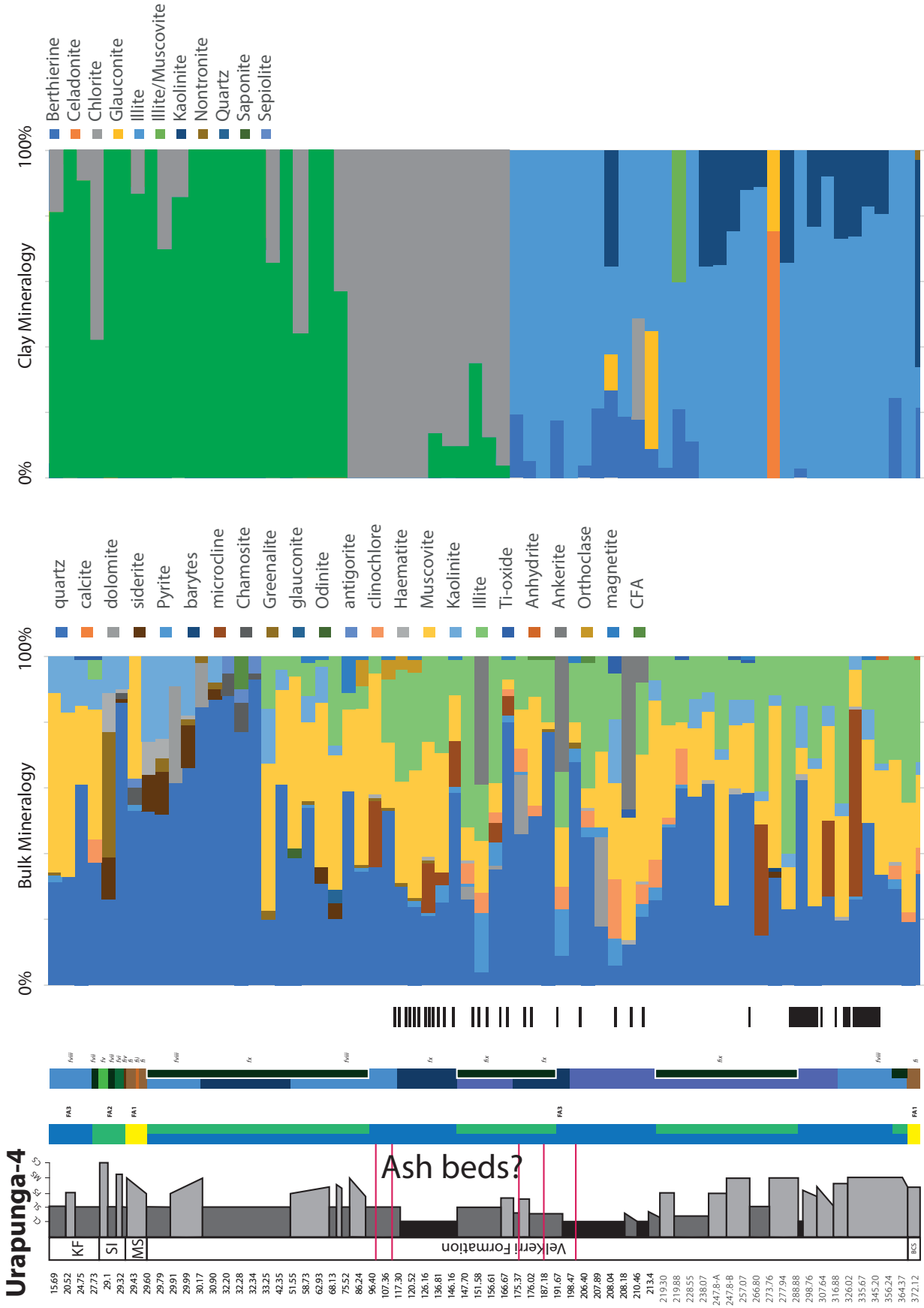

Figure 4: XRD for bulk and clay specific mineralogy for core UP4, graphic log key, facies numbering, and colour codes are the same as Figure 2 and 3. A = Facies Association, B = Facies, C = Organic rich intervals, pink horizontal bars represent possible volcanic ash beds.

Facies Association 3: Marine

Description Facies association 3 (FA3) consists of fine- to medium- grained sandstones with a mature texture and sub-arenite composition, in decimeter to meter scale beds, as well as thin silts in cm to decimeter scale = beds with erosive bases (Fig 2C, Fig 7,). These detrital rich beds are interbedded with decimeter to meter scale beds of blue-grey, grey, green, and black mudstone that variably silt-rich, and decimeter to meter scale beds of finely laminated to massive claystone (Fig 7). Bed contacts are sharp and undulose, erosive at the base of sandstone and mudstone beds, and draping at the base of claystone beds (Fig 2C). Convolute bedding and dewatering structures are common throughout, (Fig 7N, P, S, W, X, Y) while the mudstone beds also feature common vertical sub-aqueous mud cracks. These mud cracks are ptygmoidally folded and filled with coarser material than the host bed (Fig7B, C). Sedimentary structures in the sandstone beds consist of unidirectional, and trough cross beds (Fig7B, L, N, Q, R, T, U, V) . Observations of inclined bedding suggesting bedforms larger than core width are here interpreted as hummocks, it is also possible these structures could be meter scale wave, trough or combined flow cross bedding. The thin siltstone beds and laminations contain unidirectional, combined flow, and small-scale trough cross beds and laminations (Fig 2C, Fig 7D, G, M). Mudstone beds contain combined flow, trough and hummocky cross beds and cross lamination and well as intervals of inclined planar and wrinkly lamination (Fig 7D, D, D). Beds in this facies are arranged in cycles of coarsening or fining-up that are expressed at several scales. A large cycle may range from ~10 – 20 m in thickness and contain several decimeter to meter scale sub cycles. Large cycles generally feature a complete sequence from silt-poor mudstone, through to sandstone, smaller cycles may contain a full or partial sequence, or may coarsen-up over part of the cycle and then fine back upwards or vice-versa. Sandstone at the top of full cycles is commonly overlain by thin cm scale glauconite rich horizons which are draped by the overlying mudstones (Fig 2C). In thin section, siltstones host mm scale unidirectional trough and cross laminations. Similarly, mudstones and laminated claystone host mm scale unidirectional laminations formed from imbricated mm to μm scale chips semi-lithified laminated clay, and mm to μm scale rounded bundles of clay. Massive claystone beds range in colour from black through grey, blue grey, to green. These beds may contain rare poorly defined structures that that appear to be decimeter-spaced mud foresets but whose width may exceed the core (Fig 7K , J, O). The upper surfaces of these structures may be picked out in rare detrital silt and fine sand, or more commonly by bedding parallel shreds of organic matter (Fig 7O). Laminated claystone is generally inclined planar to wrinkly finely laminated but also commonly feature small scale trough, combined flow and hummocky cross lamination (Fig 2C, Fig 7K). Thin

cm scale glauconitic and granular claystone beds are also locally common in both the massive and laminated beds. Claystone intraclast breccias are also locally common and most are *in situ* e.g., the pieces fit together (Fig 7). Microbial Carbonates are found in the upper part of the Battle Creek Formation, and Moroak Sandstone in the core 12BC (Fig 3B & 3I). Microbial carbonates dominantly consist of fenestral to thrombolitic textures with rare domal stromatolites (Fig 2C, Fig 7Z, AA, AB). The internal structure of the microbial carbonates consists of a low-Mg calcite micro spar framework with upper surfaces intergrown and coated with organic matter. The organic matter is intergrown with ferrous-clays and both contain detrital clastic grains. The detrital clastic grains are dominated by quartz with minor feldspar, zircons and other heavy detrital minerals. Dolomite is present as discrete rhombs within the lower part of organic matter laminations where textural relationships indicate growth during earliest diagenesis. Dolomite is also present as a late diagenetic component emanating from post lithification fractures and faults.

*Processes and Interpretation*The combination of sedimentary structures in this facies association indicates variable flow energy levels within the depositional environment. That the same scale and size of sedimentary structures are observed across a range of lithologies indicates that it was the availability of coarser grain sizes in the detrital clastic supply that controlled lithology rather than energy level or water depth. The presence of hummocks indicates periods when the seabed was within storm wave base, while combined flow cross bedding and lamination suggests fair weather wave action. Similarly, the imbricated mud chips and clay bundles indicated that even in the absence of sand sized detrital grains, seafloor flow energy levels were enough to erode semi-lithified seabed and then transport and distribute sand sized mud and clay grains. Therefore, the intervals that contain these features were likely deposited between fair weather wave base and storm wave base. Additionally, fair weather and storm wave mobilisation of the seabed appears to have been an important process for transporting fine grained sediments across the basin. Mudstone and claystone with inclined and horizontal laminations indicate that active working by laminar flow currents was a persistent feature of the seabed. In support of this, horizontal planar laminated mudstone and claystone host μm scale unidirectional cross laminations and imbricated stacks of clay mineral plates.

Microbial carbonates are restricted to the Proximal Regions, with only diagenetic carbonates reported from the Basinal and and Distal Regions during this interval. The microbial carbonates show signs of extensive erosion and sub-aerial exposure, and rare domal stromatolites have low synoptic relief of a few cm. Together these features indicate that the microbial carbonates were deposited in shallow high energy environments where waters levels regularly fluctuated. Repair of

erosional damage indicates that these fluctuations occurred on short timescales. The presence of intergrown green clays indicates that authigenic ferrous silicate growth was also occurring within the life time of the stromatolites micro flora. The relative enrichment of heavy detritals in carbonates in addition to authigenic clay growth indicates, that clastic input was slow and associated with condensation. Therefore, detrital clastic sedimentation may have been a major control on the deposition of primary carbonates within the studied interval.

Massive mudstones are poor in detrital clastics and rich in authigenic clay minerals, and sedimentary structures associated with deposition above storm wave base. Authigenic clays accumulate slowly, so massive claystones represent deposition during periods of very low detrital input, but not necessarily due to an increase in water depth. Wrinkle laminations consist of intergrown fibrous to amorphous organic matter, authigenic minerals and detrital grains. The organic matter envelopes, bridges, and entrains detrital grains indicating synsedimentary lateral growth of the organic matter in addition to suspension settling. Therefore, the wrinkled laminations indicate the presence of benthic microbial mats living on and just below the sediment surface. Bedding planes hosting microbial mats contain features attributed to adhesion and contraction of a robust adhesive substance which is further evidence supporting the presence of benthic microbial mats (Fig 7F, H, & I). Convolute bedding and laminations, and dewatering structures indicates disturbance of a waterlogged seabed. The source of this disturbance could be related to rapid sediment influx, storm activity, localised mass movement or seismic activity. The cause for the disturbed beds and laminations cannot be uniquely identified from the current dataset. However, the presence of erosively based coarse-grained beds and laminations directly overlying finer grained beds indicates rapid sedimentation events were common, so sediment loading probably accounted for some of the convolute bedding. The origin of sub-aqueous mud cracks is still ambiguous, though the cracks observed here are clearly synsedimentary. The wedge-shaped cracks appear to be a produced by by the intrusion of sand into, semi-lithified clay rich seabed. The origin of the elliptical cracks is less clear as they have no observable connection to overlying coarse grained material and appear to have occurred while the sediment was still ductile.

The interbedded sandstones, siltstones and mudstones are grouped together as *facies viii: interbedded sandstone to mudstone* and were deposited in a storm dominated marine shelf environment and represent a sub-set of environments from sub-aqueous delta front through to pro delta inner shelf. The interlaminated siltstones and mudstones are grouped together as *facies ix: Interlaminated siltstones and mudstones* and were deposited in a mid to outer shelf environment on a storm dominated marine shelf. The laminated to massive claystones are grouped together as

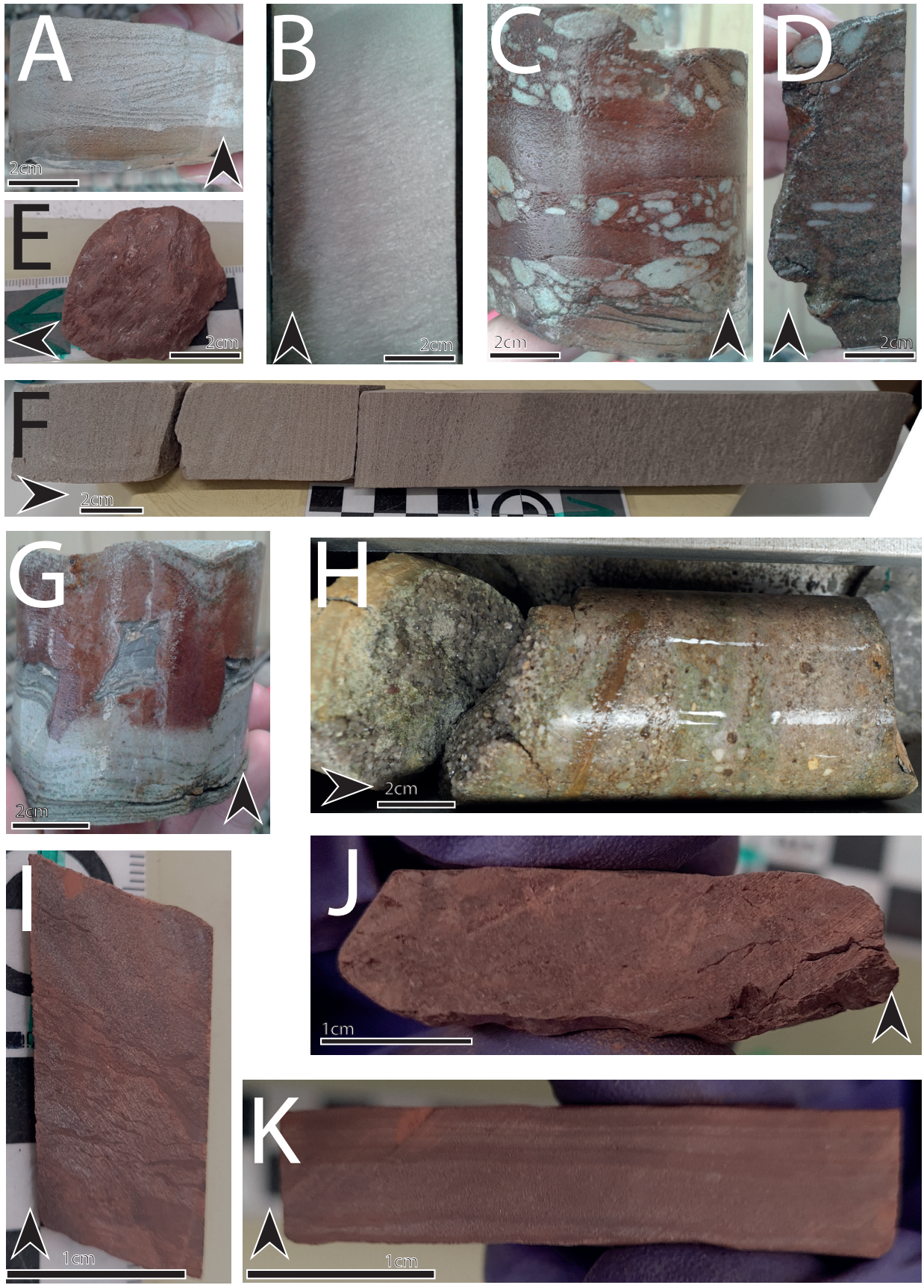

Figure 5: Typical examples from FA1 Paralic to fluvio-terrestrial facies, balck arrow shows sedimentary way up. A) Facies i ripple cross laminated sandstone with ferruginous mud drapes MM1 726.34. B) Facies i cross laminated sandstone with mud drapes MM1 692.13.

facies x: Laminated and massive claystone and were deposited on a storm dominated shelf, distal to sources of detrital clastic input. Finally, *facies ix: Microbial carbonates* was deposited in a shallow marine wave dominated setting that was distal to sources of detrital clastic input.

2.4.2. Sequence Stratigraphy

Sequence stratigraphic surfaces and their identifying characteristics are summarised in Table 2. These surfaces were correlated between cores by comparing stratigraphic position, composition, and similarity of sedimentary packages adjacent to each surface (Fig 3D &3K).

Correlation between cores was performed by lithostratigraphic and chemostratigraphic comparison, in addition to the sequence stratigraphic methods above (Fig 3). The contact between the Velkerri Formation and overlying Moroak Sandstone was used as a datum within the Roper Group due to its basin wide occurrence and because its nature as a correlative surface is unambiguous (Abbot and Sweet, 2000). The presence of green ferruginous sediments with ferrous clay coated grains was used to correlate the Tijunna Group with the Roper Group in the first instance, and is supported by chemostratigraphy, and facies and sequence stratigraphic correlations (Fig 3).

Parasequences were defined based on the identification of flooding surfaces that were correlatable over the length of each transect (Fig 3C & 3J). In proximal areas flooding surfaces were recognised as erosively based fine-grained sediments, usually but not always clay-rich, directly overlying sandy courser grained sediments. In addition to the above criteria, recognition of flooding surfaces in distal areas also included beds rich in, or dominated by authigenic minerals e.g., ferrous-clays or cherts (Fig 3D, J & 3E, L). Characteristics of flooding surfaces and sequence boundaries are summarised in Table 2.

Figure 5 continued: C) Facies iv cross laminated and cross bedded ferruginous sandstone with chert and claystone imbricated pebble laminae MM1 634.81. D) Facies iv cross laminated ferruginous granular sandstone with imbricated pebble laminae MM1 634.72. E) Facies iii typical regolith clay ped with slicken lines clearly visible, 12BC 320.19. F) Facies ii cross laminated sandstone with ferruginous interlaminations that transitions upwards into facies ii silty cross laminated mudstone MM1 621.70. G) Facies ii ripple to undulose laminated ferruginous sandstone, red oxides are overprinting a green grey authigenic mineralogy of glauconite and berthierine, polygonal shapes are here interpreted as ferrous clay moulds after halite hopper crystals, these structures are possibly the origin of the "glendonites" reported from this interval in the core Elliot-1 by Gorter and Grey (2012), MM1 632.72. H) Facies iv cross bedded granular sandstone with chert, vein quartz and carbonate granules and a ferruginous cement, dark graphitic substance on broken surface is a residue of migrated hydrocarbon, yellow staining on the broken surface is modern sulphate from oxidation of sulphides in the hydrocarbons, SC1 100.60. I) Facies iii ferruginous silty mud with wrinkled laminations and a clotted texture, 12BC 404.14. J) Cross section through E showing alternating undulose laminations and convoluted/clotted texture, 12BC 320.19 K) Facies iii ferruginous silty mudstone with alternating silt rich and poor undulose and inclined planar laminations with erosive contacts, 12BC 363.42.

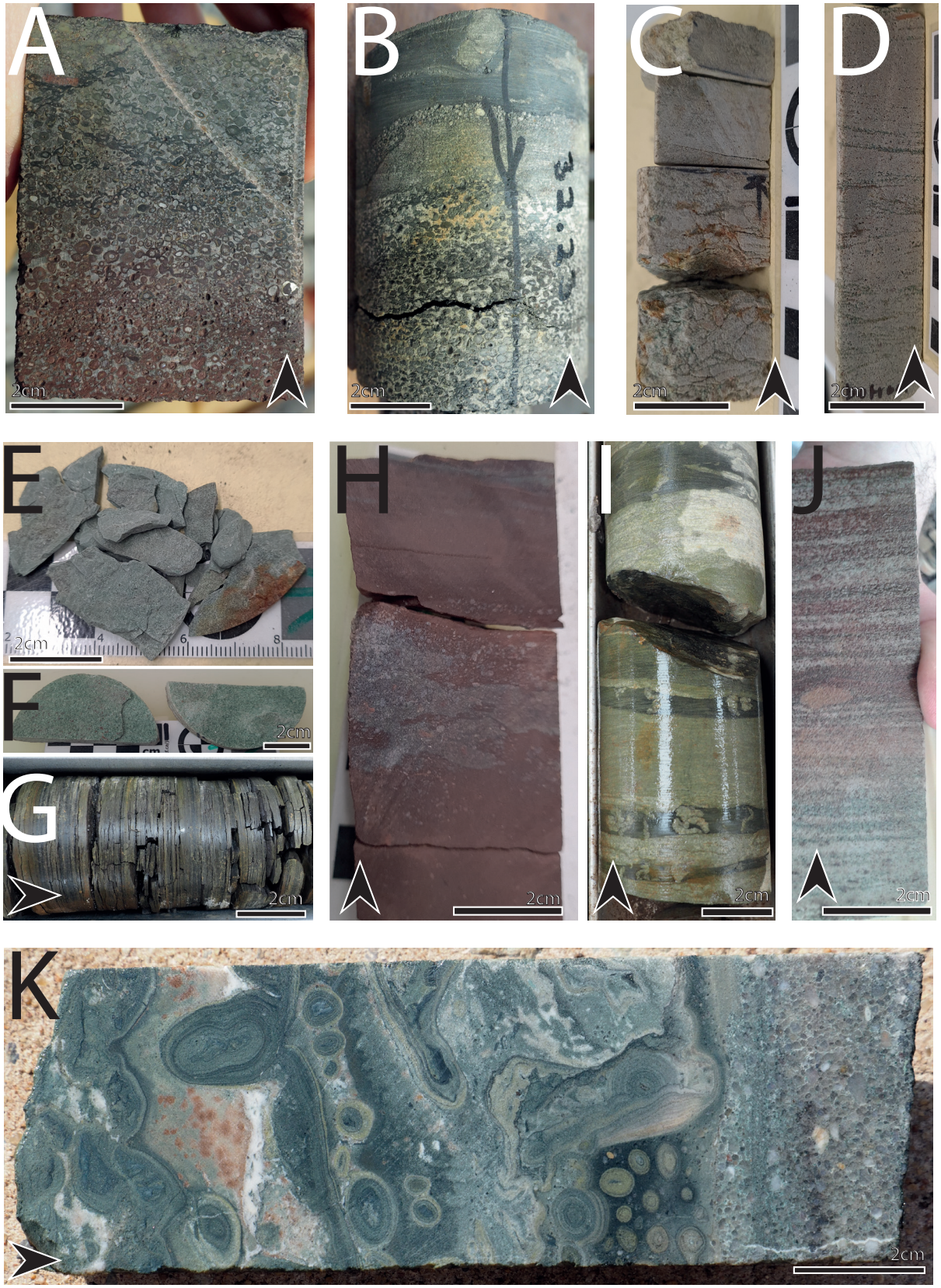

Figure 6: Typical examples from FA2 Ferruginous marine facies black arrows show sedimentary way up. A) Facies v coated grain sandstone, grains superficially resemble ooids, oncoids and pisoids and are composed of ferrous clay, matrix is fine to medium sandstone with a ferrous clay cement, secondary oxidation grades upwards from the base of the sample and over prints the primary mineralogy, UP4 32.00.

Figure 6 continued: B) Upper part, facies vii green mudstone with inclined and undulose laminations. Middle part, facies vi cross laminated green cemented sandstone of fine to coarse sand with a ferrous clay cement, that erosively truncates the underlying bed. Lower part, facies v coated grain sandstone, yellow patch is secondary siderite that overprints the original mineralogy. Note, in this sample, the ink arrow points down core UP4 32.23. C) Facies vi green cemented sandstone undergoing secondary oxidation, the upper part is cross laminated, while the lower part has a peloidal reworked texture. The sand grains have a haematite coating and are cemented by berthierine and glauconite, MM1 664.33. D) Facies vi cross laminated and ripple cross laminated green cemented sandstone with a berthierine cement and glauconite granules concentrated on lamination surfaces, MM1 633.92. E) Facies vii green mudstone composed of berthierine and glauconite with minor quartz silt, MM1 822.23. F) Facies vi bedding surface view cross laminated glauconitic medium sandstone, MM1 584.71. G) Facies vii green mudstone with low angle cross laminations and minor quartz silt, dark colour comes from organic matter, yellow staining is from secondary sulphates, SC1 110.30. H) Facies vi cross laminated fine sandstone where original ferrous clay cement has been oxidised, white/grey patches appear to be post oxidation leaching, 12BC 588.88. I) Interbedded facies vi green cemented sandstone, and facies vii green mudstone. Sandstone shows erosive contacts, is cross laminated and intrudes the mudstone as folded sand dykes. Mudstone drapes sandstones with shallow inclined laminations and shows erosive and loading structures on upper surfaces. Orange patches are secondary oxidation of primary ferrous clays, SC 110.30. J) Facies vi planar to inclined laminated medium sandstone with rare mud pebbles (orange elipse), green cement is berthierine, glauconite grains and cement coat the upper surfaces of cross laminations, red colouring is secondary oxidation, MM1 633.12. K) Facies v coated grains that superficially resemble oncoids but are formed of fine to medium sand cemented by berthierine and greenalite, glauconite is common through out the sandstone matrix, top most part of sample is facies vi inclined laminated sandstone with berthierine cement and common glauconite grains, 99VR 123.00.

4th Order Sequences were defined as a cycle between two or more systems tracts that are bound by a forced regression surface and a ravinement surface and are correlatable between two or more cores (Fig 3O and 3P). As not all systems tracts will be recorded or preserved in all areas of the basin, a sequential order of systems tracts was not used as a defining characteristic when recognising 4th order cycles. In total 23-28 possible 4th order cycles were recognised between the base and top of the studied interval as illustrated in (Fig 3O and 3P).

3rd Order Sequences were defined as a sequential cycle through systems tracts correlatable across the length of each transect and bound by basinwide erosion surfaces that were correlated across each transect (Fig 3C & 3J). One full 3rd order sequence and one partial 3rd order sequence were recognised in the studied Roper Group section. The full 3rd order sequence corresponds to the "Veloak" cycle of Abbott and Sweet (2000) which contains the Velkerri Formation and Moroak Sandstone. The partial 3rd order sequence corresponds to the "Shermi" cycle of Abbott and Sweet (2000) which contains the Sherwin Ironstone, Kyalla Formation, and Bukalorkmi Sandstone which was not part of this study (Fig 3C & 3J). One full 3rd order sequence and one partial 3rd order sequence were recognised in the Tijunna Group which to my knowledge has not previously been subject to sequence stratigraphic analysis (Fig 3C & 3J). The full sequence comprises of sandstones of the Bynoe Formation and Weaner Sandstone, which are overlain by siltstones,

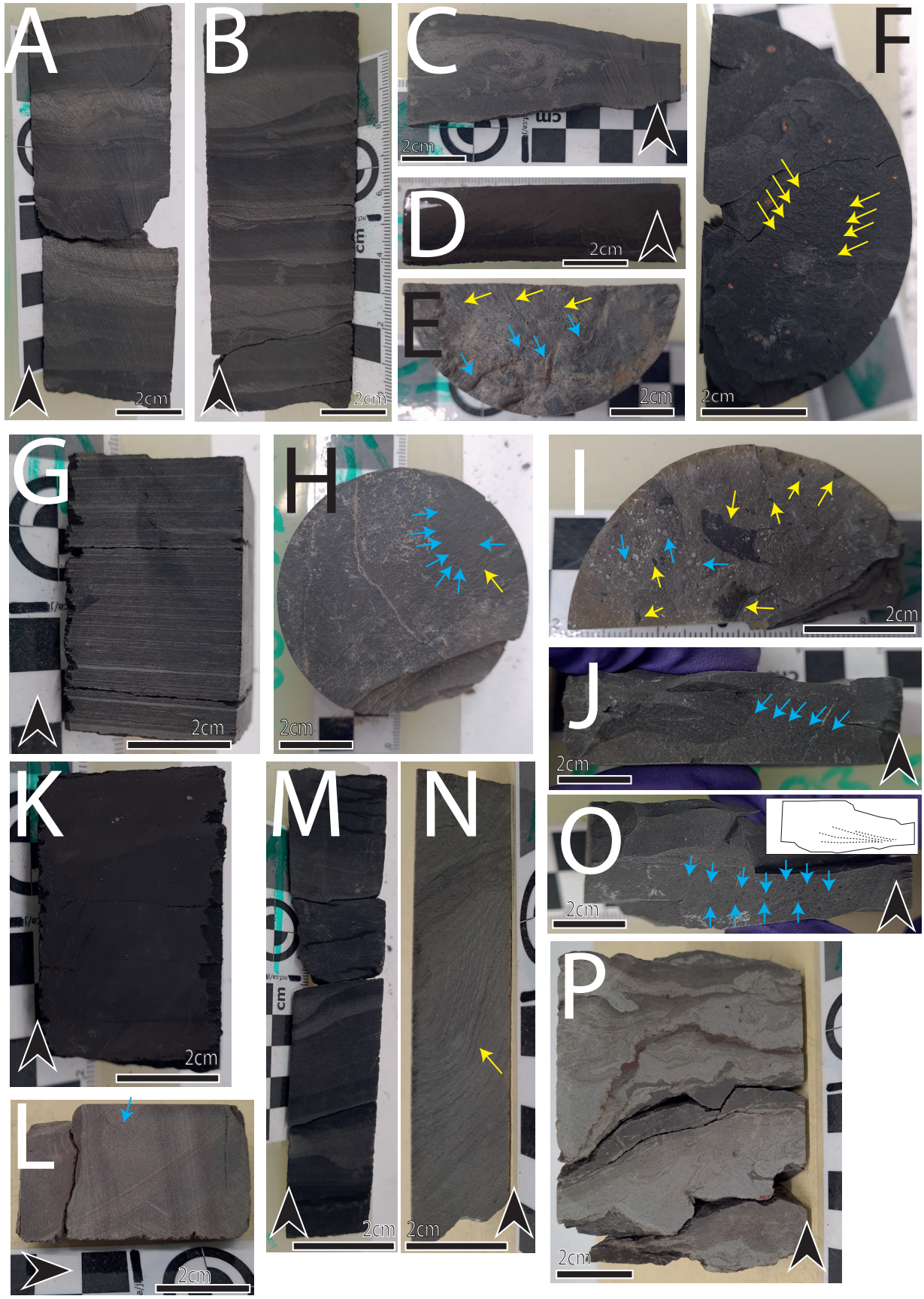

Figure 7 Part 1: Typical examples from FA3 Marine facies scale in cm, black arrows show sedimentary way up, dark colour throughout is organic matter. A) Facies viii cross laminated mudstone in erosive interbeds with cross laminated sandstone, SD1 1588.30.

mudstones and microbial carbonates of the Battle Creek Formation. This cycle is then overlain by a partial 3rd order sequence consisting of mudstones, siltstones and sandstones of the Wondoan Hill Formation which is in turn overlain by siltstones and mudstones of the Stubb Formation (Fig 3C & 3J).

2.4.3. X-Ray Diffraction

XRD Data were collected from both the bulk powders and clay fractions from each core in the studied section (Fig 4). The trends of terrestrial detrital minerals, e.g., quartz, feldspars, muscovite and Ti-oxides, track the changes in RSL such that their abundance increases in periods of progradation and decreased distance from terrestrial sediments sources. Additionally, terrestrial detrital minerals are more abundant in the cores 12BC and 99VR which occupy proximal areas within the RSB (Fig 4A & 4B). Cores which occupy relatively distal areas of the basin, such as UP4, are rich in authigenic clays and relatively poor in terrestrial detrital minerals.

There is a distinct basin wide change in the abundance of feldspars from plagioclase dominated to K-spar dominated in the upper part of the Amungee member of the Velkerri Formation,

Figure 7 Part 1 continued: B) Facies viii interlaminated cross laminated siltstone and mudstone, siltstone has eroded underlying mudstone and has intruded as a small sand dyke, SD1 1588.20. C) Facies viii detail of a sandstone lamination intruding into a mudstone parallel to bedding, turbulent but defined contacts suggest the mudstone was firm but pliable, SD1 1593.67. D) (wet) Facies ix cross laminated siltstone eroding a laminated mudstone, with drapes of organic rich mud along lamination surfaces, MM1 1067.69. E) Facies ix bedding surface showing current parallel lineation's (yellow arrows), and current oblique folds (blue arrows) interpreted as microbially induced sedimentary structures, MM1 1007.01. F) Facies x bedding surface showing wrinkles interpreted as microbially induced sedimentary structures (yellow arrows), red grains are oxides after diagenetic siderite, MM1 1326.84. G) Facies xi interlaminated siltstone and mudstone, laminae have shallow angle cross lamination (left to right), silt rich laminae erode and down lap underlying surfaces, silt lenses are micro channels of silt that are oblique to perpendicular to the primary cross lamination direction, MM1 1157.16. H) Facies x underside of bedding surface showing aligned medium to fine sand size grains of flocculated and/or reworked mud (blue arrows), possible microbially induced sedimentary structures also present (yellow arrow), MM1 960.32. I) Facies x bedding surface showing coherent carbonaceous matter as large shreds and smaller blebs (yellow arrows), composition and origin of pale grey rounded patches currently unknown (blue arrows), MM1 1338.12. J) Facies x cross section showing superficially massive structure, faint low angle cross lamination is picked out by organic matter (blue arrows), MM1 1603.94. K) Facies x claystone, the organic content of this sample obscures the planar to low angle cross lamination, giving a massive appearence MM1 1411.80. L) Facies viii sand rich end member with ripple laminated fine sandstone with mud drapes transitioning upward through massive fine sandstone with dewatering structure (blue arrow), into inclined planar lamination, MM1 771.38. M) Facies ix mud rich end member with erosively based cross laminated normally graded silt laminations, overlain by ripple cross laminated mud, SD1 1589.80. N) facies viii sand cross bedded fine to medium sandstone with mud draping cross lamination surfaces, truncated fold structure is interpreted as a part of a dish shaped dewatering structure (yellow arrow), MM1 749.82. O) Facies x superficially massive mudstone cross section with cross laminations picked out by organic matter (blue arrows) inset shows schematic line interpretation, MM1 1598.32. P) Facies viii with thick convoluted heterolithic convoluted laminations, red staining is secondary oxides after glauconite, MM1 761.84.

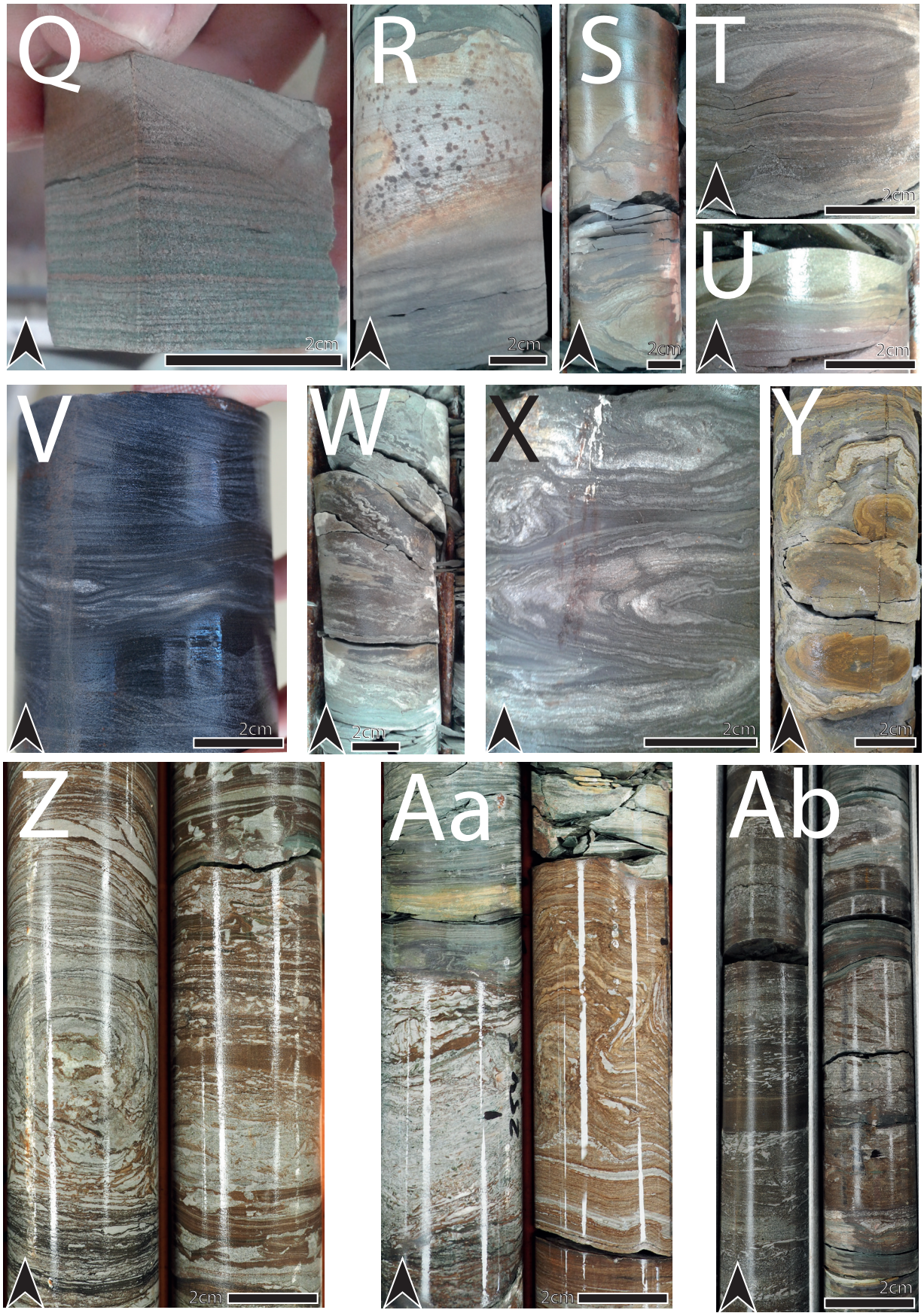

Figure 7 Part 2: Typical examples from FA3 Marine facies scale in cm, black arrows show sedimentary way up, dark colour throughout is organic matter.

and in the middle of the Battle Creek Formation. This may be related to a change in detrital grain provenance or volcanogenic input (see below).

Authigenic ferrous clays such as berthierine are a common component of the clay fraction (Fig 4). Ferrous clay abundance has two main peaks in the XRD data; the first is in the Amungee member of the Velkerri Formation/ Battle Creek Formation, and the second is in the Moroak Sandstone/Sherwin Ironstone/Wondoan Hill Formation. This Sherwin Ironstone is known to have a primary mineralogy dominated by ferrous clays (Johnson et al., 2020). Ferruginous cements and ferrous coated grains were also observed in core and thin section in the corresponding intervals of the Moroak Sandstone and Wondoan Hill Formation (Fig 4A & 4C).

Illite and kaolinite make up the largest fraction of the clay minerals. Petrographic observations suggest that these minerals were deposited by a combination of authigenic synsedimentary seafloor growth, synsedimentary reworking, and minor detrital sources. There is a general trend

Figure 7 Part 2 continued: Q) Facies viii cross laminated sandstone with glauconite grains concentrated on low angle inclined lamination surfaces, upper high angle laminations are glauconite poor, MM1 782.35. R) Facies viii cross bedded and laminated sandstone with an eroded and brecciated upper contact (upper green-yellow boundary), yellow and red staining is secondary oxidation of primary ferrous clays, white area is post oxidation leaching, MM1 746.2. S) Facies viii heterolithic cross bedded sandstone with convoluted laminations with a prominent eroded and intraclastic horizon in the middle, lower lens shape is carbonate cemented sandstone that is draped by overlying layers suggesting early diagenesis, reworking and exhumation of the seafloor, MM1 746.20. T) Facies viii cross laminated and ripple laminated sandstone with clay drapes along the surfaces of cross laminations in the middle part, MM1 851.71. U) Facies vii detail of combined flow ripple laminated sandstone showing clay drapes along cross lamination surfaces, MM1 851.71. V) Facies viii ripple and combined flow laminated sandstone, from an interval previously interpreted as laminated mudstone, hydrocarbons appear to have migrated from underlying mudstones, SC1 400.00. W) Facies ix interlaminated convoluted siltstone and mudstone, sigmoidal folding of some intervals suggests synsedimentary slumping of partially lithified sediments, siltstones are cemented by secondary carbonate and appear coarser than in reality, brown staining is from oxidation of primary ferrous clays, MM1 837.49. X) Facies ix detail of sigmoidal fold in the interlaminated siltstone and mudstone bed underlying W, different deformation styles may suggests different timings of movement, or differing levels of lithification, between the upper and lower part of the sample, MM1 875.00. Y) Facies ix highly convoluted interlaminated siltstone and mudstone that has formed sheath folds plunging towards the viewer in the lower part of the sample, this area also appears to have undergone faulting or shearing that predates the overlying material, the upper part appears to be sliding away and to the left of the image, orange staining is from oxidation of metallic sulphides, oxidising fluids appear to preferentially travel through porous silt rich areas, MM1 912.18. Z) Facies xi microbial limestone interlaminated with ferrous claystone (green weathering to brown), left core section shows domal stromatolites, right section shows flat pebble conglomerate overlain by thrombolite and fenestral limestone, and then laminated limestone/ clay, younging direction from bottom right to top left, black material is organic matter, 99VR 235.00. Aa) Facies xi interlaminated microbial limestone and ferrous claystone (green weathering to brown), right side shows flat pebble conglomerate overlain by brecciated and fenestral limestone and then wave rippled ferrous clay, left side shows wave rippled laminated limestone overlain by domal stromatolites and then laminated ferrous claystone, younging direction from bottom right to top left, 99VR 251.35. Ab) Facies xi interlaminated microbial limestone and ferrous claystone (green weathering to brown), interbedded brecciated thrombolitic and fenestral limestone, flat pebble conglomerates and wave rippled laminated claystone, younging direction from bottom right to top left, 99VR 253.28.

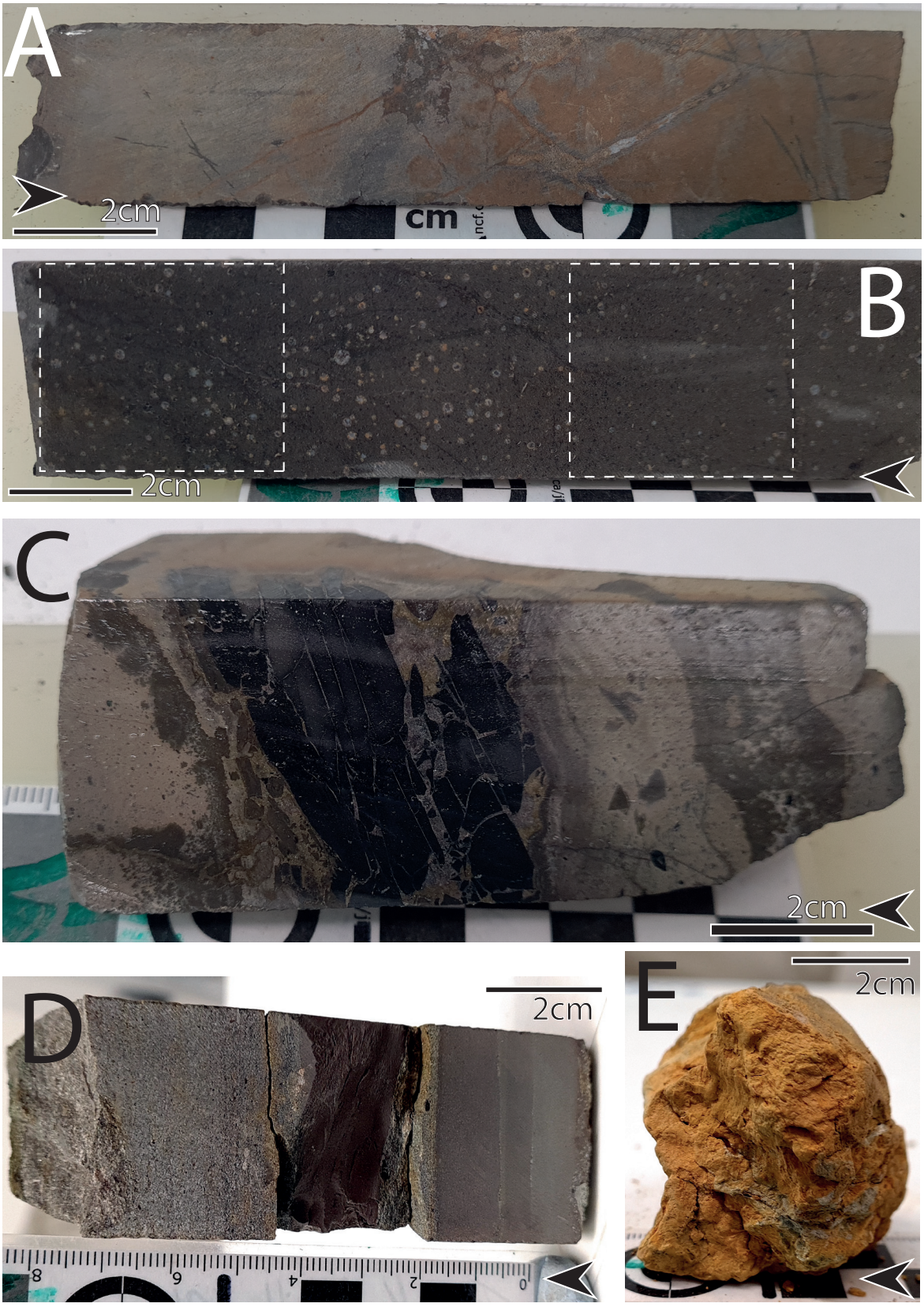

Figure 8: Peperite, dolerite and volcanogenic sediments, black arrows show way up A) Peperite previously identified as massive mudstone, cross cut by later calcite and quartz veins, MM1 1315.64.

of increasing kaolinite abundance up section across the RSB with the exception of the core UP4 where kaolinite decreases up section. In the bulk mineralogy data illite abundance is generally inverse to the abundance of detrital minerals, e.g., quartz and feldspar. In the cores AT2, SD1, SC1 and UP4, the abundance of illite in the clay fraction increases up section and then rapidly drops off in the upper Wyworrie member of the Velkerri Formation (Fig 4D, E, F & G). A similar trend is seen in the core MM1 but the drop off occurs lower in the stratigraphy in the upper part of the Amungee member (Fig 4C). In the previous examples the drop in illite abundance is coeval with increases in ferrous clay abundance. In the cores 12BC and 99VR illite abundance in the clay fraction decreases steadily up section again with a corresponding increase in ferrous clay abundance. In the cores 99VR and SD1, illite abundance in the clay fraction increases again rapidly when ferrous clay abundance starts to decline.

Dolerite Intrusions intersect the upper Roper Group in cores, UP4, MM1, AT2 and SC1, in the studied section (Fig 2). In addition to the previously described brecciated dolerite-host contacts (e.g., Munson 2016), contacts with peperite textures were observed in this study (Fig 8). The range of contact styles indicates that intrusion took place in several episodes from synsedimentary (peperite), to early burial (ductile), and finally post lithification (brecciated).

Volcanogenic Input into the studied section is suggested by several observations: a) the presence of unusual bright green or yellow beds of platy to rubbly (*cf* the 'popcorn texture' of bentonite literature) clay beds in sharp draping contact with underlying beds and limited reworking by overlying beds (Fig 8). Additionally, b) the presence of rare shattered but unaltered euhedral igneous minerals such as olivine, zircon and feldspar, and chert grains with a morphology suggestive of volcanic ash as discrete laminations observed in thin section. Finally, c) corresponding increases of K-feldspar along with nontronite, chlorite and sepiolite in XRD data (Fig 4). The above features are found basinwide in the Velkerri and Wondoan Hill Formations and are suggestive of direct volcanogenic input into the RSB, rather than from erosion and transport of detrital material from an igneous source.

Figure 8 continued: B) Dolerite (inside of dashed line) with vesicular peperite margins (outside dashed lines, MM1 1303.01. C) Peperite composed of fine grained mass of sedimentary rock, igneous minerals and hydrothermal minerals (light brown areas), brecciated country rock (black polygonal areas) and hydrothermal sulphide veins (dark brown bands with botryoidal edges), MM1 1306.86. D) possible volcanogenic layer (black) between two fine sand beds (SC1 67.10), E) possible volganogenic horizon from between two fine sand beds (contact not pictured, SC1 69.40).

2.5. Discussion

2.5.1. Interpretation of sedimentology and sequence stratigraphy

Depositional environments in the Roper Superbasin.

Previous work on the RSB has suggested a range of depositional environments. The depositional environment of the Velkerri Formation has previously been interpreted as an offshore deep marine ranging from storm dominated distal shelf, to a deep basin below storm wave base (Donnelly and Crick, 1988; Jackson et al., 1986; Jackson and Raiswell, 1991). Similarly, the Kyalla Formation has been interpreted as representing a storm dominated shelf setting (Abbott and Sweet, 2000; Munson, 2016). The depositional setting of the Moroak Sandstone and Sherwin Ironstone have previously been interpreted as a tidally influenced shelf and a shoaling bar environment respectively (Abbott and Sweet, 2000; Munson, 2016). The rocks of the Tijunna Group and the studied units of the Bullita Group have received comparatively little paleoenvironmental study but are listed as "marine shelf to shoreface settings" and "shoaling, shallow-marine platform" respectively on the Geoscience Australia map notes and stratigraphic database (Ahmad et al., 2013; Munson, 2016). As stated in the introduction, previous studies were restricted to the limited core material, wireline data and outcrop available at the time and could not make the long-distance correlations used in this study (e.g., Abbott and Sweet, 2000). However, the data presented above clearly indicates that each unit in the studied interval records deposition in several related environments, and that the proportion of the unit that represents each environment changes temporally and spatially.

The upper Roper Group

The Velkerri Formation deposition took place in environments ranging from lowermost shore face through to distal shelf in a storm dominated shelf setting as represented by FA1. Throughout this time, the majority of the Velkerri Formation was within lower fair weather to storm wave base. The change in lithology of the Velkerri Formation appears to have been controlled by the input and transport of detrital clastic material. This can be seen clearly in the abundance of detrital clastics across the N-S transect (Fig 4). Even though the abundance of detrital clastic material decreases northwards, away from the inferred paleocoast, the presence and abundance of wave and storm generated sedimentary structures does not. A key example is the presence of poorly preserved wave generated bedforms and *in situ* clay breccia in the massive claystones in UP4 at the far north of the N-S transect. Several studies have shown that sedimentary structures, including those generated by waves, are poorly preserved in clay rich sediments, especially those formed authigenically and with high water contents (Schieber, 2016; Schieber and Yawar, 2009). It is therefore expected

that the clay-rich intervals of the Velkerri Formation would preserve fewer wave and storm induced sedimentary structures. However, the clay chips and bundles attest to the fact that the waves and storms must have been interacting with the seabed, even when wave generated bed forms are not preserved (Abbott and Sweet, 2000; Plint, 2014; Schieber, 2016) The energy required to erode, rework and transport sand sized chips of semi-lithified clay and clay bundles is unlikely to be supplied by the weak bottom currents found below storm wave base. Similarly, the beds hosting the chips and bundles are not in or adjacent to features that could suggest transport by short-lived high-energy events such as turbidites or wave generated gravity flows. While wave generated gravity flows probably played a part in fine sediment dispersal within the RSB (see below), the shallow gradient of the RSB would not support the formation of turbidites. While some intervals of the Velkerri Formation feature planar lamination, and no observable evidence of wave or storm influence, these intervals make up only a small proportion of the total thickness of the Velkerri Formation (Fig 3B, I). These intervals contain abundant evidence of current reworking and transport of sediments up to fine sand sized grains. Geostrophic currents are known to produce features similar to these in modern sediments, and in some ancient examples (Birgenheier et al., 2017; Buckley et al., 2016; Plint, 2014; Schieber, 2016). However, lack of oriented current data from drill core material means that such interpretations cannot be confirmed for the present study.

The Moroak Sandstone was previously interpreted to represent deposition in inner shelf to shoreface settings on a tidally dominated shelf (Abbott and Sweet, 2000). Data presented above indicate that the Moroak Sandstone additionally also records deposition in several related paralic to fluvio-terrestrial settings (Fig 2A, Table 1). The proportion of each facies recorded in the Moroak Sandstone in a given location is a consequence of the distance from the paleocoast (Fig 3B & 3I). Hence in the core 12BC in a relatively proximal position, the majority of the Moroak Sandstones records fluvio-terrestrial deposition with relatively thin intervals of paralic to shoreface deposition. Conversely, in the core UP4, 375 km north of 12BC and in a relatively distal position, the Moroak Sandstone is both thinner than in 12BC and dominated by shoreface facies, and with a relatively thinner paralic facies (Fig 3B & 3I). This is consistent with a paleo shoreline to the present day south of the RSB, in the region of the 12BC core (but see below discussion of basin architecture). The Moroak Sandstone and FA1 is thickest in the Beetaloo area to the northwest of the core 12BC, e.g., the core SD1. This observation is consistent with a rapidly subsiding Beetaloo area acting as a clastic trap, progradation of a shoreline out into the basin from the southeast (Fig 3A & 3H), and consistent with paleocurrent data reflecting offshore flow from the north (Gorter and Grey, 2012). However, the Moroak Sandstone and FA1 in the core SC1, directly to the north of 12BC, retain a

similar thickness and proportion of fluvio-terrestrial to paralic and shoreface intervals to 12BC, suggesting the progradation was also simultaneously occurring from the east-northeast of the RSB (Fig 3A & 3H).

The Sherwin Ironstone was originally interpreted to represent deposition in a shallow shoaling or shoreface setting, subject to an increased Fe input (Ahmad et al., 2013; Munson, 2018). Johnson *et al* (2020), confirmed this interpretation and suggested deposition took place during the early stages of a transgression, and that increased Fe input was a consequence of deep ocean upwelling and fluvial input. The Sherwin Ironstone *sensu stricto* is found interbedded between the Kyalla Mudstone and Moroak Sandstone as discontinuous lenses in the north-northeast of the central RSB (Fig 3E). However, an interval of FA2 ferruginous sandstones at an equivalent stratigraphic position to the Sherwin Ironstone was observed basinwide in this and previous studies e.g., the ferruginous sandstones of the Beetaloo area in Lanigan et al (1994). Facies analysis suggests that ferruginous conditions were a regular feature of the basin, but that ferruginous conditions during deposition of other units were diachronous in space and time e.g., the Velkerri Formation (Fig 3E & 3L). Therefore, the Sherwin Ironstone and its stratigraphically lateral equivalents represent a confluence of conditions that produced a particularly Fe-rich sediment across the basin. The observation that this ferruginous interval is stratigraphically lower, and therefore earlier in time, to the north of the basin, and in the inferred direction of the open ocean, supports Johnson et al's (2000) hypothesis that additional Fe input came from oceanic upwelling. Deposition of the Sherwin Ironstone and other ferruginous sediments appears to take place early in the transgressive stand systems tract of the 3rd order cycle (Fig 3C & J, see sequence stratigraphy discussion below). This observation suggests that it was the interaction of upwelling deep oceanic waters, and riverine waters being delivered directly to distal oceanic edge of the basin by a prograding coastline, that promoted formation of the highly ferruginous interval (Michalopoulos and AIIer, 1995; Pufahl et al., 2013, Pufahl et al., 2020)

The Kyalla Formation is superficially similar to the Velkerri Formation and was also deposited on a storm dominated marine shelf in comparable FA1 depositional settings to the Velkerri Formation. However, the Kyalla Formation lacks the laminated clay-rich, detrital-poor intervals of the Velkerri Formation. A possible explanation for this contrasting feature is that during deposition of the Velkerri Formation, the northern and western areas of the Beetaloo sub-basin was a site of relatively rapid subsidence and sediment accommodation (Fig 3A & 3H). However, by the time of Kyalla Formation deposition, the subsidence in the Beetaloo area appears to have migrated further south. In addition to providing enhanced accommodation, rapid subsidence in

a relatively proximal area would act as a trap for detrital clastic material (Varban and Guy Plint, 2007). A similar clastic trapping mechanism has been proposed for other ancient cratonic basins to account for similar distributions of detrital-rich and clay-rich sediments between geographically and stratigraphically adjacent units (Buckley et al., 2016; Hallam and Bradshaw, 1979; Huber and Garrels, 1953; Macnaughton et al., 1997; Plint, 2014; Varban and Guy Plint, 2007). A more evenly distributed subsidence rate during deposition of the Kyalla Formation in a basin with a shallow dip may have allowed transport of detrital clastic material over a far wider area and account for the differences and similarities between the Kyalla and Velkerri Formations.

Tijunna Group and Bullita Group

The Bynoe Formation and Weaner Sandstone are dominated by FA1 indicating that deposition took place in a range of paralic to fluvio-terrestrial environments, with an increasing paralic influence up section where shallow marine, paralic and fluvio-terrestrial facies directly overlie each other with minor erosive contacts (Fig 3A & 3H). These observations suggest that the fluvio-terrestrial environments occupied a low-lying area laterally adjacent to the coast and were sensitive to relatively minor changes in relative sea level. In the core 99VR, the contact between the Bynoe Formation and Weaner Sandstone, and the overlying Battle Creek Formation is erosive but is not considered to be a significant unconformity (Munson, 2016 and refs therein).

The Battle Creek Formation is dominated first by FA1 and then FA3 and represents deposition in a variety of shallow water near shore environments. The lower part of the Battle Creek Formation is mudstone dominated and was originally interpreted as shallow shelf deposition (Munson, 2016 and refs therein). However, the presence of minor coarsening up cycles that switch rapidly between mudstone and fine sandstone topped with coarse sand and granule beds and regolith horizons suggests deposition close to shore and frequent, extended, sub-aerial exposure. In light of this, an estuarine or mudflat environment is a more likely depositional setting. The smaller coarsening up cycles culminate in an interval of *facies i,* sandstones indicating deposition in a shoreface to beach setting. The area was apparently still low lying and sensitive to minor changes in RSL as the *facies i* sandstones are interbedded with many sharp based and topped cycles of sandstone and mudstone. Above the middle sandstone is a thick interval of *facies viii* indicating deposition in shallow marine lower shoreface to inner shelf setting (Fig 3B & 3I).

Published core and mapping reports describe the mudstones in this interval as “dolostones” but petrographic and XRD data confirm these are siliciclastic sandstones, mudstones and clay-

stones. Some minor diagenetic dolomitization is present locally and is clearly related to the presence of carbonate-bearing mineralised fractures. The top of the Battle Creek Formation is dominated by *facies xi* and represents one of the few significant examples of carbonate deposition in the RSB. The microbial carbonates host evidence for frequent short-term sub-aerial exposure and so represent a shallower marine environment than the underlying facies. The remainder of the Battle Creek Formation is again dominated by *facies viii* indicating another relative increase in water depth and a shift back to clastic deposition. The contact between the Battle Creek Formation and overlying Wondoan Hill Formation has previously been recognised as an erosional unconformity representing a significant break in time. However, the contact observed in the core 99VR shows erosion of still ductile semi-lithified sediments suggesting the gap in time was less significant than that between the Battle Creek Formation and underlying Weaner Sandstone and Bynoe Formation. In the lower units, the overlying units are clearly eroding lithified material and there appears to be development of parakarst at the contacts.

The Wondoan Hill Formation is dominated by FA1 in the lower half and FA3 in the upper half. In the lower half *facies iii* is dominant and interpreted to represent fluvio-terrestrial deposition in a low-lying area. The rocks of this interval were previously interpreted as "dolostones", however, petrographic and XRD analysis confirm that these beds are dominated by siliciclastic minerals, and that dolomite is a minor secondary phase associated with mineralised fractures. The *facies iii* mudstones and claystones are sedimentologically and mineralogically indistinguishable from "flint clays" *sensu* North American coal mining literature, particularly those of the lower Palaeozoic (see above for mineralogy and sedimentology, analogous to "seat earths" in the UK, Besly and Turner, 1983; Goldbery, 1979; Keller, 1981, 1968; Moore, 2000; Valeton et al., 1983). Flint clays develop in low lying waterlogged areas where ground water flow is able to leach the clay of metal over long time periods leaving a sediment relatively enriched in Si and Al. Petrographic, SEM and XRD analysis of the *facies iii* mudstones and claystones reveals that the dominant mineralogy is microcrystalline quartz with minor illite, and detrital quartz and feldspar silt. However, the micro crystalline quartz also contains appreciable Al, and has retained the habit of the clay precursor, and so the term 'chert' is not appropriate for this rock.

The presence of the flint clay in *facies iii* further supports that the Tijunna Group was deposited in a persistently low-lying area of the RSB. The flint clay interval is topped by a coarsening up over a short interval to *facies v* and *facies vii* which correspond the Sherwin Ironstone in the northern and north-eastern parts of the RSB. These depositional environments are near shore shallow marine with a low clastic input rate. The transition from a terrestrial to a marine facies over a

thin coarsening up interval with minimal erosional reworking of underlying material, also suggests relatively rapid flooding of a low-lying area. Above the ferruginous interval, the Wondoan Hill and partial Stubb Formation are dominated by FA2 shallow marine conditions of *facies viii*.

The 3rd order RSL cycle recorded by the upper Roper Group in the central and eastern RSB is also recorded in the west in the Tijunna and upper Bullita Group rocks intersected in the core 99VR. However, the different local depositional environments and paleotopography cause the 3rd order cycle to be expressed via deposition of a suit of distinct sedimentary rocks. These differences are probably the reason why lithostratigraphic correlation between the different regions has been so difficult, even with the aid of recent detrital zircon and Hf isotope dating (Kositcin and Carson, 2019; Munson, 2018; Yang et al., 2019)

2.5.2. Intra basinal sediment transport

The Velkerri Formation was previously interpreted to reflect deposition below storm wave base in deep water (Abbott and Sweet, 2000; Donnelly and Crick, 1988; Jackson et al., 1986; Jackson and Raiswell, 1991). Data presented above suggest most of the Velkerri Formation was deposited above storm wave base. However, the mechanisms by which fine grained sediments were transported around the basin still requires an explanation. Recent work has shown that suspension settling of fine-grained sediments from gravity driven hyperpycnal riverine flux is unlikely to be sufficient to transport sediments into distal depositional settings in cratonic basins (Plint, 2014; Schieber, 2016; Schieber and Yawar, 2009). This is particularly problematic for settings such as the RSB where a very shallow incline is unlikely to supply the gravitational potential energy to transport even clay sized grains more than 100 km offshore (Plint, 2014; Schieber, 2016).The problem is further complicated in the RSB by the presence of grains up to fine sand sized being present in distal settings. Experimental work and observations of ancient cratonic basin successions has led to the suggestion that wave action, particularly associated with storms, is capable of resuspending fine grained sediments, and in combination with geostrophic currents, transporting of sediments to up fine sand size into distal depositional sites in cratonic basins (Plint, 2014; Schieber, 2016). Evidence of these Wave Enhanced Sediment Gravity Flows (WESGF) has now been observed in a number of ancient cratonic basins (Macquaker et al., 2010; Plint, 2014; Schieber, 2016). Warren, et al., (1998) suggested that the mud-silt/sand couplets may represent Bouma sequences from turbidites at the head of a prograding delta. However, Jackson and Raiswell (1991) note a lack of convincing evidence for Bouma sequences and instead suggest storm driven turbidity flows. Additionally, the shallow dip of the RSB is unlikely to have been capable of generating such tur-

bidity currents and features of the couplets more closely match those observed in experimental and ancient WESGF deposits (Plint, 2014; Schieber, 2016; Schieber and Yawar, 2009). Given the areal extent and shallow incline of the RSB, and the ubiquity of transported detrital grains across the basin, it is likely that WESGFs were the primary mechanism of sediment transport within the RSB depocenter, beyond the effective range of hyperpycnal flows. A shallower depositional setting for the Velkerri Formation with WESGF as a major sediment transport mechanism, ties together core scale and petrographic observations with interpretations of the facies analysis above and the sequence stratigraphy discussed below. The observations also indicate that the dominant physical control on lithology in the Velkerri Formation was not water depth, but rather the supply of detrital clastic material, e.g., the seafloor was still above storm wave base when authigenic clays beds were forming in the most distal parts of the basin.

2.5.3. Paleobathymetry during Velkerri Formation deposition

Constraining paleobathymetry in ancient offshore marine sedimentary successions with any certainty is difficult, more so in Proterozoic successions where paleontological data are not usually present or diagnostic. Qualitative estimates of deposition below storm wave base (SWB) have previously been given for the Velkerri Formation on the basis of sedimentological observations (Abbott and Sweet, 2000; Jackson and Raiswell, 1991). However, the data presented above in this thesis suggest that the average greatest water depths may have been above SWB, and heterogenous in time and space, during deposition of the Velkerri Formation. We can use basic trigonometry to solve for the depth as the vertical side of an right-angled triangle, to provide a back of the envelope estimate of water depth during deposition of the Velkerri Formation (*cf* Plint et al., 2009). Using a distance of 187.5 km, the distance from the coast (12BC) to the depocenter of the basin during Velkerri deposition (MM1), then basin dip gradients of 0.01º to 0.001º (based on gradients typical for cratonic basins, e.g., Plint et al., 2009 and refs elsewhere in this chapter) give a range of water depths between 32 m – 320 m. The lower end of this estimate is consistent with the observations and evidence outlined above and throughout this thesis. For example, the forced regression style implied by facies analysis, and the stratigraphic position of shallow water to paralic facies observed in the Distal Regions of the basin, are not consistent with an average paleobathymetry in the at the higher end of the calculated range.

Therefore, considering the sedimentary, facies analysis and sequence stratigraphic evidence, average water depths in the range of ~30 m to 50 m seem likely during deposition of the Velkerri Formation. This rough water depth estimate comes with the caveats that the gradient range of the

basin is also an estimate, the assumption that the gradient of the basin slope was constant across the basin, and that water depth during HST was also homogenous across the basin. As shown in the facies analysis (Fig 3B & I), it is likely that water depth was heterogeneous across the basin during deposition of the Velkerri Formation within the HST, perhaps as a result of localised seabed subsidence or uplift. Additionally, the restricted and sheltered paleogeography of the basin may have also influenced the perception of water depth by reducing wave fetch and the depth to which oscillatory and combined could penetrate (Peters and Loss, 2012). Finally, this estimate does not take into account decompaction of the sedimentary pile, or restoration of the tectonically shorterend basin. With further core data, a more detailed estimate of paleobathymetry following the methods demonstrated by Plint et al., (2009), could be attempted.

2.5.4. 3rd Order Relative Sea Level Cycles

The data presented above support the 3rd order sea level cycles proposed by Abbott and Sweet (2000) and the studied interval corresponds to their "Veloak" and "Shermi" cycles. In their model, Abbot and Sweet (2000) suggest that the sequence stratigraphy of the Velkerri to

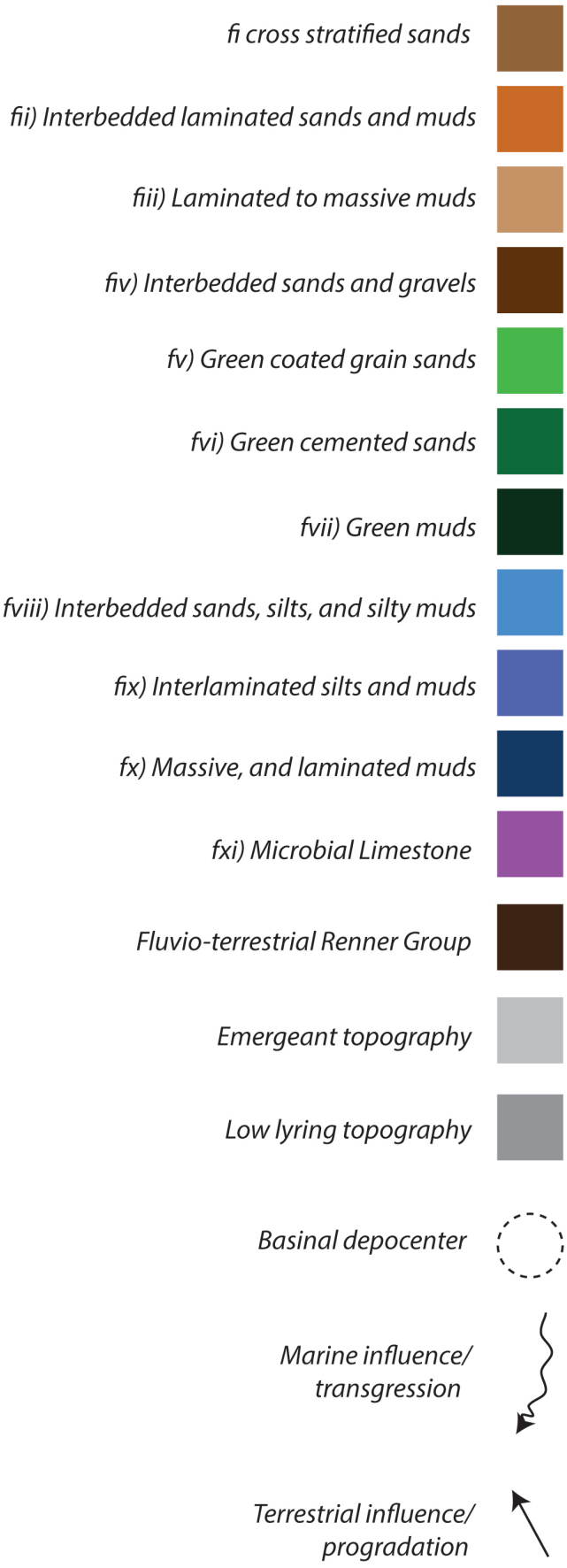

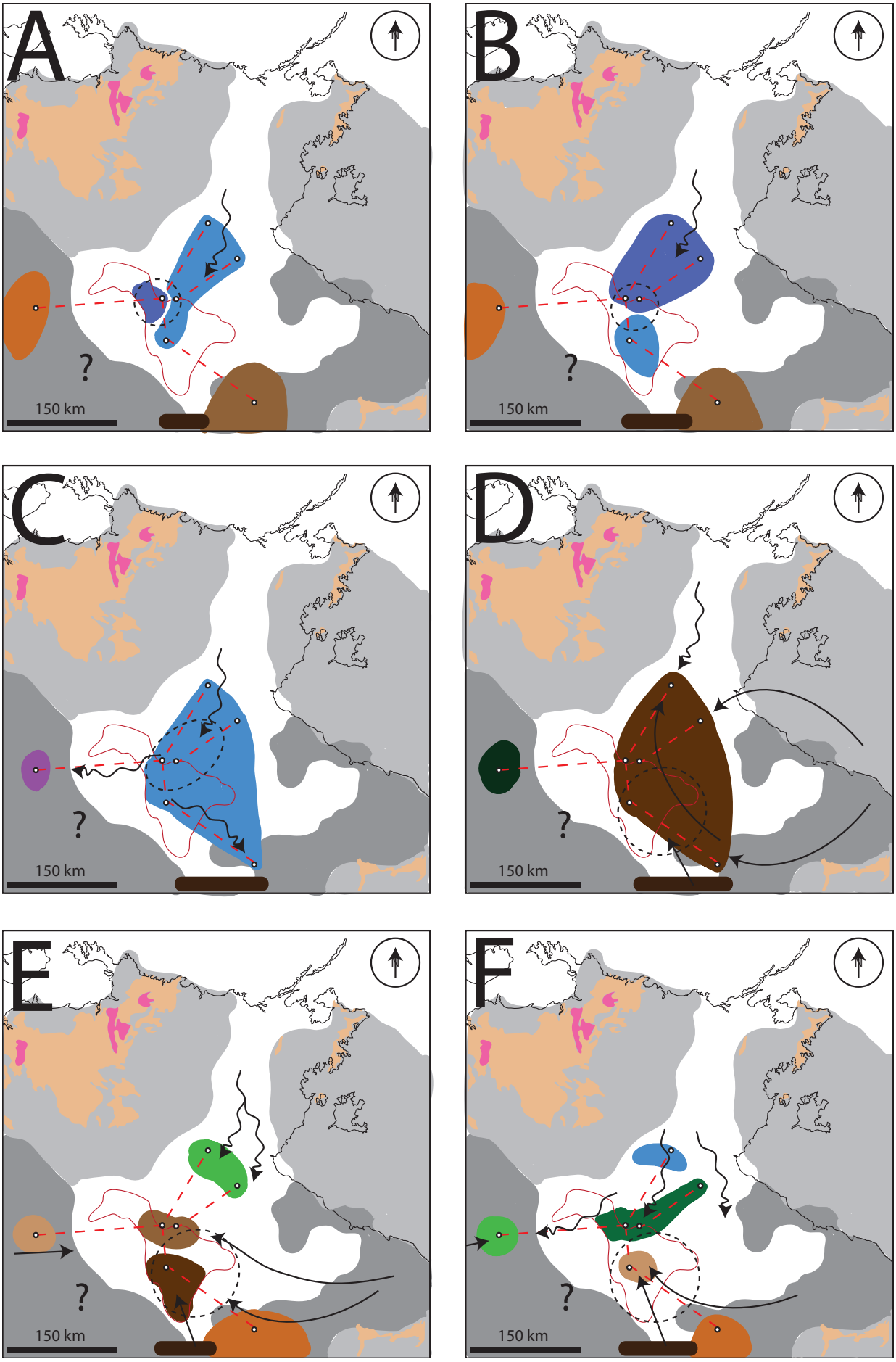
A
?
150 km
B
?
150 km
C
?
150 km
D
?
150 km
E
?
150 km
F
?
150 km

Kyalla interval is progradational and transgressive in nature. The Velkerri, and Kyalla Formations were interpreted to represent a late transgressive to high stand systems tract. The transition from TST to HST was placed in the lower Velkerri Formation, and since a distinct condensed section was not recognised, the maximum flooding surface was also placed in the lower Velkerri (Abbot and Sweet, 2000). The Moroak and Bukalorkmi Sandstones were interpreted to represent a HST during aggradation, and the Sherwin Ironstone was interpreted to represent the earliest TST (Abbott and Sweet, 2000). Accommodation was generated by orogenic flexural loading from the hinterland, with the peripheral uplift providing the sediment for basin fill (Abbott and Sweet, 2000). Flexural loading created a "peripheral bulge" (analogous to the forebulge of a foredeep) that migrated southward along the N-S transect during flexural relaxation (Abbott and Sweet, 2000).

Migration of the bulge created localised uplift, leading to reduction in accommodation and erosion of 10+ of meters of strata deposited during the LST, FST and upper HST (Abbott and Sweet, 2000). The resulting erosional surface between the Velkerri Formation and the Moroak Sandstone was considered to be an intersequence erosional surface, rather than a sequence boundary (Abbott and Sweet, 2000). A forced regression model for the observed sequences was rejected because a) the single regressive erosive surface produced would require a reduction of accommodation to such an extent, that deposition of the surviving thickness of Moroak Sandstone would be unlikely, b) subsequent increases in accommodation following the forced regression would produce multiple erosion surfaces within the Moroak Sandstone which were not observed, and c) type 1 subaerial sequence boundaries were not observed in the Velkerri to Kyalla interval (Abbott and Sweet, 2000). Consequently, Abbott and Sweet (2000) suggested that low stand sediments had been eroded by uplift leaving an intrasequence submarine erosional surface and asymmetrical two-step sequence stack comprising the transgressive and high stand systems tracts.

Significant marine erosion must have taken place once the Velkerri Formation permanently crossed the FWWB, regardless of the mechanism causing the drop in relative sea level. However, the contact observed across the cores in the Proximal and Basinal Regions in this study appears to have been caused by subaerial erosion that took place after any initial marine erosion. Abbott and Sweet (2000) attribute marine erosion in the distal area of the Velkerri Formation to southward migration of a peripheral bulge which formed in response to proximal flexural loading. We might expect that this migration and erosion would result in a levelling of the Velkerri Formation

Figure 9: Facies distributions maps as time slices based on Figure 3b & i. A) Basal Velkerri equivalent. B) Lower Velkerri equivalent. C) Middle Velkerri equivalent. D) Lower Moroak Equivalent. E) Upper Moroak equivalent. F) Sherwin/Early Kyalla equivalent. See previous page for key and main text for details.

to a similar stratigraphic level across the N-S transect. Additionally, we might also expect to see a pause or even reversal of the rapid subsidence in the Beetaloo sub-basin depocenter. Instead, we observe that the upper Velkerri Formation is eroded to different stratigraphic levels during the period of proposed bulge migration (Fig 3). Further, we also observe a continuation of the enhanced subsidence in the Beetaloo sub-basin resulting in greater thicknesses of Velkerri Formation in this area relative to the distal or proximal margins (Fig 3). However, if the peripheral bulge was confined to the distal margin of the transect, then this would reconcile the marine and subaerial erosion, the continued rapid central basin subsidence, and the deposition of a relatively thinner sediment packages in the distal region of the transect (Fig 3, Catuneanu et al., 2011). An architecture analogous to the pattern observed in the Velkerri to Kyalla interval was observed by Varban and Plint, (2007) in Cretaceous successions from Alberta, Canada. In this example, development of a rapidly subsiding proximal foredeep resulted from downward flexure and increased sedimentation related to the Rocky Mountain orogeny (Varban and Plint, 2007).

The resulting sedimentary sequence features storm dominated proximal to distal mudstones that grade laterally into sand and silt poor authigenic sediments which onlap a distal forebulge and remain within storm wave base (Varban and Plint, 2007). Despite the proximal foredeep, the basin retained a shallow slope (Varban and Plint, 2007). As a consequence, even relatively minor reductions in relative sea level were able to produce progradational sandstones with sharp erosive bases marking a maximum regressive surface that is correlatable across 100+ Km in both outcrop, core and wireline data (Varban and Plint, 2007). These regressive sandstones thinned onto the distal forebulge but retained depositional thickness in the proximal depocenter due to relatively rapid subsidence in the proximal area (Varban and Plint, 2007). Forced regression in a shallow cratonic basin with a proximal foredeep and stationary distal forebulge/peripheral bulge reconciles the observations made here with those of Abbott and Sweet (2000), while accounting for the issues that led Abbott and Sweet (2000) to reject a forced regression model.

The maximum flooding surface for the 3rd order sequence is here defined as a glauconitic horizon that overlies an eroded and reworked mudstone bed, both of which are correlatable across the Distal, Basinal and southern Proximal Regions (Fig 3D & 3K). This places the MFS just below the Velkerri–Moroak contact in UP4 at the distal north end of the transect. In the Basinal Region, the MFS is ~100 m and ~25 m below the contact in MM1 and SD1 respectively (Fig 3D & 3K). In 12BC at the southern proximal end of the transect, the MFS is ~10 m below the contact. Variation in the position of this correlatable chronostratigraphic surface supports continued rapid subsidence through the HST, into the FST and LST, and increased rates of erosion and/or relative uplift at the

proximal and distal margins of the transect (Fig 3D & 3K). Subsequently this condensation marks the start of a HST which is much reduced in comparison to the model from Abbott and Sweet (2000).

The corresponding expansion of the TST is supported by the presence of several coarsening upwards cycles topped by ravinement surfaces indicating basinwide shallowing then sudden deepening, which are correlatable across the transect (Fig 3D & 3K). An interpretation of continued relative sea level rise is also supported by the backstepping behaviour of paralic facies in the lower part of the core 12BC on the proximal southern end of the transect (Fig 3D & 3K). If sea level were in a stable high stand, then we would expect the paleocoast to show an ascending aggradational or progradational trajectory, instead of the ascending retrogradational trajectory observed here (Catuneanu et al., 2011). The newly assigned position of the MFS is one of the few correlatable intervals where the character of the sediments suggests a stable high relative sea level across the RSB within the 3rd order sequence (Fig 3D & 3K).

Paralic and fluvio-terrestrial facies are present throughout the Velkerri Formation in the core 12BC, where they top coarsening up cycles, or form the base of fining up cycles (Fig 2A, Fig 3A & 3H). These facies are only present in the Distal Region of the transect within the Moroak Sandstone of the cores SD1 and MM1 where they hold the same relationship with coarsening and fining up cycles (Fig 3A & 3H). The Moroak Sandstone in UP4 at the distal end of the transect contains only paralic and shoreface facies, consistent with the leading edge of the paleocoast prograding into the sea (Fig 3B & I). As predicted by Abbott and Sweet (2000), multiple erosion surfaces are found though out the Moroak Sandstone in 12BC, SD1 and MM1(Fig 3A & 3H). These surfaces mark erosion by both regression and flooding, but it is unclear if they form the composite forced regression surface suggested by Abbott and Sweet (2000). The Moroak Sandstone is much thinner in UP4 and is interbedded with the Sherwin Ironstone, it is therefore difficult to ID any erosional surfaces with certainty. However, this lack of erosive surfaces may simply be a consequence of intraformational erosion and reworking in the high energy coastal setting where the distal Moroak Sandstone was deposited. Alternatively, as the Sherwin Ironstone is interpreted to represent transgressing marine waters, the Sherwin Ironstone interbeds may represent expanded equivalents of the flooding surfaces found in the more proximal intervals of the Moroak Sandstone.

2.5.5. 4th Order Relative Sea Level Cycles

The 3rd order cycles discussed above are overprinted by multiple 4th order cycles recorded as parasequences of alternating adjacent systems tracts (Fig 3O & 3P). The style of alternation varies across the transect with TST and HST parasequences dominating the distal end of the transect (e.g. UP4), and TST and FST dominating the proximal ends of the transect (e.g., 12BC, Fig 3O & 3P). The current data set lacks the temporal and spatial resolution to be able to interpret the driver of these smaller scale relative sea level changes. The 4th order cycles appear to show a periodicity that runs in and out of phase with the 3rd order cycles, e.g., the 3rd and 4th order cycles sync up during the 3rd order HST and LST, though this may be an artefact of aliasing (Fig 3O & 3P). Similar types of cyclic periodicity have been attributed to RSL and/or climatic changes driven by Milankovitch cycles (e.g., Grotzinger, 1986; Mingxiang and Tucker, 2013; Mitchell et al., 2020). However, without a much improved temporal calibration, Milankovitch cyclicity cannot be supported with any certainty. Alternative explanations for 4th order RSL cyclicity include tectonically induced changes in the local subsidence or sedimentation rates, sea level fluctuations from regional oceanic spreading centres, or localised uplift from igneous intrusions. As all of these local or regional processes were active during deposition, it is likely that they all played a part in producing the 4th order sequence stratigraphic cycles observed in the upper Roper Group (Munson, 2016; Yang et al., 2019). However, until temporal calibrations are improved, and more core material is collected and studied, it is not possible to ascertain with any certainty which processes were dominant at which time in a given area of the RSB.

2.5.6. Dolerite intrusions and volcanogenic horizons

Observations above suggest that RSB sediments record syndepositional magmatism in the form of dolerite peperite and beds containing volcanogenic material characteristic of a distal ash fall. Ash beds may allow correlation between cores within the basin and potentially further afield and have the potential to improve the chronostratigraphy of the upper Roper Group through direct dating of zircons. Further to this, observation of ash beds also supports previous work that shows an influx of P derived from a mafic to intermediate source prior to and during deposition of the organic-rich Amungee member of the Velkerri Formation, co-eval with a change in feldpsar type as also reported in this thesis (Cox et al., 2016). Yang et al., (2019) suggest a change in drainage to the south of the RSB in the Arunta Region, and to the east from northern Queensland thus providing an influx of nutrient rich detrital sediments into the RSB leading to increased primary productivity and the generation of organic rich shales (Cox et al., 2016). Volcanism associated with

regional extensional tectonics may also have contributed nutrient rich ash to the RSB (Cox et al., 2016). Further study is required to understand the timing and extent of any volcaniclastic input into the RSB, but the observation that the ash bearing beds also coincide with the deposition of organic rich shales is conspicuous.

The presence of peperite in several cores may indicate synsedimentary intrusion of the upper Roper Group during a period of mafic magmatism in the region. New Re-Os and detrital zircon dates for the Velkerri Formation give a depositional age range of 1390 ± 0.01 Ma and 1360 ± 0.02 Ma (Bodorkos et al., 2021; Kendall et al., 2009; Yang et al., 2019). The age of the mafic units that intrude the upper Roper Group have been recently dated to ~1327.5± 0.6 Ma and 1295± 14 Ma, and so postdate the Velkerri Formation deposition. However, dating of the mafic intrusives is ongoing, and those described in this thesis are as yet undated directly. Even if peperite formation postdates Velkerri and upper Roper deposition, their presence helps illustrate differential diagenesis within a fine grained organic rich succession. Further, the new data on the mafic intrusives and peperite help to correlate the upper Roper Group with other mafic intruded northern Australian successions and tectonic events and potentially co-eval strata in north China and Siberia (Bodorkos et al., 2021; Yang et al., 2019; Zhang et al., 2018).

If correct, these correlations would place the RSB on the edge of a larger rift basin that is proposed to have formed as Protoaustralia, North China, and Siberia rifted from Laurentia (Kirscher et al., 2020; Mitchell et al., 2020; Zhang et al., 2018). This tectonic setting is analgous to early stages of the formation of the Gulf of Mexico during the Cretaceous, with basins such as the RSB occupying an equivalent geographic position to the Mississippi embayment in the Western Interior Seaway (Kirscher et al., 2020; Mitchell et al., 2020; Zhang et al., 2018). This would make the RSB a continental basin on the periphery of a larger, possibly oceanic, rift basin and adds another level of disconnection from the global ocean (Kirscher et al., 2020; Mitchell et al., 2020; Zhang et al., 2018). Further, this interval of the late Ectasian to early Stennian period is now known to host several Large Igneous Provinces that have been linked to rifting association with the peripheral reorganisation of Nuna during the amalgamation of Rodinia (Kirscher et al., 2020; Zhang et al., 2018).

These new data suggest that the Ectasian-Stennian boundary may have been similar to the Cretaceous with increased oceanic crust production causing flooding of low-lying continents and an increased CO_2 flux to the atmosphere. If this hypothesis is correct, cratonic basins such as the RSB would be exactly the locations were we would expect to see rapid transgressions coupled with forced regression, and the formation of restricted water bodies that accumulated organic

matter deposits. Firstly, the igneous data discussed above supports oceanic ridge production as potential driver of the 4th order sea level cycles. Secondly, recognising that sedimentary rocks were deposited in a restricted basin network on the periphery of a larger restricted ocean basin, indicates that any geobiological influence from the global ocean was likely overprinted by local and regional influences. Finally, deposition of RSB sedimentary rocks during a period of LIP volcanism would mean that rather than recording 'typical' Mesoproterozoic environmental conditions, we are instead sampling an ancient hyperthermal event. This interpretation is currently conjectural but could be tested by acquiring more radiometric ages for existing successions to improve age constraints and correlations, and to perform similar high resolution paleoenvironmental studies using a first principles sedimentological and sequence stratigraphic approach.

2.5.7. A new paleogeographic depositional model of the RSB

I propose a new paleogeographic model for the RSB where deposition takes place in a basin that undergoes periodic separation from the open ocean (Fig 9). The basin is bound by emergent topography around most of its periphery and deposition on the oceanward side took place on a submerged topographic high (Fig 9). The geometry of the basin was of a relatively shallow ramp dipping to the present north northeast with a maximum average water depth of 30 m – 50 m during RSL HST. The shallow dip of the basin allowed relatively rapid transgressive-regressive cycles which produced a distinct two-step forced regression sequence (Fig 9). The basin centre experienced rapid subsidence in the Beetaloo region during deposition of the upper Roper Group, further accentuating the 3rd order forced regressive pattern.

The depocenter shifted southward during deposition of the middle Velkerri Formation coincident with a change in detrital sediment provenance (Fig 9). The shift in depocenter position, and provenance probably represent tectonic reorganisation of the hinterland drainage networks and a shift in tectonic loading closer to the RSB (Fig 9). The western, south and eastern proximal periphery of the basin were dominated by fluvio-terrestrial and shallow marine to paralic depositional environments throughout the studied interval (Fig 9). The central depocenter of the basin varied between storm dominated marine, through to shallow marine, through to paralic and fluvio-terrestrial depositional environments (Fig 9). The northern distal periphery of the basin hosted storm dominated shelf environments during high relative sea level, and paralic environments during low sea level. Intermediate environments are recorded on the northern distal periphery but are much thinner compared to the rest of the succession, probably as a result of erosion during sea level

rise and fall (Fig 9). During transgression, marine environments approached from the present day north to the south. During regression, progradation occured from the present day south and from the north and northeast (Fig 9).

2.5.8. Implications for previous interpretations of RSB depositional environments and geochemistry.

Previous interpretations of upper Roper Group environmental geochemistry have assumed that the RSB was in open communication with the global ocean (e.g., Jackson and Raiswell, 1991; Johnston et al., 2008; Mukherjee and Large, 2016; Shen, 2002). However, the data presented above indicate that the RSB was in fact relatively restricted with respect to the global ocean. Initially because of the local basinal geography during deposition of the upper Roper Group, and potentially because the RSB may have been peripheral to a larger but still restricted intracontinental gulf (Kirscher et al., 2020; Mitchell et al., 2020; Zhang et al., 2018). In either circumstance, the RSB was not in communication with the global ocean during deposition of the upper Roper Group and Tijunna Group. Therefore, any global ocean geochemical signals recording during deposition of the Roper and Tijunna groups are likely to have been overprinted by regional and local conditions. Even during sea level high stands, the close proximity of terrestrial environments and fluvial systems would overprint any oceanic signal with a local signature. In this respect alone, geochemical signatures recorded in the sedimentary rocks of the RSB do not record global ocean conditions, and so cannot be used to infer wider environmental conditions during this interval of the Mesoproterozoic. Additionally, local tectonic processes such as the intrusion of syn-depositional lavas, and nutrient loading from hinterland reorganisation and volcanic input, have combined to make the RSB a highly atypical depositional environment. However, these new data, and interpretation do not change the fact that cratonic basins such as the RSB appear to have been environments central to the early evolution of eukaryotic life (Javaux et al., 2001; Javaux and Knoll, 2017). If as some authors have suggested, the open ocean was indeed relatively poor in P and other nutrients, environments such as the RSB may have acted as nutrient traps where early eukaryotes could thrive. This theme is explored in detail in the following chapters of this thesis.

2.6. Conclusion

Based on a combined sequence stratigraphic, sedimentological and petrographic study, the ~1350 Ma Roper Superbasin of northern Australia is shown to be a fairly typical cratonic basin. Rather than a deep clinoform dipping towards the open ocean, the RSB is shown to be a relatively shallow ramp with a dip angle in the range of 0.01º to 0.001º and with water depths ~30 m - 50 m. Accommodation was created by flexural loading of the depocenter during coeval orogenesis, which also provided the detrital sediment fill for the basin. Rapid subsidence in a proximal foredeep in the south of the basin created a thick sediment fill that thinned onto a distal forebulge to the north. Subsidence controll of 3rd order relative sea level changes, was recorded by deposition of storm dominated shelf mudstones, which were erosively topped by fluvio-terrestrial to paralic sandstones. The shallow dip of the basin promoted rapid changes in relative sea level resulting in a two-step sequence stack characteristic of forced regression. Additional 4th order sequences, possibly recording relative sea level change driven by regional rifting and localised tectonics, are also recorded in the RSB succession. However, the current data set lacks the resolution to firmly attribute a likely cause to the 4th order cycles. The RSB experienced synsedimentary regional volcanism which may have contributed enhanced primary productivity and the accumulation of organic rich shales. Continued regional tectonism caused a southward shift of the depocentre and a change in detrital sediment provenance. The provenance shift may also have contributed to enhanced primary productivity through delivery of nutrient rich sediments derived from uplifted mafic terrains. The combination of restricted connection to the global ocean, and strong local controls on sedimentation, mean that any global ocean geochemical signals have likely been heavilly influenced, if not completely overprinted by local signatures. As such, the RSB does not reflect Mesoproterozoic global ocean conditions, and cannot be used as a model for the global ocean during this interval. However, this particular set of geographical and geochemical circumstances may have made the RSB a haven for early eukaryotic life by trapping and concentrating nutrients into a relatively clement environment.

2.7 References

Abbott, S.T., Sweet, I.P., 2000. Tectonic control on third-order sequences in a siliciclastic ramp-style basin: An example from the Roper Superbasin (Mesoproterozoic), northern Australia. Aust. J. Earth Sci. 47, 637–657. https://doi.org/10.1046/j.1440-0952.2000.00795.x

Ahmad, M., Munson, T.J., Northern Territory Geological Survey, 2013. Geology and mineral resources of the Northern Territory.

Besly, B.M., Turner, P., 1983. Origin of red beds in a moist tropical climate (Etruria Formation, Upper Carboniferous, UK). Geol. Soc. Lond. Spec. Publ. 11, 131–147. https://doi.org/10.1144/GSL.SP.1983.011.01.14

Birgenheier, L.P., Horton, B., McCauley, A.D., Johnson, C.L., Kennedy, A., 2017. A depositional model for offshore deposits of the lower Blue Gate Member, Mancos Shale, Uinta Basin, Utah, USA. Sedimentology 64, 1402–1438. https://doi.org/10.1111/sed.12359

Bodorkos, S., Crowley, J.L., Claoué-Long, J.C., Anderson, J.R., Jr, C.W.M., 2021. Precise U–Pb baddeleyite dating of the Derim Derim Dolerite, McArthur Basin, Northern Territory: old and new SHRIMP and ID-TIMS constraints. Aust. J. Earth Sci. 68, 36–50. https://doi.org/10.1080/08120099.2020.1749929

Buckley, R.A., Plint, A.G., Henderson, O.A., Krawetz, J.R., Vannelli, K.M., 2016. Ramp sedimentation across a middle Albian, Arctic embayment: Influence of subsidence, eustasy and sediment supply on stratal architecture and facies distribution, Lower Cretaceous, Western Canada Foreland Basin. Sedimentology 63, 699–742. https://doi.org/10.1111/sed.12235

Carson, C.J., 2013. The Victoria and Birrindudu Basins, Victoria River region, Northern Territory, Australia: a SHRIMP U–Pb detrital zircon and Sm–Nd study. Aust. J. Earth Sci. 60, 175–196. https://doi.org/10.1080/08120099.2013.772920

Catuneanu, O., Galloway, W.E., Kendall, C.G.S. t. C., Miall, A.D., Posamentier, H.W., Strasser, A., Tucker, M.E., 2011. Sequence Stratigraphy: Methodology and Nomenclature. Newsl. Stratigr. 44, 173–245. https://doi.org/10.1127/0078-0421/2011/0011

Cox, G.M., Jarrett, A., Edwards, D., Crockford, P.W., Halverson, G.P., Collins, A.S., Poirier, A., Li, Z.-X., 2016. Basin redox and primary productivity within the Mesoproterozoic Roper Seaway. Chem. Geol. 440, 101–114. https://doi.org/10.1016/j.chemgeo.2016.06.025

Derry, L.A., 2015. Causes and consequences of mid-Proterozoic anoxia. Geophys. Res. Lett. 42, 8538–8546. https://doi.org/10.1002/2015GL065333

Donnelly, T.H., Crick, I.H., 1988. Depositional environment of the middle proterozoic velkerri formation in Northern Australia: Geochemical evidence. Precambrian Res. 42, 165–172. https://doi.org/10.1016/0301-9268(88)90015-0

Goldbery, R., 1979. Sedimentology of the Lower Jurassic flint clay bearing Mishhor Formation, Makhtesh Ramon, Israel. Sedimentology 26, 229–251. https://doi.org/10.1111/j.1365-3091.1979.tb00352.x

Gorter, J., Grey, K., 2012. Velkerri Formation Depositional Model - Beetaloo Sub-basin, Northern Territory, Australia : Biostratigraphy and Organic Enrichment 6.

Grotzinger, J.P., 1986. Upward shallowing platform cycles: A response to 2.2 billion years of low-amplitude, high-frequency (Milankovitch band) sea level oscillations. Paleoceanography 1, 403–416. https://doi.org/10.1029/PA001i004p00403

Hallam, A., Bradshaw, M.J., 1979. Bituminous shales and oolitic ironstones as indicators of transgressions and regressions. J. Geol. Soc. 136, 157–164. https://doi.org/10.1144/gsjgs.136.2.0157

Huber, N.K., Garrels, R.M., 1953. Relation of pH and oxidation potential to sedimentary iron mineral formation. Econ. Geol. 48, 337–357. https://doi.org/10.2113/gsecongeo.48.5.337

Jackson, M.J., Muir, M.D., Plumb, K.A., 1987. Geology of the southern McArthur Basin,Northern Territory 315.

Jackson, M.J., Powell, T.G., Summons, R.E., Sweet, P., 1986. Hydrocarbon shows and petroleum source rocks in sediments as old as 1.7 X 109 years 3.

Jackson, M.J., Raiswell, R., 1991. Sedimentology and carbon-sulphur geochemistry of the Velkerri Formation, a mid-Proterozoic potential oil source in northern Australia. Precambrian Res.,

Proterozoic Petroleum 54, 81–108. https://doi.org/10.1016/0301-9268(91)90070-Q
Jarrett, A., Cox, G.M., Edwards, D., Boreham, C., Crockford, P.W., Halverson, G.P., Collins, A.S., Poirier, A., Li, Z.-X., 2019. Organic and inorganic geochemistry of the Mesoproterozoic Roper Seaway 1.
Javaux, E.J., Knoll, A.H., 2017. Micropaleontology of the lower Mesoproterozoic Roper Group, Australia, and implications for early eukaryotic evolution. J. Paleontol. 91, 199–229. https://doi.org/10.1017/jpa.2016.124
Javaux, E.J., Knoll, A.H., Walter, M.R., 2001. Morphological and ecological complexity in early eukaryotic ecosystems. Nature 412, 66–69. https://doi.org/10.1038/35083562
Javaux, E.J., Knoll, A.H., Walter, M., 2003. Recognizing and Interpreting the Fossils of Early Eukaryotes 20.
Johnson, B.R., Tostevin, R., Gopon, P., Wells, J., Robinson, S.A., Tosca, N.J., 2020. Phosphorus burial in ferruginous SiO2-rich Mesoproterozoic sediments. Geology 48, 92–96. https://doi.org/10.1130/G46824.1
Johnston, D.T., Farquhar, J., Summons, R.E., Shen, Y., Kaufman, A.J., Masterson, A.L., Canfield, D.E., 2008. Sulfur isotope biogeochemistry of the Proterozoic McArthur Basin 14.
Keller, W.D., 1981. The sedimentology of flint clay. J. Sediment. Res. 51, 233–244. https://doi.org/10.1306/212F7C57-2B24-11D7-8648000102C1865D
Keller, W.D., 1968. Flint Clay and a Flint-Clay Facies. Clays Clay Miner. 16, 113–128. https://doi.org/10.1346/CCMN.1968.0160202
Kendall, B., Creaser, R.A., Gordon, G.W., Anbar, A.D., 2009. Re–Os and Mo isotope systematics of black shales from the Middle Proterozoic Velkerri and Wollogorang Formations, McArthur Basin, northern Australia. Geochim. Cosmochim. Acta 73, 2534–2558. https://doi.org/10.1016/j.gca.2009.02.013
Kirscher, U., Mitchell, R.N., Liu, Y., Nordsvan, A.R., Cox, G.M., Pisarevsky, S.A., Wang, C., Wu, L., Murphy, J.B., Li, Z.-X., 2020. Paleomagnetic constraints on the duration of the Australia-Laurentia connection in the core of the Nuna supercontinent. Geology 49, 174–179. https://doi.org/10.1130/G47823.1
Kositcin, N., Carson, C.J., 2019. GEOSCIENCE AUSTRALIA RECORD 2017/16 New SHRIMP U-Pb zircon ages from the Birrindudu and Victoria Basins, Northern Territory. Geosci. Aust. 89.
Laakso, T.A., Schrag, D.P., 2019. A small marine biosphere in the Proterozoic. Geobiology 17, 161–171. https://doi.org/10.1111/gbi.12323
Laakso, T.A., Schrag, D.P., 2018. Limitations on Limitation. Glob. Biogeochem. Cycles 32, 486–496. https://doi.org/10.1002/2017GB005832
Laakso, T.A., Schrag, D.P., 2014. Regulation of atmospheric oxygen during the Proterozoic. Earth Planet. Sci. Lett. 388, 81–91. https://doi.org/10.1016/j.epsl.2013.11.049
Lindsay, J.F., Brasier, M.D., 2000. A carbon isotope reference curve for ca. 1700–1575 Ma, McArthur and Mount Isa Basins, Northern Australia. Precambrian Res. 99, 271–308. https://doi.org/10.1016/S0301-9268(99)00062-5
Macnaughton, R.B., Dalrymple, R.W., Narbonne, G.M., 1997. Early Cambrian braid-delta deposits, MacKenzie Mountains, north-western Canada. Sedimentology 44, 587–609. https://doi.org/10.1046/j.1365-3091.1997.d01-41.x
Macquaker, J.H.S., Bentley, S.J., Bohacs, K.M., 2010. Wave-enhanced sediment-gravity flows and mud dispersal across continental shelves: Reappraising sediment transport processes operating in ancient mudstone successions. Geology 38, 947–950. https://doi.org/10.1130/G31093.1
Michalopoulos, P., AIIer, R.C., 1995. Rapid Clay Mineral Formation in Amazon Delta Sediments: Reverse Weathering and Oceanic Elemental Cycles 270, 5.
Mingxiang, M., Tucker, M.E., 2013. Milankovitch-driven cycles in the Precambrian of China: The Wumishan Formation. J. Palaeogeogr. 2, 369–389. https://doi.org/10.3724/SP.J.1261.2013.00037
Mitchell, R.N., Kirscher, U., Kunzmann, M., Liu, Y., Cox, G.M., 2020. Gulf of Nuna: Astrochronologic correlation of a Mesoproterozoic oceanic euxinic event. Geology 49, 25–29. https://doi.org/10.1130/G47587.1
Moore, D.M., 2000. Ordovician and Pennsylvanian Berthierine-Bearing Flint Clays. Clays Clay Miner. 48, 145–149. https://doi.org/10.1346/CCMN.2000.0480118

Mukherjee, I., Large, R.R., 2016. Pyrite trace element chemistry of the Velkerri Formation, Roper Group, McArthur Basin: Evidence for atmospheric oxygenation during the Boring Billion. Precambrian Res. 281, 13–26. https://doi.org/10.1016/j.precamres.2016.05.003

Munson, T.J., 2018. Summary of results. NTGS laser ablation ICP–MS U–Pb and Lu–Hf geochronology project: Roper Group (McArthur Basin), overlying ungrouped units (Beetaloo Sub-basin), Renner Group (Tomkinson Province), and Tijunna Group (Birrindudu Basin). Northern Territory Geological Survey, Record 2018-007. 82.

Munson, T.J., 2016. Sedimentary characterisation of the Wilton package, greater MacArthur Basin, Northern Territory. Northern Territory Geological Survey.

Peters, S.E., Loss, D.P., 2012. Storm and fair-weather wave base: A relevant distinction? Geology 40, 511–514. https://doi.org/10.1130/G32791.1

Plint, A.G., Tyagi, A., Hay, M.J., Varban, B.L., Zhang, H., Roca, X., 2009. Clinoforms, Paleobathymetry, and Mud Dispersal Across the Western Canada Cretaceous Foreland Basin: Evidence from the Cenomanian Dunvegan Formation and Contiguous Strata. J. Sediment. Res. 79, 144–161. https://doi.org/10.2110/jsr.2009.020

Plint, G.A., 2014. Mud dispersal across a Cretaceous prodelta: Storm-generated, wave-enhanced sediment gravity flows inferred from mudstone microtexture and microfacies. Sedimentology 61, 609–647. https://doi.org/10.1111/sed.12068

Porter, S.M., 2020. Insights into eukaryogenesis from the fossil record. Interface Focus 10, 20190105. https://doi.org/10.1098/rsfs.2019.0105

Porter, S.M., Agić, H., Riedman, L.A., 2018. Anoxic ecosystems and early eukaryotes. Emerg. Top. Life Sci. 2, 299–309. https://doi.org/10.1042/ETLS20170162

Poulton, S.W., Canfield, D.E., 2011. Ferruginous Conditions: A Dominant Feature of the Ocean through Earth's History. Elements 7, 107–112. https://doi.org/10.2113/gselements.7.2.107

Pufahl, P.K., Grimm, K.A., 2003. Coated phosphate grains: Proxy for physical, chemical, and ecological changes in seawater. Geology 31, 801. https://doi.org/10.1130/G19658.1

Pufahl, P.K., Pirajno, F., Hiatt, E.E., 2013. Riverine mixing and fluvial iron formation: A new type of Precambrian biochemical sediment 4.

Reinhard, C.T., Planavsky, N.J., Gill, B.C., Ozaki, K., Robbins, L.J., Lyons, T.W., Fischer, W.W., Wang, C., Cole, D.B., Konhauser, K.O., 2017. Evolution of the global phosphorus cycle. Nature 541, 386–389. https://doi.org/10.1038/nature20772

Reinhard, C.T., Planavsky, N.J., Ward, B.A., Love, G.D., Le Hir, G., Ridgwell, A., 2020. The impact of marine nutrient abundance on early eukaryotic ecosystems. Geobiology 18, 139–151. https://doi.org/10.1111/gbi.12384

Schieber, J., 2016. Mud re-distribution in epicontinental basins – Exploring likely processes. Mar. Pet. Geol. 71, 119–133. https://doi.org/10.1016/j.marpetgeo.2015.12.014

Schieber, J., Yawar, Z., 2009. A New Twist on Mud Deposition—Mud Ripples in Experiment and Rock Record. Sediment. Rec. 7, 4–8. https://doi.org/10.2110/sedred.2009.2.4

Shen, Y., 2002. Middle Proterozoic ocean chemistry: Evidence from the McArthur Basin, northern Australia. Am. J. Sci. 302, 81–109. https://doi.org/10.2475/ajs.302.2.81

Sweet, I., 1977. The precambrian geology of the victoria river region, northern territory. Precambrian geol. Vic. River reg. North. Territ.

Sweet, I., Ir, p., Cm, m., 1974. The geology of the auvergne 1: 250000 sheet area, northern territory (excluding bonaparte gulf basin). Geol. Auvergne 1 250000 sheet area north. Territ. Bonaparte gulf basin.

Valeton, I., Stütze, B., Goldbery, R., 1983. Geochemical and mineralogical investigations of the Lower Jurassic flint-clay bearing Mishhor and Ardon Formations, Makhtesh Ramon, Israel. Sediment. Geol. 35, 105–152. https://doi.org/10.1016/0037-0738(83)90047-7

Varban, B.L., Guy Plint, A., 2007. Palaeoenvironments, palaeogeography, and physiography of a large, shallow, muddy ramp: Late Cenomanian-Turonian Kaskapau Formation, Western Canada foreland basin. Sedimentology 0, 071120035017003-??? https://doi.org/10.1111/j.1365-3091.2007.00902.x

Warren, J.K., George, S.C., Hamilton, P.J., Tingate, P., 1998. Proterozoic Source Rocks: Sedimentology

and Organic Characteristics of the Velkerri Formation, Northern Territory, Australia. AAPG Bull. 82 (1998). https://doi.org/10.1306/1D9BC435-172D-11D7-8645000102C1865D

Yang, B., Collins, A.S., Blades, M.L., Capogreco, N., Payne, J.L., Munson, T.J., Cox, G.M., Glorie, S., 2019. Middle–late Mesoproterozoic tectonic geography of the North Australia Craton: U–Pb and Hf isotopes of detrital zircon grains in the Beetaloo Sub-basin, Northern Territory, Australia. J. Geol. Soc. 176, 771–784. https://doi.org/10.1144/jgs2018-159

Zhang, S.-H., Ernst, R.E., Pei, J.-L., Zhao, Y., Zhou, M.-F., Hu, G.-H., 2018. A temporal and causal link between ca. 1380 Ma large igneous provinces and black shales: Implications for the Mesoproterozoic time scale and paleoenvironment. Geology 46, 963–966. https://doi.org/10.1130/G45210.1

3. Phosphorus burial in ferruginous SiO_2-rich Mesoproterozoic sediments

Abstract Persistently low atmospheric O_2 requires that net organic carbon burial was muted through much of Earth's middle age. In order to achieve global mass balance with respect to O_2, recent models have suggested that redox-dependent mechanisms, such as Fe(II)-phosphate precipitation, limited phosphate availability in dominantly anoxic and ferruginous oceans, in turn limiting net primary production (NPP), and therefore organic carbon burial. Nevertheless, observational constraints on phosphorus cycling in ferruginous Proterozoic systems are rare, leaving these models largely untested. Here, we present high-resolution petrographic and mineralogical data showing that the 1.3 Ga Sherwin Ironstone (Roper Group, Australia) was dominated by syndepositional precipitation of the Fe(II)-silicate minerals greenalite and berthierine, interlaminated with abundant authigenic calcium-fluorapatite (CFA). Set in a quantitative geochemical framework, these data reveal that elevated marine $SiO_2(aq)$ concentrations facilitated extensive Fe(II)-silicate production, leaving CFA, rather than Fe(II)-phosphate, as the principal inorganic P sink in shallow water Roper Group sediments. More broadly, the physical and chemical factors that triggered Fe(II)-silicate and CFA burial in the Roper Seaway may highlight semi-restricted basins as important loci of phosphorus removal from the mid-Proterozoic ocean.

3.1 Introduction

Low atmospheric O_2 is considered a defining characteristic of the Precambrian Earth, and recent models have highlighted the biogeochemical implications of a stable low-oxygen world. In order to stabilise low atmospheric O_2, some models hypothesise that the rate of net primary production (NPP) must have been lower (up to 10-100x) than present, reducing organic carbon burial (Derry, 2015; Laakso and Schrag, 2018). Phosphorus limitation has emerged as the most likely mechanism to have attenuated NPP (Laakso and Schrag, 2019, 2018) and organic carbon burial. Several hypotheses have focused on redox-dependent mechanisms that might have limited P availability in anoxic and ferruginous oceans (Derry, 2015; Laakso and Schrag, 2014). Recently, a compilation of the total P concentration ([P]) in marine shales with Al > 15 wt% > has revealed a four-fold increase that began in the early to mid-Neoproterozoic, continuing to the modern (Reinhard et al., 2017). This record is thought to reflect a major shift from redox-dependent P limitation to widespread P availability in the water column with the demise of Fe-rich waters (Reinhard et al., 2017).

However, direct observations that constrain P cycling in ferruginous Proterozoic systems are rare. For example, low [P] in many mid-Proterozoic shales has been interpreted to reflect P-limitation through Fe(II)-phosphate precipitation in ferruginous systems (Derry, 2015), P scavenging through green rust precipitation (Zegeye et al., 2012), and adsorption or coprecipitation with Fe(III)-oxides (Jones et al., 2015). Although these mechanisms receive support from environmental analogues and geochemical models, they have not been tested against detailed mineralogical and sedimentological data from Proterozoic rocks. In addition, the stratigraphic distribution of syndepositional and early diagenetic chert in Proterozoic rocks reflects a marine system

characterized by elevated $SiO_2(aq)$ concentrations (Maliva et al., 2005), yet silica does not feature in current models or analogues for the mid-Proterozoic P cycle.

Here, to investigate the role of ferruginous and SiO_2-rich conditions on phosphate cycling in shallow marine environments, we conducted a high resolution sedimentological, mineralogical, and geochemical study of the 1.3 Ga Sherwin Ironstone of the Roper Superbasin (RSB), Northern Territory, Australia. The Sherwin Ironstone records an episode of Fe-rich chemical sedimentation in the Mesoproterozoic, offering a valuable window into contemporaneous Fe and P cycling.

3.2 Geological background and methods

The RSB hosts an exceptionally well-preserved record of sedimentation across multiple epicratonic basins of northern Australia (Munson, 2016). Sediment fill is packaged into six transgressive sequences of basinal shales and proximal sands, bound by inter cycle erosional surfaces, and ironstones (Abbott and Sweet, 2000). Local flexural tectonics controlled both relative sea level and sedimentation whereby flexural loading of the basin caused subsidence in the depocenter (Abbott and Sweet, 2000; Munson, 2016).

Iron-rich chemical sediments are common across the RSB as ironstones and/or sandstones with Fe-rich cement, which were deposited during the initial stages of regional transgression (Abbott and Sweet, 2000, Chapter 2: Fig 3E & L this thesis). The most significant of these, the 1.3 Ga

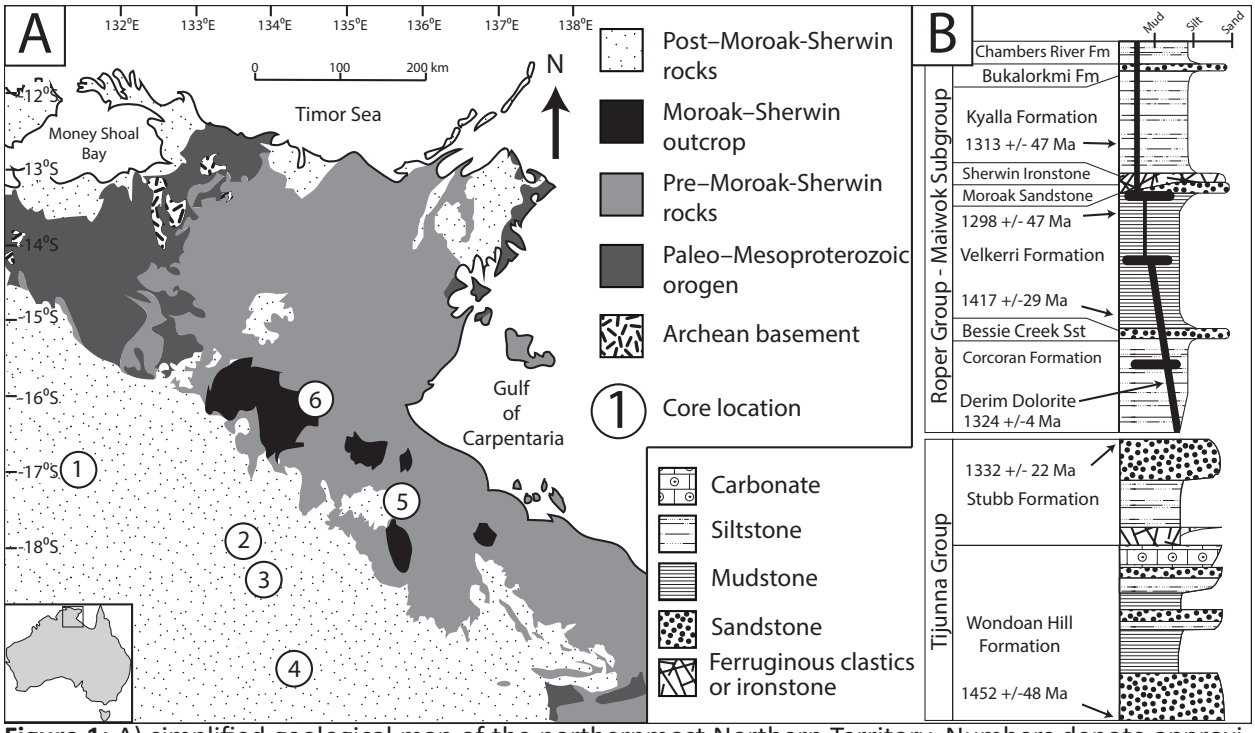

Figure 1: A) simplified geological map of the northernmost Northern Territory. Numbers denote approximate core locations. 1 = 99VRNTGSDD2 (99VR), 2 = McMannus-1a (MM1a), 3 = Shenandoah-1a (SD1a), 4 = 12BC, 5= Scarborough 1 (Sc1), 6 = Urapunga 4 (UP4) and Sherwin Ironstone Quarry. B) generalized stratigraphy of the upper Roper and Tijunna Groups, Sst—sandstone (from Munson, 2016; Yang et al., 2018)

Sherwin Ironstone, is dominated by iron-cemented sandstones and subordinate beds of Fe-silicate coated grains and laminated Fe-silicate chemical sediment, reflecting shallow marine upper shore face sedimentation (Cochrane and Edwards, 1960; Munson, 2016).

To examine ferruginous chemical sedimentation in the RSB, we logged and sampled six drill cores through the unit and examined 120 thin sections by optical microscopy and scanning electron microscopy-energy dispersive X-ray spectroscopy (SEM-EDS) using a FEI Quanta 650 FEG SEM. Sub-samples of petrographic facies were micro-drilled and analysed for bulk and clay-specific mineralogy at the University of Oxford (Oxford, UK) using a Panalytical Empyrean Series 2 X-ray diffractometer (XRD) equipped with a Co Kα source at 40 kv and 40 ma (See appendix at the end of this chapter for details).

3.3 Results

3.3.1 Ferruginous Sediment Lithofacies

Iron-rich sediments in the upper Roper Group and the correlative Tijunna Group form a ferruginous facies association (FA) that is interbedded with different lithologies and accurs in multiple formations. The ferruginous FA is summarised here, further details, such as sedimentary structures, can be found in Chapter 2; Table 1, Fig 2, and Fig 3E & L of this thesis.

FA2 Ferruginous Marine

Facies v) Coated grain sandstones – medium to coarse cross bedded sandstones with moderately sorted rounded quartz sand grains in an authigenic cement of ferrous silicate clays. Coated grains superficially resemble ooids, pisoids, oncoids, and 'roll-up' structures and range from 0.5 mm to ~ 5 cm in diameter. Ooidal and pisoidal forms consist of a tangential cortex of ferrous silicate around a nucleus of detrital quartz, rare detrital pyrite, or reworked ferrous silicate clay either as a massive pellet or a broken reworked ooidal grain. Roll-up type coated grains consist of medium to coarse well-rounded quartz, feldspar and heavy detrital grains e.g., zircon, bound in sheets of organic matter and authigenic ferrous silicate cement. These sheets are arranged in loose to complex spirals with internal disconformities, some examples show multiple phases of folding. Roll-up type coated grains resemble carbonate roll-up structures in cross section, but form cm scale spheroids rather than cylindrical sheets and host only minor diagenetic carbonate. The observed sedimentary structures and mineralogy suggest deposition in a shallow marine environment with varying levels of energy and periods of low detrital clastic input such as an intertidal shore face.

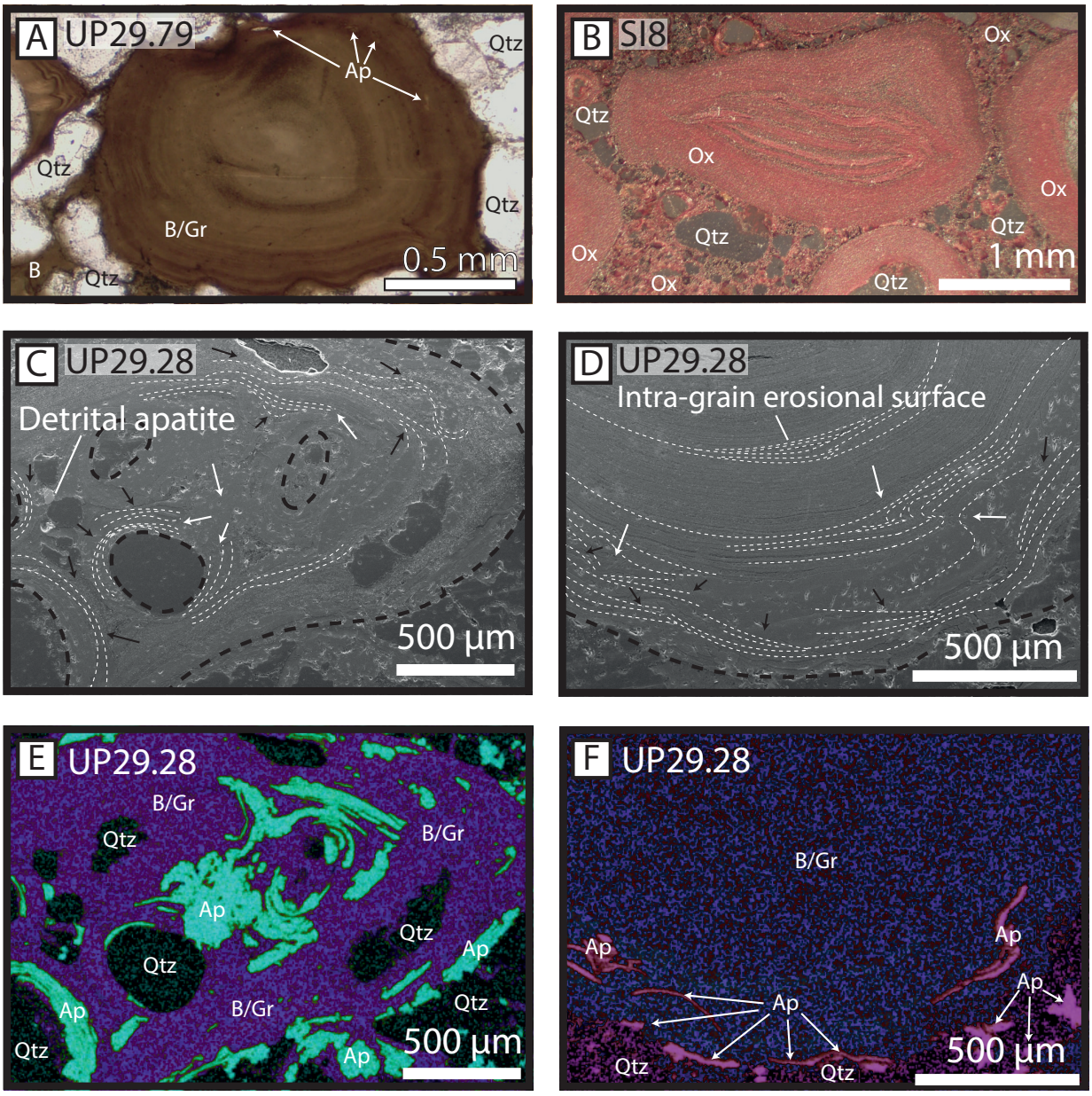

Figure 2: Coated grains from the Sherwin Ironstone (Northern Territory, Australia); sample names in the top left. (A) Pristine greenalite-berthierine coated grains in plane polarised light. (B) Ooid from a surface quarry in reflected light. The ooid has undergone complete oxidation to haematite and goethite. Quartz sand matrix now contains a haematite and silica cement. (C, D) show Scanning electron microscopy-back-scatter electron maps with key features highlighted: Black dashes = grain boundary and nucleus; white dashes = primary internal lamina; black arrows = onlap and infill of lamina over apatite grains; white arrows = displacement of lamina by adhesion and continued growth of apatite grains. Note the difference between the eroded sub-hedral apatite grain, and the fine-grained authigenic CFA. (E, F) show Energy dispersive X-ray spectroscopy element maps for phosphorus (green in E, Pink in F), Fe (light blue in E, dark blue in F) and Si Dark green in E, grey in F). Note the negative correlation between P and Fe. Abbreviations: B/Gr = Greenalite and Berthierine; Ap = Calcium fluorapatite; Qtz = quartz; Ox -iron oxide. A and C-F taken from core UP4, B from surface quarry. See Fig. 1 for geographic locations.

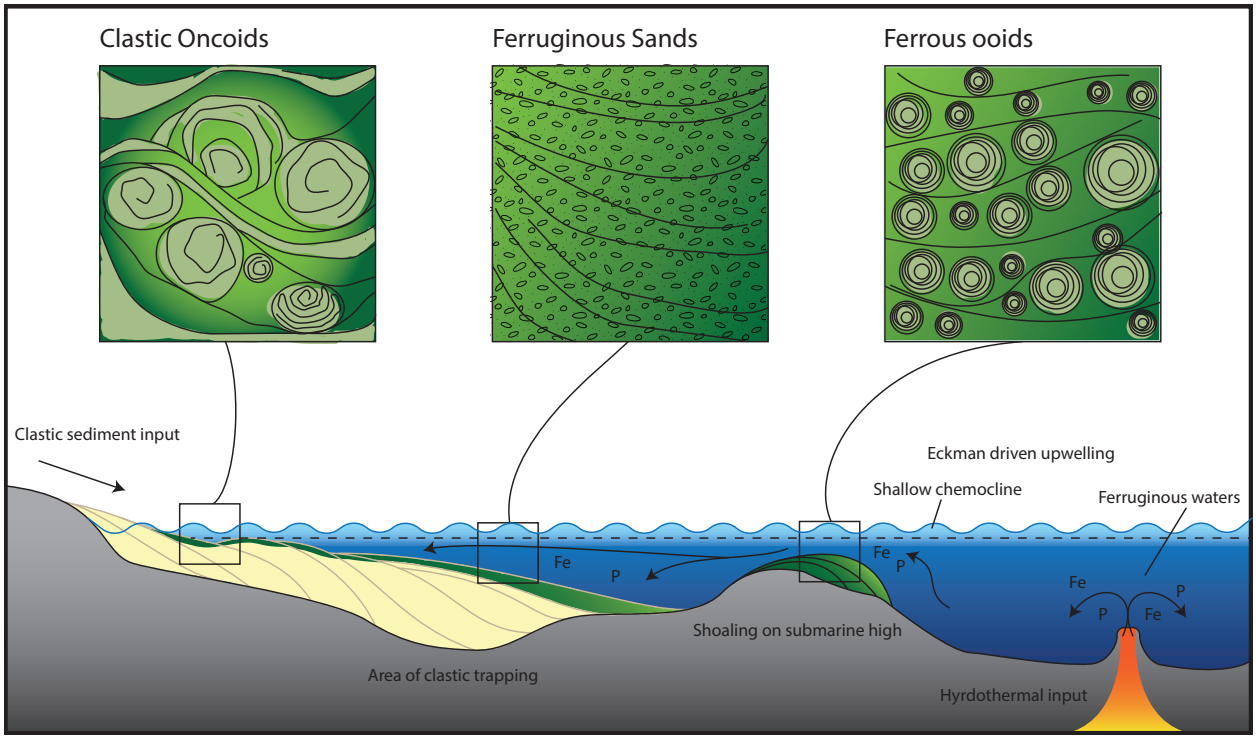

Figure 3: Schematic model proposed for ferruginous sediment formation in the RSB during the early stages of transgression when upwelling Fe- and P-rich oceanic waters encroach into the basin and interact with riverine waters. A) in the western Proximal Region, shallow high energy waters with low detrital clastic deposition rates promote the formation of oncoid-like coated grains. B) in the southern Proximal and Basinal Regions, the detrital clastic sedimentation rate is too high, and organic matter content too low, to allow coated grain formation, but clastic sedimentation rates are low enough to allow the accumulation of sandstone cemented by ferrous silicate clays. C) Ooid-like coated grains form at in the Distal Region of the basin where waters are relatively shallow, but detrital clastic dilution rate is low and irregular so that ferrous silicate clays have time to accumulate in pore space and on the seafloor.

Facies vi) Green cemented sandstone – Nearly identical to facies v but without the coated grains. Facies vi hosts the same sedimentary structures as facies v indicating a similar depositional setting. However, the presence of convolute bedding and laminae in facies vi indicates a higher detrital input level.

Facies vii) Green mudstone – features varying ratios of quartz silt to ferrous silicate clay in undulose, wrinkly, inclined and horizontally planar laminated beds. Sedimentary structures present include ripple cross lamination, convoluted lamination and combined flow laminations suggesting deposition in low energy environments punctuated by occasional higher energy conditions such as lower shore face and storm influenced inner shelf. However, the geographic and stratigraphic position of some facies vii examples indicates a paralic setting such as a coastal mud flat e.g those in the cores 12BC and 99VR (Chapter 2; Fig 3E & L, this thesis).

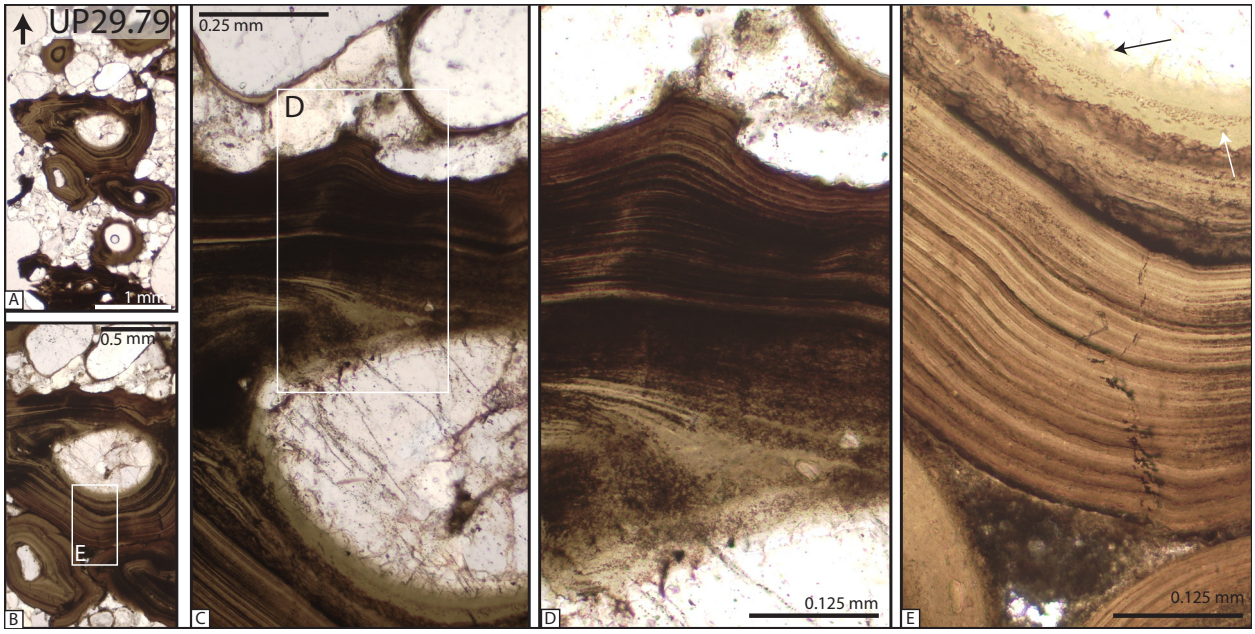

Figure 4: Detail of a greenalite-berthierine ooid-like coated grain in PPL. Matrix is quartz sand with minor feldspar, detrital pyrite and other heavy detritals. Soft spastolithic deformation can be observed clearly throughout e.g., left side of main ooid in A and the lamina in the upper part of D. Greenalite and berthierine can be distinguished in E as light greenalite lamina and darker berthierine lamina. Grains incorporated into laminae are quartz silt and CFA. Black lamina are rich in organic matter which also forms the cross-cutting trail in E. Silica for the Fe-silicate may have also come from quartz nucleus grains as observed in E. Greenalite appears to 'seep' into the outer surface of the quartz grain (black arrow). The original quartz grain surface can be seen as a lamina of kaolinite and haematite (white arrow).

3.3.2 Sequence stratigraphy

FA2 facies are found in the transgressive systems tract during deposition of the studied interval (Chapter 2, Fig 3E & L). Facies v and facies vi are found interbedded with non-ferruginous cross-bedded sandstones and mudstones (facies i of FA1-Paralic to Fluvio-terrestrial). While facies vii is also observed interbedded with facies i, it is most commonly found interbedded with facies ix and facies x of FA3-Marine (Chapter 2, Fig 3E & L).This range of associations for FA2 facies suggests that facies v) and facies vi) were deposited as a result of the interaction of fluvial and marine waters, possibly related to coastal upwelling during transgression, and that the geographic and stratigraphic distribution of these facies reflects the migration of the fluvial-marine front coastwards during transgression. Similarly, the distribution of facies vii) which is heterogeneous in time and space throughout the studied interval, may represent the incursion of ferruginous oceanic waters into the basin during the later stages of transgression. Facies vii) interpreted as coastal mud flat deposits may be explained by a) fluvio-terrestrially derived Fe^{3+} being reduced within the upper sediment column, b) direct deposition of fluvio-terrestrial Fe^{2+} from riverine waters, c) direct deposition of marine Fe^{2+}, or d) reduction of Fe^{3+} by incursions of upwelling ferruginous marine waters, or some variation and interplay between these end members. However, further work is required to refine a depositional model for this environment beyond the speculation here.

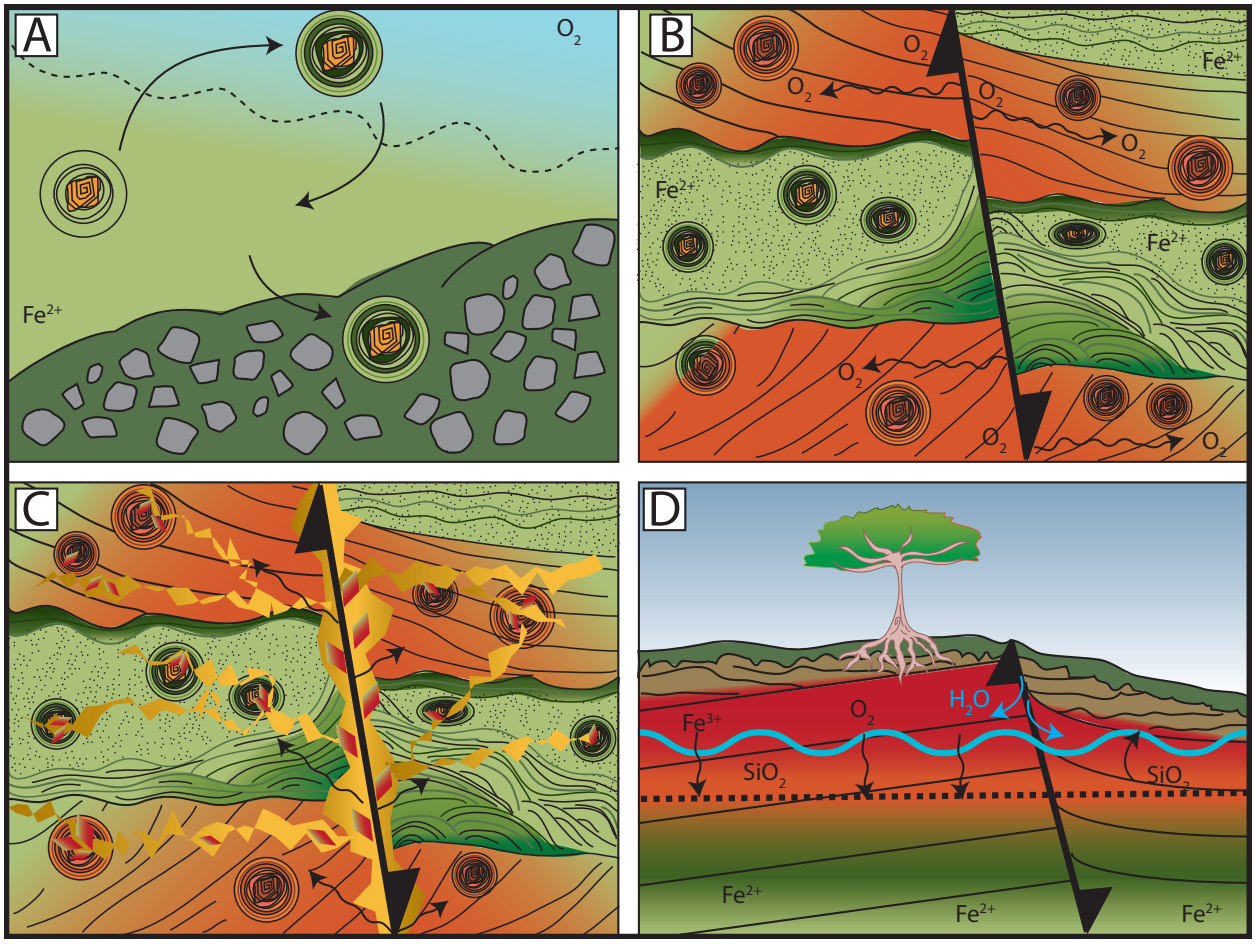

Figure 5: Schematic models to explain the alteration observed in RSB ferruginous sedimentary rocks. A) Formation of coated grains through redox aggradation and phsyical reworking. B) oxidising fluids pass through the rocks using faults, fractures and porous beds as pathways forming the first phase of diagenetic oxides. C) Reducing fluids follow similar pathways and over print earlier phases with siderite and pyrite. D) Another wave of oxidising fluids and supergene weathering produces the final surface expression of the ferruginous sedimentary rocks, e.g., the haematite and opal facies of the Sherwin Ironstone in surface exposures (Cochrane & Edwards, 1960).

3.3.4 Oxidation and Weathering

Authigenic ferrous silicates in all lithofacies have undergone several stages of oxidation. However, petrographic inspection of oxidised material from core samples reveals that all but the most heavily weathered sediments are still ~90% ferrous-silicates interspersed with individual micron scale goethite and Fe-oxyhydroxide crystals, which cut primary authigenic minerals and fabrics. In core samples of the Sherwin Ironstone for example, oxidation appears to be related to the presence of porous clastic layers which may have served as a conduit for oxidising fluids. Oxidation fronts can also be clearly seen emanating from fractures and faults whose relationship to the matrix is cross cutting with sharp brittle fractures. In some cases, individual coated grains are bisected by oxidation fronts. This indicates that faulting and fracture occurred after deposition and lithification. Oxidation fronts are also clearly abruptly halted by clay, microbial and organic rich laminae. Often the reaction front is discordant with the primary depositional features and will

circle around impermeable areas following fractures or porous laminae.

This initial stage of alteration appears to have then been overprinted by localised re-reduction that followed the same fluid conduits as the initial oxidation. In this stage, both primary Fe-silicates, and secondary oxides are overprinted by Fe-Mg-Mn-carbonates, pyrite, and silica, all of which occur as laminae disruptive grains and nodules, and as diffuse masses that infiltrate previously porous areas of matrix. Petrographic relationships show that this episode of re-reduction clearly post-dates primary deposition and authigensis, and the initial phase of oxidation.

The final stage of alteration is probably related to supergene weathering at or near the surface during the Quaternary (Kastellorizos, 2014; Morris, 2012). This has resulted in the destruction of most primary features via the mobilisation of Fe-oxides and silica from coated grains, and their redistribution throughout the matrix. Rare microscopic remnants of the original Fe-silicate mineralogy can be found as relicts within protected grain nuclei. In the most advanced cases of weathering, heavy silicification has replaced most of the Fe-oxides with quartz and opal. Kastellorizos (2014) and Morris (2011) hypothesise that it was the recent supergene weathering that concentrated iron to economic levels in the ore grade beds.

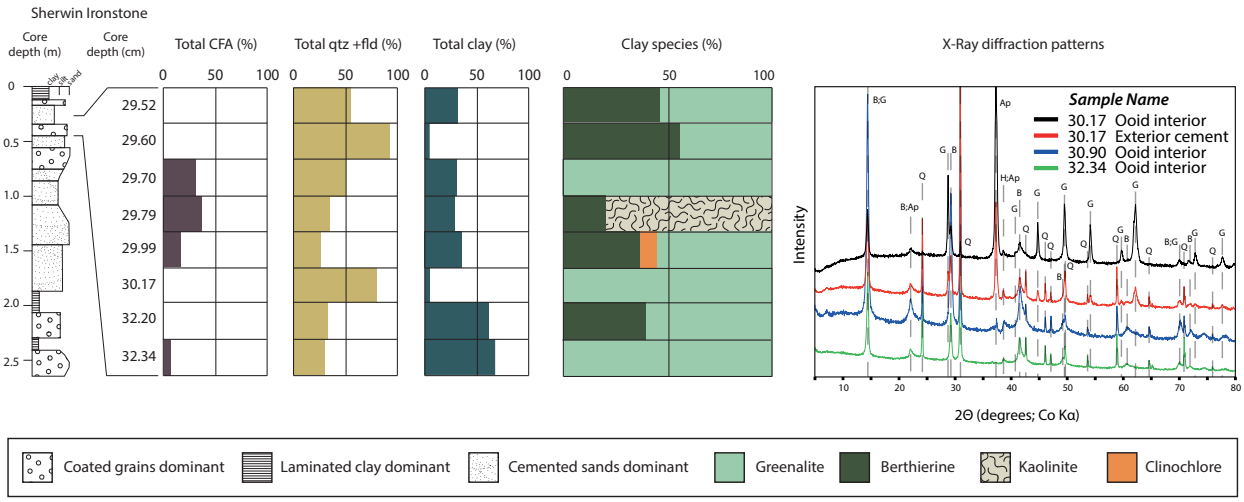

Figure 6: A simplified graphic log of the Sherwin Ironstone from Core UP4, Northern Territory, Australia (left, Fig. 1); associated X-ray diffraction results from microdrilled authigenic cements and coated grains from the interval 29.52 cm – 32.34 cm (centre). Typical X-ray diffraction profiles of powders micro-drilled from ferruginous ooids of the Sherwin Ironstone (right), dominated by varying abundances of quartz (Q), berthierine (B), greenalite (G), and carbonate-fluorapatite (Ap). Trace amounts of hematite (H) are present in the samples. CFA—Calcium fluorapatite; Qtz—quartz Fld—feldspar.

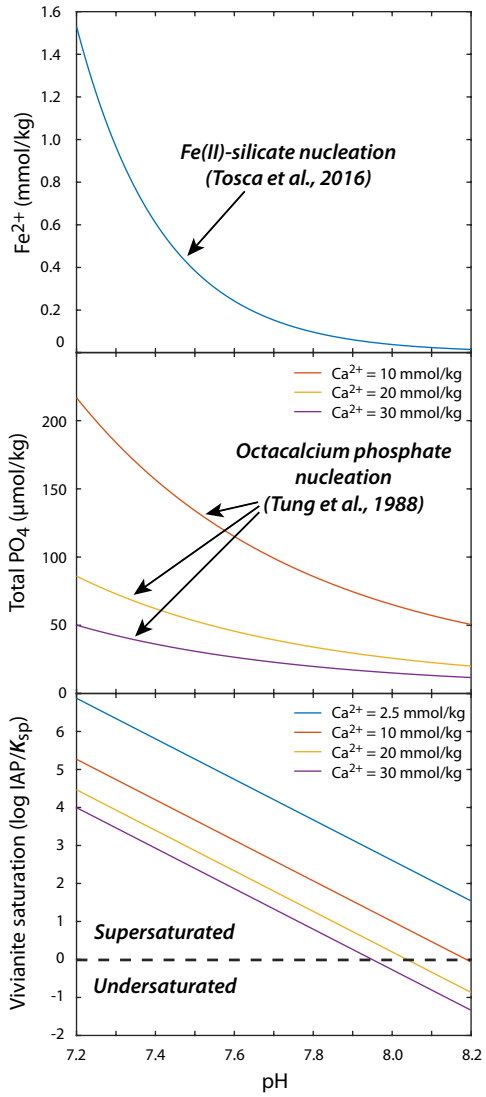

Figure 7: Chemical requirements for contemporaneous Fe(II)-silicate and Ca-phosphate nucleation at 25˚C, which, together result in Fe(II)-phosphate supersaturation. Apparent solubility product for Fe(II)-silicate precursor and subsequent greenalite nucleation from Tosca et al. (2016). Total PO4 concentrations correspond to solubility of octacalcium phosphate, demonstrated as an initial precursor phase to apatite precipitation; solubility product from Tung et al., (1988). Resulting supersaturation with respect to vivianite, a common Fe(II)-phosphate (Ksp from (Al-Borno and Tomson, 1994) IAP—ion activation product.

It is hard to reconcile these alteration features with deposition of primary authigenic oxides that have then been latterly reduced to ferrous silicates, or mixed ferric/ferrous phase deposition. Considering these observations, the simplest explanation is that the primary authigenic phases were ferrous silicates. All other extensive and pervasive oxidation and alteration took place in later diagenesis and during surface exposure following percolation of alternately oxidising and reducing fluids. These observations are consistent with those made by Cochrane & Edwards (1960), Morris (2011), Ferenczi, (2001) and Kastellorizos (2014).

3.3.5 Primary deposition of Fe^{2+} silicates and phosphate in the Sherwin Ironstone

Petrographic and mineralogical data delineate three facies of chemical sediments; facies v Coated grains sandstones, facies vi Green cemented sandstones, and facies vii Green mudstone. In all facies, authigenic berthierine and greenalite represent the principal building blocks of the Sherwin Ironstone (Figure 2 and 6). The Sherwin Ironstone was deposited in a range of high energy shallow water settings, from shoaling bars to upper shore face, as indicated by swaley, combined flow, and unidirectional cross stratification, and erosive surfaces (Cochrane and Edwards, 1960, Munson, 2016). Recent experimental work has shown that greenalite precipitation occurs under fully anoxic and ferruginous conditions (Tosca et al., 2016). Unlike berthierine (an Fe(II)- and Al-bearing silicate), the formation of which requires pore water Fe^{2+} and pre-existing aluminosilicate minerals (Bhattacharyya, 1983), the near absence of Al in the greenalite structure facilitates nucleation from the water column (Tosca et al., 2016,). Thus, ferruginous waters commonly expanded

onto the shallow shelf in the RSB.

Powder XRD and SEM-EDS (Figure 2 and 3) indicate that calcium-fluorapatite (CFA) is an important constituent of the Sherwin Ironstone. CFA occurs as aggregates of anhedral grains within authigenic Fe-silicate cements, as well as within Fe-silicate coated grain laminae (Figure 2 and 3). In both cases textural relationships indicate that CFA precipitated along with Fe-silicates (Figure 3). CFA within Fe-silicate coated grains, indents underlying Fe-silicate lamina, indicating the coated grain was plastic when the CFA adhered to its outer surface (Figure 3). Further deformation probably occurred during reworking of the coated grains, as indicated by broken coated grains and intra-grain erosional surfaces (Fig 10, *cf* Pufahl and Grimm, 2003). Abundant examples of coated grains with spastolithic textures indicate the grains were still pliable during burial. These petrographic relationships indicate that both greenalite, berthierine, and CFA are primary precipitates. Detrital apatite in the Sherwin Ironstone can be distinguished based on its tabular habit, enrichment in Ca and rare earth elements, and lack of detectable F. Our petrographic observations also indicate that most Fe-oxides present within the Sherwin Ironstone, are the products of late-stage alteration (Fig 3B. Cochrane & Edwards., 1960,).

3.4 Discussion

Together, petrographic and mineralogical constraints indicate that CFA was precipitated with Fe(II)-silicates of the Sherwin ironstone at or just below the sea floor (Figure 3A, C & D and Figure 6). Although these data do not rule out the possibility that some of the PO_4 in CFA minerals was derived through dissolution of fluvial and aeolian delivered Fe-oxides, they support the inference that the high aqueous PO_4 concentrations necessary for CFA nucleation extended above the sediment-water interface. In addition, the decoupling between detrital mineral phases and CFA suggests that aqueous PO_4 accumulation was not strongly linked to input derived from riverine sources (Figure 2, see also Chapter 2). Similarly, while organic matter diagenesis would be expected to have released PO_4 and fuel CFA precipitation (i.e., an expression of a process known as "sink-switching", Ruttenberg and Berner, 1993), the Sherwin Ironstone is conspicuously organic-poor, with total organic carbon <0.1 wt. % (data not shown). As the CFA was incorporated within the coated grains at or near the sea floor, it is unlikely that it is derived from P released by organic matter diagenesis. It is also possible that the coated grain bound CFA represents fossilised organic matter that was trapped prior to burial. Relatively high PO_4 concentrations in the water column, could also be due to recycling of organic matter derived from primary production (Lenton and Daines, 2018; Poulton, 2017) or a limited supply of fixed nitrogen (Koehler et al., 2017; Sánch-

Baracaldo et al., 2014).

Regardless of how PO_4 accumulated in the water column during Sherwin Ironstone deposition, our data demonstrate that CFA was an important terminal P sink during Roper Group chemical sedimentation, precipitating contemporaneously with Fe(II)-silicates from a ferruginous water column. These data, combined with extensive sea floor deposition of authigenic ferruginous phases in the conformably underlying and overlying units, illustrates that ferruginous chemical sedimentation, and therefore ferruginous water conditions were a persistent long-term feature of RSB across multiple depositional settings during this time interval. Available constraints on apatite and greenalite formation pathways define the chemical solution space required to stabilise these two minerals in Roper Group sediments. Once a specific combination of pH, $[SiO_2]$, and $[Fe^{2+}]$ is crossed, then an Fe(II)-silicate gel precipitates, and eventually re-orders to form greenalite (Tosca et al., 2016). Assuming saturation with respect to amorphous silica (supported by shallow water chert deposition in proximally equivalent sediments), minimum $[Fe^{2+}]$ at greenalite nucleation may be determined across a range in pH from 7.2, below which Fe(II)-silicate precipitation is too slow to occur over reasonable diagenetic timescales (Tosca et al., 2016), to 8.2, a reasonable upper limit based on current constraints on Proterozoic pH (Halevy and Bachan, 2017).

Both experimental and observational evidence support an apatite formation pathway which first involves the nucleation of octacalcium phosphate, then subsequent recrystallisation to apatite (Cappellen and Berner, 1991; Gunnars et al., 2004; Jahnke et al., 1983). Thus, a conservative upper limit for total $[PO_4]$ may be determined across the same pH window if marine $[Ca^{2+}]$ is known. Although few constraints on Mesoproterozoic marine $[Ca^{2+}]$ are available, 2.5 mmol/kg serves as a reasonable minimum, below which Ca-sulphate would not precipitate upon evaporation (inconsistent with RSB and other Mesoproterozoic sediments; Grotzinger and Kasting, 1993). An upper limit of 30 mmol/kg $[Ca^{2+}]$ serves as a maximum based on Ca-isotope constraints of marine evaporites of the ~2.0 Ga Tulomozero Formation (northwestern Russia), and from evaporite geochemistry of the ~1.2 Ga Society Cliffs Formation (northern Baffin Island, Canada) which indicates $[Ca^{2+}]$, $[K^{+}]$, and $[Na^{+}]$ were close to modern values (Blättler et al., 2018; Kah et al., 2001).

Combining these constraints yields the saturation state of RSB water relative to vivianite, an Fe(II)-phosphate mineral known to precipitate in modern atypical marine and lacustrine sediments (more readily than the Mg-rich end members bobierrite and baricite; Dijkstra et al., 2016; Egger et al., 2015 Figure 4). These calculations show that, for all conditions except those associated with alkaline pH and very high marine $[Ca^{2+}]$, the contemporaneous precipitation of greenalite and Ca-phosphate would be expected to occur despite significant vivianite supersaturation.

This combination of petrographic and mineralogical data with geochemical constraints reveals a significant kinetic barrier associated with vivianite precipitation, a conclusion reinforced by pore water data from modern sediments. For example, a number of studies have reported significant supersaturation with respect to Fe(II)-phosphate in lacustrine, estuarine, and marine systems, despite the presence or absence of solid Fe(II)-phosphate phases (Postma, 1980; Rothe et al., 2016). This further indicates that when the threshold for nucleation has been reached in some diagenetic systems, Fe(II)-phosphate minerals may not grow rapidly enough to buffer PO_4 to equilibrium solubility levels. This kinetic limitation implies that Fe(II)-phosphate precipitation should not occur in sedimentary environments that are routinely associated with excessive supersaturation. In fact, a number of recent studies have shown that modern marine Fe(II)-phosphate precipitation is dominantly confined to sedimentary environments below the sulphate-methane transition zone (SMTZ; Dijkstra et al., 2016; Egger et al., 2015; März et al., 2018).

One significant difference between Proterozoic and modern sedimentary environments conducive to Fe(II)-phosphate nucleation and the Sherwin Ironstone is the absence of other Fe(II)-bearing phases that kinetically compete for Fe^{2+}. Indeed, at the Fe^{2+} concentrations and alkalinities associated with modern sediments below the SMTZ, very low $SiO_2(aq)$ concentration typically precludes Fe(II)-silicate formation. However, in Proterozoic marine systems where $SiO_2(aq)$ was much higher than the modern ocean (Maliva et al., 2005), experimental constraints indicate that high $[Fe^{2+}]$ and alkalinities (and thus Fe(II)-phosphate supersaturation) may not have been reached without rapidly nucleating Fe(II)-silicates such as greenalite (Tosca et a., 2016). As our data indicate, the presence of elevated $SiO_2(aq)$ in mid-Proterozoic marine systems appears to have efficiently sequestered Fe^{2+} in Fe(II)-silicate phases, while leaving CFA as the dominant inorganic sink for phosphorus.

Our conclusions receive additional support from a number of examples where Fe(II)-silicate minerals have precipitated in close association with Ca-phosphate. For instance, the Paleoproterozoic Sokoman iron formation of the Labrador Trough, eastern Canada (Pufahl et al., 2014) and Ordovician oolitic ironstones of Bell Island, Newfoundland, Canada (Todd et al., 2019). Oolitic ironstones composed of Fe-silicate and authigenic phosphates also occur in the early Jurassic Cleveland Ironstone, Northern England, UK, in the Passwang Formation, Switzerland (Burkhalter, 1995; Macquaker and Taylor, 1996), and in the Cretaceous of south-eastern Australia (Boyd et al., 2004).

3.5 Conclusions

Together, a variety of data indicate that elevated [SiO_2] and Fe(II)-silicate precipitation may have prevented Fe(II)-phosphate burial in Proterozoic seas, in contrast with models that envisage a link between PO_4 limitation and ferruginous chemistry (Derry, 2015; Planavsky et al., 2011; Reinhard et al., 2017). In modern oceans, particulate organic matter is a shuttle for the sedimentary sequestration of marine P (Delaney, 1998). Given the relative scarcity of organic matter in the Sherwin Ironstone compared to stratigraphically adjacent units, it is perhaps unsurprising then that mineralisation should appear to be the primary sedimentary P sink. Nevertheless, the requirement for global oxygen mass balance implies that other mechanisms may have regulated marine PO_4 availability through the Proterozoic (Cox et al., 2019; Diaz et al., 2008). Our analyses also indicate that shallow epeiric seas such as the RSB served as key depositional loci for both Fe(II)-silicates and Ca-phosphates. Unique physical and chemical factors, such as partial regional restriction, coastal upwelling and the interaction of riverine and marine waters, coupled with enhanced alkalinity from the metabolization of organic matter (possibly why so little is found in the Sherwin Ironstone) and input from surrounding volcanic catchment (Cox et al., 2016), may have established these environments as permanent chemical sedimentary traps of PO_4. This unusual set of geological conditions, apparently common in the mid-Proterozoic, would have impacted the global marine PO_4 reservoir until the Tonian/Cryogenian breakup of Rodinia (Horton, 2015). A tectono-sedimentary influence on P burial also reconciles shale-hosted P and Fe-speciation records which, when viewed together, suggest that Proterozoic P burial increased even though anoxic and/or ferruginous waters persisted well into the Palaeozoic (Sperling et al., 2015). Nevertheless, further examination of Fe- and P-mineralogy preserved in ancient sediments will continue to re-shape our understanding of Proterozoic biogeochemical cycling.

3.6 Sherwin chapter appendix

3.6.1 Age Model

The Sherwin Ironstone has been assigned a maximum depositional age of ~1320 Ma on the following basis:

• The Kyalla Mudstone which conformably overlies the Sherwin Ironstone and Moroak Sandstone has a maximum depositional age of 1313 ± 47 Ma based on detrital zircons (Yang et al., 2019).

• The Moroak Sandstone, which is contemporaneous to, and in some locations, conformably underlies the Sherwin Ironstone, has a maximum deposition age between 1345 Ma and 1320 Ma based on detrital zircons (Yang et al., 2019).

• The Velkerri Formation, which conformably underlies the Moroak Sandstone, has a maximum depositional age of between 1349 Ma and 1320 Ma based on detrital zircons (Yang et al. 2019) which overlaps with the whole rock Re-Os age of 1361 ± 21 Ma obtained by Kendall et al., (2009) from the Upper Velkerri Formation.

• All units of the upper Roper Group are intruded by a suite of dolerite dykes and sills which have been assigned a baddeleyite age of 1324 ± 4 Ma using SIMS (Abbott and Sweet, 2000) and 1312.9 ± 0.7 Ma using U–Pb TIMS (Abbott and Sweet, 2000).

3.6.2 Core Details

Detailed reports for all cores can be found on the publicly accessible Northern Territories Geological Survey Gemis archive (https://geoscience.nt.gov.au/gemis/ntgsjspui/community-list). Documentation for each core can be found with the report ID below.

- 12BC001 – CR2012-0215
- Mcmanus 1a - PR1989-0086
- Shenandoah 1a - PR2010-0050
- Altree 2 - PR1989-0016
- 99VRNTGSDD1 - NTGS Record 2002-006
- Scarborough 1 - PR1989-0094

The UP4 report is available through the Geoscience Australia E-catalogue

Urapunga 4 - https://ecat.ga.gov.au/geonetwork/srv/eng/catalog.search#/metadata/14111

3.6.3 Extended Methods

Sample Collection

Surface samples were collected from a commercial quarry at Mt McMinn (14°41'57.2"S 134°22'30.6"E, Fig 3, main text) with one sample collected every 1 m across the 8 m thickness of section. Core material was obtained from the Northern Territory Geological Survey core facility in Darwin, and the Geoscience Australia core facility in Canberra. Details of cores sampled, and their geographic locations can be found in Fig 3 of the main text. Samples were collected every ten meters for the full extent of each section with higher resolution scale logging and continuous sampling of important transitions. Cores were graphically logged in decimeter scale and detailed petrographic notes and photographs taken.

Sample Preparation

Samples were cut on a standard industrial rock saw fitted with a diamond blade and water coolant. Samples were ground flat with on a standard industrial grinder fitted with a copper and carborundrum grinding wheel. Samples were then hand lapped with 15 µm Aluminium oxide powder. Samples were attached to pre-lapped glass slides with Struers Epo Fix two part Epoxy resin, or Loctite 365 UV resin. Sections were lapped to a thickness of 30 µm using 15 µm Aluminium Oxide powder, on a Logitech LP50 precision lapping machine. Final polish for SEM work was achieved with 0.3 µm Aluminium Oxide powder, on a Struers Labopol polishing machine. All sample preparation was carried out at the University of Oxford, Department of Earth Sciences, UK.

XRD Peak Correction

All samples were corrected for sample height displacement error, which causes whole-pattern peak shifts, by normalising to the quartz 011 reflection at 3.343 angstroms. In addition to other distinctive diffraction peaks, differentiation of greenalite from berthierine is perhaps clearest in terms of the 002 reflection which, for berthierine occurs at 3.52–3.54 angstroms (Bailey, 1982 *in:* Brown, 1982), and for greenalite occurs at 3.60–3.62 angstroms (Bailey, 1982 *in:* Brown, 1982) . With Co radiation, the corresponding diffraction angles of these peaks are suitably separated from one another; all samples contain either one or both of berthierine and greenalite.

3.7 References

Abbott, S.T., Sweet, I.P., 2000. Tectonic control on third-order sequences in a siliciclastic ramp-style basin: An example from the Roper Superbasin (Mesoproterozoic), northern Australia. Aust. J. Earth Sci. 47, 637–657. https://doi.org/10.1046/j.1440-0952.2000.00795.x

Bhattacharyya, D.P., 1983. Origin of Berthierine in Ironstones. Clays Clay Miner. 31, 173–182. https://doi.org/10.1346/CCMN.1983.0310302

Blättler, C.L., Claire, M.W., Prave, A.R., Kirsimäe, K., Higgins, J.A., Medvedev, P.V., Romashkin, A.E., Rychanchik, D.V., Zerkle, A.L., Paiste, K., Kreitsmann, T., Millar, I.L., Hayles, J.A., Bao, H., Turchyn, A.V., Warke, M.R., Lepland, A., 2018. Two-billion-year-old evaporites capture Earth's great oxidation. Science 360, 320–323. https://doi.org/10.1126/science.aar2687

Boyd, G.A., Wallace, M.W., Holdgate, G.R., Gallagher, S.J., 2004. Marine clays and porosity evolution in the Nullawarre Greensand, Otway Basin, southeastern Australia 17.

Brown, G., 1982. Crystal Structures of Clay Minerals and their X-Ray Identification. The Mineralogical Society of Great Britain and Ireland.

Burkhalter, R.M., 1995. Ooidal ironstones and ferruginous microbialites: origin and relation to sequence stratigraphy (Aalenian and Bajocian, Swiss Jura mountains). Sedimentology 42, 57–74. https://doi.org/10.1111/j.1365-3091.1995.tb01271.x

Cappellen, P.V., Berner, R.A., 1991. Fluorapatite crystal growth from modified seawater solutions. Geochim. Cosmochim. Acta 55, 1219–1234. https://doi.org/10.1016/0016-7037(91)90302-L

Cochrane, G.W., Edwards, A.B., 1960. The Roper River oolitic ironstone formations (No. 1).

Cox, G.M., Jarrett, A., Edwards, D., Crockford, P.W., Halverson, G.P., Collins, A.S., Poirier, A., Li, Z.-X., 2016. Basin redox and primary productivity within the Mesoproterozoic Roper Seaway. Chem. Geol. 440, 101–114. https://doi.org/10.1016/j.chemgeo.2016.06.025

Cox, G.M., Sansjofre, P., Blades, M.L., Farkas, J., Collins, A.S., 2019. Dynamic interaction between basin redox and the biogeochemical nitrogen cycle in an unconventional Proterozoic petroleum system. Sci. Rep. 9, 5200. https://doi.org/10.1038/s41598-019-40783-4

Delaney, M.L., 1998. Phosphorus accumulation in marine sediments and the oceanic phosphorus cycle. Glob. Biogeochem. Cycles 12, 563–572. https://doi.org/10.1029/98GB02263

Derry, L.A., 2015. Causes and consequences of mid-Proterozoic anoxia. Geophys. Res. Lett. 42, 8538–8546. https://doi.org/10.1002/2015GL065333

Diaz, J., Ingall, E., Benitez-Nelson, C., Paterson, D., de Jonge, M.D., McNulty, I., Brandes, J.A., 2008. Marine Polyphosphate: A Key Player in Geologic Phosphorus Sequestration. Science 320, 652–655. https://doi.org/10.1126/science.1151751

Dijkstra, N., Slomp, C.P., Behrends, T., 2016. Vivianite is a key sink for phosphorus in sediments of the Landsort Deep, an intermittently anoxic deep basin in the Baltic Sea. Chem. Geol. 438, 58–72. https://doi.org/10.1016/j.chemgeo.2016.05.025

Egger, M., Jilbert, T., Behrends, T., Rivard, C., Slomp, C.P., 2015. Vivianite is a major sink for phosphorus in methanogenic coastal surface sediments. Geochim. Cosmochim. Acta 169, 217–235. https://doi.org/10.1016/j.gca.2015.09.012

Ferenczi, P.A., 2001. Iron ore, manganese and bauxite deposits of the Northern Territory. Dept. of Business, Industry and Resource Development, Darwin.

Grotzinger, J.P., Kasting, J.F., 1993. New Constraints on Precambrian Ocean Composition. J. Geol. 101, 235–243. https://doi.org/10.1086/648218

Gunnars, A., Blomqvist, S., Martinsson, C., 2004. Inorganic formation of apatite in brackish seawater from the Baltic Sea: an experimental approach. Mar. Chem. 91, 15–26. https://doi.org/10.1016/j.marchem.2004.01.008

Halevy, I., Bachan, A., 2017. The geologic history of seawater pH 4.

Horton, F., 2015. Did phosphorus derived from the weathering of large igneous provinces fertilize the Neoproterozoic ocean?: NEOPROTEROZOIC FLOOD BASALT WEATHERING. Geochem. Geophys. Geosystems 16, 1723–1738. https://doi.org/10.1002/2015GC005792

Jahnke, R.A., Emerson, S.R., Roe, K.K., Burnett, W.C., 1983. The present day formation of apatite in Mexican continental margin sediments. Geochim. Cosmochim. Acta 47, 259–266. https://doi.org/10.1016/0016-7037(83)90138-2

Jones, C., Nomosatryo, S., Crowe, S.A., Bjerrum, C.J., Canfield, D.E., 2015. Iron oxides, divalent cations, silica, and the early earth phosphorus crisis. Geology 43, 135–138. https://doi.org/10.1130/G36044.1

Kah, L.C., Lyons, T.W., Chesley, J.T., 2001. Geochemistry of a 1.2 Ga carbonate-evaporite succession, northern Baffin and Bylot Islands: implications for Mesoproterozoic marine evolution. Precambrian Res. 111, 203–234. https://doi.org/10.1016/S0301-9268(01)00161-9

Kastellorizos, P., 2014. Exploration Licence: 26114 SIXTH ANNUAL REPORT OVER THE ROPER IRON ORE AND URANIUM PROJECT.

Kendall, B., Creaser, R.A., Gordon, G.W., Anbar, A.D., 2009. Re–Os and Mo isotope systematics of black shales from the Middle Proterozoic Velkerri and Wollogorang Formations, McArthur Basin, northern Australia. Geochim. Cosmochim. Acta 73, 2534–2558. https://doi.org/10.1016/j.gca.2009.02.013

Koehler, M.C., Stüeken, E.E., Kipp, M.A., Buick, R., Knoll, A.H., 2017. Spatial and temporal trends in Precambrian nitrogen cycling: A Mesoproterozoic offshore nitrate minimum. Geochim. Cosmochim. Acta 198, 315–337. https://doi.org/10.1016/j.gca.2016.10.050

Laakso, T.A., Schrag, D.P., 2019. A small marine biosphere in the Proterozoic. Geobiology 17, 161–171. https://doi.org/10.1111/gbi.12323

Laakso, T.A., Schrag, D.P., 2018. Limitations on Limitation. Glob. Biogeochem. Cycles 32, 486–496. https://doi.org/10.1002/2017GB005832

Laakso, T.A., Schrag, D.P., 2014. Regulation of atmospheric oxygen during the Proterozoic. Earth Planet. Sci. Lett. 388, 81–91. https://doi.org/10.1016/j.epsl.2013.11.049

Lenton, T.M., Daines, S.J., 2018. The effects of marine eukaryote evolution on phosphorus, carbon and oxygen cycling across the Proterozoic–Phanerozoic transition. Emerg. Top. Life Sci. 12.

Macquaker, J.H.S., Taylor, K.G., 1996. A sequence-stratigraphic interpretation of a mudstone-dominated succession: the Lower Jurassic Cleveland Ironstone Formation, UK. J. Geol. Soc. 153, 759–770. https://doi.org/10.1144/gsjgs.153.5.0759

Maliva, R.G., Knoll, A.H., Simonson, B.M., 2005. Secular change in the Precambrian silica cycle: Insights from chert petrology. Geol. Soc. Am. Bull. 117, 835. https://doi.org/10.1130/B25555.1

März, C., Riedinger, N., Sena, C., Kasten, S., 2018. Phosphorus dynamics around the sulphate-methane transition in continental margin sediments: Authigenic apatite and Fe(II) phosphates. Mar. Geol. 404, 84–96. https://doi.org/10.1016/j.margeo.2018.07.010

Morris, R.C., 2012. Microplaty hematite—its varied nature and genesis. Aust. J. Earth Sci. 59, 411–434. https://doi.org/10.1080/08120099.2011.626453

Munson, T.J., 2016. Sedimentary characterisation of the Wilton package, greater MacArthur Basin, Northern Territory. Northern Territory Geological Survey.

Planavsky, N.J., McGoldrick, P., Scott, C.T., Li, C., Reinhard, C.T., Kelly, A.E., Chu, X., Bekker, A., Love, G.D., Lyons, T.W., 2011. Widespread iron-rich conditions in the mid-Proterozoic ocean. Nature 477, 448–451. https://doi.org/10.1038/nature10327

Postma, D., 1980. Formation of siderite and vivianite and the pore-water composition of a Recent bog sediment in Denmark. Chem. Geol. 31, 225–244. https://doi.org/10.1016/0009-2541(80)90088-1

Poulton, S.W., 2017. Early phosphorus redigested. Nat. Geosci. 10, 75–76. https://doi.org/10.1038/ngeo2884

Pufahl, P.K., Anderson, S.L., Hiatt, E.E., 2014. Dynamic sedimentation of Paleoproterozoic continental margin iron formation, Labrador Trough, Canada: Paleoenvironments and sequence stratigraphy. Sediment. Geol. 309, 48–65. https://doi.org/10.1016/j.sedgeo.2014.05.006

Pufahl, P.K., Grimm, K.A., 2003. Coated phosphate grains: Proxy for physical, chemical, and ecological changes in seawater. Geology 31, 801. https://doi.org/10.1130/G19658.1

Reinhard, C.T., Planavsky, N.J., Gill, B.C., Ozaki, K., Robbins, L.J., Lyons, T.W., Fischer, W.W., Wang, C., Cole, D.B., Konhauser, K.O., 2017. Evolution of the global phosphorus cycle. Nature 541, 386–389. https://doi.org/10.1038/nature20772

Rothe, M., Kleeberg, A., Hupfer, M., 2016. The occurrence, identification and environmental relevance of vivianite in waterlogged soils and aquatic sediments. Earth-Sci. Rev. 158, 51–64. https://doi.org/10.1016/j.earscirev.2016.04.008

Ruttenberg, K.C., Berner, R.A., 1993. Authigenic apatite formation and burial in sediments from non-upwelling, continental margin environments. Geochim. Cosmochim. Acta 57, 991–1007. https://doi.org/10.1016/0016-7037(93)90035-U

Sánchez-Baracaldo, P., Ridgwell, A., Raven, J.A., 2014. A Neoproterozoic Transition in the Marine Nitrogen Cycle. Curr. Biol. 24, 652–657. https://doi.org/10.1016/j.cub.2014.01.041

Sperling, E.A., Wolock, C.J., Morgan, A.S., Gill, B.C., Kunzmann, M., Halverson, G.P., Macdonald, F.A., Knoll, A.H., Johnston, D.T., 2015. Statistical analysis of iron geochemical data suggests limited late Proterozoic oxygenation. Nature 523, 451–454. https://doi.org/10.1038/nature14589

Todd, S.E., Pufahl, P.K., Murphy, J.B., Taylor, K.G., 2019. Sedimentology and oceanography of Early Ordovician ironstone, Bell Island, Newfoundland: Ferruginous seawater and upwelling in the Rheic Ocean. Sediment. Geol. 379, 1–15. https://doi.org/10.1016/j.sedgeo.2018.10.007

Tosca, N.J., Guggenheim, S., Pufahl, P.K., 2016. An authigenic origin for Precambrian greenalite: Implications for iron formation and the chemistry of ancient seawater. Geol. Soc. Am. Bull. 128, 511–530. https://doi.org/10.1130/B31339.1

Yang, B., Collins, A.S., Blades, M.L., Capogreco, N., Payne, J.L., Munson, T.J., Cox, G.M., Glorie, S., 2019. Middle–late Mesoproterozoic tectonic geography of the North Australia Craton: U–Pb and Hf isotopes of detrital zircon grains in the Beetaloo Sub-basin, Northern Territory, Australia. J. Geol. Soc. 176, 771–784. https://doi.org/10.1144/jgs2018-159

Zegeye, A., Bonneville, S., Benning, L.G., Sturm, A., Fowle, D.A., Jones, C., Canfield, D.E., Ruby, C., MacLean, L.C., Nomosatryo, S., Crowe, S.A., Poulton, S.W., 2012. Green rust formation controls nutrient availability in a ferruginous water column. Geology 40, 599–602. https://doi.org/10.1130/G32959.1

4. Unravelling sedimentary redox dynamics within the Velkerri Formation

Abstract Recent investigations of ocean–atmosphere redox derived from mid-Proterozoic sedimentary successions have yielded conflicting results. Although sedimentary geochemical datasets constraining Proterozoic redox have expanded significantly, many available datasets are derived principally from bulk rock analyses. As a consequence, the depositional and diagenetic mechanisms responsible for geochemical and isotopic enrichments, in turn forming much of the basis for paleo-redox reconstruction of Proterozoic systems, are not well understood. I present an integrated high-resolution sedimentological, sequence stratigraphic, mineralogical and geochemical study of the ~1.35 Ga Velkerri Formation of the Roper Group. Facies and sequence stratigraphic analysis shows that organic enrichment of Velkerri sediments took place during transgression and is independent of lithology, suggesting increased primary productivity was the primary driver for organic enrichment. Ferruginous facies are also associated with transgression and may have formed as a result of interacting upwelled oceanic, and terrestrial riverine waters. An anti-correlation between ferruginous facies and organic-rich hydrocarbon generating intervals suggests that ferruginous conditions were not conducive to promoting increased primary productivity, and/or were detrimental to the preservation of certain types of organic matter. I identify several generations of diagenetic and hydrothermal pyrite, which formed during hydrocarbon maturation and migration and later dolerite intrusion. Petrographic and statistical analysis of unambiguously authigenic pyrite framboids indicates that they did not originate in the water column but grew at the sediment-water interface. In addition, textural relationships show that Fe-silicate clays, glauconite and berthierine, were among the first authigenic minerals to enter Velkerri sediments, reflecting ferruginous waters regularly punctuated with at least low concentrations of $O_2(aq)$. Together these data indicate that free $H_2S(aq)$ was rare to absent in the water column, but instead frequently accumulated within sedimentary pore waters via microbial sulphate reduction. Dissolved oxygen diffused and likely interacted with $H_2S(aq)$ to sustain supersaturation necessary for framboid development; this chemical micro-environment would have provided an ecological opportunity for sulphur-oxidising bacteria, consistent with abundant and well-preserved carbonate fluorapatite spheres and known mechanisms of bacterial phosphatisation. These chemical gradients, in combination with recent biomarker evidence of phototrophic sulphur bacteria, and widespread sedimentary features reflecting deposition in close association with microbial biofilms or mats, raise the possibility that much of the Velkerri Formation may have been deposited within the photic zone. Benthic microbial mats likely obscured the connection between sedimentary and atmospheric redox state and, as a result of repeated fluctuations in $O_2(aq)$, may have strongly influenced the preservation of eukaryote-specific biomarkers. In addition to providing new and detailed constraints on redox dynamics within a critical interval of Earth history, this analysis raises the possibility that other Mesoproterozoic successions may have been shaped by similar processes.

4.1 Introduction

Constraining the redox state of mid-Proterozoic marine environments carries significant implications for Earth's biogeochemical evolution and for the early history of eukaryotic life. A number of geochemical proxy records have led to the hypothesis that atmospheric oxygen remained low and/or fluctuated through the mid-Proterozoic (Wang et al., 2020). Biogeochemical models have shown that persistently low atmospheric oxygen, in turn, would have required that net primary productivity (NPP), and perhaps nutrient availability, were suppressed through much of Earth's early history (Laakso and Schrag, 2018). At the same time, microfossil abundance and diversity, in addition to biomarker data (Brocks et al., 2017), indicate that early eukaryotic organisms did not substantively contribute to primary production until the mid to late Neoproterozoic, although

these patterns may have been subject to preservational biases, or unusual early eukaryote biomarkers (Brocks and Nettersheim, 2020; Cohen and Macdonald, 2015). Nevertheless, the apparently protracted history of early eukaryotic evolution has been interpreted to reflect largely redox-driven environmental constraints that may have influenced nutrient availability (Derry, 2015) and/or marginalised early eukaryotic organisms to specific environments in a low-oxygen world (Porter et al., 2018).

Although the initial appearance of atmospheric oxygen at ~2.4 Ga is clearly archived in the sedimentary record (Fischer et al., 2016), the subsequent course of oxygenation has attracted significant debate, with studies of mid-Proterozoic sedimentary successions yielding divergent results (Diamond and Lyons, 2018). Proterozoic ocean structure is now considered to have consisted of anoxic to ferruginous deep waters (Poulton and Canfield, 2011), overlain by a relatively oxygenated surface layer. Euxinic conditions were limited to productive continental margins (Doyle et al., 2018), however, some recent geochemical datasets indicate that oxic conditions may occasionally have extended into deeper waters (Song and Jiang, 2019).

Sedimentary rocks of the Roper Superbasin (RSB) have played a crucial role in constraining mid-Proterozoic surface environments and the paleo-ecology of early eukaryotes, partly because they are exceptionally well-preserved (Javaux and Knoll, 2017; Johnston et al., 2008). However, previous geochemical and paleontological studies of the RSB have focussed on a small number of drill cores from the distal edge of the basin and much of the environmental interpretation is based on bulk measurements of powdered sediment (Arnold et al., 2004, 2004; Donnelly and Crick, 1988; Jackson et al., 1991; Johnston et al., 2008; Kendall et al., 2009a). As a consequence, the depositional and diagenetic mechanisms responsible for geochemical signatures, which in turn form the basis of paleo-redox reconstructions, are not well understood.

To address these knowledge gaps, I conducted a sedimentological, mineralogical and geochemical study of six cores from across the RSB that included both previously investigated and unstudied material from a range of contemporaneous depositional environments. The focus of this study is on the Velkerri Formation, an organic-rich succession of shales with a basin wide stratigraphic distribution. I present facies analysis, sequence stratigraphic, petrographic and micro-analytical data from the Velkerri Formation, interpret these data in a combined sequence stratigraphic and biogeochemical framework, and highlight specific implications for Mesoproterozoic environmental evolution.

4.1.2 Geological context

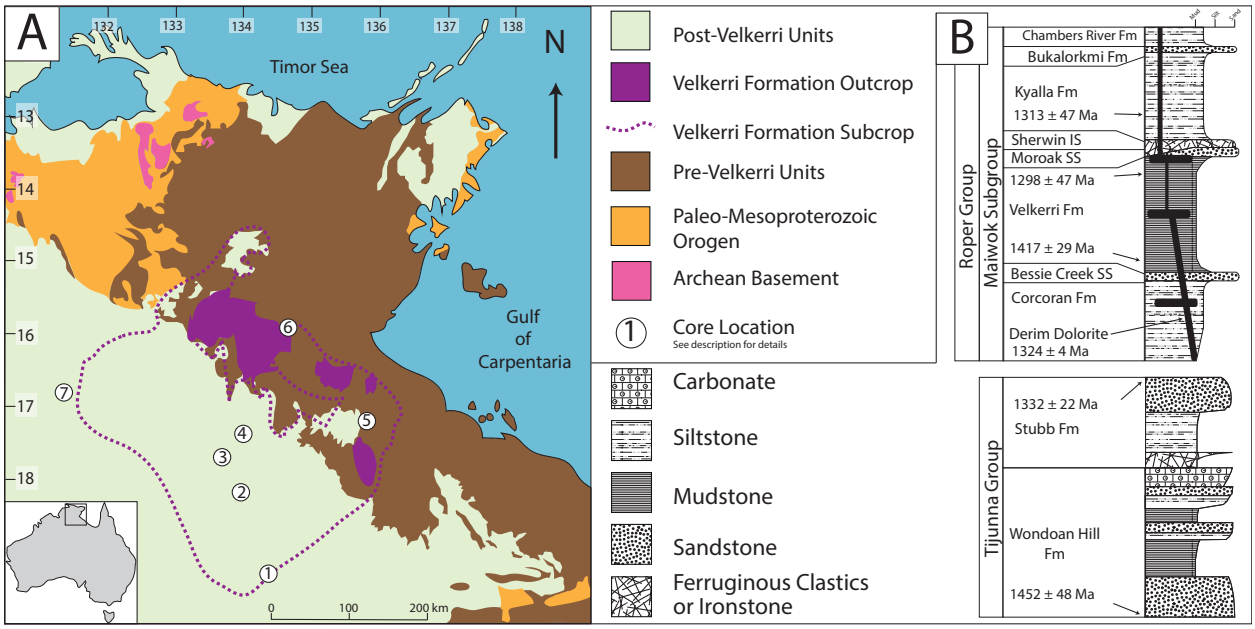

Fig 1: A) Simplified geological map of the study area showing the sampled cores, and Velkerri Formation outcrop and subcrop. B) Simplified stratigraphy of the Roper Group and Tijunna Group (Yang et al, 2018, Munson, 2016) Cores sampled; 1= 12BC, 2 = SD1, 3 = MM1, 4 = AT2, 5 = SC1, 6 = UP4, (7 = 99VR, not part of this study).

The Roper Superbasin (RSB) is a ~1.6 – 1.4 Ga dominantly siliciclastic sequence deposited in an epicratonic setting in the Northern Territory, Australia, that covers an area of ~145,000 km^2 in both outcrop and the sub-surface (Munson, 2016). The RSB is the youngest of four unconformity-bound sedimentary packages of the greater McArthur Basin (Munson, 2016). Formation of the RSB began ~1.6 Ga with subsidence and reactivation of normal faults in the underlying McArthur Basin (Munson, 2016). Sedimentation of the lowermost Roper Group and its equivalents began ~1.5 Ga, following uplift on the western and southern margins of the RSB during the later stages of the assembly of Protoaustralia (Munson, 2016). Sedimentation in the RSB continued with few geologically significant gaps until at least ~1.3 Ga (Munson, 2016; Yang et al., 2019).

Despite their age, Roper Superbasin sediments have undergone only negligible deformation and limited, highly localised, low-grade contact metamorphism (Munson, 2016). Sediment fill is packaged into six transgressive sequences of basinal shales and proximal sands, bound by intracycle erosional surfaces and ironstones (Munson, 2016). These 3rd order stratigraphic patterns have been interpreted to reflect the influence of local flexural tectonics on both relative sea level and sedimentation whereby flexural loading caused subsidence in the depocenter (Abbott and Sweet, 2000; Munson, 2016).

The Velkerri Formation is situated within the uppermost Roper Group (Figure 1). The Velkerri Formation has been divided into three formal members; the Kalala member, the Amungee member, and the Wyworrie member in stratigraphic order (Munson and Revie, 2018). The Velkerri Formation intercepted thicknesses from 12 – 1482 m in drill core, with the greatest thickness within the Beetaloo Sub-basin depocenter (Figure 1, Munson and Revie, 2018). The formation is dominated by mudstones and siltstones commonly intercalated with minor sandstones. Previous sedimentological investigations have concluded that the Velkerri Formation records mostly outer shelf to basinal deposition below storm wave base (but see Chapter 2 of this thesis; Abbott and Sweet, 2000; T. J Munson, 2016; Munson and Revie, 2018; Warren, et al., 1998)

The Velkerri Formation has generated live oil from three distinct high TOC horizons in the middle Amungee member of the formation (Jarrett et al., 2019; Munson, 2016; Munson and Revie, 2018). Correlation between cores is based on litho-, chemo- and seismic- stratigraphy, and the organic chemistry associated with each of the organic-rich shales (Jarrett et al., 2019; Munson, 2016; Munson and Revie, 2018). The maximum depositional age of the Velkerri Formation has been constrained by the combination of absolute ages (Re–Os) and maximum depositional ages (U–Pb detrital zircons) to be between 1.39 ± 0.01 Ga (2σ) and 1.36 ± 0.02 Ga (2σ) (Bodorkos et al., 2021; Kendall et al., 2009b; Yang et al., 2019)

4.2 Methods

Core material was obtained courtesy of the Geoscience Australia core store in Canberra and the Northern Territory Geological Survey Core store in Darwin, and graphically logged on a centimeter scale to assess grain size and composition, and sedimentary structures, and sampled at regular intervals (~10 meters). I collected 353 samples of the Velkerri Formation in five drill cores forming a north–south, east–west distal transect of the main Roper Superbasin depocenter (Table 1 for core names, Figure 1 for core locations). Cores SD1, AT2 and MM1 sampled the Basinal Region of the RSB, cores UP4 and SC1 sampled the Distal Region of the RSB and core 12BC sampled the Proximal Region of the RSB.

Rock powders were prepared from each core sample by powdering in a TEEMA swing mill in a tungsten carbide collar pestle for 30 seconds at 950 rpm. The process was repeated until the powder could pass through a 50 μm sieve. All powders were analysed for bulk and clay-specific mineralogy at the University of Oxford using a Panalytical Empyrean Series 2 X-ray diffractometer (XRD) equipped with a Co Kα source at 40 kV and 40 mA. Sample powders were mounted as a slurry on a zero-background silicon plate. Both bulk mineralogy and clay analyses were continu-

ous scans with a step size of 0.0262 degrees. Bulk analyses were scanned from 2θ = 4.99 – 80.00° with a scan speed of 0.067335°/second with a 1° divergence and anti-scatter slits. Clay analyses were scanned from 2θ = 69.01 – 75.00°, with a scan speed of 0.022255°/second and 2° divergence and 2° anti-scatter slits.

Semi-quantitative results were calculated by Panalytical HighScore software, using referenced scale factor and Reference Intensity Ratio (RIR) values from the International Centre of Diffraction Data (ICDD) PDF-4+ mineral database. All samples were corrected for sample height displacement error, which causes whole-pattern peak shifts, by normalising to the quartz 011 reflection at 3.343 angstroms. Individual clay mineral speciation was performed on high-angle powder diffractograms and normalised to the quartz –131 peak at 1.542 angstroms. Peaks were identified by background subtraction and profile fitting and peak positions were assigned to individual clay minerals on the basis of characteristic "060" bands or overlapping composite reflections that constrain clay mineralogy (Środoń et al., 2001).

Over the course of this study, 160 thin sections were produced. Thin sections were cut and polished to approximately 30 microns, studied using optical microscopy, and carbon coated to permit analysis by scanning electron microscopy-energy dispersive X-ray spectroscopy (SEM-EDS) using a FEI Quanta 650 FEG SEM.

4.3 Results

4.3.1 Facies analysis and sequence stratigraphy

The studied succession was divided into sedimentary facies which were then grouped into related facies associations (FA). The Velkerri Formation is dominated by facies viii, facies ix, and facies x of FA3 Marine. Additionally, facies vi Green cemented sandstone and facies vii Green mudstone, from FA2 Ferruginous Marine is also found throughout the Velkerri Formation. Details of the facies and FA are given in Table 1 and Figure 2 in Chapter 2 but are also outlined below in brief.

FA2 – Ferruginous Marine

Facies vi) Green cemented sandstone – In the Velkerri Formation this facies consists of fine to medium cross bedded quartz sandstones cemented with authigenic green silicate clay (Figure 3E & I, Chapter 2). Sedimentary structures indicate deposition within a shallow marine environment with alternating tidal and storm influence, proximal to a detrital clastic sediment source, and with a relatively rapid sedimentation rate (Figure 3E & I, chapter 2). In the Velkerri Formation, facies vi was only observed in core 12BC in the south of the study area, in the inferred direction of

the paleocoast. Facies vi is interbedded with facies vii which becomes more abundant up section at the expense of facies vi. Therefore facies vi was deposited in the early stages of the transgressive systems tract (Figure 3E & I, chapter 2).

Facies vii) Green Mudstone – In the Velkerri Formation this facies consists of variably silt rich laminated to massive claystone with a range of sedimentary structures indicating deposition on storm dominated shelf setting, distal to a source of detrital clastic input. Sedimentary structures generally reflect those of the stratigraphically adjacent FA3 beds, but also include undulose, wrinkled, convoluted, and planar and inclined laminae. The thickest intervals of facies vii within the Velkerri Formation occur within the transgressive systems tract (Figure 3E & I, chapter 2). Facies vii is less abundant and the intervals are thinner and occur within the high stand systems tract.

FA3 - Marine

Facies viii) interbedded sandstone and mudstone - consists of fine to medium sandstones and silty mudstones with a range of sedimentary structures suggesting deposition on a wave to storm dominated marine shelf. Facies analysis suggests that facies viii) was deposited during the earlier stages of the transgressive systems tract and the earliest stages of the falling stand systems tract when detrital clastic sediment was once again able to reach the offshore areas of the basin.

Facies ix) interlaminated siltstone and mudstone - shows a similar set of sedimentary structures to facies viii) but with a finer overall grainsize and a greater dominance of current generated sedimentary structures suggesting deposition on a storm dominated marine shelf and more distal to sources of detrital clastic input. Facies analysis suggests that facies ix) was deposited during the transgressive systems tract as localised changes in RSL reduced clastic input.

Facies x) Laminated and massive claystone - is the finest grained of the FA3 facies being dominated by authigenic silicate clays with relatively rare detrital quartz dominated silt bearing intervals. Sedimentary structures are poorly preserved but indicate deposition on a storm dominated shelf, distal to detrital clastic sources. Facies analysis suggests that facies x) was deposited during the transgressive systems tract.

4.3.2 Mineralogy

In addition to the detrital components that comprise the Velkerri Formation (i.e., dominantly quartz, feldspar, illite and muscovite) mineralogical and petrographic analysis has identified at least four mineral components that strongly constrain syndepositional and diagenetic geochemical conditions and their relative timing, which I focus on here: ferrous silicate clay minerals, phos-

phate minerals, pyrite, and carbonate minerals.

Ferrous silicate clays are found basinwide throughout the Velkerri Formation, and were identified by XRD (Figure 2, Chapter 2), SEM-EDS, and petrographic analysis (Figure 2, this chapter). In the cores examined here, XRD data indicate that glauconite (a K-rich Fe(II)-Fe(III) silicate) comprises on average between 10 – 30% of the clay mineral fraction. The mineral is present as fine to medium sand sized grains either distributed randomly throughout clay-rich beds, or concentrated in lags. Glauconite is also abundant in erosive scours that contain coarse clastics and continentally derived heavy detrital minerals. Glauconite also forms precipitated envelopes around pre-existing glauconite grains and is present as pore filling cements. Thus, the glauconite grains present in the Velkerri Formation are a combination of those reworked and transported from another location along the seafloor where they initially precipitated, and those that precipitated *in situ*.

Berthierine (an Fe(II)-rich serpentine) is a common component of the clay fraction of the Velkerri Formation, comprising between 2 and 80% of the clay mineral fraction. This phase is commonly present as large flakes and stacks of crystallites and pore filling cements. Within intervals of the Velkerri Formation that are poor in detrital phases, berthierine forms decimeter scale beds. The berthierine-rich beds appear to have undergone early cementation and reworking which in turn produced abundant mm-scale intraclasts. Chamosite (an Fe(II)-rich chlorite) is also present as a diagenetic alteration product of berthierine and glauconite. Chamosite can also be found in the sediment as either isolated stacks of crystallites or bound within berthierine intraclasts.

Phosphate minerals are found in all cores as spheres of carbonate-fluorapatite (CFA; Figure 3). CFA spheres are most abundant and well preserved in silicified mudstones of the Amungee member. There are two distinct morphologies of CFA spheres: ~10 μm concentrically layered spheres with organic carbon cores and ~5 μm spheres of radially arranged CFA needles. CFA spheres may be draped by overlying sediments and many appear to have undergone reworking leading to broken spheres. Where larger spheres do not host a carbon core, the core may be occupied by detrital quartz or authigenic berthierine grains indicating syndepositional reworking of the spheres. CFA spheres are also frequently enveloped by or entrained within later diagenetic phases such as carbonate rhombs. Together, these petrographic relationships indicate that the CFA spheres are syndepositional or early authigenic.

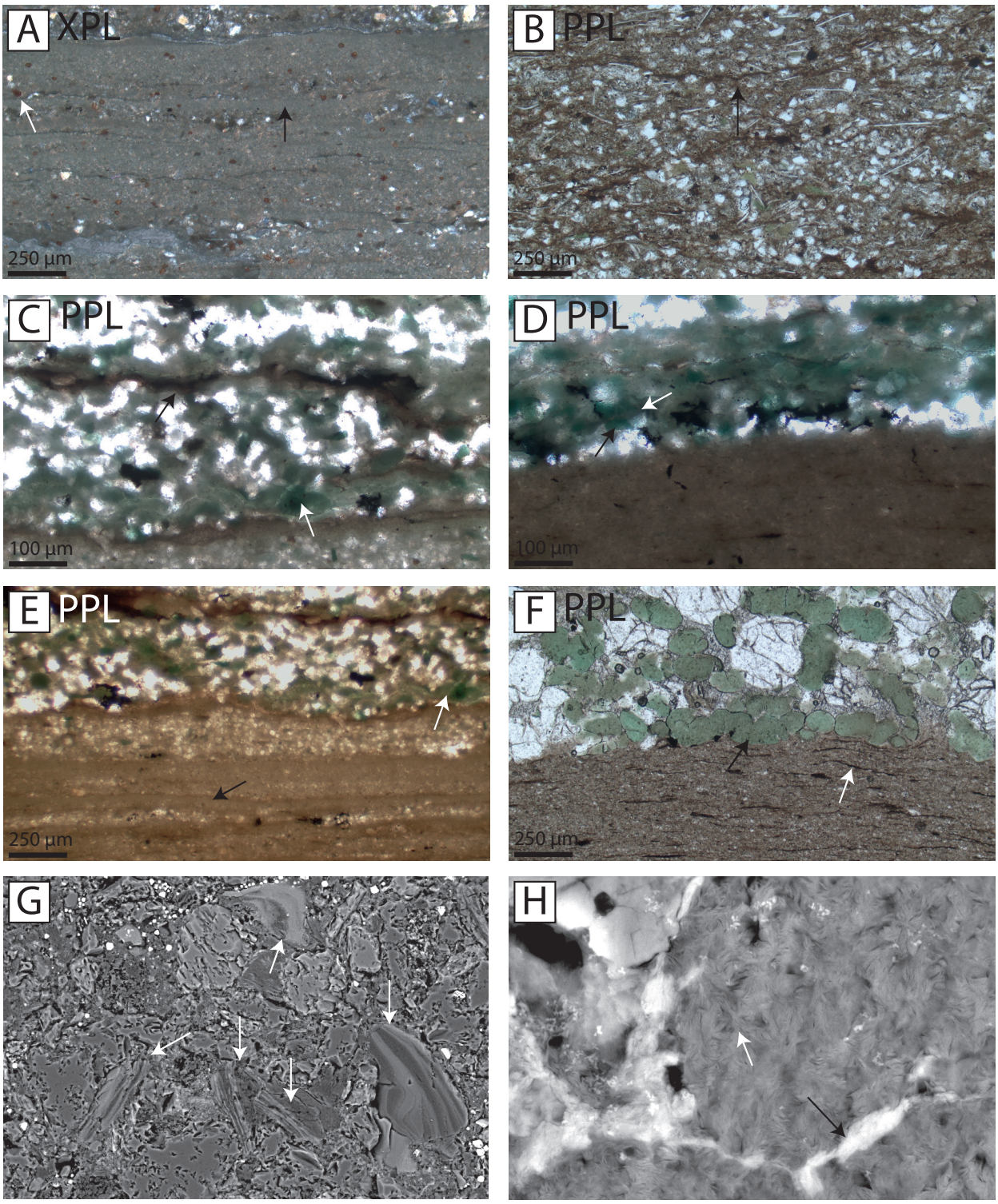

Fig 2: A) thin section with black arrow showing green brown berthierine rich laminae, white arrow shows detrital oxide grains. B) typical organic rich microbial laminae indicated by the black arrow. Overlying sediments drape the microbial laminae indicating it produced sea floor topography. Alternate wrinkled to smooth texture indicates tension and contraction caused by differential dehydration common in modern microbial mats. Note that overlying sediment is cross bedded indicating current action capable of moving silt grains, but not enough to erode a cohesive microbial mat – a common indicator of the presence of an extracellular polymeric coating of the microbes. C) glauconite rich silt beds, white arrow shows glauconite grain encased in a syn depositional glauconite and berthierine overgrowth. Black arrow shows organic and berthierine rich microbial laminae that overgrows the surface of the underlying silt bed.

Fig 2 continued: D) glauconite rich silt bed where quartz silt and glauconite are overgrown by a syn-sedimentary cement of glauconite and berthierine. Black arrows shows original glauconite grain and white arrow shows pore filling cement. E) Silt and glauconite rich bed that has erosively scoured the underlying clay and organic rich beds. Black arrow shows a berthierine rich lamina, white arrow shows a glauconite grain overgrown by a syn sedimentary cement of glauconite and berthierine. F) Lower brown part of image is a bed of berthierine and kaolinite, white arrow shows shred of disaggregated organic matter that drapes underlying sediment topography. Upper portion shows fine sand bed rich in glauconite, black arrow indicates glauconite grain overgrown with typical Fe-clay cement, glauconite grain has also undergone partial oxidation before being enclosed in cement. G) SEM-electron map of a bedding plane. White arrows show micro rip-up clasts of early cemented berthierine rich sediments. Darker bands in the clasts are relatively organic rich and berthierine poor in comparison to adjacent bands. H) SEM electron map showing detail of glauconite grain boundary where the cement is formed of intergrown blades of berthierine and clumped books of glauconite (white arrow) black arrow indicates where berthierine is growing into cracks in the cement and glauconite surface.

Pyrite is found in all cores within mudstone dominated intervals (Figure 4) and displays five distinct textures as detailed below.

i) Framboids are microscopic (sub-) spheroidal clusters of equant and equidimensional microcrystals (Rickard, 2012a) and are found throughout the Velkerri Formation, basin wide (Figure 4 A–D). The framboids have a mean diameter of 71 μm and range from 31 to 169 μm (n = 661 across all studied cores). Framboids are spherical to elliptical and are composed of octahedral microcrystals that are uniformly ~5 μm in size. Petrographic relationships indicate that framboids did not become elliptical during compaction as laminae contain both elliptical and spherical framboids. Velkerri Formation framboids show no perceptible overgrowth or infilling by later generations of pyrite in either optical or SEM-EDS microscopy. Additionally, larger framboids often contain enclosed grains of detrital quartz, silt, or authigenic berthierine further indicating a syndepositional origin.

ii) Disseminated octahedral single crystals of pyrite range from ~5 – 30 μm in diameter and are found throughout the Velkerri Formation in all examined cores. The crystals may form loosely packed clusters and strings which are distinct from framboids both in morphology and by virtue of their larger size distribution. Crystal morphology is usually octahedral or truncated octahedral, with minor populations exhibiting anhedral morphology or irregular pore-filling forms. Petrographic contacts show that the octahedral micro-crystals grew within pre-compacted pore space and actively displaced surrounding detrital and authigenic minerals (Figure 4G). Together these observations indicate that the micron-scale pyrite largely grew after most of the framboids, most likely during burial and diagenesis.

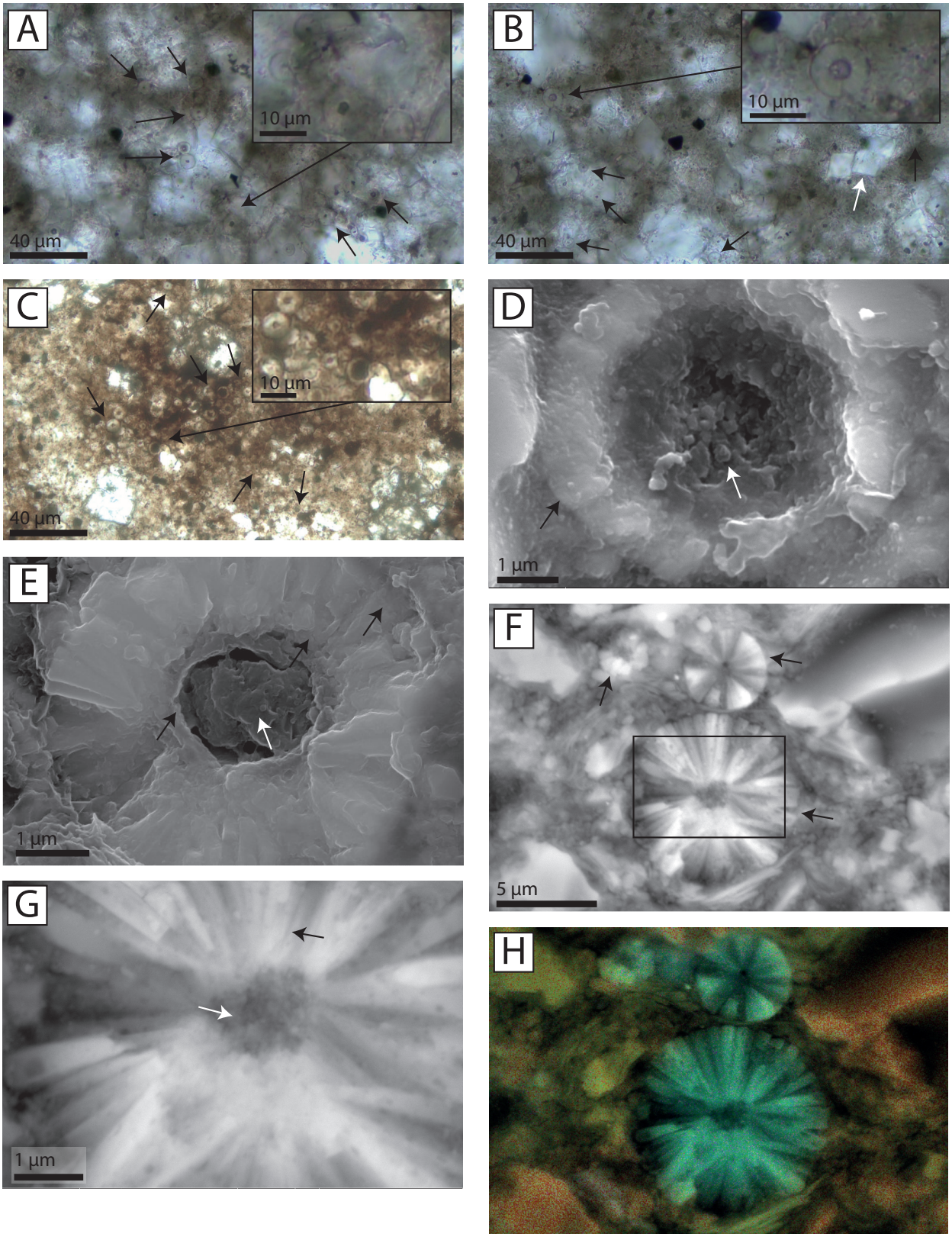
A
10 µm
40 µm
B
10 µm
40 µm
C
10 µm
40 µm
D
1 µm
E
1 µm
F
5 µm
G
1 µm
H

iii) Euhedral pyrite macro crystals range in size from ~300 µm up to ~3 mm and typically exhibit octahedral or cuboidal habits (Figure 4H). This population of pyrite crystals is destructive to enclosing fabrics but may in turn be displaced or entrained in alteration textures and minerals. This population of pyrite is principally found in association with mineralised fractures and massive pyrite and is likely hydrothermal in origin.

iv) Masses of acicular, pyritohedral and cuboidal crystals, or massive pyrite, commonly occur as discrete veins associated with mineralised faults, localised dolerite intrusion, and infilling fractures. Dolerite directly intrudes the Velkerri Formation in cores MM1 and SC1, below the Velkerri Formation in AT2, UP4 and SD1, and is not found in 12BC. Peperite textures indicate that dolerite intrusion appears to have taken place post-compaction but pre-lithification (Figure 4 I & J). For example, sediments immediately adjacent to intrusions show ductile deformation and emit vertical veins filled with pyritic carbonates, hydrocarbons, and quartz suggesting that the sediments were volatile-rich at the time of dolerite emplacement. Several cores have intersected post compactional faults (e.g. SC1) as indicated by brittle fracture and mineralisation around fault planes which are also associated with mineral veins. In addition to pyrite, these veins contain chalcopyrite, galena, sphalerite, graphitic carbon and a complex intergrowth of carbonates. Porous silt and sand-rich beds may also be cemented by massive pyrite, where they have been intercepted by pyrite-bearing veins.

v) Nano crystalline pyrite is present in sediments adjacent to veins, faults and intrusions. This form of pyrite appears as a dust disseminated through host sediment. Individual nano crystals are cuboidal when growing on an existing grain surface or may be anhedral to subhedral cuboids when growing in interstitial spaces and measure ~50 – 100 nm but are difficult to resolve due to their size.

Fig 3: (Previous page) Phosphatic spherules from the Amungee member of the Velkerri Formation. A, B and C optical images of carbon cored phosphatic spherules in bedding plane view. Large clear grains are quartz, green grains are glauconite, opaques are pyrite and brown material is kerogen. Black arrows show spherules, white arrow in B shows diagenetic Fe-carbonate. Insets show details of large spherules. D) SEM electron map of and spherule missing the carbon core. Black arrow shows edge of spherule partially buried in sediment; white arrow shows authigenic berthierine clay growing in hollow core indicating carbon core was lost prior to final burial. E) spherule with partially exposed carbon core (white arrow), black arrows show remnant internal layering. F) Spherules indicated by black arrows are of the granular phosphate cored variety (see main text). G) detail of spherule in F, white arrow shows granular phosphate core, black arrow shows acicular phosphate that forms outer shell. H) SEM-EDS element map of G, Green = P, yellow = Al and orange = Si. Spherules are distinct in form and composition from enclosing quartz (orange) and berthierine (yellow).

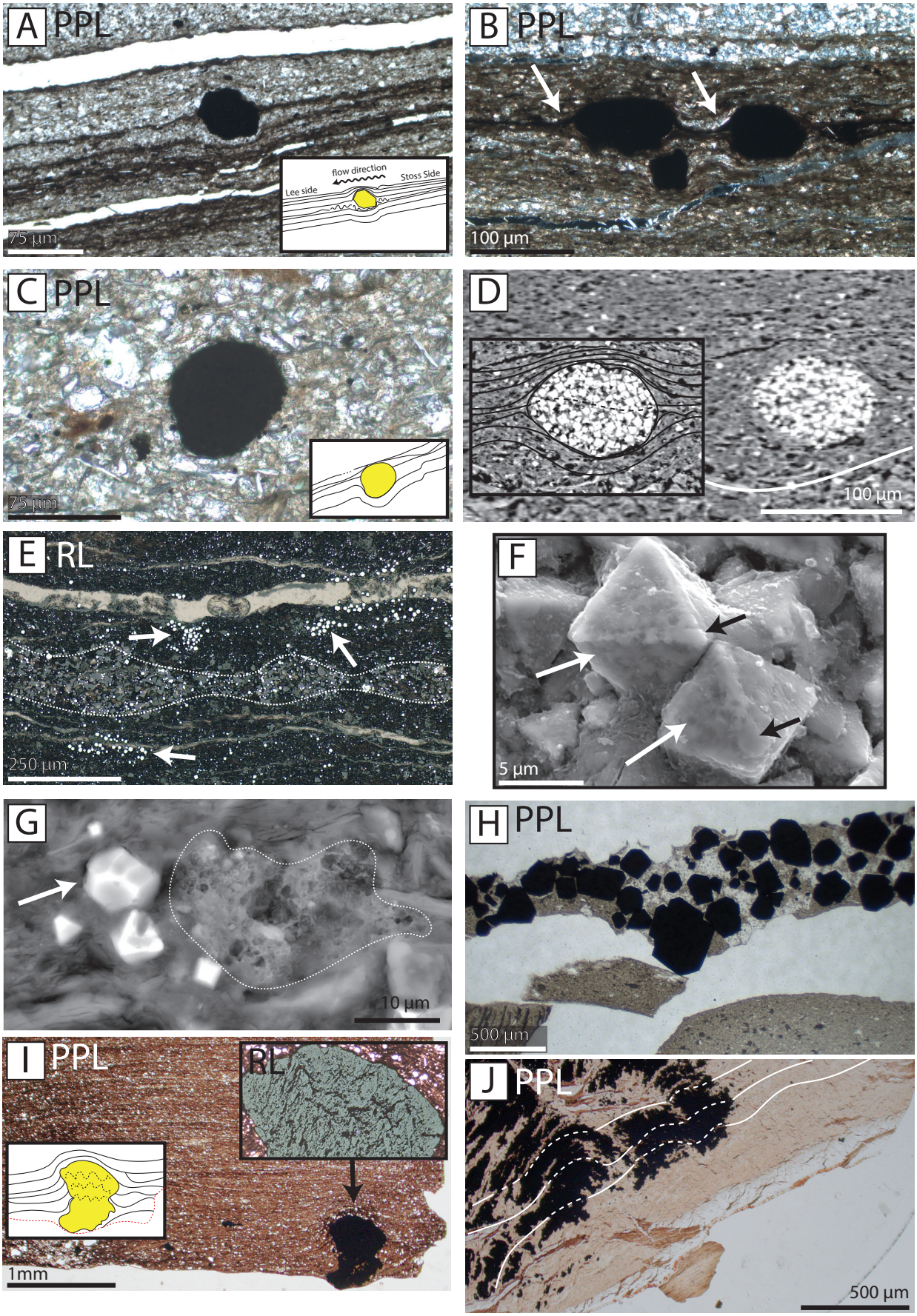
A PPL
flow direction
Stoss Side
Lee side
75 µm
B PPL
100 µm
C PPL
75 µm
D
100 µm
E RL
250 µm
F
5 µm
G
10 µm
H PPL
500 µm
I PPL
RL
1mm
J PPL
500 µm

Carbonate minerals are present basinwide as 20 – 40 µm sized saddle shaped rhombs (in addition to the above-mentioned diagenetic fault, fracture and vein fill, Figure 4A, B, C). Each rhomb is internally zoned with compositions ranging from siderite through dolomite to rhodochrosite endmembers. Rhombs preferentially grow in beds rich in ferrous clay where petrographic relationships indicate that growth of the rhombs took place during late diagenesis.

4.4 Discussion

4.4.1 Sequence stratigraphic distribution of offshore facies

Facies analysis and sequence stratigraphic data indicate that sedimentary facies indicative of water depths at or below storm wave base are temporally and spatially heterogeneous across the RSB during deposition of the Velkerri Formation (Figure 3B & I, Chapter 2). Further, facies representing deposition at or below storm wave base, are subordinate to facies representing deposition above storm wave base (Figure 3B & I, Chapter 2). Therefore, I interpret deposition of the Velkerri Formation to have dominantly taken place between storm to fair weather wave base across the RSB. Local syndepositional tectonics is one possible cause for the temporal and spatial heterogeneity in offshore facies, while a rough speculative estimate gives a likely average of 30 m – 50 m for water depth during deposition of the Velkerri Formation. These topics are discussed further in Chapter 2.

Fig 4: (Previous page) Common textures and petrographic relationship of Velkerri Formation pyrite. A – typical framboid, inset shows interpreted bedding relationships. Note the formation of a lee and stoss side indicating growth at the sediment water interface under a persistent flow regime capable of transporting silt sized particles. B – framboids growing in microbial lamina, white arrows show organic matter and clay draping framboids indicating they formed microtopography on the sediment surface. C – Framboid detail with inset showing bedding relationships. Quartz silt and clay below the framboid are displaced while quartz silt and clay above drape the framboid indicating the framboid was microtopography on the sediment surface. D – SEM electron map of a framboid with inset showing interpreted bedding relationships. Note at least one sediment lamina has been incorporated into the framboid while others are displaced or drape the framboid. White lines in the main image show boundaries of the clay rich laminae containing the framboid. Small euhedral diagenetic pyrite crystals are scattered throughout the sample. E – reflected light image of a thin section, white arrows indicate clusters or pyrite crystals aggregating into framboids. White lines and pale brown grains indicate a bed of quartz sand with erosive undulose contacts that indicate currents reworking the sediment surface. F – SEM backscatter image of pyrite octahedra exposed on the surface of a framboid, white arrows indicate corrosion pits, black arrows indicate oxides forming on the crystal surface. Both features are beneath enclosing sediment grains indicating corrosion and oxidation of the crystals occurred prior to final burial. G – SEM backscatter image of pyrite crystals in a clay rich laminae, white arrow indicates a typical pyritohedral crystal, white line indicates a mass of intergrown carbon cored phosphate spherules. H – typical fabric destructive late diagenetic euhedral pyrite macro crystals. I – typical fabric destructive massive intrusive pyrite, lower inset shows interpretation of fabric relationships, upper inset shows reflected light image where disrupted bedding can be seen within the pyrite mass. J – a typical example of massive hydrothermal pyrite that has infiltrated sediments and then precipitated between clay grains producing the feathered texture. White lines show the position of disrupted and enclosed lamina.

4.4.2 Sequence stratigraphic distribution of ferruginous facies

Ferruginous intervals in the Velkerri Formation are dominantly associated with the TST, and most frequently co-occur with facies ix and x of FA3 in offshore areas. This is consistent with deposition of ferruginous sediments in deeper waters, perhaps as a result of sedimentary condensation and a lack of detrital clastic dilution (Föllmi, 2016; Pufahl et al., 2020; Todd et al., 2019; Williams, 2003). However, in offshore areas, ferruginous facies also co-occur with facies viii, which is interpreted to have been deposited in relatively detrital clastic rich storm dominated shelf conditions. Further to this the ferruginous facies in the inferred direction of the paleocoast co-occur with sandy facies interpreted as shallow marine and fluvio-paralic in origin (Figure 3E & I Chapter 2). Together these observations indicate that though ferruginous conditions are associated with transgression, they were not solely controlled by water depth or detrital clastic sedimentation rate (Chapter 2 this thesis, Munson, 2016). One possible explanation for the observed distribution of ferruginous facies in the RSB is the interaction of ferruginous oceanic waters upwelling along the coastal margin, and riverine waters with a contrasting chemistry, pH, and Eh, e.g., carrying dissolved ferric oxides (Hallam and Bradshaw, 1979; Michalopoulos and AIIer, 1995; Michalopoulos and Aller, 2004; Todd et al., 2019; Trythall et al., 1987).

If this model were the case for the Velkerri Formation, it may indicate that rather than ferruginous conditions being a background state, ferruginous conditions in the RSB may represent a confluence of fortuitous physical, geographical, oceanographic, climatic, chemical and possibly biological conditions, and that highly ferruginous units in the RSB such as the Sherwin Ironstone, may simply represent the intervals when these conditions reach a maxima. Taking the concept further, ferruginous condition within Proterozoic marine basins may also reflect similar fortunate confluences of environmental conditions, rather than a true background state. Rather than dismissing the hypothesis of ferruginous global oceans in the Proterozoic, the idea above of intense ferruginous deposition episodes, may itself be a reflection of unique Earth surface conditions, similar to other times in Earth history that promoted deposition of ferruginous sediments in cratonic basins and shelf seas (Bayer, 1989; Van Houten and Arthur, 1989). However, developing this hypothesis further is beyond the scope of this thesis and data set.

4.4.3 Sequence stratigraphic distribution of organic matter enrichment

The stratigraphic distribution of organic rich beds is shown in Figure F & M of Chapter 2. The thickest intervals of organic enrichment occur in the Beetaloo region (analogous the Basinal Region of this study), during the TST, and not the HST as previously proposed (Munson, 2016 and refs therein). Additionally, organic enrichment appears to show no clear correlation with a particular offshore facies, except an anti-correlation with ferruginous intervals. Together these observations suggest that organic matter enrichment was not dependent on increased water depth, or a decrease in detrital clastic dilution to enhance preservation conditions. This implies that increased primary productivity was the key driver of organic enrichment during deposition of the Velkerri Formation, a hypothesis that is consistent with the observations in this and other studies (Cox et al., 2016).

The anti-correlation between organic matter enrichment and ferruginous sediments is more difficult to explain with the current data set. While ferruginous intervals contain low organic matter content, they also contain exceptionally well preserved carbonaceous material interpreted here as disaggregated microbial mats, and acritarchs (Figure 8I, Chapter 2, Javaux and Knoll, 2017, Emmanuelle Javaux, pers comms, 2019). In particular a ferruginous lithology informally known as “plywood” that is common in many Proterozoic shales, and rich in Fe-Al-silicates, is generally considered to host the best preserved acritarch fossils in the Velkerri Formation, and other Proterozoic shales (Emmanuelle Javaux, pers comms 2019, Ross Anderson, pers comms, 2019). On this basis, the ferruginous intervals may exert a taphonomic bias against the type of organic material that is the precursor for hydrocarbon generation, while preferentially preserving the organic material that forms the inferred microbial mats and acritrachs. One possible explanation is that the ferruginous conditions are not conducive to the preservation of hydrocarbon precursor material due to low sedimentation and burial rates in the presence of O_2.

Another taphonomic possibility is that the chemistry of the Fe-Al-rich authigenic clays may preferentially enhance the preservation of acritarch and microbial mat type organic matter e.g., Anderson et al., (2018). The paleobiology of the organisms themselves may also play a role. If nutrients were elevated during the proposed episodes of increased primary productivity, then there would be less need for microorganisms to form resting cysts, a common interpretation of Proterozoic acritarchs, to wait out nutrient poor conditions, resulting a bio-ecological taphonomic filter (Martin and Servais, 2020). The data collected in this study are insufficient to provide any conclusive evidence for the above speculation. For example, a detailed comparison of phosphate occurrence, as detected by XRD and petrographic observation, ferruginous facies, and hydrocarbon

bearing intervals is currently only available for AT2. In this one core there is no strong correlation between phosphate occurrence, ferruginous facies and hydrocarbon occurrence.

A more thorough study of each core to record stratigraphic occurrences of carbonaceous fossil material, hydrocarbons, ferruginous facies, and phosphate occurrence would help investigate this hypothesis. Similarly, the current data are not sufficient to explain the relatively lower abundance of hydrocarbon generating organic matter within the Proximal and Distal Regions of the RSB. Speculative explanations based on the available data include, but are not limited to, a lack of appropriate preservational conditions in the depositional environment such as higher sedimentation rates or more abundant dissolved O_2, or biological constraints such as lower nutrient abundance or rapidly fluctuating salinity.

4.4.4 Mineralogical constraints on syndepositional and early diagenetic redox

Available constraints from experimental geochemistry and petrology make it clear that each of the redox-sensitive phases discussed in the results require specific geochemical conditions and timescales of formation. Integrating these observations and data, therefore, provides new constraints on the redox state of pore and bottom waters during and shortly after sediment deposition and provides a mineralogical and microtextural basis to understand geochemical and isotopic datasets from the Velkerri Formation.

Fe-silicate mineralogy and microtextures

Textural relationships described above show that ferrous-silicate clays, specifically glauconite and berthierine, were among the first authigenic minerals to enter the sediments, often in the form of silt-sized granules. These phases were also commonly precipitated *in-situ* as rinds or pore-filling cements (Figure 2 C – F, H). Data indicate that glauconite and berthierine were forming at the sediment-water interface and in the uppermost sediment column, where they were actively reworked by bottom water currents. Because glauconite and berthierine are both redox sensitive and the chemical conditions required for their formation are constrained from laboratory experiments and observations from modern sediments and ancient sedimentary rocks, their relative timing and abundance within the Velkerri Formation provide new insight into syndepositional redox dynamics (Bhattacharyya, 1983; Logvinenko, 1982; Mazlan B. Hj. Madon, 1992; Pufahl and Grimm, 2003)1983; Logvinenko, 1982; Mazlan B. Hj. Madon, 1992; Pufahl and Grimm, 2003.

Glauconite has been identified in modern continental shelf sediments, and in many ancient marine and non-marine sedimentary successions (Chaudhuri and Chanda, 1994; Baldermann et al., 2013a; Brasier, 1980; Huggett and Cuadros, 2010; Van Houten and Purucker, 1984) and available data indicate that glauconite precipitation is favoured by oscillating ferruginous and oxic conditions (Harder, 1980, 1978; Pufahl and Grimm, 2003; Stucki, 2011). Specifically, anoxic and ferruginous systems commonly trigger the precipitation of Fe(II)-Al-silicate minerals (i.e., Fe(II)-rich smectite), widely believed to serve as glauconite precursors (Baldermann et al., 2013a; Pufahl and Grimm, 2003). Experimental data further indicate that when these Fe(II)-rich smectites are repeatedly exposed to $O_2(aq)$ and ferruginous conditions, the oxidation and reduction of structural Fe leads to irreversible K-fixation, loss of interlayer expandability, and a reduction in the Fe(II)/Fe(Total) ratio to between 0.2 and 0.4 – all defining characteristics of glauconite (Stucki, 2011). This requirement for oscillating oxic and ferruginous conditions is also consistent with data from sedimentary rocks, indicating, at least qualitatively, that glauconite tends to become enriched in sediments lying at the interface between anoxic and oxic paleo-environments (Baldermann et al., 2013b; Van Houten and Purucker, 1984).

Berthierine, on the other hand, is thought to require dominantly ferruginous conditions as well as pre-existing Al-rich phyllosilicate substrates such as kaolinite (Bhattacharyya, 1983). Experimental work has shown that exposure of kaolinite to $Fe^{2+}(aq)$ leads to Fe(II) incorporation into the crystal lattice, and the generation of powder X-ray diffraction characteristics similar to berthierine (Bhattacharyya, 1983). Alteration of kaolinite to berthierine is also supported here by petrographic observations of kaolinite partially altered to berthierine (Figure 2 G). It has also been suggested that berthierine may form through the direct reduction of odinite, a serpentine-like 1:1 layer silicate mineral with a similar composition to berthierine, but with a higher proportion of Fe(III) (Hornibrook and Longstaffe, 1996; Odin, 1990) Kaolinite, berthierine and odinite are found throughout the Velkerri Formation and so it is likely that both of these pathways contributed to berthierine formation.

Taken together, Fe-silicate mineralogy and micro-textures indicate dominantly ferruginous conditions which were repeatedly punctuated by the presence of at least minor amounts of dissolved oxygen. Although our analysis cannot constrain the timescales over which these oxygen incursions may have occurred, the documentation of glauconite *in-situ* as early pore filling cements indicate that the oxygen incursions were both rapid and frequent.

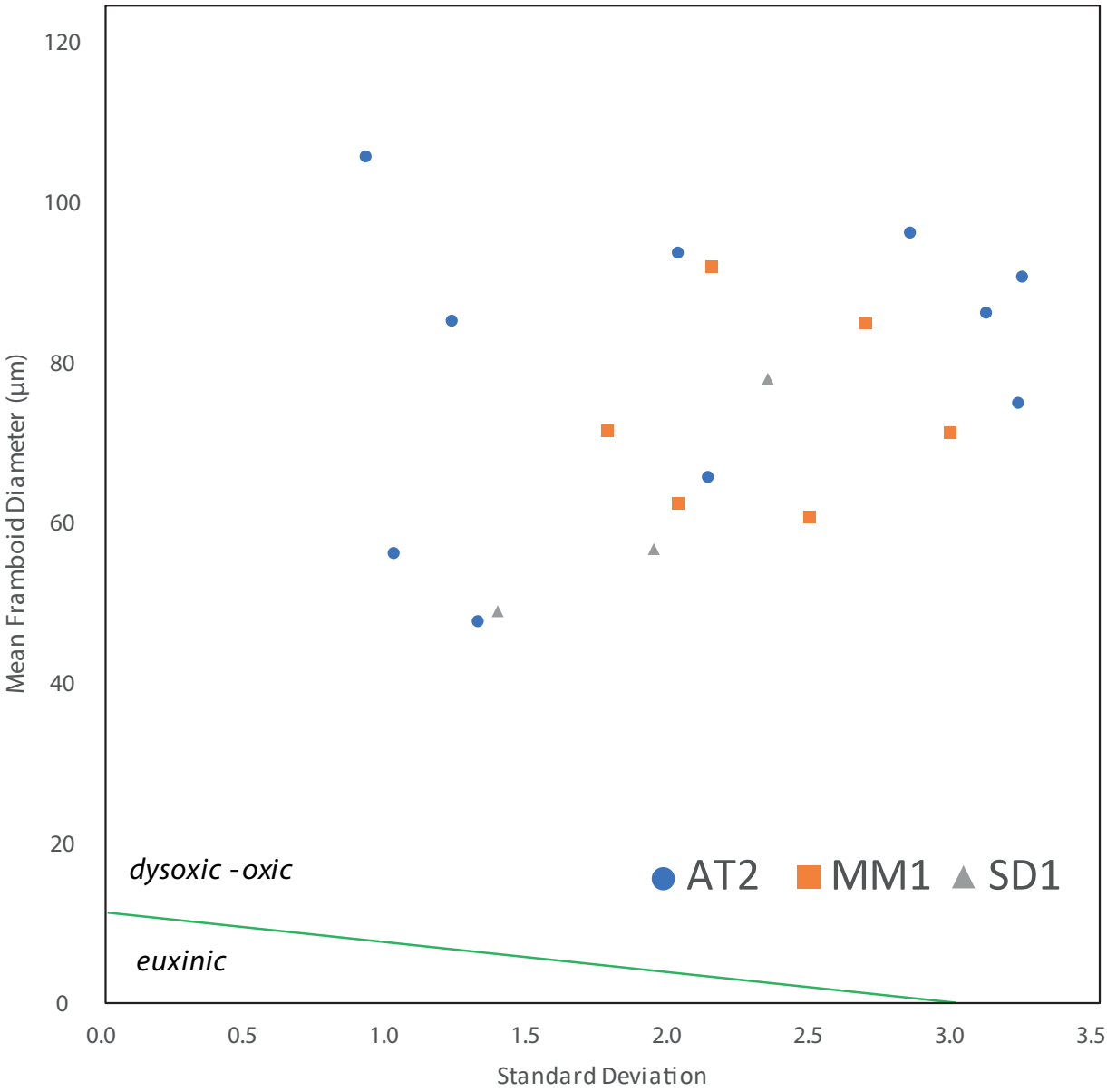

Fig 5: Plot of mean framboid diameter against the standard deviation from mean size of the whole measured framboid population for three of the studied cores. Framboids from the Velkerri formation clearly plot well outside the euxinic field indicating formation in dysoxic to oxic waters.

Fe-sulphide mineralogy and micro-textures

Framboidal pyrite is found throughout the Velkerri Formation and petrographic textures, such as draping of overlying sediments, indicate they grew at, or just below, the sediment-water interface. Because they are composed of a large number of individual crystals (Rickard, 2012b, 2012a) pyrite framboids reflect chemical conditions where the nucleation rate greatly exceeded the crystal growth rate (Rickard, 2012a). Given thermodynamic and kinetic constraints on pyrite formation mechanisms, these conditions can only be met with excessive supersaturation (Rickard, 2012a). As a consequence, pyrite framboids may initially form in the water column, or in sediments as a product of early diagenesis (Rickard, 2012a; Wilkin et al., 1996). A number of studies have

shown that framboid formation in the water column produces a statistically distinct size population compared to framboids formed within sediments (Rickard, 2012a; Wilkin et al., 1996). Because framboid size generally correlates with residence times near the oxic-anoxic boundary (where pyrite supersaturation is typically highest; Rickard, 2012a), larger framboid diameters generally reflect prolonged exposure to chemical conditions favourable for pyrite nucleation and growth in a stratified water column (Rickard, 2012a; Wilkin et al., 1996). However, because pyrite clusters nucleated within the water column are hydrodynamically unstable and susceptible to rapid sinking, framboids generated in the water column are far smaller in diameter than early diagenetic framboids and are deposited as a suspension rain, forming discrete laminae in the sediment (Rickard, 2012a; Wilkin et al., 1996). Once framboids formed within the water column reach the sediment, they may act as sites for further nucleation and crystal growth and, as such, are commonly associated with overgrowths and/or infillings of octahedral microcrystals, massive pyrite, and/or acicular pyrite or marcasite (see Figure 13D, E & Efrom Wei et al., 2015, and Figure 4 from Wei et al., 2012 for examples of framboid overgrowth and infilling; Wilkin et al., 1996).

Pyrite framboids in the Velkerri Formation are significantly larger than published sizes for water column-borne framboids (Figure 5), and are not associated with discrete framboid rich laminae, or overgrowths, leading to the conclusion that they are principally a product of authigenesis at the sediment-water interface. A synsedimentary to early diagenetic origin for Velkerri framboids is further supported by petrographic evidence, including the observation of sediments draping pyrite framboids. The draping texture is distinct from the compression of laminae which has occurred below pyrite framboids during sediment compaction (Figure 4C). I interpret such draping relationships to be result of micro-topography produced as framboids grew at the sediment-water interface. Furthermore, extensive and detailed analysis of 661 framboids in the Velkerri Formation indicated that no framboids featured signs of later diagenetic alteration such as overgrowth or infilling by subsequent generations of pyrite (*cf* those in Wei et al., 2015, 2012).

Our data indicate that $H_2S(aq)$ was rarely present in the water column, but more commonly present within sediment pore waters. On the other hand, Fe-silicate sedimentology indicates that O_2 was frequently present within the water column and sometimes within sediment pore waters. A consideration of chemical factors influencing Fe-sulphide supersaturation indicates that these two observations are compatible with one another. Experimental geochemistry and sedimentology together provide evidence that oxidants such as $O_2(aq)$, dissolved polysulphides, or elemental sulphur may enhance the formation of Fe-sulphide (i.e., pyrite or other metastable Fe-sulphide phases), and in particular Fe-sulphide framboids (Ohfuji and Rickard, 2005). One possibility may

be through the effects of oxidants on pyrite precipitation rate. For example, at the redox interface $O_2(aq)$ may oxidise $H_2S(aq)$ to form elemental sulphur (S^0) which in turn reacts with H_2S to form polysulphides that drastically increase the rate of pyrite formation (Thiel et al., 2019). Together this indicates that pyrite framboids formed at the diffusional interface between $O_2(aq)$ and $H_2S(aq)$, which micro-textural data indicate was situated close to the sediment-water interface.

Phosphate Availability and CFA spheres

The emerging picture of sedimentary redox conditions provided by Fe-silicate and Fe-sulphide minerals also provides insight into the generation of carbonate-fluorapatite (CFA) spheres. Authigenic to early diagenetic CFA spheres with similar morphology and composition have been identified in organic, phosphatic and silica-rich sediments spanning a broad age range (Bailey et al., 2013; Cosmidis et al., 2013; Cui et al., 2020; Schieber et al., 2007). Many of these occurrences have been interpreted to reflect the phosphatisation of bacteria either as a response to metabolic processes or upon death (Cosmidis et al., 2013; Cui et al., 2020; Schieber et al., 2007). Some modern to recent sediments show that phosphatised bacteria are common in depositional environments featuring $H_2S(aq)$, which in turn stimulates the growth of chemolithotrophic sulphide-oxidising bacteria (Bailey et al., 2013). Although not exclusive to this general metabolic process, sulphide oxidisers are known to accumulate intracellular polyphosphate which is subsequently hydrolysed, in turn producing a rapid local increase in dissolved PO_4 which may precipitate Ca-phosphate (Cosmidis et al., 2013; Schulz and Schulz, 2005). Large conspicuous vacuolated bacteria such as *Thiomargarita sp.*, *Beggiatoa sp*. and *Thioploca sp,* often become mineralised by Ca-phosphate during this process, leaving behind similar spherical apatite forms in the rock record (Brock and Schulz-Vogt, 2011; Cosmidis et al., 2013; Keighley et al.,2018, Schulz and Jørgensen, 2015; Schulz and Schulz, 2005). Although our analysis does not definitively constrain the biogeochemical mechanisms that produced CFA spheres, mineralisation by sulphide oxidising bacteria provides a mechanism consistent with geochemical constraints from Fe-silicates and Fe-sulphides described above. However, a distinct and smaller population of CFA spheres that display granular cores are more likely to be the product of autocatalytic enzymes released by mineralising bacteria after death e.g. *Thiothrix sp* (Cosmidis et al., 2013). On this basis, bio-available P was actively recycled during deposition of the Amungee member in all studied cores, and also within the Kalala and Wyworrie members where poorly preserved CFA spheres have been identified.

4.4.5 Merging micro-textural and mineralogical constraints on redox with geochemical proxy data

The mineralogical and micro-textural data presented here provide detailed insight into water column and diagenetic redox conditions during deposition of the Velkerri Formation. Integrating this information with geochemical proxy data provides important context for understanding the preservation of redox signals in ancient sedimentary rocks. For instance, a number of studies report Fe-speciation data from the Velkerri Formation, a widely used proxy for diagnosing bottom water redox state (Nguyen et al., 2019). Specifically, higher proportions of pyrite-associated Fe were observed through the Amungee member (in cores Urapunga-4 and -5; Amoco 82/3; Golden Grove-1, and Altree-2) leading to the interpretation that a euxinic water column was present during this interval (Nguyen et al., 2019). Recent work has also interpreted the Kalala and Wyworrie members to reflect oxic and oxic/ferruginous conditions, respectively (Cox et al., 2016; Jarrett et al., 2019; Nguyen et al., 2019). This inference was made on the basis of the proportion of highly reactive iron (FeHR) relative to total Fe which was either below (i.e., oxic) or above (i.e., ferruginous) a reference point calibrated for fine-grained siliciclastics (Poulton and Canfield, 2005).

In addition to Fe-speciation, previous studies of the Velkerri Formation have also interpreted the degree of pyritization, $S_{pyrite}/C_{organic}$, $\delta^{34}S$ pyrite and various metal isotope data (Arnold et al., 2004; Jackson et al., 1991) to reflect deposition under euxinic conditions; this evidence is largely confined to the Amungee member. In all cases, these geochemical data were extracted from bulk rock, or bulk pyrite preparations without detailed petrographic analysis.

Our data indicate that Fe-silicates and pyrite account for the overwhelming proportion of bulk Fe contained within Velkerri Formation sedimentary rocks (Figure 2). From the standpoint of Fe-speciation, iron silicate minerals would be included within the poorly reactive and unreactive iron phase, along with detrital iron minerals, since Fe extraction from silicate phases is relatively inefficient and dependent on mineralogical characteristics (Slotznick et al., 2020). Therefore, a high proportion of authigenic Fe-silicate minerals can potentially decrease FeHR/FeT values, resulting in a false “oxic” signal. Consistent with this expectation, the Velkerri Formation exhibits persistently high Fe/Al ratios, further indicating that Fe-silicates may play a dominant role in obscuring the interpretation of bulk Fe-speciation data. In addition, given the pervasive nature of the late diagenetic and hydrothermal pyrite, particularly within the Amungee member, this generation of pyrite is likely to have contributed to bulk geochemical datasets, in particular Fe-speciation, the degree of pyritization, $S_{pyrite}/C_{organic}$, $\delta^{34}S$ pyrite and metal isotope data. As the diagenetic pyrite is difficult to discern from core logs and hand specimens, petrographic screening will be essential to

ensure that future studies are not impacted by the diagenetic pyrite. Subsequently, two studies of Velkerri Formation pyrite in which samples where petrographically screened, also found evidence for increasing intermittenet oxygenation of the RSB during deposition of the Velkerri Formation (Mukherjee et al., 2019; Mukherjee and Large, 2016).

4.4.6 Biomarker evidence of redox conditions

Finally, biomarkers provide additional constraints on paleo-redox conditions. For example, recent work identified the organosulfur biomarker dibenzothiophene in the Amungee Member, which likely reflects the incorporation of H_2S into organic matter (Jarrett et al., 2019). Additionally, Green Sulphur Bacteria (GSB) and Purple Sulphur Bacteria (PSB) biomarkers were present in low but detectable abundances in the Velkerri Formation (Nguyen et al*.,* 2019, Jarrett et al., 2019b). Accordingly, Jarrett et al. (2019b) suggested that either: (1) euxinia may have been restricted to a deep-water layer below the photic zone, (2) photic zone euxinia was in fact present, but only intermittently or was otherwise spatially heterogeneous, and/or (3) that these biomarker data reflect the degradation of aromatic carotenoid derivatives in intermittently oxygenated waters. The signature of phototrophic sulphur bacteria in the Velkerri depositional system, and the role of intermittent oxygen exposure in biomarker degradation carry significant consequences for paleo-environmental interpretation of the Velkerri Formation.

4.4.7 Did benthic microbial mats influence Velkerri Formation sedimentation and redox history?

Combining new micro-textural, mineralogical, and sedimentological constraints with available geochemical data yields three principal lines of evidence that microbial mat communities influenced the sedimentation and redox history of the Velkerri Formation. First, geochemical and textural relationships between Fe-silicates, Fe-sulphides, and Ca-phosphates strongly support the existence of dynamic chemical gradients positioned close to the sediment-water interface. Specifically, these data suggest that $H_2S(aq)$ was provided within sedimentary pore waters by sulphur reducing bacteria, and that $O_2(aq)$ diffused and likely interacted with this component to sustain supersaturation necessary for framboid development. This chemical micro-environment would have provided an ecological opportunity for sulphur oxidising bacteria, consistent with known mechanisms of phosphatisation.

Second, available data indicate that new biomarker constraints from the Velkerri Formation are, in fact, consistent with the presence of photosynthetic mats at the sediment-water interface (*cf* French et al., 2014). GSB and PSB biomarkers have been reported from estuarine and lacustrine photosynthetic benthic mats with mixed trophic communities (Brocks and Schaeffer, 2008; Caumette et al., 2004; French et al., 2014; Herbert and Welsh, 1994; Hubas et al., 2013; Meyer et al., 2011). These mat systems feature GSB and PSB as minor components of the overall community which live in low abundances at the mat-sediment interface (Brocks and Schaeffer, 2008; Wahlund et al., 1991). As a consequence, GSB and PSB biomarkers are either absent or are just above detection limits in these environments, as observed for the Velkerri Formation (Jarrett et al., 2019; Nguyen et al., 2019; Shen et al., 2020). In addition, the frequent and rapid introduction of $O_2(aq)$ either from cyanobacterial communities or from bottom waters, may have played an important role in degrading GSB- and PSB- specific biomarkers (Pawlowska et al., 2013).

Finally, I observe sedimentary structures consistent with benthic microbial mats across all cores examined in this study (e.g., Figure 4B this chapter, and Figure 7E, F, & I, Chapter 2). These structures: (1) display evidence for adhesion of sediments beyond spatial scales attributed to flocculation, (2) show sediments bound in tension or compression due to an elastic binding agent, (3) exhibit sedimentary grains and beds that are stable beyond the angle of repose, and (4) preserve evidence of syndepositional growth and regrowth following erosive damage (Figure 7E, F, & I, Chapter 2 this thesis, Hubas et al., 2013; Schieber et al., 2007). In addition, clay-rich sediments often exhibit thrombolitic textures where clots of Fe-clays are infilled by coatings of wrinkled organic matter and detrital grains. At the micron scale, the accumulation of finely laminated organic matter appears to have kept pace with authigenic grain growth (e.g., Figure 4B where organic-rich lamina development shifts in apparent response to framboid growth within in the sediments). Many of these structures have been documented in other clastic rocks (particularly those rich in clay) which authors have similarly ascribed to strong microbial influences (Schieber et al., 2007). The frequent occurrence of these features through the stratigraphy in all studied cores leads to the conclusion that benthic microbial mats were a common feature during deposition of much of the Velkerri Formation.

The influence of benthic microbial mat communities during deposition carries significant implications for water depth and the interpretation of paleo-environmental redox in the mid-Proterozoic. For instance, the confinement of free $H_2S(aq)$ to sediment pore waters, combined with the presence of mat-dwelling phototrophic sulphur bacteria, implies that at least some of the Velkerri Formation must have been deposited within the photic zone. The inference of a relatively shallow

Velkerri sea floor is supported by sedimentological and sequence stratigraphic data in Chapter 2 of this thesis. Additionally, mixed community microbial mats may have exerted a strong control over the redox chemistry of the sediment pore and bottom waters, complicating interpretations of global or even regional marine chemistry, and in particular, early eukaryotic evolution through this interval.

4.4.9 Implications for eukaryote evolution in the mid-Proterozoic

Given that the Velkerri Formation hosts well-preserved and well-studied eukaryotic microfossil assemblages, our data indicate that the environmental and/or ecological factors responsible for abundance and diversity patterns may need to be re-evaluated. Eukaryotic microfossils in the RSB appear to show a trend of decreasing abundance and diversity with distance from paleoshoreline and, by extension, increasing water depth (Figure 2, Chapter 1 this thesis, Javaux and Knoll, 2017). This trend has previously been attributed to decreasing levels of dissolved O_2 and nutrients derived from continental runoff, combined with increasing $H_2S(aq)$ levels associated with offshore settings. However, our data imply that P was actively recycled during and shortly after sediment deposition and may not have been biologically limiting, even though ferruginous conditions appear to have been common and extensive. This observation is consistent with Fe(II)-silicate and CFA authigenesis within the overlying Sherwin Ironstone (Johnson et al., 2020). At the same time, I find little to no evidence from offshore settings supporting free $H_2S(aq)$ in the water column.

Nevertheless, the limitation of other bio-essential nutrients, such an N, may have played a more important role in the palaeo-environmental distribution of mid-Proterozoic eukaryotes (Anbar and Knoll, 2002; Koehler et al., 2017). Multiple studies have shown that the RSB may have been characterised by N-limitation during Velkerri deposition, which was apparently more pronounced further from the paleocoast (Cox et al., 2019; Koehler et al., 2017). Given that eukaryotic microfossils mirror this trend, bioavailable nitrogen may have been maximised in oxygenated near-shore settings (Koehler et al., 2017). In addition, rapid redox oscillations have been shown to remove N from the water column and can strip N directly from modern eukaryotic cell membranes, and experiments show that redox oscillations promote denitrification and the release of inorganic N (Gilbert et al., 2016). Thus, the environmental distribution of early eukaryotes in the RSB may have been strongly linked to spatial and temporal variations in dissolved $O_2(aq)$, which can be faithfully recorded by authigenic mineral textures.

Additionally, recent work has shown that eukaryote biomarker concentrations can be reduced by up to 98% between the surface and interior of microbial mats, even in environments characterised by abundant eukaryotes (Shen et al., 2020). These processes result in sediments that contain lower abundances of both well preserved organic walled eukaryote fossils and eukaryote biomarkers (Shen et al., 2020). Such taphonomic filtering may in fact reconcile a number of distinctive characteristics of the pre-Ediacaran biomarker record (Pawlowska et al., 2013), but as a consequence, skew our current understanding of Proterozoic eukaryotic evolution.

4.5 Conclusions

The sedimentological, mineralogical and micro-textural data presented here provide new and detailed constraints on redox and nutrient dynamics within a critical interval of Earth history. Sediments in the Velkerri Formation reflect dominantly ferruginous pore or bottom waters that were frequently oxygenated. $H_2S(aq)$, though commonly present, was restricted to sediment pore waters. At the broadest scale, our data complicate the relationships between Velkerri sediments, the open ocean, and atmospheric O_2. Our analysis, in combination with available geochemical data, indicate that much of the Velkerri may have been deposited within the photic zone, where benthic microbial mats undoubtedly obscured the connection between sediments and the atmosphere. Nevertheless, epicratonic basins such as the RSB dominate much of the Mesoproterozoic sedimentary record, and so only by continuing to build a mineralogically-calibrated picture of redox dynamics can we begin to assess to what degree non-actualistic sedimentary environments faithfully archive ocean-atmosphere redox history and the patterns of early eukaryotic evolution.

4.6 References

Abbott, S.T., Sweet, I.P., 2000. Tectonic control on third-order sequences in a siliciclastic ramp-style basin: An example from the Roper Superbasin (Mesoproterozoic), northern Australia. Aust. J. Earth Sci. 47, 637–657. https://doi.org/10.1046/j.1440-0952.2000.00795.x

Anbar, A.D., Knoll, A.H., 2002. Proterozoic ocean chemistry and evolution: A bioinorganic bridge? Science 297, 1137–1142. https://doi.org/10.1126/science.1069651

Anderson, R.P., Tosca, N.J., Gaines, R.R., Mongiardino Koch, N., Briggs, D.E.G., 2018. A mineralogical signature for Burgess Shale–type fossilization. Geology 46, 347–350. https://doi.org/10.1130/G39941.1

Arnold, G.L., Anbar, A.D., Barling, J., Lyons, T.W., 2004. Molybdenum Isotope Evidence for Widespread Anoxia in Mid-Proterozoic Oceans. Science 304, 87–90. https://doi.org/10.1126/science.1091785

Asru K. Chaudhuri (1), S.K. Chanda, 1994. Proterozoic Glauconitic Peloids from South India: Their Origin and Significance. SEPM J. Sediment. Res. Vol. 64A. https://doi.org/10.1306/D4267EB5-2B26-11D7-8648000102C1865D

Bailey, J. V., Corsetti, F.A., Greene, S.E., Crosby, C.H., Liu, P., Orphan, V.J., 2013. Filamentous sulfur bacteria preserved in modern and ancient phosphatic sediments: Implications for the role of oxygen and bacteria in phosphogenesis. Geobiology 11, 397–405. https://doi.org/10.1111/gbi.12046

Baldermann, A., Warr, L.N., Grathoff, G.H., Dietzel, M., 2013a. The rate and mechanism of deep-sea glauconite formation at the Ivory Coast-Ghana Marginal Ridge. Clays Clay Miner. 61, 258–276. https://doi.org/10.1346/CCMN.2013.0610307

Baldermann, A., Warr, L.N., Grathoff, G.H., Dietzel, M., 2013b. The Rate and Mechanism of Deep-Sea Glauconite Formation at the Ivory Coast – Ghana Marginal Ridge. Clays Clay Miner. 61, 258–276. https://doi.org/10.1346/CCMN.2013.0610307

Bayer, U., 1989. Stratigraphic and environmental patterns of ironstone deposits. Geol. Soc. Lond. Spec. Publ. 46, 105–117. https://doi.org/10.1144/GSL.SP.1989.046.01.11

Bhattacharyya, D.P., 1983. Origin of Berthierine in Ironstones. Clays Clay Miner. 31, 173–182. https://doi.org/10.1346/ccmn.1983.0310302

Bodorkos, S., Crowley, J.L., Claoué-Long, J.C., Anderson, J.R., Jr, C.W.M., 2021. Precise U–Pb baddeleyite dating of the Derim Derim Dolerite, McArthur Basin, Northern Territory: old and new SHRIMP and ID-TIMS constraints. Aust. J. Earth Sci. 68, 36–50. https://doi.org/10.1080/08120099.2020.1749929

Brasier, M.D., 1980. The Lower Cambrian transgression and glauconite-phosphate facies in western Europe. J. Geol. Soc. 137, 695–703. https://doi.org/10.1144/gsjgs.137.6.0695

Brock, J., Schulz-Vogt, H.N., 2011. Sulfide induces phosphate release from polyphosphate in cultures of a marine Beggiatoa strain. ISME J. 5, 497–506. https://doi.org/10.1038/ismej.2010.135

Brocks, J.J., Jarrett, A.J.M., Sirantoine, E., Hallmann, C., Hoshino, Y., Liyanage, T., 2017. The rise of algae in Cryogenian oceans and the emergence of animals. Nature 548, 578–581. https://doi.org/10.1038/nature23457

Brocks, J.J., Nettersheim, B.J., 2020. Lost world of complex life: Molecular traces of our deep eukaryotic ancestors [WWW Document]. URL https://goldschmidtabstracts.info/abstracts/abstractView?doi=10.46427/gold2020.263 (accessed 7.15.21).

Brocks, J.J., Schaeffer, P., 2008. Okenane, a biomarker for purple sulfur bacteria (Chromatiaceae), and other new carotenoid derivatives from the 1640 Ga Barney Creek Formation. Geochim. Cosmo-

chim. Acta 72, 1396–1414. https://doi.org/10.1016/j.gca.2007.12.006

Caumette, P., Guyoneaud, R., Imhoff, J.F., Süling, J., Gorlenko, V., 2004. Thiocapsa marina sp. nov., a novel, okenone-containing, purple sulfur bacterium isolated from brackish coastal and marine environments. Int. J. Syst. Evol. Microbiol. 54, 1031–1036. https://doi.org/10.1099/ijs.0.02964-0

Cohen, P.A., Macdonald, F.A., 2015. The Proterozoic Record of Eukaryotes. Paleobiology 41, 610–632. https://doi.org/10.1017/pab.2015.25

Cosmidis, J., Benzerara, K., Menguy, N., Arning, E., 2013. Microscopy evidence of bacterial microfossils in phosphorite crusts of the Peruvian shelf: Implications for phosphogenesis mechanisms. Chem. Geol. 359, 10–22. https://doi.org/10.1016/j.chemgeo.2013.09.009

Cox, G.M., Jarrett, A., Edwards, D., Crockford, P.W., Halverson, G.P., Collins, A.S., Poirier, A., Li, Z.X., 2016. Basin redox and primary productivity within the Mesoproterozoic Roper Seaway. Chem. Geol. 440, 101–114. https://doi.org/10.1016/j.chemgeo.2016.06.025

Cox, G.M., Sansjofre, P., Blades, M.L., Farkas, J., Collins, A.S., 2019. Dynamic interaction between basin redox and the biogeochemical nitrogen cycle in an unconventional Proterozoic petroleum system. Sci. Rep. 9, 5200. https://doi.org/10.1038/s41598-019-40783-4

Cui, L., Liu, W., Zhang, X., 2020. Phosphatized microbial fossils from the lowest Cambrian of South China and their ecological and environmental implications for the Kuanchuanpu biota. Precambrian Res. 338, 105560. https://doi.org/10.1016/j.precamres.2019.105560

Derry, L.A., 2015. Causes and consequences of mid-Proterozoic anoxia. Geophys. Res. Lett. 42, 8538–8546. https://doi.org/10.1002/2015GL065333

Diamond, C.W., Lyons, T.W., 2018. Mid-Proterozoic redox evolution and the possibility of transient oxygenation events 235–245.

Donnelly, T.H., Crick, I.H., 1988. Depositional environment of the middle proterozoic velkerri formation in Northern Australia: Geochemical evidence. Precambrian Res. 42, 165–172. https://doi.org/10.1016/0301-9268(88)90015-0

Doyle, K.A., Poulton, S.W., Newton, R.J., Podkovyrov, V.N., Bekker, A., 2018. Shallow water anoxia in the Mesoproterozoic ocean: Evidence from the Bashkir Meganticlinorium, Southern Urals. Precambrian Res. 317, 196–210. https://doi.org/10.1016/j.precamres.2018.09.001

Fischer, W.W., Hemp, J., Johnson, J.E., 2016. Evolution of Oxygenic Photosynthesis. Annu. Rev. Earth Planet. Sci. 44, 647–683. https://doi.org/10.1146/annurev-earth-060313-054810

Föllmi, K.B., 2016. Sedimentary condensation. Earth-Sci. Rev. 152, 143–180. https://doi.org/10.1016/j.earscirev.2015.11.016

French, K.L., Sepúlveda, J., Trabucho-Alexandre, J., Gröcke, D.R., Summons, R.E., 2014. Organic geochemistry of the early Toarcian oceanic anoxic event in Hawsker Bottoms, Yorkshire, England. Earth Planet. Sci. Lett. 390, 116–127. https://doi.org/10.1016/j.epsl.2013.12.033

Gilbert, F., Hulth, S., Grossi, V., Aller, R.C., 2016. Redox oscillation and benthic nitrogen mineralization within burrowed sediments: An experimental simulation at low frequency. J. Exp. Mar. Biol. Ecol. 482, 75–84. https://doi.org/10.1016/j.jembe.2016.05.003

Hallam, A., Bradshaw, M.J., 1979. Bituminous shales and oolitic ironstones as indicators of transgressions and regressions. J. Geol. Soc. 136, 157–164. https://doi.org/10.1144/gsjgs.136.2.0157

Harder, H., 1980. Syntheses of Glauconite at Surface Temperatures. Clays Clay Miner. 28, 217–222. https://doi.org/10.1346/CCMN.1980.0280308

Harder, H., 1978. Synthesis of Iron Layer Silicate Minerals under Natural Conditions. Clays Clay Miner.

26, 65–72. https://doi.org/10.1346/CCMN.1978.0260108

Herbert, R.A., Welsh, D.T., 1994. Establishment of phototrophic purple sulphur bacteria in microbial mat systems, in: Stal, L.J., Caumette, P. (Eds.), Microbial Mats, NATO ASI Series. Springer, Berlin, Heidelberg, pp. 51–60. https://doi.org/10.1007/978-3-642-78991-5_5

Hornibrook, E.R.C., Longstaffe, F.J., 1996. Berthierine from the Lower Cretaceous Clearwater Formation, Alberta, Canada. Clays Clay Miner. 44, 1–21. https://doi.org/10.1346/CCMN.1996.0440101

Hubas, C., Jesus, B., Ruivo, M., Meziane, T., Thiney, N., Davoult, D., Spilmont, N., Paterson, D.M., Jeanthon, C., 2013. Proliferation of Purple Sulphur Bacteria at the Sediment Surface Affects Intertidal Mat Diversity and Functionality. PLOS ONE 8, e82329. https://doi.org/10.1371/journal.pone.0082329

Huggett, J.M., Cuadros, J., 2010. Glauconite formation in lacustrine/palaeosol sediments, Isle of Wight (Hampshire Basin), UK. Clay Miner. 45, 35–49. https://doi.org/10.1180/claymin.2010.045.1.35

Jackson, Raiswell, R., Jackson, M.J., Raiswell, R., 1991. Sedimentology and carbon-sulphur geochemistry of the Velkerri Formation, a mid-Proterozoic potential oil source in northern Australia. Precambrian Res. 54, 81–108. https://doi.org/10.1016/0301-9268(91)90070-Q

Jarrett, A.J.M., Cox, G.M., Grosjean, E., Boreham, C.J., Edwards, D.S., 2019. Microbial assemblage and palaeoenvironmental reconstruction of the 1 . 38 Ga Velkerri Formation , McArthur Basin , northern Australia 360–380. https://doi.org/10.1111/gbi.12331

Javaux, E.J., Knoll, A.H., 2017. Micropaleontology of the lower Mesoproterozoic Roper Group, Australia, and implications for early eukaryotic evolution. J. Paleontol. 91, 199–229. https://doi.org/10.1017/jpa.2016.124

Johnson, B.R., Tostevin, R., Gopon, P., Wells, J., Robinson, S.A., Tosca, N.J., 2020. Phosphorus burial in ferruginous SiO_2-rich Mesoproterozoic sediments. Geology 48, 92–96. https://doi.org/10.1130/G46824.1

Johnston, D.T., Farquhar, J., Summons, R.E., Shen, Y., Kaufman, A.J., Masterson, A.L., Canfield, D.E., 2008. Sulfur isotope biogeochemistry of the Proterozoic McArthur Basin. Geochim. Cosmochim. Acta 72, 4278–4290. https://doi.org/10.1016/J.GCA.2008.06.004

Kendall, B., Creaser, R.A., Gordon, G.W., Anbar, A.D., 2009a. Re–Os and Mo isotope systematics of black shales from the Middle Proterozoic Velkerri and Wollogorang Formations, McArthur Basin, northern Australia. Geochim. Cosmochim. Acta 73, 2534–2558. https://doi.org/10.1016/j.gca.2009.02.013

Kendall, B., Creaser, R.A., Gordon, G.W., Anbar, A.D., 2009b. Re-Os and Mo isotope systematics of black shales from the Middle Proterozoic Velkerri and Wollogorang Formations, McArthur Basin, northern Australia. Geochim. Cosmochim. Acta 73, 2534–2558. https://doi.org/10.1016/j.gca.2009.02.013

Koehler, M.C., Stüeken, E.E., Kipp, M.A., Buick, R., Knoll, A.H., 2017. Spatial and temporal trends in Precambrian nitrogen cycling: A Mesoproterozoic offshore nitrate minimum. Geochim. Cosmochim. Acta 198, 315–337. https://doi.org/10.1016/j.gca.2016.10.050

Laakso, T.A., Schrag, D.P., 2018. A small marine biosphere in the Proterozoic. Geobiology 161–171. https://doi.org/10.1111/gbi.12323

Logvinenko, N.V., 1982. Origin of glauconite in the recent bottom sediments of the ocean. Sediment. Geol. 31, 43–48. https://doi.org/10.1016/0037-0738(82)90006-9

Martin, R.E., Servais, T., 2020. Did the evolution of the phytoplankton fuel the diversification of the marine biosphere? Lethaia 53, 5–31. https://doi.org/10.1111/let.12343

Mazlan B. Hj. Madon, 1992. Depositional Setting and Origin of Berthierine Oolitic Ironstones in the Lower Miocene Terengganu Shale, Tenggol Arch, Offshore Peninsular Malaysia. SEPM J. Sediment. Res. Vol. 62. https://doi.org/10.1306/D4267A0A-2B26-11D7-8648000102C1865D

Meyer, K.M., Macalady, J.L., Fulton, J.M., Kump, L.R., Schaperdoth, I., Freeman, K.H., 2011. Carotenoid biomarkers as an imperfect reflection of the anoxygenic phototrophic community in meromictic Fayetteville Green Lake. Geobiology 9, 321–329. https://doi.org/10.1111/j.1472-4669.2011.00285.x

Michalopoulos, P., AIIer, R.C., 1995. Rapid Clay Mineral Formation in Amazon Delta Sediments: Reverse Weathering and Oceanic Elemental Cycles 270, 5.

Michalopoulos, P., Aller, R.C., 2004. Early diagenesis of biogenic silica in the Amazon delta: alteration, authigenic clay formation, and storage. Geochim. Cosmochim. Acta 68, 1061–1085. https://doi.org/10.1016/j.gca.2003.07.018

Mukherjee, I., Large, R.R., 2016. Pyrite trace element chemistry of the Velkerri Formation, Roper Group, McArthur Basin: Evidence for atmospheric oxygenation during the Boring Billion. Precambrian Res. 281, 13–26. https://doi.org/10.1016/j.precamres.2016.05.003

Mukherjee, I., Large, R.R., Bull, S., Gregory, D.G., Stepanov, A.S., Ávila, J., Ireland, T.R., Corkrey, R., 2019. Pyrite trace-element and sulfur isotope geochemistry of paleo-mesoproterozoic McArthur Basin: Proxy for oxidative weathering. Am. Mineral. 104, 1256–1272. https://doi.org/10.2138/am-2019-6873

Munson, T J, 2016. NO RTH E R N TE R R ITO RY G EO LOG I CA L SURV E Y NTGS RECORD 2016-003 Sedimentary characterisation of the Wilton package , greater McArthur Basin , Northern Territory.

Munson, T. J, 2016. Sedimentary characterisation of the Wilton package, greater MacArthur Basin, Northern Territory. Northern Territory Geological Survey.

Munson, T.J., Revie, D.J., 2018. NO RTH E R N TE R R ITO RY G EO LOG I CA L SURV E Y NTGS RECORD 2018-006 Stratigraphic subdivision of the Velkerri Formation , Roper Group , McArthur Basin , Northern Territory.

Nguyen, K., Love, G.D., Lyons, T.W., Zumberge, J.A., Kelly, A.E., Owens, J.D., Rohrssen, M.K., Bates, S.M., Cai, C., 2019. Absence of biomarker evidence for early eukaryotic life from the Mesoproterozoic Roper Group : Searching across a marine redox gradient in mid- Proterozoic habitability 247–260. https://doi.org/10.1111/gbi.12329

Odin, G.S., 1990. Clay mineral formation at the continent-ocean boundary: the verdine facies. Clay Miner. 25, 477–483. https://doi.org/10.1180/claymin.1990.025.4.06

Ohfuji, H., Rickard, D., 2005. Experimental syntheses of framboids - A review. Earth-Sci. Rev. 71, 147–170. https://doi.org/10.1016/j.earscirev.2005.02.001

Pawlowska, M.M., Butterfield, N.J., Brocks, J.J., 2013. Lipid taphonomy in the Proterozoic and the effect of microbial mats on biomarker preservation. Geology 41, 103–106. https://doi.org/10.1130/G33525.1

Porter, S.M., Agić, H., Riedman, L.A., 2018. Anoxic ecosystems and early eukaryotes. Emerg. Top. Life Sci. 2, ETLS20170162. https://doi.org/10.1042/ETLS20170162

Poulton, S.W., Canfeld, D.E., 2011. Ferruginous conditions: A dominant feature of the ocean through Earth's history. Elements 7, 107–112. https://doi.org/10.2113/gselements.7.2.107

Poulton, S.W., Canfield, D.E., 2005. Development of a sequential extraction procedure for iron: Implications for iron partitioning in continentally derived particulates. Chem. Geol. 214, 209–221.

https://doi.org/10.1016/j.chemgeo.2004.09.003

Pufahl, P.K., Grimm, K.A., 2003. Coated phosphate grains: Proxy for physical, chemical, and ecological changes in seawater. Geology 31, 801–804. https://doi.org/10.1130/G19658.1

Pufahl, P.K., Squires, A.D., Murphy, J.B., Quesada, C., Lokier, S.W., Álvaro, J.J., Hatch, J., 2020. Ordovician ironstone of the Iberian margin: Coastal upwelling, ocean anoxia and Palaeozoic biodiversity. Depositional Rec. 6, 581–604. https://doi.org/10.1002/dep2.113

Rickard, D., 2012a. Sedimentary Pyrite, Developments in Sedimentology. https://doi.org/10.1016/B978-0-444-52989-3.00006-4

Rickard, D., 2012b. Sulfidic Sediments and Sedimentary Rocks, Developments in Sedimentology. https://doi.org/10.1016/B978-0-444-52989-3.00017-9

Schieber, J., Bose, P., Eriksson, P.G., Banerjee, S., Sarkar, S.A., Wladyslaw Catuneanu, O., 2007. Atlas of Microbial Mat Features Preserved within the Siliciclastic Rock Record, 2nd ed. Elsevier.

Schulz, H.N., Jørgensen, B.B., 2015. Thiomargarita, in: Bergey's Manual of Systematics of Archaea and Bacteria. American Cancer Society, pp. 1–3. https://doi.org/10.1002/9781118960608.gbm01226

Schulz, H.N., Schulz, H.D., 2005. Large Sulfur Bacteria and the Formation of Phosphorite. Science 307, 416–418. https://doi.org/10.1126/science.1103096

Shen, Y., Thiel, V., Suarez-Gonzalez, P., W Rampen, S., Reitner, J., 2020. Sterol preservation in hypersaline microbial mats. Biogeosciences 17, 649–666. https://doi.org/10.5194/bg-17-649-2020

Slotznick, S.P., Sperling, E.A., Tosca, N.J., Miller, A.J., Clayton, K.E., van Helmond, N.A.G.M., Slomp, C.P., Swanson-Hysell, N.L., 2020. Unraveling the Mineralogical Complexity of Sediment Iron Speciation Using Sequential Extractions. Geochem. Geophys. Geosystems 21. https://doi.org/10.1029/2019GC008666

Song, H., Jiang, G., 2019. A pulse of oxygen increase in the early Mesoproterozoic ocean at ca . Earth Planet. Sci. Lett. 527, 115797. https://doi.org/10.1016/j.epsl.2019.115797

Środoń, J., Drits, V.A., McCarty, D.K., Hsieh, J.C.C., Eberl, D.D., 2001. Quantitative X-ray diffraction analysis of clay-bearing rocks from random preparations. Clays Clay Miner. 49, 514–528. https://doi.org/10.1346/CCMN.2001.0490604

Stucki, J.W., 2011. Revue sur les effets des cycles redox du fer sur les propriétés des smectites. Comptes Rendus - Geosci. 343, 199–209. https://doi.org/10.1016/j.crte.2010.10.008

Thiel, J., Byrne, J.M., Kappler, A., Schink, B., Pester, M., 2019. Pyrite formation from FeS and H 2 S is mediated through microbial redox activity. Proc. Natl. Acad. Sci. U. S. A. 116, 6897–6902. https://doi.org/10.1073/pnas.1814412116

Todd, S.E., Pufahl, P.K., Murphy, J.B., Taylor, K.G., 2019. Sedimentology and oceanography of Early Ordovician ironstone, Bell Island, Newfoundland: Ferruginous seawater and upwelling in the Rheic Ocean. Sediment. Geol. 379, 1–15. https://doi.org/10.1016/j.sedgeo.2018.10.007

Trythall, R.J.B., Eccles, C., Molyneux, S.G., Taylor, W.E.G., 1987. Age and controls of ironstone deposition (Ordovician) North Wales. Geol. J. 22, 31–43. https://doi.org/10.1002/gj.3350220505

Van Houten, F.B., Arthur, M.A., 1989. Temporal patterns among Phanerozoic oolitic ironstones and oceanic anoxia. Geol. Soc. Lond. Spec. Publ. 46, 33–49. https://doi.org/10.1144/GSL.SP.1989.046.01.06

Van Houten, F.B., Purucker, M.E., 1984. Glauconitic peloids and chamositic ooids - favorable factors, constraints, and problems. Earth Sci. Rev. 20, 211–243. https://doi.org/10.1016/0012-8252(84)90002-3

Wahlund, T.M., Woese, C.R., Castenholz, R.W., Madigan, M.T., 1991. A thermophilic green sulfur bacterium from New Zealand hot springs, Chlorobium tepidum sp. nov. Arch. Microbiol. 156, 81–90. https://doi.org/10.1007/BF00290978

Wang, H., Zhang, Z., Li, C., Algeo, T.J., Cheng, M., Wang, W., 2020. Spatiotemporal redox heterogeneity and transient marine shelf oxygenation in the Mesoproterozoic ocean. Geochim. Cosmochim. Acta 270, 201–217. https://doi.org/10.1016/j.gca.2019.11.028

Warren, J.K., George, S.C., Hamilton, P.J., Tingate, P., 1998. Proterozoic Source Rocks: Sedimentology and Organic Characteristics of the Velkerri Formation, Northern Territory, Australia. AAPG Bull. 82 (1998). https://doi.org/10.1306/1D9BC435-172D-11D7-8645000102C1865D

Wei, H., Algeo, T.J., Yu, H., Wang, J., Guo, C., Shi, G., 2015. Episodic euxinia in the Changhsingian (late Permian) of South China: Evidence from framboidal pyrite and geochemical data. Sediment. Geol. 319, 78–97. https://doi.org/10.1016/j.sedgeo.2014.11.008

Wei, H., Chen, D., Wang, J., Yu, H., Tucker, M.E., 2012. Organic accumulation in the lower Chihsia Formation (Middle Permian) of South China: Constraints from pyrite morphology and multiple geochemical proxies. Palaeogeogr. Palaeoclimatol. Palaeoecol. 353–355, 73–86. https://doi.org/10.1016/j.palaeo.2012.07.005

Wilkin, R.T., Barnes, H.L., Brantley, S.L., 1996. The size distribution of framboidal pyrite in modern sediments: An indicator of redox conditions. Geochim. Cosmochim. Acta 60, 3897–3912. https://doi.org/10.1016/0016-7037(96)00209-8

Williams, M.E., 2003. The development of hiatal surfaces in the Osmington Mills ironstone member of the upper jurassic ringstead formation of south Dorset, England. Proc. Geol. Assoc. 114, 193–210. https://doi.org/10.1016/S0016-7878(03)80013-5

Yang, B., Collins, A.S., Blades, M.L., Capogreco, N., Payne, J.L., Munson, T.J., Cox, G.M., Glorie, S., 2019. Middle–late Mesoproterozoic tectonic geography of the North Australia Craton: U–Pb and Hf isotopes of detrital zircon grains in the Beetaloo Sub-basin, Northern Territory, Australia. J. Geol. Soc. 176, 771–784. https://doi.org/10.1144/jgs2018-159

5. Discussion and Synthesis

5.1. Introduction

To better understand the environmental conditions inhabited by early eukaryotes, I conducted a combined high-resolution sedimentological, mineralogical and geochemical study of mid-Proterozoic sediments from the Roper Superbasin (RSB), northern Australia. Sediments of the RSB are exquisitely preserved and contain a well-documented suite of acritarchs that are interpreted to be early eukaryotes (Javaux and Knoll, 2002). In addition to the extensive marine sequence, RSB sediments contain previously understudied, contemporaneous paralic and terrestrial sediments. This combination of coeval depositional settings provides a rare glimpse into a broader mid-Proterozoic world, allowing environments that are normally preserved separately to be placed into a regional context.

Geochemical studies of mid-Proterozoic sedimentary successions have previously provided key-hole glimpses of a world interpreted as being polarized between oxygenated surface environments, and deeper marine and aquatic environments that were apparently locked in near total anoxia for close to a billion years (e.g., Arnold et al., 2004). Subsequently, it is this long interval of anoxia that is most often highlighted as a primary cause for the apparent delay in the evolution and diversification of eukaryotes (Knoll, 2014, 1996; Laakso and Schrag, 2014). Oxygen is required for large complex organisms, for both the metabolic advantage of oxygenic respiration, and as a basic unit of organo-molecules for structures such as the cytoskeleton. However, it is the link between oxygen and the cycling of bio-essential elements such as C, Fe and P, that have been the focus of much recent research into how the Proterozoic environment may have impacted early eukaryote evolution (Derry, 2015; Laakso and Schrag, 2018; Planavsky et al., 2010; Reinhard et al., 2020). It is argued that low atmospheric oxygen slowed the release of P from the chemical weathering of continental rocks, thereby lowering net primary productivity and oxygen production by cyanobacteria (Planavsky et al., 2010; Reinhard et al., 2017). The limited volume of oxygen produced was quickly consumed in the re-mineralization of organic carbon and then sequestered into sediments as carbonate, or returned to the atmosphere as CO_2 (Planavsky et al., 2010; Reinhard et al., 2017).

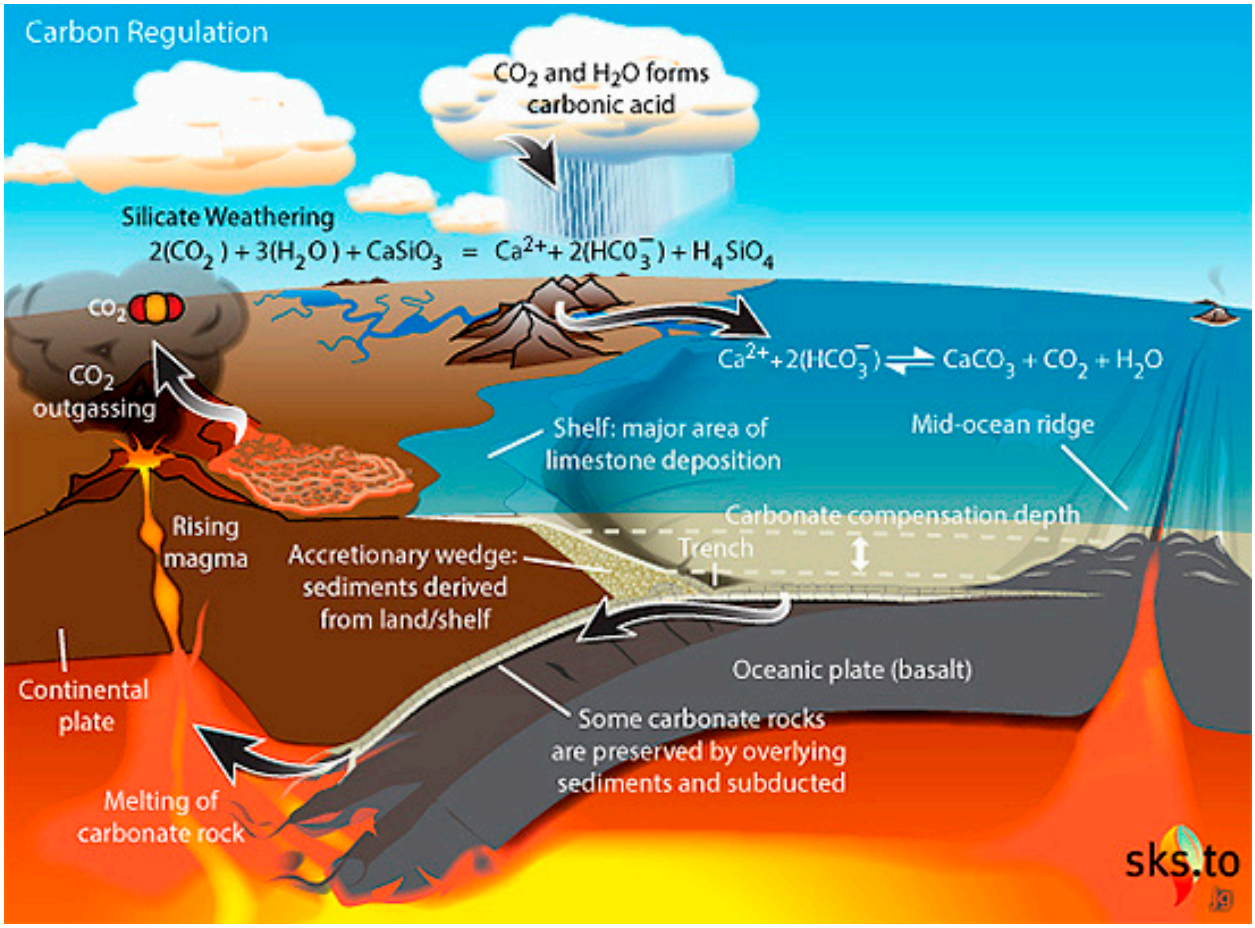

Fig 1A: a schematic of the geological carbon-silicate cycle as it would operate without biology (https://skepticalscience.com/print.php?n=1959)

Similarly, P within the water column released by the decay of organic matter, weathered from rocks, or transported with aeolian dust, was thought to have been sequestered within sediments as Fe-phosphate minerals such as vivianite, after reacting with the abundant Fe^{2+} present in anoxic Proterozoic marine waters (Derry, 2015). Together, this combination of geochemical cycles, all influenced by the paucity of atmospheric and dissolved oxygen, is proposed to have stalled the evolution of early eukaryotic organisms for close to a billion years (Derry, 2015; Laakso and Schrag, 2018; Planavsky et al., 2010; Reinhard et al., 2020).

The hypothesis described above is based on a combination of theoretical modelling, and from geochemical studies of a largely one-dimensional time sequences in the key basins where mid-Proterozoic sedimentary rocks are sufficiently preserved to allow investigation of their depositional environments. Within these basins, thorough sampling may be restricted by outcrop or core material availability. However, results from these relatively small glimpses into local mid-Proterozoic environments are often used as proxies for the global environment across the entire mid-Proterozoic (e.g., Arnold et al., 2004). For example, despite the abundant available drill core containing RSB sedimentary rocks, only a small number of relatively geographically close cores

have been investigated. Each new study of RSB rocks has built on the conclusions of preceding studies, allowing potential inaccuracies or assumptions to perpetuate (for example Table 1, Ch 1, this thesis). Additionally, most previous geochemical work has relied heavily upon analyses of whole rock powders (Arnold et al., 2004; Johnston et al., 2008; Shen et al., 2002). Using this method, it is not possible to distinguish between the influence of primary authigenic phases, and those which may be detrital or diagenetic, and which are therefore not reflective of original depositional environments.

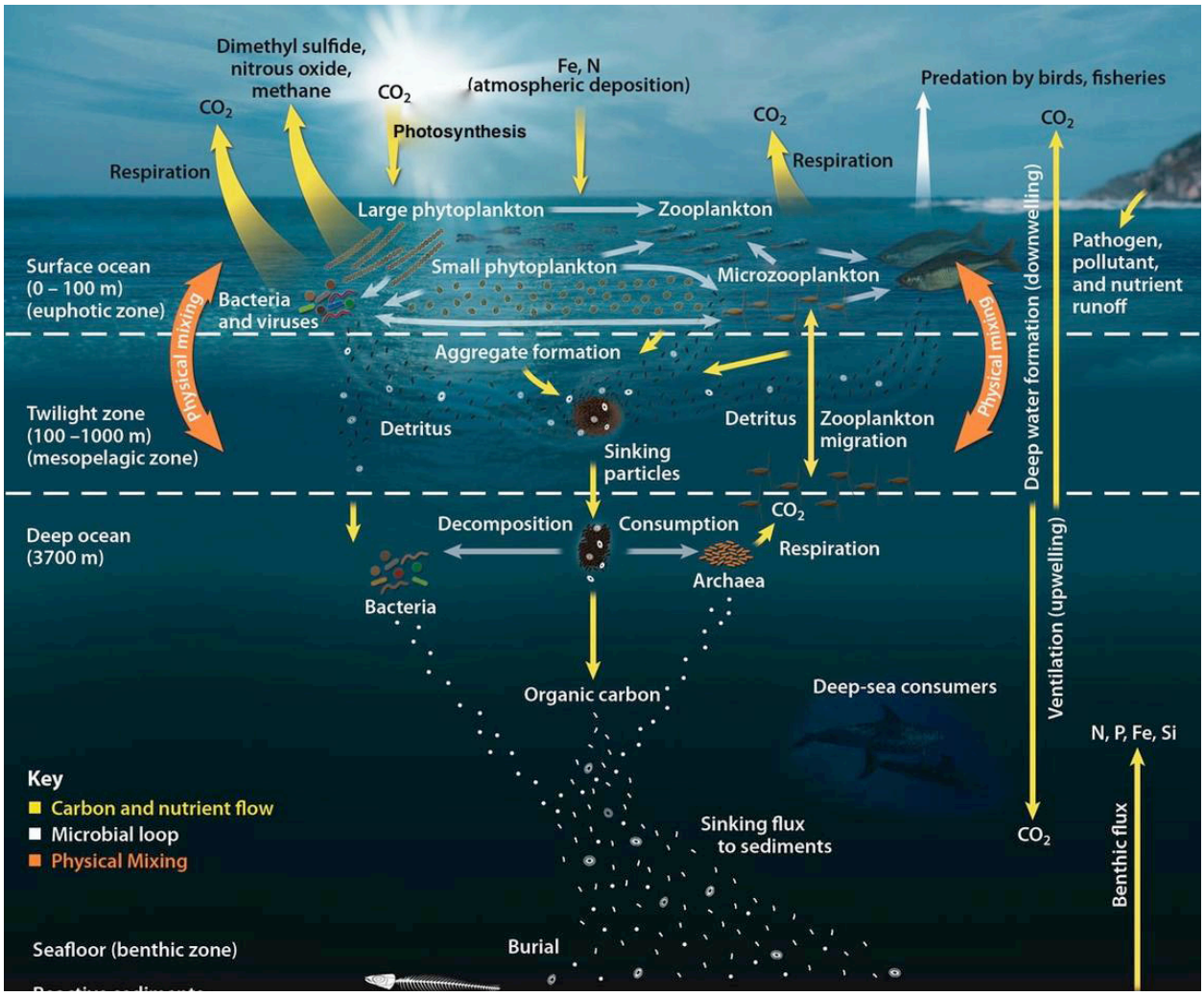

Fig 1B: a schematic of the modern marine carbon cycle (https://serc.carleton.edu/eslabs/carbon/6a.html)

This is a consequence of a lack of detailed petrographic work; where such analyses have been performed, it is not tied into the wider sedimentological, mineralogical, and geochemical context of the depositional environment (e.g., Planavsky et al., 2018). Because of the limitations discussed above, our knowledge of depositional environments within the RSB is incomplete at best and inaccurate or just plain wrong at worst. On this basis, it is impossible to use the RSB as a model for global marine environments during the mid-Proterozoic interval because even localized

environments within the RSB are so poorly understood. However, this is precisely how data from the RSB have been used in previous studies (Arnold et al., 2004; Johnston et al., 2008; Shen et al., 2002). Interpretations of environmental redox and nutrient cycling from the RSB have been applied to the whole of the Earth's surface and used to explain ~1000 Ma of apparent environmental and evolutionary stasis. Data presented in this thesis call into question the early interpretations of depositional environments, sedimentology and mineralogy, that became the foundation of the current interpretations of the RSB. Many of these interpretations, such as deep-water deposition in a euxinic basin for the Velkerri Formation, have not been revisited in the decades since initial publication (Donnelly and Crick, 1988; Jackson et al., 1987; Jackson and Raiswell, 1991). As such, the early studies have formed the basis for much of the work that has followed, work which has far reaching implications for our understanding of mid-Proterozoic life and environments. If these early assumptions and studies are flawed, then so is much of the work on the RSB that has followed, and so too is our understanding of mid-Proterozoic life and environments.

It is not surprising that a single location and time interval, represented by a handful of drill cores, should not accurately reflect wider global or even regional conditions. The modern oceans and shelf seas are known to host a variety of water, sediment, and pore water conditions, some of which can change on seasonal or even shorter timescales. For example, the oxygen structure and biogeochemical cycles of the modern Baltic Sea are not representative of the wider global ocean (Holtermann et al., 2020; Kuliński et al., 2021). The differences are even more profound

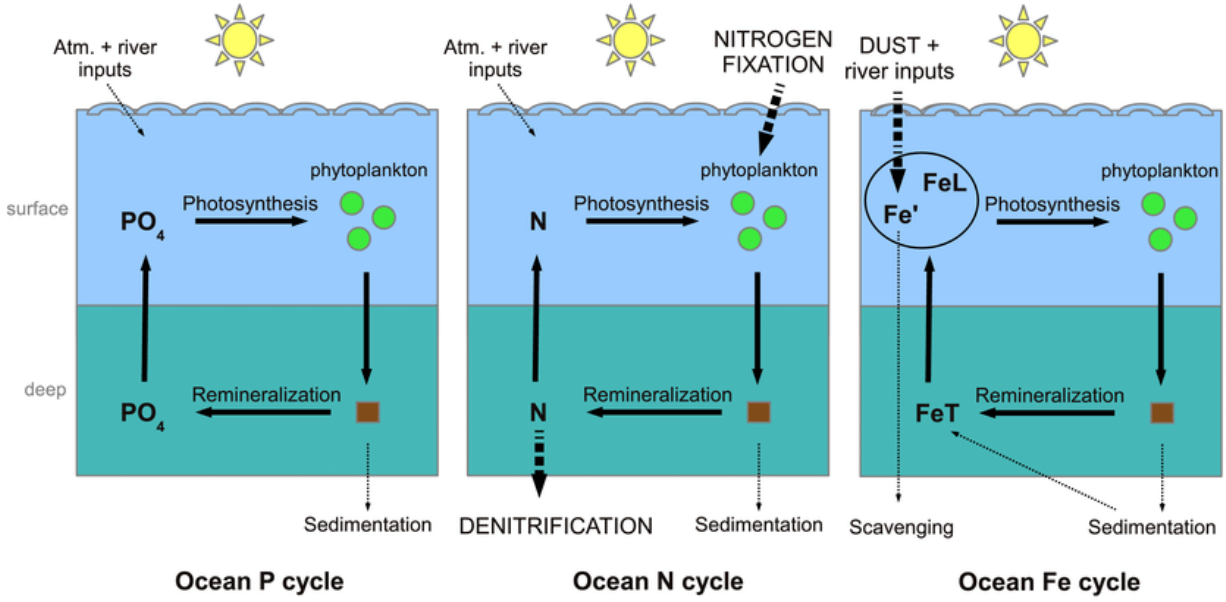

Fig 1C: a schematic of the modern marine phosphorus, nitrogen and iron cycles (https://www.researchgate.net/publication/42539103_Mechanistic_models_of_oceanic_nitrogen_fixation)

when compared to more stratified basins such as the Black Sea (Gomez-Saez et al., 2021; Özsoy and Ünlüata, 1997; Tuğrul et al., 2014) The geochemical variation in these marine basins occurs despite being in contact with an oxygen-rich atmosphere. If such geochemical and environmental heterogeneity exists in modern oceans, why would it not be so in the restricted seas, and oceans of the mid-Proterozoic? If we applied a similarly limited suit of geochemical studies to a handful of sediment cores taken from basins such as the Black Sea, and without wider environmental context, would we also wrongly conclude that the modern global ocean was also euxinic and in contact with an oxygen poor atmosphere?

In Phanerozoic sedimentary successions, geochemical proxies are paired with sedimentological, and paleontological observations that assist with diagnosis of anoxic environments (e.g., Caswell and Coe, 2013). The early Jurassic Mulgrave shale from the Cleveland Basin, northern UK, for example, hosts organic-rich intervals that are geochemically and sedimentologically similar to organic-rich intervals in the Velkerri Formation (Harries and Little, 1999). However, the Mulgrave shale also contains abundant macro- and microfossils that show that finely laminated organic rich,

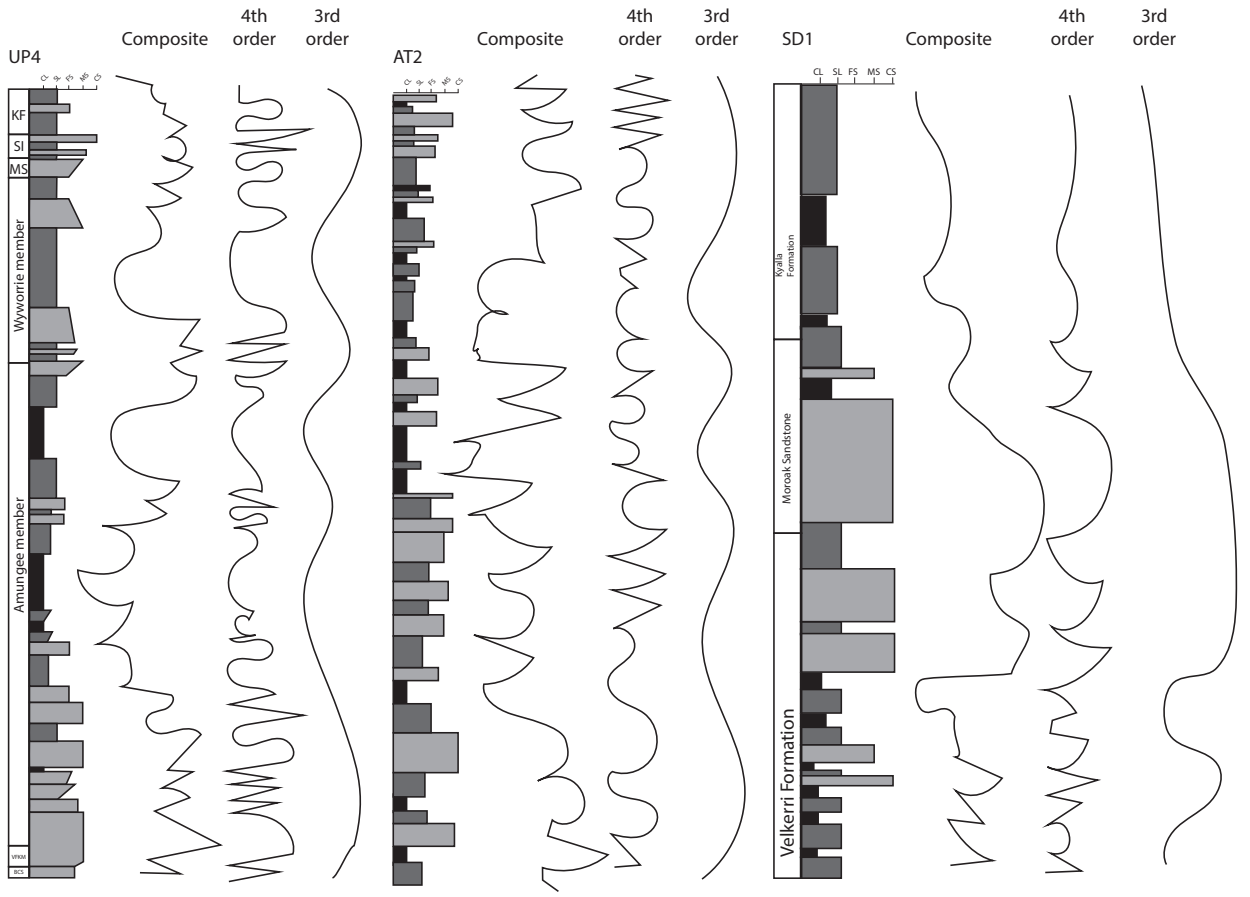

Fig 2: Sketch relative sea level curves for the studied cores from the RSB. the Left side of each curve represents RSL rise, and the right side represents RSL fall, 'impossible' parts of the curve are an artifact of the graphics software.

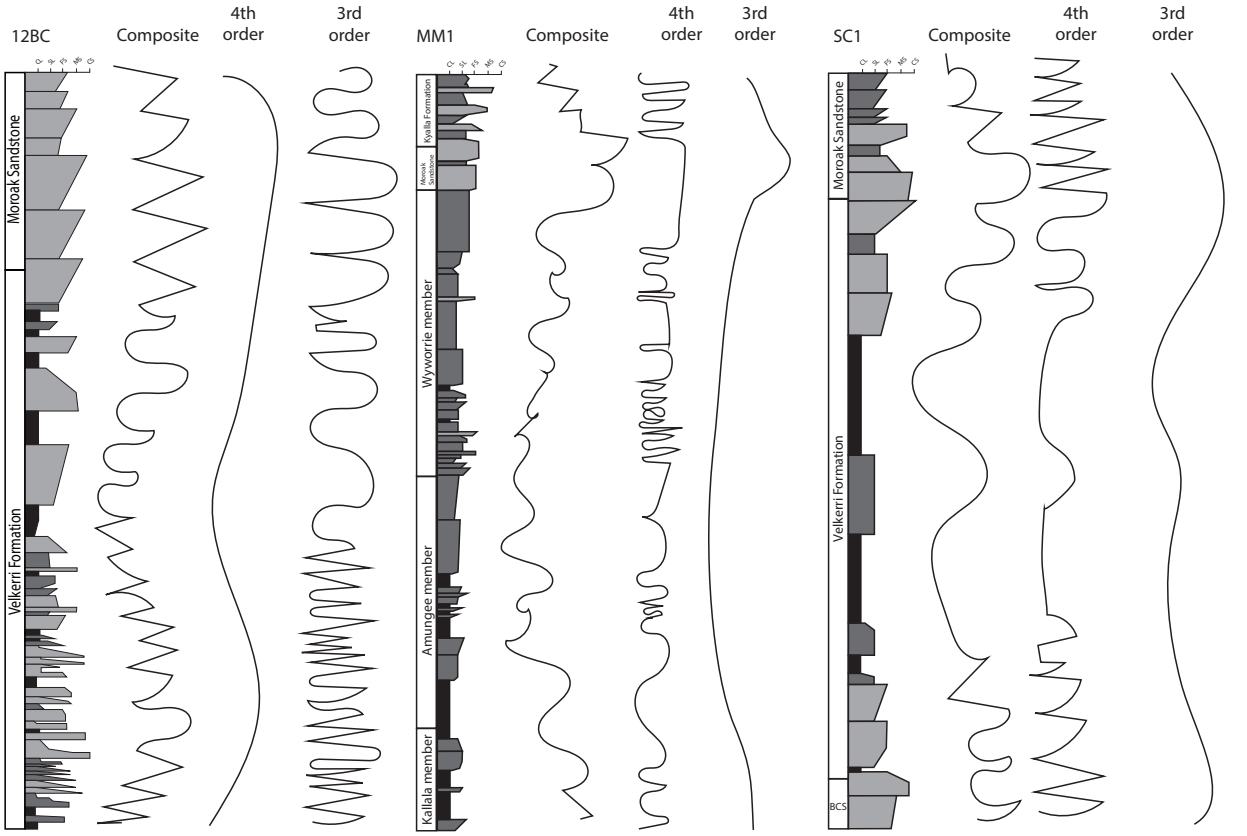

Fig 2 continued: Sketch relative sea level curves for the studied cores from the RSB. the Left side of each curve represents RSL rise, and the right side represents RSL fall, 'impossible' parts of the curve are an artifact of the graphics software.

pyritic mud rocks do not necessarily need to be deposited under euxinic water columns. (Caswell and Coe, 2014). Similarly, even though the Mulgrave shale was deposited during the Toarcian Oceanic Anoxic Event, it is not considered to represent the geochemical state of the global ocean during deposition. The paleogeographic context of the Mulgrave shale indicates the Cleveland Basin was semi restricted, subject to strong local terrestrial input controls, and therefore was not representative of the global ocean during deposition of the Mulgrave shale (Powell, 2010). The validity of the Mulgrave shale in geochemical studies of the TOAE, comes from the fact it can be compared to stratigraphically equivalent successions deposited in different environments world-

wide. This way, local and global geochemical signals can be at least some way differentiated (Hesselbo and Jenkyns, 1995).

Such observational rigour is considered standard when conducting geochemical studies of Phanerozoic sedimentary successions but is hampered by a lack of global stratigraphic correlation in the mid-Proterozoic. Undoubtedly, the lack of diagnostic fossils, and a paucity of well-preserved correlatable successions compared to the Phanerozoic, makes any direct application of these palaeontological and stratigraphic tools difficult to impossible. However, there is still plenty of scope to place specific Proterozoic sedimentary successions within at least a working regional sequence stratigraphic framework, and certainly enough material within each core or outcrop to apply basic petrographic screening. Again, however, these methods appear to be underutilised in Proterozoic paleoenvironmental studies.

Therefore, the present study was conducted to address the current gaps in our knowledge of mid-Proterozoic surface environments.

My primary goals were:

- *Characterize the wider depositional context of the RSB.*
- *Understand how heterogenous depositional environments were across the RSB.*
- *Understand if the RSB was fully marine and if contemporaneous paralic and terrestrial environments survived.*
- *Investigate how accurately bulk powder studies capture environmental redox conditions within the RSB.*
- *Investigate how local redox conditions may have influenced nutrient cycling in the mid-Proterozoic.*

By generating new data sets that combine sedimentology, mineralogy and geochemistry, I have created a new environmental and depositional model for the RSB during deposition of sediments from the upper Roper Group and the co-eval Tijunna and Bullita Groups. My findings in this study are contrast much of the published literature, and place published geochemical data in a new environmental context. As such, my findings suggest that the RSB, and potentially other contemporaneous cratonic basins, are not suitable proxies for the global ocean in the mid-Proterozoic. Yet these data highlight how such basins may have been important components of major geobiological cycles during this interval. Also, I place the RSB into a wider regional setting for the first time and show the environmental heterogeneity between even relatively close localities within the basin.

I correlate contemporaneous marine, paralic and terrestrial sediments from across the basin and begin providing the spatial and temporal resolution missing from many studies of mid-Proterozoic sedimentary successions. Further, my results are synthesized into a model that combines sedimentology, mineralogy and geochemistry, and shows how environments within the RSB change through space and time. Finally, I discuss the wider implications of the new RSB model for both the wider mid-Proterozoic world and for the evolution of early eukaryotic life.

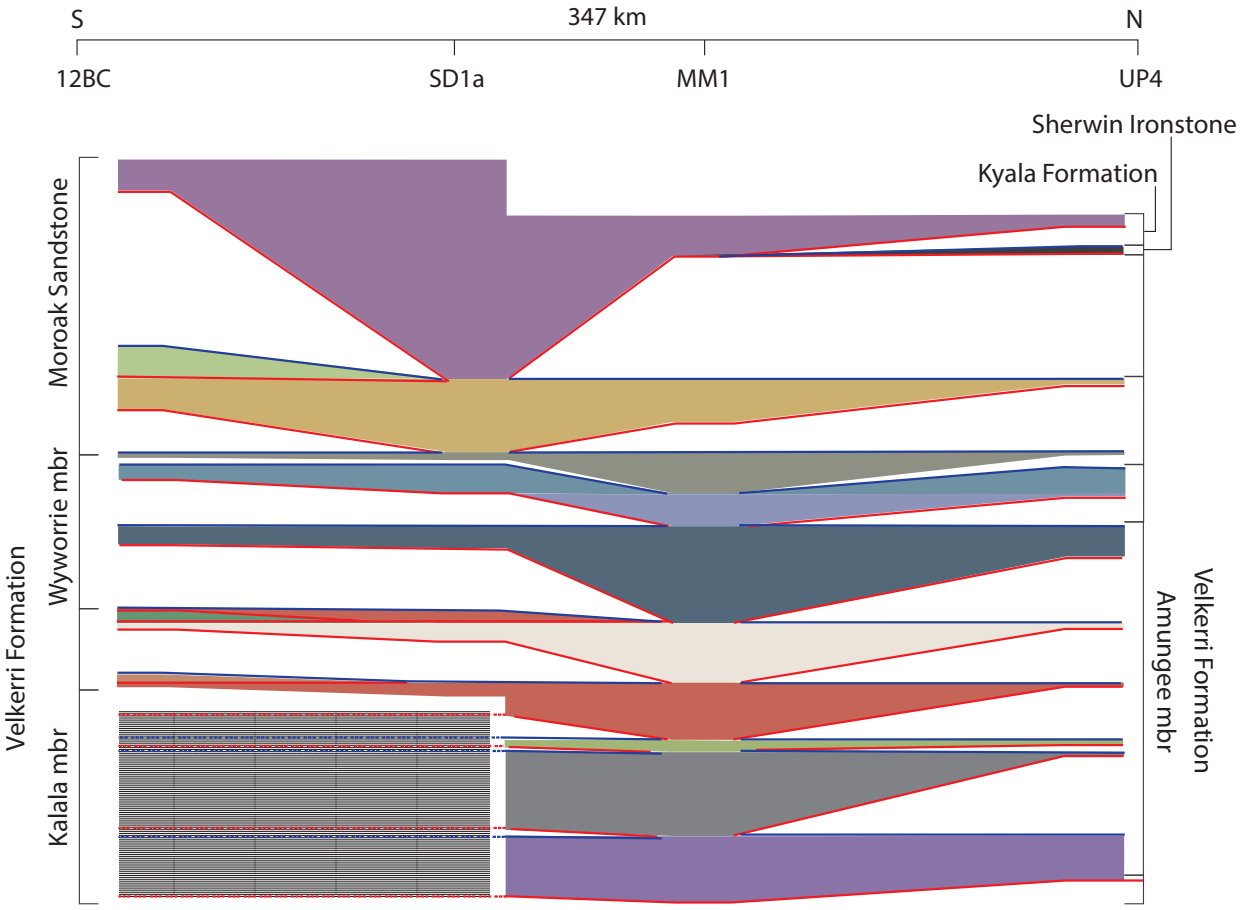

Fig 3: Schematic Wheeler diagram to visualise missing and/or condensed time (white areas) on the north-south transect, coloured polygons represent parasequence sets bound by a lower surface of forced regression red line) and an upper surface of ravinement (or marine erosion, blue line) and based on possible 4th order cycles (Fig 3, Chapter 2), colours are for differentiation only and hold no geological significance, sediments in the shaded area bottom left were not intercepted during drilling, upper surface of top most polygon represents unconformity at the top of the Kyalla Formation.

5.2. A new environmental and depositional model for the Roper Superbasin

Before discussing the specific environments of the RSB and considering their implications, it is important to understand the wider context of the whole basin. Previous models suggested the RSB had a simple ramp-shelf geometry which extended into a deep open ocean shelf (Abbott and Sweet, 2000, Jackson and Raiswell, 1991). I suggest instead that sediments of the RSB were deposited into a bowl-shaped structure surrounded by topographic highs and with limited connection to the open ocean. This model is supported by the following lines of evidence: i) cratonic basins are generally bowl shaped and not ramp-shelves ii) I find evidence for a submerged topographic high at the distal (inferred) oceanward edge of the basin (e.g., Chapter 2 Fig 3 and 9), and iii) heterogenous chemical sedimentation indicating bodies of water with varying chemistry within the basin. Additionally, rather than the simple sheet-like deposition of clastic sediments proposed in previous models, clastic sedimentation within the RSB also appears to be heterogeneous in space and time (Fig 3, Chapter 2). Further, the data presented in this thesis indicate that sedimentation of the studied sequence was not continuous or complete (Fig 3, Chapter 2).

As stated in Chapter 2, the prominent 3rd order RSL changes are overprinted by relatively shorter possibly 4th order changes (Fig 2, and Fig 3, Chapter 2). While these curves are interpretive sketches, they serve to illustrate how the different scales of RSL change interact to produce different composite curves across the basin. For example, contrast the Velkerri Formation portions in the RSL curve of MM1 in the Basinal Region to SC1 in the Distal Region or 12BC in the Proximal Region (Fig 2). This further highlights that the greatest water depths were probably in the Basinal Region, rather than the Distal Region, and shows how deeper waters can mute sedimentary responses to RSL changes relative to shallow waters.

In addition to major erosional breaks such as the forced regression surface between the Moroak Sandstone and Velkerri Formation, there are numerous other indicators of intraformational erosion and condensation through out the studied section. This is summarised approximately in Fig 3 where the extent of missing time can be visualised. However, without greater chronostratigraphic or temporal control, it will be difficult to further quantify the amount of time the upper Roper Group represents, and thus the amount of time missing through erosion or represented by condensation horizons. Fig 4 (below) shows a conjectural sequence of depositional environments based on the facies analysis and distribution described in Chapter 2 (See Table 1, Chapter 2 for details). Formation and member names are used to describe intervals of time during the deposition of those sediments.

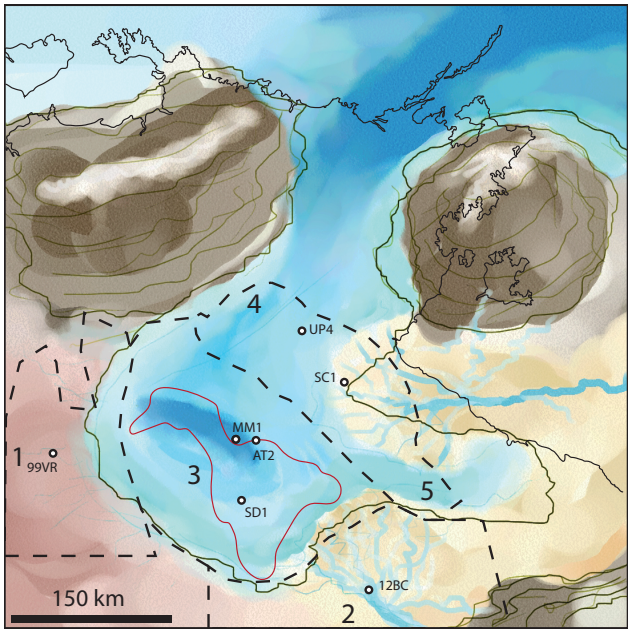

Fig 4: A) Velkerri, earliest Kalala. Brown = orogenic topography, light blue = marine within wave base or fluvial, mid blue = marine within storm wave base, dark blue = marine below storm wave base, yellow = paralic to fluvio-terrestrial, red = regolith terrestrial, green = ferruginous water/sediment

1 = Western Proximal Region, 2 = Southern Proximal Region, 3 = Basinal Region, 4 = Northern Distal Region, 5 = Southern Distal Region.

Core abbreviations as per Table 1 in Chapter 1

Velkerri Formation/Bynoe Formation and Weaner Sandstone

Velkerri, earliest Kalala (Fig 4A).

At the start of this interval, deposition in the Basinal and Distal Regions alternates between the interbedded sands and the interlaminated silts facies of fully marine FA3. The interlaminated silts facies becomes progressively more abundant up section in this region indicating a progressive increase in distance from detrital clastic sediment sources, possibly due to RSL rise. Where the Bessie Creek sandstone is intersected beneath the relatively thinner Velkerri Formation in the Distal Region, it transitions from FA1 Cross stratified sands upwards into FA3 interbedded sands over a few meters. In the Basinal Region, the Bessie Creek sandstone was not intersected beneath the expanded Velkerri Formation. This observation suggests that offshore marine conditions were present in the Basinal Region before the Distal Region and supports the inference that the Distal Region represented a relative topographic high, while the Basinal Region was an area of relatively rapid subsidence.

During this interval deposition in southern Proximal Region alternates between the cross stratified sands, and the interbedded laminated sands facies of the Paralic to Fluvio-Terrestrial FA1, with rare thin occurrences of the interbedded sands facies of FA3 Marine, in thin stacked cycles that decrease in thickness and abundance up section. In the western Proximal Region, this interval is dominated first by the interbedded laminated sands facies, and then by the cross stratified sands facies of FA1. Facies analysis suggests that the cycles seen in the southern Proximal Region indicate that though RSL rise was occurring in this region, it was being outpaced by depositional rates leading to progradation. In contrast, the western Proximal Region experienced fluvial depo-

sition through this interval (the interbedded laminated sands and muds facies) until a transition to the paralic cross stratified sands up section. The two facies are separated by a thin bed of laminated red and green mud which drapes the underlying facies and is eroded by the overlying beds. This facies change could be explained by rapid flooding of a coastal fluvial system, formation of an estuarine environment, and then progradation of a coastline due to slow steady state subsidence during a relatively rapid RSL rise and fall. A different style of subsidence would also help explain the differences observed between the two proximal regions. However, until more data is acquired, this is entirely speculation.

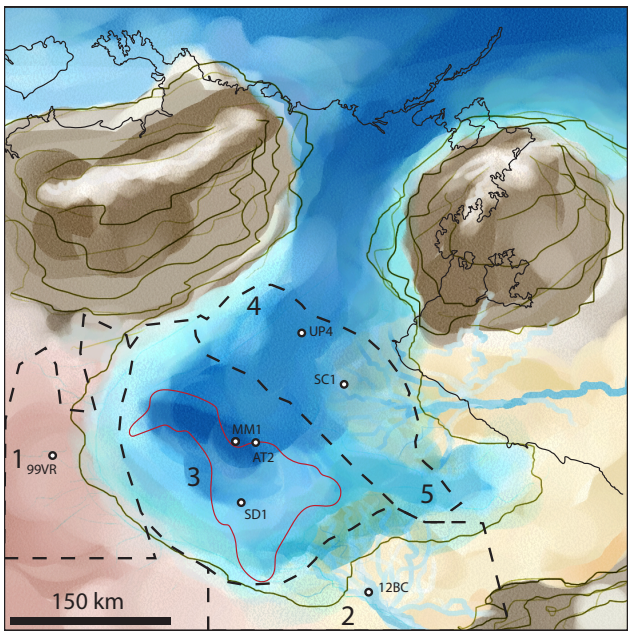

Fig 4: B) Velkerri, middle to late Kalala Brown = orogenic topography, light blue = marine within wave base or fluvial, mid blue = marine within storm wave base, dark blue = marine below storm wave base, yellow = paralic to fluvio-terrestrial, red = regolith terrestrial, green = ferruginous water/sediment

1 = Western Proximal Region, 2 = Southern Proximal Region, 3 = Basinal Region, 4 = Northern Distal Region, 5 = Southern Distal Region.

Core abbreviations as per Table 1 in Chapter 1

Velkerri Formation/Battle Creek Formation

Velkerri, middle to late Kalala (Fig 4B)

During this interval, the interlaminated sands and massive laminated muds facies of FA3 dominate the Distal and Basinal Regions. These facies represent distal depositional environments and indicate that the RSL rise which began in the previous interval is now outpacing sedimentation across these regions. However, the distribution of these facies is heterogenous in time and space across the Distal and Basinal Regions suggesting an interaction between regional and local controls on RSL. Additionally, while fine grained facies dominate the Distal Region, the observation of possible hummocky cross bedding and wave reworking of substrate surfaces, suggests that the dominance of fine grained authigenic clays in the Distal Region, is a consequence of clastic detrital starvation, and not increased water depth. During this interval, the Basinal Region still contains appreciable detrital clastic material that forms into many thin coarsening up cycles, that indicate a

persistent detrital flux and ongoing progradation. Currently available seismic data show a thickening of sedimentary units into the Basinal Region, and a depositional thinning towards the Proximal and Distal Regions. However, the low resolution of available seismic data does not allow differentiation of packages below the formation level of stratigraphy. In the southern Proximal Region, progradation reaches a maximum in the early part of this interval followed by a retrogradational trend as RSL rise begins to outpace sedimentation. The coastline retreats landward leaving an interval of thin fining up cycles similar to those observed in the previous interval, but with FA3 facies that increase in abundance and thickness up section. In the western Proximal Region, the FA1 interbedded sands and muds are draped by FA3 interlaminated silts indicating another episode of rapid flooding.

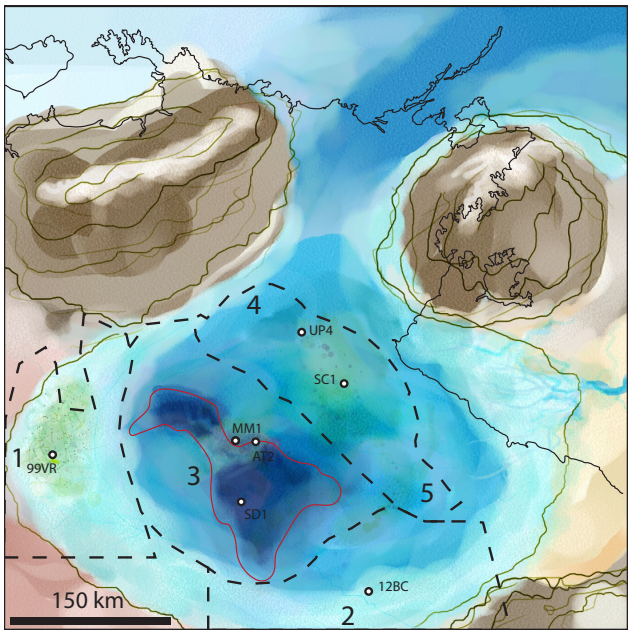

Fig 4: C) Velkerri, early to middle Amungee Brown = orogenic topography, light blue = marine within wave base or fluvial, mid blue = marine within storm wave base, dark blue = marine below storm wave base, yellow = paralic to fluvio-terrestrial, red = regolith terrestrial, green = ferruginous water/sediment

1 = Western Proximal Region, 2 = Southern Proximal Region, 3 = Basinal Region, 4 = Northern Distal Region, 5 = Southern Distal Region.

Core abbreviations as per Table 1 in Chapter 1

Velkerri Formation/Battle Creek Formation

Velkerri, early to middle Amungee (Fig 4C)

The Distal and Basinal Regions are still dominated by FA3 with alternating deposition of interbedded sands, interlaminated silt, and massive to laminated mudstone facies. It is during this interval that enhanced organic enrichment occurs across the basin. The facies independent nature of the organic rich beds indicates that organic enrichment was not linked simply to detrital clastic sedimentation rate or RSL rise. Both Basinal and Distal Regions contain coarsening upward cycles through this interval indicating that RSL is still rising and so this interval is here interpreted as being part of the TST.

In the southern Proximal Region, the fining up cycles are now dominated by FA3 interbedded sands indicating the coastline in this region has retreated further south and just beyond the

study area. In the western Proximal Region, the FA3 interlaminated silts are erosively truncated by a thin interval of FA1 cross stratified sands that correlates with two thick coarsening up cycles in the Basinal Region indicating a temporary fall in RSL and progradation from the west. The cross stratified sands are draped by FA3 interbedded sands and interlaminated silts that coarsen upwards across two ~25 m thick cycles.

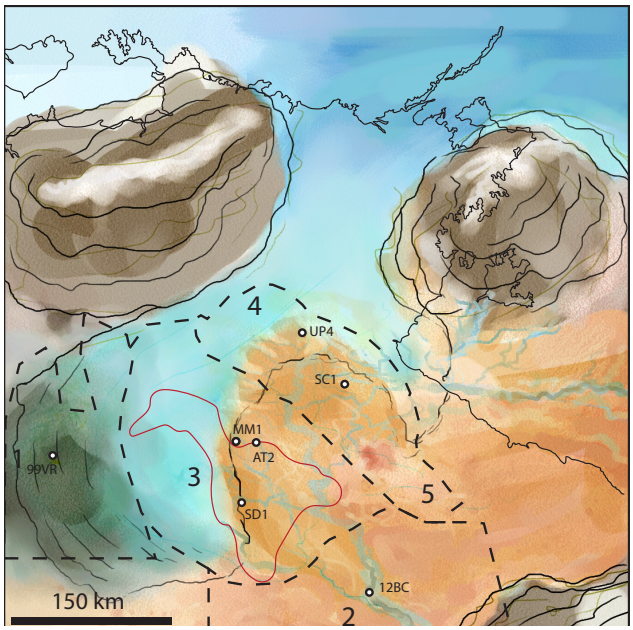

Fig 4: D) Velkerri late, late Amungee to middle Wyworrie. Brown = orogenic topography, light blue = marine within wave base or fluvial, mid blue = marine within storm wave base, dark blue = marine below storm wave base, yellow = paralic to fluvio-terrestrial, red = regolith terrestrial, green = ferruginous water/sediment

1 = Western Proximal Region, 2 = Southern Proximal Region, 3 = Basinal Region, 4 = Northern Distal Region, 5 = Southern Distal Region.

Core abbreviations as per Table 1 in Chapter 1

Velkerri Formation/Battle Creek Formation

Velkerri, late Amungee to middle Wyworrie (Fig 4D)

The southern Proximal, and Distal and Basinal Regions continue to be dominated by FA3 but with facies showing lateral continuity across the basin, with minor local variation in grain size and sedimentary structure. Organic rich beds are still common in this interval, but are thinner, and increasingly restricted to the Basinal Region up section. By the end of the interval, coarsening up cycles are no longer observed in the Basinal or Distal Regions. Instead, there are a number of erosively based ~10-20 m fining up cycles topped with intervals of mudstone that become thicker up section. The southern Proximal Region experiences a single fining up cycle where medium sandstones grade to claystone over ~5 m with claystone dominating for the remainder of the interval. A notable feature of the southern Proximal, and Distal and Basinal Regions in this interval, are the winnowed glauconite and carbonate laminae, silica rich beds, and brecciated clay beds. These are interpreted as being condensation surfaces indicative of a hiatus in sedimentation. As the interval immediately above these features displays little variation in grain size trends or sedimentary structure style, the condensation horizons are here interpreted as representing maximum flooding

surfaces and mark the start of the HST.

In the western Proximal Region, the FA3 interbedded sands and interlaminated silts transition into FA3 microbial limestones; a facies restricted to the Proximal Regions. The microbial limestones are interlaminated and interbedded with thin glauconitic and heavy detrital rich sands, and ferrous clays. This particular combination of features suggests prolonged, but shallow flooding of the western Proximal Region, and detrital sediment starvation and condensation. The microbial limestones host features resulting from sub-aerial exposure and erosion, and sub-aqueous wave erosion and reworking. But as many of these surfaces also show 'healing' and regrowth of the microbial fabric, these intervals must have been relatively short. The microbial carbonates are interpreted here as representing maximum flooding in the western Proximal Region due to the association of chemical sedimentation, and detrital clastic condensation, interpreted as a depositional hiatus.

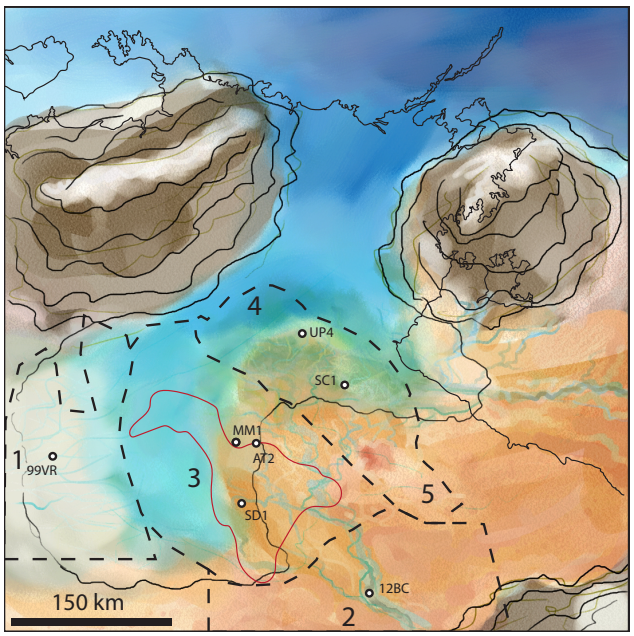

Fig 4: E) Velkerri, late Wyworrie Brown = orogenic topography, light blue = marine within wave base or fluvial, mid blue = marine within storm wave base, dark blue = marine below storm wave base, yellow = paralic to fluvio-terrestrial, red = regolith terrestrial, green = ferruginous water/sediment

1 = Western Proximal Region, 2 = Southern Proximal Region, 3 = Basinal Region, 4 = Northern Distal Region, 5 = Southern Distal Region.

Core abbreviations as per Table 1 in Chapter 1

Velkerri Formation/Battle Creek Formation

Velkerri, late Wyworrie (Fig 4E)

The southern Proximal, Distal, and Basinal Regions all remain dominated by FA3 facies, with beds of the interbedded sands facies becoming more abundant and thicker up section at the expense of the other FA3 facies. Convoluted bedding and dewatering structures also become more abundant up section indicating increasing rates of detrital clastic sedimentation, and thus increasing proximity to detrital clastic sources. A similar pattern is seen in the western Proximal Region where the microbial carbonates are drowned by renewed clastic deposition dominated by the FA3

interbedded sands facies. All regions display a coarsening upward trend during this interval with sedimentary evidence of decreasing water depth and progradation of the coast. However, facies analysis suggests that the initial progradation comes from the Distal Region in the north-northeast, rather than from the inffered coast to the south. As the top of the Velkerri and Battle Creek Formations are truncated by the overlying units, it is not possible to fully map how facies change across the basin prior to full regression. Initial erosion probably occured early in the FSST when the sea floor entered the zone of wave erosion.

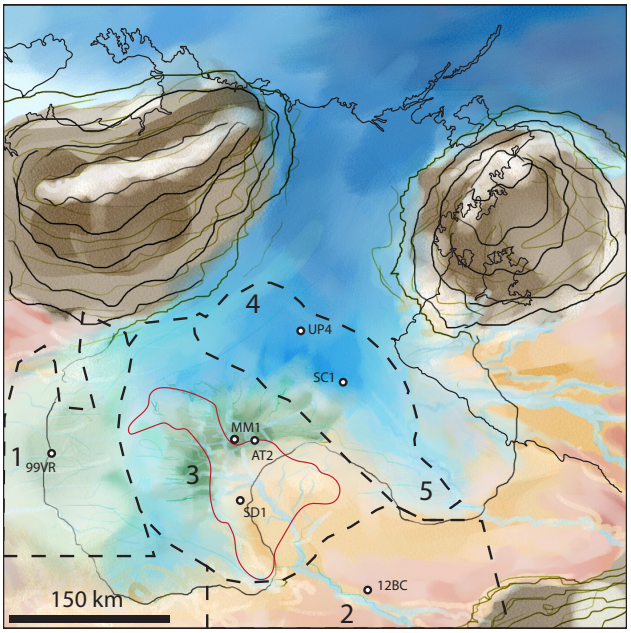

Fig 4: F) Moroak, early to middle Moroak Brown = orogenic topography, light blue = marine within wave base or fluvial, mid blue = marine within storm wave base, dark blue = marine below storm wave base, yellow = paralic to fluvio-terrestrial, red = regolith terrestrial, green = ferruginous water/sediment

1 = Western Proximal Region, 2 = Southern Proximal Region, 3 = Basinal Region, 4 = Northern Distal Region, 5 = Southern Distal Region.

Core abbreviations as per Table 1 in Chapter 1

Moroak Sandstone/Wondoan Hill Formation

Moroak, early to middle Moroak (Fig 4F)

In the southern Proximal, and Basinal and Distal Regions, the base of the Moroak Sandstone is composed of lags and gravels rich in fragments of the underlying Velkerri Formation. The top of the Velkerri Formation also locally shows signs of weak sub-aerial erosion e.g., oxidation that wanes down section over a few decimeters to meters. This interval of the Moroak is dominated by the FA1 facies of cross bedded sands and laminated sands and muds. The FA1 facies laminated to massive muds, and interbedded sands are gravels are also present throughout at the tops of meter scale coarsening up cycles. Facies analysis shows that the paralic and fluvio-terrestrial facies thicken to the south, with the greatest thickness in the Beetaloo sub-basin of the Basinal Region, while thinning to the north. This is suggestive of progradation from south to north into a relatively rapidly subsiding proximal depocenter, followed by lapping onto a relative structural high to the north. However, when viewed on the E-W transect (Fig 3I, Chapter 2), there is no thinning ob-

served suggesting that these areas represented paralic to terrestrial environments with relatively steady states of subsidence compared to the more central parts of the basin on the N-S transect (Fig 3B, Chapter 2). By the end this interval, the FA1 cross bedded sands in the Distal Region feature erosively based interbeds of FA2 ferruginous sands. The observed cycle of facies in this interval is here interpreted as representing the FSST (Cross stratified sands), the LST (laminated sands and muds, laminated to massive muds, interbedded sands and gravels), and the earliest stage of the TST (the ferruginous sands).

During this interval, the western Proximal Region diverges more from the easterly regions with the deposition of relatively thin intervals of FA2 ferruginous sands and muds during the initial stages of RSL fall. As with the other regions, the top of the underlying marine units are eroded and shows signs of brief sub-aerial exposure. The remainder of this interval in the western Proximal Region is composed of FA1 laminated to massive muds that are composed of Al poor kaolinite, minor quartz silt, and interbedded thin erosively based intervals of FA1 cross bedded sands. The laminated muds are reminiscent of heavily weathered and leached terrestrial clays associated with low lying areas with a relatively high and stable water table. In this context the ferruginous sands and muds could be interpreted as estuarine mud flats and sandy shore faces, while the overlying cross bedded sands and laminated to massive muds may represent river channels and flood plains, respectively. Such an interpretation would be consistent with the observations made from the underlying succession, and in the other regions of the basin. In the western Proximal Region, the ferruginous sands and muds would represent the FSST, and the laminated to massive muds and cross stratified sands represent the LST.

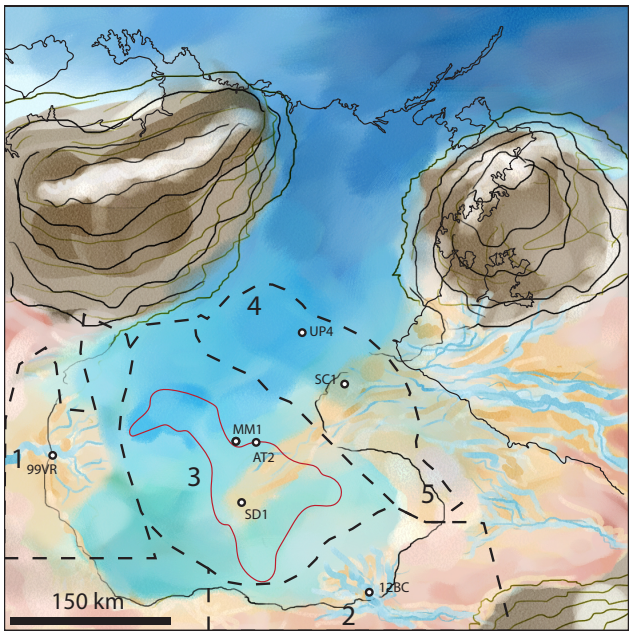

Fig 4: G) Moroak, late Moroak/Sherwin Brown = orogenic topography, light blue = marine within wave base or fluvial, mid blue = marine within storm wave base, dark blue = marine below storm wave base, yellow = paralic to fluvio-terrestrial, red = regolith terrestrial, green = ferruginous water/sediment

1 = Western Proximal Region, 2 = Southern Proximal Region, 3 = Basinal Region, 4 = Northern Distal Region, 5 = Southern Distal Region.

Core abbreviations as per Table 1 in Chapter 1

Moroak Sandstone/Sherwin Ironstone/Wondoan Hill Formation

Moroak, late Moroak/Sherwin (Fig 4G)

In this interval the Distal Region is dominated by FA2 with interbeds of the green cemented sands and green coated grain facies being most abundant in the lower part of the interval, and with the green mud facies becoming dominant up section. The Basinal Region remains dominated by FA1 cross stratified sands and laminated sands and muds facies, but by the upper part of the interval, the FA2 green cemented sands facies dominates. A similar trend is seen in the Southern Proximal region where FA1 facies dominate until a transition to FA2 green cemented sands in the uppermost part of the interval. The FA2 facies are interpreted in Chapter 3 as paralic to shallow marine environments such as shoreface or near shore shoals with varying levels of detrital clastic input. Here ferrous clay formation is driven by the interaction of upwelling deep ocean waters and riverine waters in the early stages of transgression (Johnson et al 2020). This interpretation is supported here by the observation of ferruginous sediments migrating coastwards up section as the transgressing marine waters move inland and the coastline retreats (Fig 3, Chapter 2). Additionally, when mapped in plan view, the ferruginous sediments form a halo around a point source as may be expected when a plume of riverine water enters a basin and meets a water mass with a contrasting chemistry. However, in the western Proximal Region, the corresponding interval continues to be dominated by FA1 laminated to massive muds, indicating that terrestrial conditions prevail in the far western portion of the RSB.

Kyalla Formation/Wondoan Hill Formation

Kyalla, early to middle Kyalla (Fig 4H)

In the northern part of the Distal Region, the FA2 green muds facies transitions up section into the FA3 interbedded sands and muds facies, indicating a return to open marine clastic storm dominated shelf sedimentation. In the eastern part of the Distal Region, the FA1 cross bedded sands facies dominates through the interval. Thin beds of intra clastic conglomerate, pebble and grain conglomerates, and flat pebble conglomerates suggest that shallow water high energy environments, e.g. shoreface or fluvial, remained dominant in this area. In the Distal Region, FA1 facies are succeeded by alternating intervals of the FA3 interbedded sands, and interlaminated silts facies. The Elliot Sandstone member of the Kyalla Formation is only found in the Basinal Region and consists of the FA1 cross bedded sands, and interlaminated sands facies. The similarity of facies and lithologies between the Elliot Sandstone member, and the much sandier lower Kyalla Formation in the eastern part of the Distal Region suggests the two may be related, however nei-

ther the Elliot Sandstone member, or, indeed, any sandy facies, have been reported from this stratigraphic interval in the intervening areas or cores. A possible reconciliation of these observations is that the Elliot Sandstone member of the Basinal Region represents a package of stranded low stand facies (*cf* Hunt and Tucker, 1992), following a short-lived episode of rapid regression and progradation from the east. Without a more complete dataset, this is currently conjecture, however progradation from the east during this interval is consistent with recent provenance data (Yang et al 2020)

In the southern Proximal Region FA1 interbedded sands and gravels, and laminated sands dominate throughout this interval in coarsening up packages that increase in number and decease in thickness (from 10's m to ~1 m) up section. In the upper most part of this interval, thin <1 m beds of FA3 microbial limestone can be found at the base of coarsening up cycles. This package of facies and coarsening cycles suggests increasing subsidence and a transition to more marine influenced paralic environments. In the western Proximal Region, the FA1 laminated to massive muds are erosionally truncated by FA2 green cemented sandstones and green coated grain stones indicating a rapid transition to a high energy shallow marine environment with a relatively low detrital clastic sedimentation rate. Around halfway through this interval, the ferruginous sediments gradationally transition to FA3 interbedded sands interpreted as a storm dominated shelf environment which dominates for the remainder of the interval.

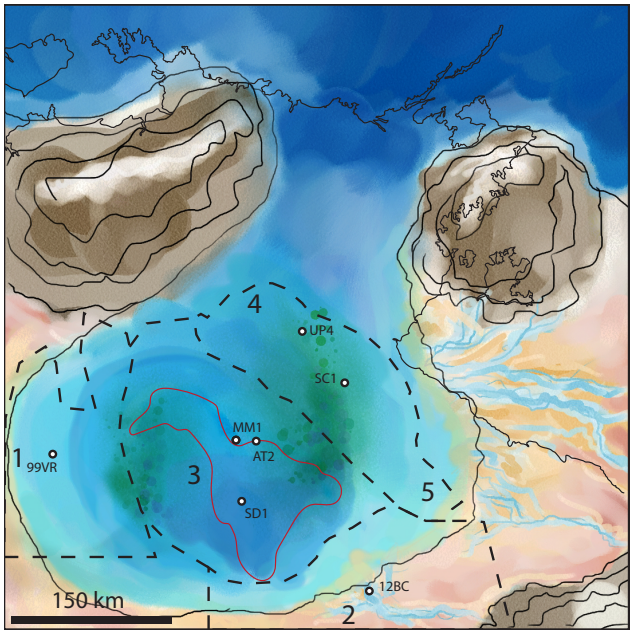

Fig 4: H) Kyalla, early to middle Kyalla Brown = orogenic topography, light blue = marine within wave base or fluvial, mid blue = marine within storm wave base, dark blue = marine below storm wave base, yellow = paralic to fluvio-terrestrial, red = regolith terrestrial, green = ferruginous water/sediment

1 = Western Proximal Region, 2 = Southern Proximal Region, 3 = Basinal Region, 4 = Northern Distal Region, 5 = Southern Distal Region.

Core abbreviations as per Table 1 in Chapter 1

5.3. Constraints on mid-Proterozoic marine redox from the RSB

5.3.1. The spatial and temporal distribution of euxinic conditions

Current models of mid-Proterozoic marine redox are largely based on studies of the Velkerri Formation (Arnold et al., 2004; Johnston et al., 2008; Shen et al., 2002). In brief, the most commonly cited models propose an offshore marine and open ocean redox structure consisting of a thin surface layer of relatively oxygenated water, above a dominantly ferruginous to euxinic water column (Nguyen et al., 2019; Poulton and Canfeld, 2011). Specifically, early hypotheses explained the sedimentary organic matter and authigenic sulphide enrichment, the results of Fe-speciation, and the Mo and S isotope distributions found in the Velkerri Formation, as a direct result of the deposition of sediments below a euxinic water column. In this model, increased water depths during the HST reduced detrital clastic dilution and promoted widespread euxinic conditions. This resulted in the increased preservation potential of organic matter and promoted the formation of abundant sedimentary pyrite through authigenic growth mediated by both microbial sulphate reduction, and abiotic growth of pyrite in sulphide saturated waters (Arnold et al., 2004; Johnston et al., 2008; Shen et al., 2002).

The depositional models interpreted from the data collected in the studies cited above envisage the water column in the RSB as representing an extreme endmember of long-term marine anoxia as a consequence of low atmospheric pO_2. Subsequently, as the RSB was thought to be in full connection and water exchange with the open ocean, these geochemical interpretations were taken to be representative of global ocean conditions throughout the mid-Proterozoic; an interval of ~1000 million years. However, the data presented in this thesis do not support; i) organic enrichment as a consequence of increased preservation potential related to RSL increase, ii) extensive water column euxinia, either as a base line state for the basin, or in relation to RSL increase, or iii) deposition in a deep basinal setting.

i) Organic enrichment in the Velkerri Formation is not restricted to the HST as shown in Fig 3, Chapter 2 of this thesis. Additionally, organic enrichment is not always synchronous across the basin, and occurs at multiple different times in different places, and is independent of depositional facies (Fig 3 Chapter 2). These observations suggest that organic enrichment is not related to water depth or clastic depositional rate and so another mechanism is required to explain the increased TOC found in throughout the Velkerri Formation. Cox et al (2016) have suggested that organic enrichment in the Velkerri Formation may have been a consequence of increased primary production. These authors show a change in detrital sediment provenance, and an increase in P being delivered

to the Velkerri Formation, durinng deposition of the middle Amungee member of the Velkerri Formation. Subsequently Cox et al.,(2016) suggest the two are linked and that regional tectonics resulted in increased primary productivity within RSB waters due to an influx of nutrients.

The data and interpretations of Cox et al (2016) complement the data presented in this study which show a marked change in the detrital clastic mineralogy (e.g., a shift in feldspar composition from plagioclase to orthoclase rich), preceding and during deposition of the most organic rich intervals in the Amungee member of the Velkerri Formation (Fig 4, Chapter 2). An influx of P into a restricted basin and a subsequent increase in primary productivity, explains the facies and lithology independent distribution of organic matter in RSB sediments, far better than simply invoking improved preservation in anoxic waters with a low sedimentation rate, though these also undoubtedly played a part. For example, organic rich beds are relatively rarer and thinner in the Proximal Regions where the shallower waters may have been more oxygenated and had higher sedimentation rates, compared to the Basinal and Distal Regions.

The facies and sequence stratigraphic analysis in Chapter 2 suggest that the RSB was not openly connected to the global ocean and possibly underwent short lived periods of disconnection. Restricted basins are known to be major centres of organic carbon production throughout earth history (Wignall, 1999). In such basins, eutrophic conditions develop and are maintained by poor water circulation and overturning, a persistent flux of riverine water which delivers nutrient rich fresh waters, which also promote stratification. Internal nutrient recycling is also common within restrictured basins through mechanisms such as the auto catalytic anoxia of Van Cappellen and Ingels (1994). It is therefore unsurprising that we find organic rich intervals within the RSB. Even without the external source of nutrient loading proposed for the Velkerri Formation, the RSB seems to have been geographically and geobiologically primed to become a eutrophic basin. An observation supported by the abundance of organic rich intervals throughout the Roper Group, e.g., the Kyalla Formation, which was deposited in shallower, more clastic rich and wave mixed waters than the Velkerri Formation, yet is also organic rich (Munson., 2016). Therefor based on the evidence provided by this thesis and in addition to published data, deep euxinic waters are not required to explain the organic enrichment in the Velkerri Formation.

ii) Extensive water column euxinia was previously proposed on the basis of abundant sedimentary pyrite, high TOC, $\delta^{34}S_{pyrite}$, Fe speciation and degree of pyritization (DOP), and $\delta^{97/95}Mo$ isotopes (Arnold et al., 2004; Donnelly and Crick, 1988; Jackson and Raiswell, 1991; Johnston et al., 2008; Shen et al., 2002; Yang et al., 2017). Pyrite is abundant throughout the Velkerri Forma-

tion. However certain intervals contain, or are dominated by, late diagenetic pyrite, and hydrothermal sulphides that post-date lithification. It is unclear from the literature review if any petrographic screening of pyrite took place in the published whole rock studies, beyond avoiding obvious macroscopic diagenetic nodules and veins (e.g., Johnston et al., 2008). Given that much of the late pyrite observed in this study is only visible in thin section or SEM (e.g., the nanoscale pyrite), it is likely that any bulk or whole rock analysis will have sampled late diagenetic and hydrothermal pyrite. Petrographic textures suggest that the late diagenetic pyrite may be related to maturation and migration of hydrocarbons, consistent with the S-rich nature of organic matter in the Velkerri Formation. Additionally, all cores sampled for previously published pyrite-based studies have been either been intruded by dolerite or are adjacent to major fault systems. Both the dolerite intrusions and faulting are associated with hydrothermal sulphide mineralisation (e.g., Garven et al., 2001).

My petrographic observations show that the pyrite framboids found in the Velkerri Formation are syndepositional to authigenic and formed at the sediment-water interface; early diagenetic pyrite grew while pore waters were still in communication with the overlying water column and prior to sediment compaction. Therefore, both framboids and other early diagenetic pyrite textures potentially record bottom and pore water redox during deposition of the Velkerri Formation. Pyrite framboid size has previously shown to be a robust indicator of water column or sediment redox when mean size is plotted against the standard deviation from mean size within a given framboid population. Velkerri Formation framboids unambiguously fall far into the ferruginous-oxic waters field of the plot. Pyrite framboid sizes indicate that the framboids were too large to have grown in the water column (i.e., they would not have been hydrodynamically stable) and show no signs of overgrowth, so did not grow from smaller seed framboids that were derived from the water column. At face value, it appears that ferruginous–oxic conditions appear to have dominated the background redox state of the upper sediment column, sediment-water interface, and water column during deposition of the Velkerri Formation, including during deposition of the ‘euxinic’ organic-rich Amungee member. Pyrite framboids deposited from euxinic waters often create framboid-rich laminae where framboids sink (rain) en masse once they are too large to float (Raiswell and Berner, 1985; Rickard, 2012; Wilkin and Barnes, 1997). Similarly, when pore water and water column sulphide levels reach critical supersaturation, then rather than framboids, pyrite forms as disseminated nano crystalline dust within the water and sediment (Rickard, 2012). No “framboid rain” laminae were observed in the current study, and all nano crystalline pyrite observed was clearly associated with hydrothermal textures and post-dated lithification (e.g., Guan et al., 2014).

However, as early diagenetic pyrite textures clearly indicate, euxinic conditions were not completely absent from the RSB during Velkerri Formation deposition. Sediments of the Amungee member contain an increased abundance of truncated, pyritohedral and cuboidal pyrite microcrystals relative to the rest of the Velkerri Formation. Pyrite microcrystal morphology is a consequence of the pore water saturation state with respect to pyrite and can therefore be used as a semi-quantitative proxy for pyrite supersaturation and thus the relative concentration of pore water $H_2S(aq)$ (Rickard, 2012; Suits and Wilkin, 1998). Pyrite octahedra can grow in sediment pore waters that are locally supersaturated with respect to pyrite. However, the same sediment package may also experience episodes of oxic or ferruginous conditions at separate times during the total integrated time of its deposition. As euxinia becomes more pervasive and the saturation state with respect to pyrite increases, microcrystal morphology moves to increasingly cuboidal forms (Wilkin and Barnes, 1997: Rickard, 2012). When limiting supersaturation with respect to pyrite is reached, spontaneous nucleation of pyrite nano crystals proceeds until growth nutrients are depleted (Ohfuji and Rickard, 2005; Wilkin and Barnes, 1997). The abundance of truncated octahedra and pyritohedral pyrite microcrystals within the Amungee Member indicates an elevated saturation state with respect to pyrite. Cuboidal pyrite microcrystals are rare throughout the Velkerri Formation but become relatively more abundant within the Amungee Member. However, cuboidal pyrite microcrystals, and indeed a large number of pyrite microcrystals, are found within organic rich microbial laminae.

Pyrite microcrystal morphologies support the presence of euxinic pore waters, or at least an increased supersaturation state with respect to pyrite, in the Amungee member of the Velkerri Formation. Euxinic pore waters are common in sediments enriched in organic matter, and not necessarily a sign of a euxinic water column (Rickard, 2012; Schenau et al., 2002). However, framboid sizes within the same beds (and laminae) indicate a ferruginous-oxic water column and sediment water interface. This contradiction is explained by the abundance of sulphur in organic matter found in the Velkerri Formation (Flannery and George, 2014; Piane et al., 2019; Warren et al., 1998). Localised decay of organic matter released S and H_2S, which in addition to the bacterial sulphate reduction of pore water SO_4 supplied from the water column, increased the supersaturation state with respect to pyrite within pore waters. As the rate of microbial sulphate reduction increased, the pore water saturation state increased leading to pyrite microcrystal morphologies recording higher supersaturation. Subsequently, a redox interface between the ferruginous and euxinic waters developed at the sediment water interface in those locations. The chemocline was stabilised by mixotrophic benthic microbial mats where the upper part of the mat (and overlying

waters) remained ferruginous-oxic, while the lower part of the mat and underlying sediment became relatively euxinic.

In this way, large framboids indicative of free pore water $H_2S(aq)$ formed within the mat and upper sediment where the hydrodynamic regime could supply nutrients and there was space to grow. Pyrite microcrystals, which are associated with higher, but localised pyrite supersaturation states could grow below in the lower mat and upper sediment. The absence of sedimentary nano crystalline pyrite suggests that limiting supersaturation with respect to pyrite was not reached in the sediment (or water column) at least in any of the examined cores. Additionally, pyrite framboids, and microcrystals throughout the Velkerri Formation can be observed with synsedimentary corrosion pits, and Fe-oxide and sulphate crusts, alongside Fe-oxide and sulphate pseudomorphs of framboids and pyrite microcrystals, including in the Amungee member. These observations suggest that oxygenated waters were present even during deposition of the "euxinic interval", in the Amungee member, a state commonly observed in modern organic rich sediments, and that pore waters oscillated between a ferruginous background state and relatively shorter euxinic and oxic periods (e.g., Schenau et al., 2002). In light of the above, and assuming that the $\Delta^{34}S$ data do not reflect any late diagenetic or hydrothermal influences, then previous $\Delta^{34}S$ data are illustrating the occurrence of euxinic conditions within the sediment, rather than the water column. However, future work is still needed to untangle the imprint of diagenetic and hydrothermal sulphur, from any remaining authigenic signal.

It may seem unusual that euxinic water conditions did not develop in the RSB during this interval, even though the basin seemed geographically and geochemically primed for it. However, as any reactive Fe^{3+} would be reduced to Fe^{2+} on entering the basinal waters, there would be little to react with H_2S to begin pyrite formation in the water column (*cf* Schenau et al., 2002). Additionally previous workers have noted that pyrite $\Delta^{34}S$ data do appear anomalously light compared to model marine $\Delta^{34}S$ data, which was interpreted as pyrite formation from low-sulphate waters (Donnelly and Crick, 1988). This combination of low sulphate, and low reactive Fe may have meant that euxinic conditions could only be reached within the sediment as organic matter was reduced, S was released, and ferrous silicate formation ceased as pore waters were disconnected from the source of dissolved silica. However, Jackson and Raiswell, (1991) interpreted the anomalous $\Delta^{34}S$ data to indicate fractionation caused by synsedimentary reworking of the seafloor and the authigenic pyrite it contained. However, both Donnelly and Crick (1998) and Jackson and Raiswell (1991) sampled the core UP4 (among others) which has been shown in this thesis to contain abundant hydrothermal sulphides (see Chapter 2 and 4).

Rapid localised shifts in pore water redox state were a response to changes in the rate of microbial sulphate reduction, itself a response to changing rates of organic matter export to the sediment. This apparent cyclicity further suggests that some external forcing may have played a part in controlling the rate of primary production in RSB waters and hence the production of pyrite. Perhaps periodic increases in riverine flux, or coastal upwelling derived nutrients increased primary productivity and produced the conspicuously rhythmic alterations of organic rich and lean beds in the Velkerri Formation. Orbital Forcing has been suggested as a driver for formation of the rhythmic banding in the Velkerri Formation (Mitchell et al., 2020). In this model, the silty rich laminae represent increased clastic detrital input during periods with a wetter climate (Mitchell et al., 2020). However, without any sense of absolute time and depositional rates, it is impossible to test these ideas robustly, and it might be expected that climatically driven organic carbon enrichment would produce synchronous basin wide high TOC beds, which are not observed here (Chapter 2 this thesis, Andrews et al., 2010). Additionally, the changes in lithology do not correspond to the changes in TOC and increases in clastic detrital deposition are just as easily explained by 4th order or higher RSL changes. Currently, the most parsimonious explanation for organic enrichment is the input of volcanogenically derived P which is supported by sedimentary and geochemical data (Chapter 2 this thesis, Cox et al., 2016)

Microbial sulphate reduction of organic matter was probably the main driver for generating the pyrite that produced the euxinic signal within the Velkerri Formation. While the later hydrothermal sulphides have undoubtedly caused a local overprint in the affected cores, they are not observed across all cores in this study. However, the pyrite microcrystals with morphologies indicative of relatively higher pore water saturation with respect to pyrite, are found basin wide within the Amungee member, including in cores that have experienced no late-stage mineralisation. The late diagenetic pyrite also shares the morphologies typical of increased pyrite saturation state but are clearly post lithification, a probable explanation for this form of pyrite is the maturation and migration of hydrocarbons during inversion of the RSB between the Stennian and Tonian periods (Munson, 2016).

In summary, pyrite microtextures in the Velkerri Formation do not support formation beneath a euxinic water column. Instead, pyrite framboids indicate growth at the sediment-water interface with free $H_2S(aq)$ confined to within sediment pore waters. Pyrite microcrystals support framboid data and indicate that sediment pore waters featured locally and intermittently sulphide rich conditions. The relatively higher abundance of pyrite microcrystals within the Amungee member indicates porewaters were more often supersaturated with respect to pyrite perhaps to a greater

degree than other intervals. However, framboids in the same beds still indicate ferruginous–oxic waters at the seabed, so sulphidic conditions were probably restricted to the sediment column. The relative increase in porewater H_2S concentrations in the Amungee member was likely a result of increased organic matter fluxes to the sediments as a result of enhanced primary productivity in the over lying waters.

Molybdenum isotopes from whole rock extractions have also been used to support deposition of the Velkerri Formation under a euxinic water column (Arnold et al 2004). Measurement of $\delta^{97/95}$Mo of five samples from the core UP4 gave values that were on average 1.1‰ lighter than those measured in the euxinic sediments from the Black Sea (Arnold et al 2004). The authors suggested these anomalous values were a result of widespread euxinic conditions in the global ocean, and rejected fractionating effects from hydrothermal input, riverine input, and from deposition in a restricted setting because at the time, there was no evidence for these processes, and the RSB was thought to be fully connected to the global ocean (Arnold et al 2004). In light of data presented in this thesis, it is clear that hydrothermal and riverine input, and a restricted depositional setting could all have contributed to the anomalous $\delta^{97/95}$Mo readings in Arnold et al (2004). The organic-rich Corcoran Formation, which underlies the Velkerri Formation in UP4, is intersected by a dolerite sill which would have likely generated hydrothermal fluids (Munson, 2016). Additionally, UP4 is also situated on a fault bound block that is known to have experienced movement, and probably fluid flow, following deposition of the Roper Group, providing ample opportunity for low temperature hydrothermal fluid interactions with the Velkerri Formation (Munson, 2016). Subsequently, the Velkerri Formation in UP4 features abundant hydrothermal pyrite, including the disseminated nanocrystalline variety normally attributed to deposition under a euxinic water column. Without explicit mention of any petrographic screening, it is therefore likely that the bulk powder analysed by Arnold et al (2004), sampled some of the diagenetic and hydrothermal pyrite.

Given the observations presented above, and in this thesis, it is likely that geochemical data derived from whole rock methods were influenced by the later generations of sulphides. Therefore, published whole rock geochemical data should be interpreted with caution until some attempt is made to isotopically differentiate between the authigenic, diagenetic and hydrothermal signals within the Velkerri Formation. Future workers on the RSB succession should apply rigorous petrographic screening to their samples in an attempt to identify for which generations of sulphides are present, before analysis, or at least before the interpretation of results.

iii) Water depths during organic shale deposition

Deposition of the Amungee member was interpreted to coincide with the HST during Abbott and Sweet's (2000) "Veloak" sequence (Fig 3, Chapter 2). It was subsequently assumed that terrestrial sediment starvation and water column stratification were both direct consequences of increased water depth during the HST (e.g., Wignall, 1994, Munson 2016). However, this is a circular argument: deep water stratification and terrestrial sediment starvation led to the relatively rapid accumulation of organic matter, but the rapid accumulation of organic matter is the evidence for transgression, terrestrial sediment starvation and deep-water stratification. However, my detailed examination of Velkerri Formation core material from across the wider RSB has shown that organic enrichment in the Velkerri and Kyalla Formations, is independent of lithology, and therefore independent of water depth (Fig 3F , M, Chapter 2 this thesis).

The presence of finely laminated clay rich sediments is also cited as evidence for deposition below storm wave base in a deep-water setting where fine grained sediments accumulated through suspension settling. While fine planar lamination is certainly abundant throughout the Velkerri Formation, the observations detailed in Chapter 2 of this thesis, e.g., cross laminations composed of fine sand sized clay aggregate grains, indicates that even these finely laminated sediments probably experienced wave activity, even if only in the largest storms.

Undulose and cross-bedded sediments, scouring of bedding surfaces and convolute bedding are common throughout the Velkerri Formation. If the fine planar laminations do indeed represent waters below storm wave base (or over 100 m deep as proposed in Munson, 2016), then these relatively deep intervals appear to have been infrequent and short lived, even during the transgressive high stand. If as previous models suggest, there was a contemporaneous increase in RSL across the basin so that waters below SWB were ubiquitous and widespread, we would expect to see a fairly uniform basin wide blanket of laminated detrital-poor mudstones at the same stratigraphic level across the basin. Instead, we see a lateral basin wide migration of the offshore sedimentary facies association towards the palaeocoast, coupled with specific sedimentary facies that are heterogenous in time and space, including the finely planar laminated and massive mud stones.

Finally, the sharp but conformable contacts between the planar finely laminated beds and those hosting cross-beds and terrestrial clastics, etc., would require geologically very rapid changes in accommodation, and on a highly localised scale to account for the temporal and spatial heterogeneity. The collective petrographic observations are difficult to reconcile with the model of basinwide deep water below storm wave base during a widespread transgressive high stand. This heterogeneity can be accounted for with the observation of localised sub-basins such as the Beeta-

loo sub-basin. These sub-basins appear to have been major local depocenters during deposition of the studied interval and may have had different rates of tectonically driven subsidence at different times (Munson, 2016). The sub-basin explanation also satisfies the observation that intervals of organic enrichment are diachronous in space and time.

In summary, facies analysis indicates that the majority of the Velkerri Formation was probably deposited mostly around storm wave base with relatively short periods below storm wave base. If finely planar laminated sediments do represent water depths below storm wave base, then such environments were localised and heterogeneous in space and time during deposition of the Velkerri Formation. Organic enrichment as a consequence of enhanced primary productivity explains the observed distribution of organic rich sediments better than enhanced preservation in deep waters stratified waters with low sedimentation rates.

5.3.2. Evidence for extensive ferruginous waters

Fe-clays are abundant and widespread through space and time in the RSB. Berthierine and glauconite are the dominant authigenic Fe-clays, although greenalite becomes locally important during deposition of the Sherwin Ironstone (Fig 2, Chapter 3). I have previously explained that both berthierine and glauconite formation require rapid oscillation between anoxic and oxic conditions on, or at the Fe redox boundary (Chapter 3). Therefore, it is probable that bottom and early porewaters in the RSB were dominantly ferruginous, but frequently and rapidly punctuated by the presence of dissolved O_2.

I was not able to directly correlate all of the Fe-clay-rich ferruginous horizons and beds across the entire RSB. This maybe as consequence of ferruginous facies representing condensation and so contributing to aliasing in the offshore sections. At face value, this suggests that the distribution of $O_2(aq)$ was heterogenous in both space and time. This is perhaps unsurprising since recent sedimentary Cr isotope data, including samples from the Sherwin Ironstone, suggest that atmospheric O_2 was ~0.01 % of present atmospheric levels during deposition of the upper Roper Group (Cole et al., 2018; Planavsky et al., 2018, with the caveat that the Sherwin Ironstone Cr was extracted from secondary oxides, see Chapter 3 of this thesis. Additionally, Cr systematics of environmental redox are still very much debated). Lower atmospheric O_2 levels would have resulted in lower $O_2(aq)$ concentrations and a shallower depth of diffusion before $O_2(aq)$ would have been depleted by reducing constituents such as Fe^{2+}. It might therefore be expected that penetration of oxygenated surface waters down to the seabed would be unevenly distributed. Bottom water oxygenation may have relied on large storms, tectonic events, or unusually large riverine fluxes

to transport oxygenated waters down to the seabed. This heterogeneity would be further amplified during times of high primary productivity, and if the floor of the RSB was divided into discrete localised and short-lived micro basins which further restricted circulation.

Taking these scenarious further, the heterogeneity in seafloor oxygenation, as expressed by the distribution of Fe-clays, could simply be a response to changes in primary productivity or tectonic activity e.g., the formation of fault bound sub-basins where it was possible for ferruginous waters to pond. Perhaps higher productivity by cyanobacteria temporarily produced enough oxygen to locally overcome the loss of oxygen during the mineralisation of carbon, though this is unlikely to have had such a localised effect. Conversely, increased primary productivity is just as likely to consume oxygen through the breakdown and mineralisation of organic matter. However, the prevalence of Fe-clay in shallow waters and terrestrial environments suggests that fluctuating oxygenation of marine environments was widespread and not restricted to offshore settings. Additionally, the large-scale trends observed in the XRD data for Fe-clays do not show any obvious correlation with TOC. However, modern ferruginous environments clearly show that it is possible to have a ferruginous water body even with a relatively O_2-rich atmosphere (Michiels et al., 2017; Swanner et al., 2020). Until more accurate, less ambiguous environmental oxygen paleoproxies are developed, it will not be possible to constrain ancient water and atmospheric oxygen levels further.

Ferruginous waters were not just restricted to the offshore areas of the basin. For example, lagoonal stromatolites in the upper Battle Creek Formation are intergrown with laminae of berthierine and glauconite (Chapter 2, Fig 7Z, AA, AB). Fe-clay grew on and within the stromatolite while the colony was alive and active. This is best illustrated in Fig 7Z, where a mammiform stromatolite (sample name; *Big Bertha*) has suffered storm damage and sub-aerial exposure and erosion, followed by regrowth of both the carbonate skeleton and Fe-clay coatings. The adhesion of detrital clastics to, and entrained in, both the Fe-clay and organic-rich laminae of the stromatolite, support a syn-sedimentary timing for these processes.

Another striking example of a shallow paralic chemocline, is the glauconitic shore face sands and ‘clastic oncoids’ (Fig 6K, Chapter 2) found stratigraphically above the stromatolites in the overlying Wondaon Hill Formation. The interval coarsens rapidly into laminated beach sands with abundant glauconite grains and reworked syn-sedimentary berthierine cement. Data compilations of Fe-clays, including glauconite, show that shallow water associations such as this are common in the sedimentary record into the early Palaeozoic (Boyd, et al., 2004; Chafetz and Reid, 2000; Mingxiang et al., 2008). Taken with the data here, marine waters appear to have been

commonly ferruginous, even in shallow settings, until the widespread Neoproterozoic to early Phanerozoic ventilation of the oceans.

Another conspicuous observation is the association between microbial textures and shallow water and terrestrial ferruginous sediments. In addition to the stromatolites and clastic oncoids in the Tijunna Group, ferruginous shallow water sediments in the Roper Group also contain abundant microbial fabrics. The Sherwin Ironstone contains cm-scale stromatolites, and oncoid-like coated grains composed entirely of berthierine and greenalite, while wrinkled, lamina-bearing, organic and berthierine-rich horizons in silty shales of the Velkerri Formation and Moroak Sandstone are also of probable microbial origin.

The role of mixotrophic mat communities cannot be underemphasised when it comes to using the sedimentary record to interpret past environmental conditions. Modern bacterial mats can be physically tough and are capable of modulating both the geochemistry and physical sedimentology of their environments (Schieber et al., 2007; Shen et al., 2020). For example, mats up to 10 cm thick in the alpine streams of Sulfur(*sic*) Mountain, California, separate high energy stream waters saturated with respect to O_2, from euxinic bottom and pore waters (Aronson et al., in prep). The chemocline in this example was a layer of sulphur oxidising cells just 2 μm thick. The black, sulphide and organic rich, silty laminated muds below the mats were both sedimentologically and geochemically similar to much of the Velkerri Formation, and completely separate from the sands and gravels that formed the sediment above the mats (Aronson et al., in prep). Sadly, the Sulfur Mountain examples were destroyed by flooding in winter 2018/19 so further study is not possible. Clearly though, microbial mats can alter sediments so that they appear to have been deposited in environments with much lower energy levels, and with much more reducing conditions, than in reality. Similar microbial mat mediated modifications of sedimentology and geochemistry, have also been suggested for 'deep water' laminated shales of the Belt Supergroup (Schieber, 1986).

5.4. Mid-Proterozoic marine phosphorus availability

Available data indicate that the global ocean had low dissolved P concentrations for much of the Precambrian, primarily due to the oxygenic weathering feedback discussed in Chapter 1 (Planavsky et al., 2010; Reinhard et al., 2017). Phosphate delivery to the oceans is thought to have been initially negligible but to have increased to modern levels through the Archean as a result of continental amalgamation, emergence, and subsequent erosion (Hao et al., 2020a). Terrestrial input was bolstered by oceanic hydrothermal plumes and seafloor alteration of basalt in anoxic deep oceans (Rasmussen et al., 2021). By the late Archean, the flux of P to the oceans is thought to have

been enough to support a global net primary productivity equivalent to 7% of modern NPP (Hao et al., 2020b). Despite the abundance of reactive Fe in the oceans at this time, P is not thought to have been sequestered into Fe rich sedimentary rocks due to it being less efficient at competing for Fe sorption than silica (Konhauser et al., 2007; Rasmussen et al., 2021). However, despite the apparent abundance of P in Archean oceans, major phosphorite deposits from this interval are currently unknown (though this may be a preservational bias).

By the early to mid-Paleoproterozoic, data from ferruginous sedimentary rocks, and those from distal hydrothermal sedimentary rocks suggests that global ocean P levels may have been at least as high as that of the modern oceans (Planavsky et al., 2010). Subsequently the first major phosphatic deposits were formed during this interval (Khan et al., 2012; Nelson et al., 2010). Deposition of these early phosphorites took place during an interval known as the Lomagundi Event, a large, long lived carbon isotope excursion interpreted to represent enhanced organic carbon burial following increased oxygenation of the atmosphere and enhanced terrestrial weathering of sulphide and P rich sedimentary rocks (Bekker and Holland, 2012). A subsequent slowdown of the weathering rate reduced the flux of P to the oceans, muting NPP and oxygen production, and setting the stage of the mid-Proterozoic low marine phosphate interval of stability that followed (Bekker and Holland, 2012).

Marine P levels appear to remain low until the Cryogenian period when marine P levels increase relative to the preceding interval, and phosphorite deposits become larger and more abundant (Planavsky et al., 2010; Reinhard et al., 2017; Zhang et al., 2019). The apparent increase in marine P levels at this time is interpreted to have been a result of an abnormally large post glacial nutrient flux to the oceans following the end of the Cryogenian ice ages (Planavsky et al., 2010; Reinhard et al., 2017). Though some phosphorite deposition may have been a direct result of extensive Cryogenian sea ice (Hiatt et al., 2020). The post glacial nutrient super-flux is suggested to have greatly enhanced the NPP of cyanobacteria and other photosynthetic oxygen producers, leading to sustained oxygen production and phosphorite deposition, and thus pushing the atmosphere and oceans out of the mid-Proterozoic low oxygen-low phosphorus feedback loop (Caird et al., 2017; Planavsky et al., 2010; Reinhard et al., 2017).

(Derry, 2015) proposed that the extensively ferruginous oceans of the Proterozoic would sequester phosphorus as Fe(II)-phosphate minerals such as vivianite, therefore limiting net primary production and oxygen production across geologically significant intervals. As above, this does not appear to have been the case for Archean or early Palaeoproterozoic oceans, or during deposition of RSB sedimentary rocks (Johnson et al., 2020; Konhauser et al., 2007; Rasmussen

et al., 2021). A possible line of support for the Fe-sink hypothesis in the sedimentary record was presented by Reinhard et al., (2017), who found that the level of bulk phosphorus hosted in marine shales was much lower in mid-Proterozoic sediments relative to younger sediments. In addition to Derry (2015), the role of Fe(II)-phosphate in Proterozoic P cycling is inferred from Fe-P-speciation studies of ancient sedimentary successions, and modern vivianite forming environments, e.g., Guilbaud et al., (2020 and refs therein). However, I was unable to find any direct observations of primary authigenic Fe(II)-phosphate minerals from the mid-Proterozoic sedimentary record in published literature.

However, Mesoproterozoic marine sedimentary rocks appear to have levels of bioavailable P comparable to modern marine sediments (Canfield et al., 2020). A data compilation using C_{org}/P_{react} ratios as a proxy for the Redfield ratio (summarised in Fig 5) indicates that key Mesoproterozoic sedimentary succession, including the Velkerri Formation, had C_{org}/P_{react} ratios in line with modern oxygenated marine shelves (Canfield et al., 2020). Additionally, Mesoproterozoic euxinic depositional settings, including the middle Velkerri Formation, appear to be far more enriched in P relative to organic carbon, than modern euxinic settings. This is inline with observations made in this study of abundant bio available P throughout the Velkerri Formation and overlying sediments. Further, this data compilation also contrasts bulk sediment P studies, such as Reinhard et al., (2017), which show that P was less abundant and a limited resource prior to the Cryogenian period, though the Velkerri Formation was not included in that particular study. Aside from issues caused by organic carbon loss and diagenesis, direct comparisons between ancient and modern C_{org}/P_{react} ratios must be made with caution. Firstly, it is thought that biological C_{org}/P_{react} ratios have varied across geological time, and secondly, because prokaryotic organisms do not necessarily use the same C:N:P ratio as eukaryotic organisms (Pahlow and Riebesell, 2000; Planavsky, 2014).

To investigate the Fe-phosphate sink hypothesis, I analysed sediments deposited in a variety of settings from the upper Roper Group, Bullita Group, and Tijunna Group, where sediments preserve evidence for ferruginous conditions and phosphorus availability (Chapter 3 and 4 this thesis, Johnson et al., 2020). I found primary authigenic Ca-phosphate minerals to be widespread, abundant and apparently bio-available across the basin for the duration of the studied interval. Additionally, no Fe-phosphates were observed by any of the methods used in this study (Johnson et al., 2020). Recent experimental work on Fe(II)-phosphate formation has shown that these phases are difficult to form in typical sedimentary environments unless Fe^{2+} and P concentration is very high, (Brady et al., in prep). This work also shows that there is a strong salinity control on the formation of vivianite which explains why modern vivianite is predominantly found in brackish and

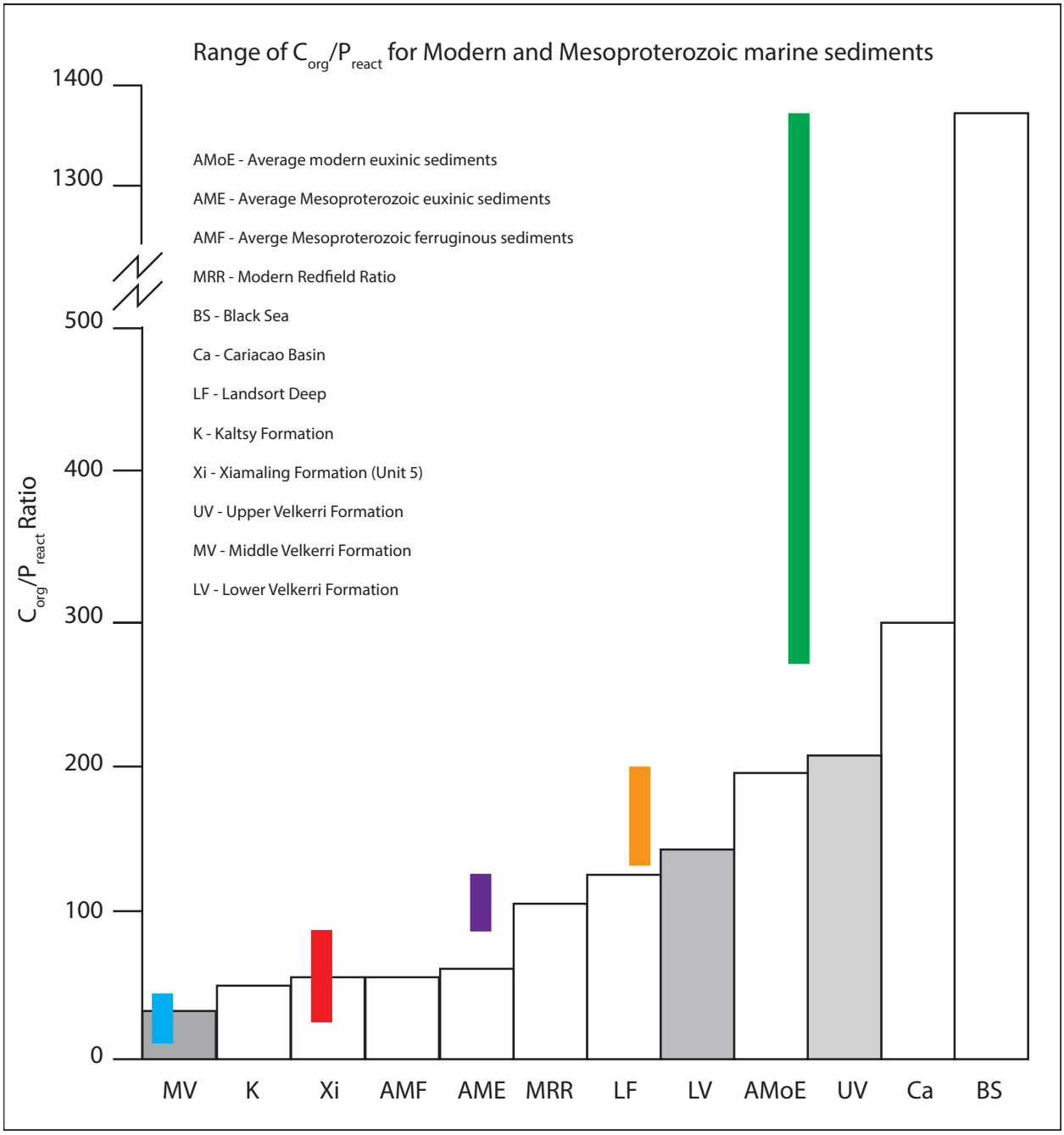

Fig 5: Summary of data collected in Canfield et al 2020 comparing the C_{org}/P_{react} ratios of modern marine depositional envrionments with average and specific Mesoproterozoic sedimentary rocks, grey shaded bars are the Velkerri Formation, green bar is the C_{org}/P_{react} range of modern euxinic marine sediments, orange bar is the C_{org}/P_{react} range sediments above modern marine oxygen minimum zones (OMZ), purple bar is the C_{org}/P_{react} range of modern sediments deposited within OMZ, red bar is the C_{org}/P_{react} range of sediments deposited below OMZ and the blue bar is the C_{org}/P_{react} range of sediments deposited on oxic marine shelves.

lacustrine settings (Egger et al., 2015). Subsequently, it appears that Fe-phosphates are rare from nearly all phosphatic depositional systems through Earth history. Therefore, I favour a lack of Fe-phosphates in the primary depositional environment as the simplest explanation for their paucity in the record of phosphatic and ferruginous sedimentary rocks (Johnson et al., 2020). However, the depositional and diagenetic fate of Fe-phosphates such as vivianite is unknown on geologic timescales, so there may be other explanations for their absence from the studied sediments.

In searching for Fe(II)-Phosphates, I focussed on the Sherwin Ironstone which was deposited in a shore face setting at the distal edge of the preserved basin during the early stages of a transgression, as this would give the closest approximation of open ocean conditions available from the studied succession. My reasoning was that, even though the RSB was restricted or semi-restricted during deposition of the studied succession, it was unlikely that the open ocean contained more, or even as much Fe^{2+}, as the RSB during deposition of the Sherwin Ironstone. The absence of Fe(II)-phosphate in the Sherwin Ironstone, but the presence of early authigenic phosphate, suggests that the same could be true for open ocean settings where dissolved Fe concentrations were probably lower. Therefore, it is probable that Fe(II)-phosphate minerals did not act as a major P sink during the mid-Proterozoic.

The data set of Reinhardt et al., (20176) examined fine grained sedimentary rocks from settings interpreted as marginal shelf settings or epicontinental sea (though they included data from several units of the Belt-Purcell Group for which the depositional environment is contested, e.g., there is abundant evidence of deposition within a lacustrine setting). Reinhardt et al., (2017) also filtered out coarse quartz sand-rich samples to avoid the effects of clastic dilution, and those with an Al content below 15 wt% which were not considered to be representative of detrital fine-grained sedimentation. Given that the sedimentary rocks of the RSB fit all of these criteria, it is interesting that no RSB sediments were included in the Reinhardt et al., (2017) study, even though sample material and data are abundant.

I proposed in Chapter 3 of this thesis and Johnson et al., (2020) that restricted epicratonic basins could act as large scale sedimentary sinks for phosphorus during the mid-Proterozoic. Such basins appear to be common during the mid-Proterozoic, suggesting a preservation bias for this type of basin. It is therefore possible that the apparent mid-Proterozoic low in sedimentary phosphate could simply be due to a sampling bias, which amplifies a preservation bias. Throughout Earth history, sedimentary phosphogenesis has commonly taken place via upwelling along continental margins (Baturin, 1971; Brasier, 1980; Burnett et al., 1983; Ruttenberg, 2003). Though Reinhardt et al., (2017) were trying to assess the P evolution of average sea water through time, the

relative paucity of well-preserved upwelling margins from the mid-Proterozoic, may have introduced a bias into the data for this interval. It would be interesting to see if and how the Reinhardt et al., (2017) data set changes with the addition of locations such as the RSB, and when possible mid-Proterozoic preservation biases are accounted for.

However, a mid-Proterozoic open ocean P cycle and reservoir may be of little importance when considering the early history of eukaryotes. Our primary archive for eukaryote microfossils is overwhelmingly from settings such as the RSB, indicating that such locations were important habitats for such organisms, or at least for the preservation of these organisms. In light of epicratonic basins such as the RSB acting as 'concentrating ponds' for P, it is perhaps of little surprise to find that these locations also contain relatively abundant eukaryote fossils. Though again this may be due to preservation and sampling bias. Such biases may have skewed the Proterozoic eukaryotic fossil record sufficiently to produce statistical anomalies in abundance and diversity data (Cohen and Macdonald, 2015). Additionally, "diversity" in the discussion of Proterozoic eukaryotes is really the morphological diversity of the preserved forms. As discussed in Chapter 1, the acritarch fossils presumed to be eukaryotes, are thought to be resting cysts similar to those used by modern unicellular eukaryotes. These cysts are used to hibernate during periods of environmental stress (Martin and Servais, 2020). It would be interesting to compare the diversity of the morphologies of modern resting cysts to the organisms that made them, to try and understand how that would skew our view of modern unicellular eukaryotic organisms. Additionally, the majority of unicellular eukaryotes do not produce resting cysts or have an equivalent stage, therefore, how would our view of modern eukaryote diversity be affected if we could only calculate diversity from resting cyst morphology? However, even as resting cysts, acritarchs may still be informative about ancient environmental conditions. Martin and Servais (2020) suggest that as resting cysts form in response to stresses such as nutrient limitation, therefore decreases in acritarch abundance and diversity may imply a decreases in environmental stresses. Applied to the RSB, the organic rich shales of the Velkerri Formation contain the most P, but also the lowest abundance and diversity of acritarchs (Javaux and Knoll, 2017). Applying the hypothesis of Marin and Servais (2020), would invert the eco structure of the Velkerri Formation waters, such that diversity and abundance of eukaryotes increased away from shore, instead of towards it, and the apparent lower diversity and abundance of acritarchs in open water sediments is an ecological and preservation bias (Javaux et al., 2001).

Phosphorous was also present in the Basinal Region of the RSB (Chapter 4 this thesis). Here, phosphate was present in the Velkerri Formation as possible phosphatised bacteria – likely S-oxidisers – and as microspheres that probably formed as a by-product of microbial phosphogen-

esis. Phosphate is also found as precipitated grains similar to those found in the Sherwin Ironstone, but with a lower abundance. The concentration of phosphate by S-oxidisers is well documented in modern settings (Bailey et al., 2013; Schulz and Schulz, 2005), and there are several candidates in the sedimentary record that are almost identical in form and chemistry to the Velkerri examples described here (Cosmidis et al., 2013; Keighley et al., 2018). Interestingly, no phosphatic sediments or authigenic P-bearing phases were observed in the Proximal Regions of the RSB. However, no bulk P measurements were made, or are available for the cores 99VR and 12BC which sampled the Proximal Regions, so the bulk abundance is unknown in these cores. This may simply be an issue of sampling bias; I prioritised making thin sections of lithologies that were exclusive to the Proximal Regions, rather than lithologies that overlapped with the other regions of the RSB. I made this choice so as to maximise the variety of depositional environments investigated with the time and resources available. In this respect, the fine-grained sediments of the Proximal Regions are still relatively understudied compared to their Basinal and Distal Region counter parts.

The data presented here indicate that P was abundant and bioavailable in the RSB, but that abundance and bioavailability may have varied locally. Relative C_{org}/P_{react} enrichment in the 'euxinic' middle Velkerri Formation suggests that standard "anoxic water" mechanisms of P regeneration were not operational during deposition (e.g., Van Cappellen and Ingall, 1994). The reasons for this are unclear from the current data set, but one hypothesis could be that as euxinic conditions were restricted in time and space, and mostly confined to the seabed or below, there was not a physically large enough of a redox interface for large scale euxinic P regeneration to occur. Additionally, as other authors have suggested, low abundance or bioavailability of other nutrients, or nutrient co-limitations, may have impeded the biological cycling of P during deposition of the middle Velkerri (Cox et al., 2016). If the data of Reinhard et al (2017) are taken at face value, and we assume that the sampled locations all represent oceanic margins, then the P enrichment in the RSB (and other basins on the margin of the McArthur-Yangliao gulf) relative to oceanic shelves of the same age, may represent a confluence of conditions that allowed the collection, concentration and entrapment of riverine and upwelling P within the RSB. As a result of this palaeogeography, much of the P deposited by rivers into the RSB remained trapped there for the last ~1400 Ma. In this respect, the RSB was extremely efficient P trap.

5.5. Mid-Proterozoic paralic and terrestrial environments

5.5.1. Local terrestrial environments and paleohydrology

In the lower part of the studied succession, paralic and terrestrial environments in the RSB are typical of those in the subtropics: evaporite prone shoreface and carbonate lagoons at the coast with arid fluvial systems and thin regolith inland. In this respect, the RSB is very similar to other mid-Proterozoic sequences such as the Torridonian of Scotland or the Bylot of Baffin Island (Gibson et al., 2017; Williams, 1968). Evidence of surface oxygenation is plentiful in the form of haematite coated grains, and goethite and limonite rich cambisol- to vertisol-like regolith. Although these primary phases show that atmospheric oxygen was present, they cannot quantify the concentration of oxygen. Additionally, depositional, diagenetic and hydrothermal processes complicate the formation and preservation of palaeosols and regolith, such that quantifying the redox state of the depositional environment is far from straightforward (Bankole et al., 2016; Beukes et al., 2002; Blodgett et al., 1993; Chemtob et al., 2017; Pufahl and Hiatt, 2012; Rasmussen et al., 2020; Walker, 1976). Oxygen isotopes have been used elsewhere to investigate ancient oxygen levels recorded by paleosols (Mack and Cole, 2005; Retallack, 2005), but these studies required pedogenic calcite and gypsum which were only present in minor amounts in the studied samples. However, the lack of caliche, calcrete or other indicators of persistent ground waters in RSB regolith does indicate that conditions must have been particularly arid (though again this could be a preservational artifact). Even in terrestrial environments of the RSB, the oxygen penetration depth was very shallow below surface regolith, as evidenced by the abundant primary ferrous clays. This observation could indicate very low oxygen content in the overlying atmosphere, though there are other explanations. As I showed in the Velkerri Formation, microbial mats can act as effective seals between contrasting environmental redox states. There are abundant microbial textures in the terrestrial sediments that support the existence of a terrestrial microbiota (e.g., micro stromatolites between sol peds and cutans, webbed fabrics in thin sections). Therefore, it is likely that reducing conditions were mediated by this microbiota, either as a direct modification of the environment to suit their requirements, or as a by-product of their metabolism. It is also possible that microbial EPS helped to seal the underlying sediments, enabling early cementation by ferrous clays. Given the limited number of sampled drill cores, our observations may be skewed by having sampled the localities where microbial influence or reducing conditions were most abundant. However, the sampled cores are tens to hundreds of km apart, and these conditions are persistent through the cores suggesting that reducing conditions were not a localised phenomenon in terrestrial settings of the RSB. Later diagenetic or hydrothermal reduction of the primary terrestrial oxides is also not

supported by data presented here. Primary sedimentary soil structures (e.g., slickensides in rotated cutans), are still evident in both oxidised and reduced sediments. It is unlikely that such delicate structures, or the microbial structures, would survive any extensive diagenetic or hydrothermal recrystallisation. Finally, the chemistry of the reduced minerals, berthierine, odinite and low Mg pedogenic chlorite are typical of reducing conditions in low temperature surface environments close to a chemocline (Retallack, 1997).

The upper part of the studied succession documents a shift towards a wetter climate. The formation of laterite soil indicates periods of intense wetting and drying (Rasmussen et al., 2020; Retallack, 1997). Similarly, the formation of kaolinitic flint clays supports an increased hydrological cycle (Keller, 1968). Flint clays typically form in wet, low-lying areas that are fed with sediments from a granitic hinterland. Rather than forming a laterite, the repeated wetting and drying, combined with a steady groundwater flow, strips all the mobile ions from the clay, leaving behind an Si-rich kaolinite (Keller, 1968). Kaolinite itself is a sedimentological indicator of granite that has been weathered under warm, wet conditions. The fact that there is a basinwide shift from illite to kaolinite observed in XRD data, combined with sedimentological evidence for a similar shift in adjacent terrestrial localities, strongly suggests a change in the climate and hydrology of the RSB (Corentin et al., 2020).

These data also highlight heterogeneity in the hydrogeography of the terrestrial environments in the RSB. Laterites are most common and well developed along the southern Proximal Region (Fig 5, Chapter 2). Conversely, laterites are rare, but flint clays are well developed and up to tens of meters thick in the western Proximal Region (Fig 5, Chapter 2). This heterogeneity suggests major differences in paleo groundwater flow within the wider RSB. This may have been controlled by local subsidence rates related to regional tectonics (Fig 3, Chapter 2). The southern Proximal Region was a stable tectonic block throughout deposition of the studied succession (Munson, 2016). By contrast, the western Proximal Region experienced multiple tectonic episodes in the immediate vicinity, and significant uplift in the granitic hinterland that formed the sediment source, and presumably the rainwater catchment (Munson, 2016).

The accumulation of lateritic soil and primary oxides in terrestrial sediments is consistent with changes in the marine realm, where an increase in primary productivity is associated with increasing oxygenation during deposition of the Amungee member of the Velkerri Formation. Trace element data from authigenic pyrite from the RSB suggest that this represents a global oxygenation event (Large et al., 2019; Mukherjee et al., 2019; Mukherjee and Large, 2016; Yang et al., 2020). A localised carbon burial event would only produce a modest release of oxygen. However,

this oxygenation/carbon burial event may have occurred on a larger scale due to contemporaneous tectonic events. During this time, the Nuna supercontinent underwent the rifting and rotation that would lead to the formation of Rodinia. Regionally, the rifting of Protoaustralia, North China and Siberia, from Laurentia is associated with the emplacement of several mafic intrusive suits over a ~15 million year period (Bodorkos et al., 2021; Ernst et al., 2008; Yang et al., 2020; Zhang et al., 2017).

Elsewhere in the geologic record, LIP eruptions are associated with global warming, an enhanced hydrological cycle and deposition of organic rich black shales in marine environments (Föllmi, 2012; Kidder and Worsley, 2010; Rudmin et al., 2020; Wignall, 1994). A similar process could have taken place during continental reorganisation in the mid-Proterozoic, with nutrients released from the LIP eruptions bolstered by increased run-off from the naked continents. Palaeogeographic reconstructions during this interval place northern Australia and the RSB on the westward facing margin of a larger intracontinental actively rifting marine basin known as the McArthur-Yanliao gulf – comparable to the early stages of the Gulf of Mexico in the Cretacous (Kirscher et al., 2020; Mitchell et al., 2020). This paleogeographic position would place the RSB in the correct oceanographic position to receive nutrient rich waters derived from coastal upwelling. Sheltered epicratonic seas such as the RSB, would be host to enhanced eutrophication and organic carbon burial. These basins would effectively remove organic carbon and nutrients such as P from global cycles and store them indefinitely. The epicratonic basins of the mid-Proterozoic would essentially perform the same function as the epicontinental shelf seas of the Phanerozoic, but being much longer lived, they had the capacity to capture, and then store, more nutrients over longer timescales (Allen et al., 2015).

5.6. Implications for the wider mid-Proterozoic world

5.6.1. Environments in the rear-view mirror are not as reducing as they appear

The Roper Superbasin was a partially to fully restricted during deposition of the studied interval, and so not reflective of the global ocean. Any global signal recorded within the authigenic sediments of the RSB will undoubtedly be overprinted by much stronger local signals, sometimes representing conditions which may only be present in the immediate vicinity of the core or outcrop that is being sampled.

Given that such epicratonic basins are the primary source of data on mid-Proterozoic surface environment, it may seem troubling that they cannot give us a globally relevant information the way open ocean sediments can. But these localised time capsules are still important archives and

can shed light on important processes that may have been common or universal in mid-Proterozoic environments. We do not have enough information to generalise a global model for oceanic redox during the mid-Proterozoic. The preservation bias imposed by the plate configuration and tectonics of the mid-Proterozoic means that the majority of the surviving sediments will come from these atypical basins such as the RSB (Allen et al., 2015). As is well demonstrated with modern marine basins, the degree of restriction can have a large impact on the ability of sedimentary fill to record information about the global ocean, and that in such environments, sediments may record redox processes and products that are fundamentally different than those characterising the overlying water column, even without the interference of microbial mats. Therefore, it is necessary that future studies combine geochemistry with sedimentology and mineralogy and petrography and a full knowledge of the regional geology so that they can assess whether sediments reflect the overlying water column, and if those waters are reflective of the wider global ocean. It is interesting to note that the Kaltasy Formation, Siberia, a mid-Proterozoic succession which may actually record open ocean conditions, shows an ocean redox structure much closer to the modern ocean, albeit on an upwelling margin (Sperling et al., 2014). Even if my interpretation of the RSB as a restricted atypical setting is incorrect, and it does in fact represent the open ocean, then my observations of redox environments are still valid. In this case, previous interpretations of the mid-Proterozoic global ocean would still need to be reassessed.

5.6.2. Eukaryote evolution

Geographical restriction from the wider contemporaneous global ocean, means that the RSB was probably not representative of global oceanic biogeochemistry. Observations made in this study align with data compilations indicating that the RSB and other basins bordering the intracontinental McArthur-Yanliao gulf had sedimentary C_{org}/P_{react} ratios and P abundances comparable to modern oxic marine settings, even in high TOC units that are thought to represent deposition under a euxinic water column such as the middle Velkerri Formation (Canfield et al., 2020). These data are in contrast with P abundances from bulk sedimentary P compilations for mid-Proterozoic sedimentary rocks (Reinhard et al., 2017). At face value these data indicate that the waters of the RSB were not typical of marine shelves during the mid-Proterozoic. However, the C_{org}/P_{react} of ancient life and environments may have changed over geological time and may not be directly comparable to modern equivalents, not least because of the apparent dominance of prokaryotes in mid-Proterozoic marine environments (Canfield et al., 2020; Pahlow and Riebesell, 2000; Planavsky, 2014).

Even though the RSB does not reflect the global ocean in terms of biogeochemistry, it was clearly an important habitat for early eukaryotes because their fossils are abundant within the RSB succession. As demonstrated throughout this thesis, phosphorus was not limited during deposition of the studied sediments. So perhaps some other environmental factor suppressed their evolution and diversification. Recent work has shown that N may have been limited in RSB waters (Cox et al., 2019; Koehler et al., 2017; Stüeken, 2013). As N is another essential macro-nutrient, severe limitation on geological timescales could have had a negative impact on eukaryote evolution and diversity (Lloyd et al., 2004). The limitation of N during deposition of RSB sediments is thought to have been caused by oscillating redox conditions, but redox oscillations are also harmful to micro-eukaryotes directly, such as by weakening the cell membrane (Lloyd et al., 2004; Porter et al., 2018; Pörtner, 2001; Rickaby and Eason Hubbard, 2019).

Even though many microorganisms are capable of fixing their own N, meeting these needs may not be possible if essential metals such as Mo are limitied, as was possibly the case for the RSB (Cox et al., 2016). While P was not limited, this thesis has shown that rapid redox oscillations were common across the RSB during the studied interval. N limited oceans with constant redox fluctuations harmful to eukaryotes would tally with data from biomarker studies that suggest that eukaryotes were a minor component of mid-Proterozoic ecosystems (Jarrett et al., 2019). However, the N limiting cycles reported above occurred on geologically short timescales of perhaps 5 million years and may have been a local phenomenon. A detailed investigation of successions from across the mid-Proterozoic and from a range of depositional environments would help further illuminate the role of N cycling in eukaryote evolution.

Our knowledge of micro-eukaryotes is skewed towards highly derived taxa that have an economic benefit (e.g., yeast), are relevant to other scientific problems (e.g., foraminifera), or are human parasites (e.g., giardia, malaria). The vast majority of micro-eukaryotes are unknown and unstudied. It is therefore difficult to use the ecological preferences and tolerances of modern eukaryotes as models for their ancient ancestors. Additionally, as noted above, the apparent lack of diversity in mid-Proterozoic eukaryotes may be a biological and preservational artefact. Modern eukaryotes thrive in environments far less hospitable than proposed here for the mid-Proterozoic, such as the sulphidic waters of the Black Sea (Behnke et al., 2010; Wylezich and Jürgens, 2011). Studies of these organisms have shown that the traits that allow these organisms to survive in hostile environments are conserved, meaning that low oxygen, sulphur-rich conditions were adapted to early in the organism's evolutionary history. Perhaps it makes sense then that modern, derived eukaryote biomarkers are less abundant in ancient sediments. It is possible that the early eukary-

otic ancestors were biochemically indistinguishable from the prokaryotes they shared the world with, a hypothesis supported by recent studies of micro-eukaryotes .

In reality, though, we do not know that there was a delay. We look at the biological world through the inevitable bias of being complex metazoans ourselves. It's understandable that we want to understand why the life that gave rise to us, and that looks like us appeared so recently in Earth history. But does 'recent' mean 'late' or 'delayed'? Even if permissible environments for more complex eukaryotes existed prior to the late Neoproterozoic, it does not mean that organisms would immediately be able to exploit those environments or their resources. It takes time to evolve the molecular machinery to be able to more efficiently utilise resources that are already available, so why would new adaptations to new resources appear and develop so quickly? There was abundant oxygen, and enough nutrients to support sauropod sized reptiles in Carboniferous, yet reptiles remained relatively small for another 100 Myrs (Benson et al., 2014; Müller and Reisz, 2006).

The temporal and evolutionary distance between the first reptile and a giant dinosaur is vastly less than that between the earliest eukaryotes and modern protists, so why would they be expected to evolve any faster (even accounting for relative reproductive rates)? It also seems like a fundamental misunderstanding of evolutionary processes to assume that biological complexity is an inevitability that is achieved by adding ingredients such as oxygen. Any environmental influence is likely a complex interplay between the different abiotic elements of the environment influencing each other in different ways and on different temporal and spatial scales. Adding biology and evolution through natural selection into this already complex web seems like it may be beyond the scope of modern science to grasp just yet. It's little wonder then, that humans are drawn to the idea of single important pivots as the cause for the major step changes in biological evolution. It makes a neat story, and stories are how humans like to best understand the world around them.

Each evolutionary step change; prokaryote to eukaryote, eukaryote to metazoan etc., has occurred progressively quicker, with less time between each major biological innovation. Similar patterns of exponentially increasing complexity are seen in areas as far removed from evolutionary biology such as the growth of civilisations, or the development of new technologies, though you could argue that they are both consequences of biology (Sood and Tellis, 2005). It is inevitable that the environment in which early eukaryotes lived influenced their evolution and diversification. But it is an oversimplification to think that an otherwise rapid trajectory from the first eukaryotes to the first animals, was slowed to a crawl for lack of a single missing resource.

It is a conceit of humans to assume that we, as complex multicellular organisms, represent a goal towards which all life is striving. The fact that endosymbiosis occurred successfully only twice (as far as we know, counting initial endosymbiosis and then the acquisition of chloroplasts), suggests that life does not have an evolutionary drive to become more complex. If anything, it is the other way around. Compare for example, the 'highly evolved' earth worm to the more 'primitive' rag worm. If not for the happy accident of the successful endosymbiotic event, the Earth may still have been inhabited only by bacteria and archaea today. Becoming eukaryotic opened up a vast new evolutionary landscape to life, it is unsurprising that it took time for life to explore that territory and stumble on the opportunities of complex multicellularity in yet another happy accident. But complex multicellularity is just one way to solve the problems of life, most eukaryotes did just as well to stay as single cells. There was no 'delay' in eukaryote evolution because there was, and is, no schedule. Eukaryotes stumbled through their evolution in a series of happy accidents. The story of life is no less enthralling or incredible for this, and personally, I quite like being a happy accident.

5.7. Future work

Emphasising integrated basin studies

This thesis highlights the importance of integrating methods and sub-disciplines when using the sedimentary record to investigate and reconstruct ancient environments. Many studies are heavily reliant on a single method, e.g., bulk geochemistry or petrography. But results are given greater depth, and our understanding of the past becomes richer, when we combine the tools and expertise available. This is not a slight against previous RSB studies. Previous studies have been limited by the sample materials, methods and time available. Jackson and contemporaries in the late 1980s had a limited number of cores and outcrop available. Subsequent studies relied on the interpretations of previous works, as we all must. This integrated method could be of great use when applied to a number of 'anoxic' basins throughout Earth history. The early Jurassic of the Cleveland Basin of north eastern UK has a similar sediment fill and paleogeography to the Roper Superbasin and was partially deposited during the Toarcian Oceanic Anoxic Event. Petrographic observations of coastal outcrop I made during my undergrad project suggested an environmental model analogous to the Velkerri Formation. An integrated study of core material and mine facings from the wider basin could add a layer of detail that is currently missing from our understanding of how anoxia develops and moves around such basins.

Testing the resolution of bulk geochemical proxies

When relying on bulk geochemical data, we tend to overinterpret the duration and geographic extend of a particular redox state. The Precambrian rock record is particularly prone to these pitfalls. But how many claims about younger intervals are made on similar grounds? In my undergraduate work on the early Jurassic of Yorkshire (UK), I found a number of sedimentological features that contradicted environmental interpretations based on geochemical data and limited petrology. Rocks allegedly deposited below storm wave base with water column euxinia contained cross bedding, macro benthos and in-faunal traces. The Yorkshire Lias is relatively well studied compared to the RSB, with abundant core and outcrop material. Yet geochemical interpretations still clash with petrological and sedimentological observations (Bennet and Canfield, 2020). Bulk geochemical proxies tells us that a particular redox environment has been recorded in those sediments. However, they do not tell us the geographic or temporal extent of those redox environments. This could be rectified by integrating geochemical and petrological studies of ancient sediments, paired with studies of modern environments prone to redox fluctuations (Appalachian et al., 2019; Bennett and Canfield, 2020; Yamaguchi et al., 2010).

The origin of sedimentary pyrite in the RSB

Sedimentary pyrite has been a major piece of evidence for widespread euxinia in previous studies of the RSB and beyond. My petrogeological observations indicate that bulk sampling probably captured results from several generations of pyrite, only some of which was authigenic. Targeted geochemical studies have shown that authigenic pyrite in the RSB supports suggestions that RSB waters were more oxic than previously thought (Murkherjee and Large, 2016). However, time did not permit targeted geochemical investigation of the various pyrite generations in this study. A campaign that included more framboid measurements and petrographically targeted geochemical study of sulphides using nanoSIMS and LA-ICP-MS, would help to investigate the origin of the various stages of pyrite, and quantify how much, if at all, they had contributed to previous environmental models.

Re-evaluation of Cr isotope data

Planavsky et al., (2018) have proposed mid-Proterozoic atmospheric O_2 levels as low as 0.01 % of present atmospheric levels. This hypothesis is based on Cr isotope data obtained from various iron-rich chemical sediments including the Sherwin Ironstone. However, in Chapter Two of this thesis, I showed that previous studies had been carried out on heavily weathered material, and that the original mineralogy of the Sherwin Ironstone was composed of ferrous-clays, rather than ferric-oxides. Cr isotope studies of unaltered Sherwin Ironstone would help us to quantify how different, if at all, previous Cr values are in fresh versus unaltered Sherwin Ironstone. This would improve both our understanding of Cr isotopes as an environmental redox proxy and help us quantify atmospheric O_2 levels during the mid-Proterozoic.

Extending the Roper Superbasin

The full extent of the RSB is still unknown despite an increasing abundance of drill core and known outcrop. The South Nicholson Basin (SNB) to the southeast of the RSB, and the Tennent Creek (TC) Province, directly south of the RSB, both hold sediment packages that are of an equivalent age to the Roper Group. Future studies could perform similar style studies on SNB and TC sediments held by Geoscience Australia to characterise their depositional environments and correlate them with the Roper Group. Additionally, there is no available core material for the southwest sector of the RSB, and Proterozoic sediments remain buried below Phanerozoic cover. A desk-based study of available geophysical data could help to ascertain if RSB sediments survive in that area, and if so, highlight prospective areas for drilling.

Taphonomy of microfossil preservation

Previous palynological studies have highlighted possible ecological preferences in RSB microfossils (e.g., Javaux and Knoll, 2002). However, the effect of taphonomy on fossil preservation, and how this may skew observed trends, has not been fully assessed. Preservation and abundance of organic walled microfossils is noted to be lower in high TOC bearing sediments. As my sample set contains contemporaneous shallow water and deeper water sediments, with both high and low TOC, Eukaryote ecological preferences and the taphonomic effect of high TOC could be examined and compared to published data.

Preservational biases

How do preservational biases in the rock record skew our view of the ancient world? The mid-Proterozoic is 'known' to be a time of unusual stability on the C and O isotope record, but is that a reflection of reality or sampling resolution? If the Phanerozoic was randomly sampled at the same temporal resolution as an equivalent interval of the mid-Proterozoic, how many of the major $\partial^{13}C$ and $\partial^{18}O$ isotope excursions would be captured? Similarly, how many different environments or depositional settings are really sampled in the mid-Proterozoic? There may be a bias towards epicratonic settings such as the RSB, which do not represent typical marine environments. A targeted study would help to answer both these questions, by helping us quantify the spatial and temporal resolution of this bias by showing that true deep-water deposits from continental margins and the open ocean are indeed rare in the mid-proterozoic. This study could be paired with detailed modelling to understand how deep open oceans would behave with respect to the important geobiological cycles (Canfield et al., 2020).

5.8. Conclusion

The upper Roper Group and Tijunna Group were deposited between 1.4 and 1.3 Ga across the Roper Superbasin, Northern Territory, Australia. This thesis provides a new depositional and environmental model for the RSB based on a combined high-resolution sedimentological, mineralogical and geochemical study. The RSB was partially to fully restricted during deposition of the studied succession, and as such, any global ocean signal may have been overprinted by the local environmental conditions. Environmental conditions within the RSB, including sedimentation style and environmental redox, were highly heterogeneous in both space and time within the RSB. As such, both sedimentology and environmental chemistry could change rapidly between locations within the RSB on scales from a few km to a few mm. Black shales were deposited above storm wave base, or shallower, during periods of increased primary productivity driven by an enhanced hydrological cycle and weathering, themselves a consequence of LIP eruption. Euxinic conditions did not extend above the sediment-water interface, and bottom and shallow pore waters oscillated rapidly between ferruginous to oxic conditions.

Ferruginous conditions were widespread from offshore to shallow marine waters, and even within the terrestrial ground water table. During periods of oceanic connection, the upwelling of deep oceanic waters promoted the deposition of ironstones and other Fe-rich authigenic sediments across the RSB. Despite widespread ferruginous conditions, and contrary to expectations, P remained abundant and bioavailable throughout deposition of the studied interval across all

environments. The extensive deposition of Fe-clays and the absence of Fe(II)-phosphates suggests that Fe-phosphate was not an effective sink for P during the mid-Proterozoic, perhaps because silica outcompeted P for Fe. As a consequence, the precipitation of calcium-fluorapatite in large epicratonic basins such as the RSB was probably the major sink for P during the mid-Proterozoic.

Terrestrial environments record an up section change from an arid to a wetter climate, as well as increasing atmospheric oxygen, coincident with the eruption of a large igneous province, an increase in marine primary productivity and carbon burial. A global increase in the production and burial of organic matter in restricted epicratonic seas is proposed as a mechanism to drive an increase in atmospheric oxygen content. The rise in oxygen is supported by other studies of the RSB, and equivalent successions globally.

Even though the restricted nature of the RSB limits its use for understanding global ocean redox and geobiological cycles, it is still an important location for understanding the co-evolution of Earth surface environments and early eukaryotic life. The abundant acritarch fossils found in RSB sediments indicate that early eukaryotes thrived in such places which may have acted as nutrient traps. Even at the best of times, viewing the past through sedimentary rocks is like trying to describe a whole planet through key holes that have been chosen at random. Attempting to use the information gleaned from one or two keyholes, to characterise an entire planet, for geologically significant intervals of time, will at best only ever give an outline of what is on the other side, or at worst give the wrong impression completely. This study therefore highlights the importance of using sequence stratigraphy, sedimentology, petrography, mineralogy and geochemistry together, with multiple sample sources, to place data and interpretations into the correct context. This intergrated approachs allows us increase the number of keyholes so we can more accurately describe what is on the other side. However, the RSB represents only one small part of the Earth surface during the interval of deposition. No matter how big the keyhole, we are still attempting to describe the life of a whole planet by looking at a single hole full of mud.

5.9. References

Allen, P.A., Eriksson, P.G., Alkmim, F.F., Betts, P.G., Catuneanu, O., Mazumder, R., Meng, Q., Young, G.M., 2015. Chapter 2 Classification of basins, with special reference to Proterozoic examples. Geol. Soc. Lond. Mem. 43, 5–28. https://doi.org/10.1144/M43.2

Andrews, S.D., Trewin, N.H., Hartley, A.J., Weedon, G.P., 2010. Solar variance recorded in lacustrine deposits from the Devonian and Proterozoic of Scotland. J. Geol. Soc. 167, 847–856. https://doi.org/10.1144/0016-76492009-105

Appalachian, C., Liu, J., Algeo, T.J., Jaminski, J., Kuhn, T., Joachimski, M.M., 2019. Evaluation of high-frequency paleoenvironmental variation using an optimized cyclostratigraphic framework : Example for C-S-Fe analysis of. Chem. Geol. 525, 303–320. https://doi.org/10.1016/j.chemgeo.2019.07.019

Arnold, G.L., Anbar, A.D., Barling, J., Lyons, T.W., 2004. Molybdenum Isotope Evidence for Widespread Anoxia in Mid-Proterozoic Oceans. Science 304, 87–90. https://doi.org/10.1126/science.1091785

Bailey, J. V., Corsetti, F.A., Greene, S.E., Crosby, C.H., Liu, P., Orphan, V.J., 2013. Filamentous sulfur bacteria preserved in modern and ancient phosphatic sediments: Implications for the role of oxygen and bacteria in phosphogenesis. Geobiology 11, 397–405. https://doi.org/10.1111/gbi.12046

Bankole, O.M., Albani, A.E., Meunier, A., Rouxel, O.J., Gauthier-Lafaye, F., Bekker, A., 2016. Origin of red beds in the Paleoproterozoic Franceville Basin, Gabon, and implications for sandstone-hosted uranium mineralization. Am. J. Sci. 316, 839–872. https://doi.org/10.2475/09.2016.02

Baturin, G.N., 1971. Stages of Phosphorite Formation on the Ocean Floor. Nat. Phys. Sci. 232, 61–62. https://doi.org/10.1038/physci232061a0

Behnke, A., Barger, K.J., Bunge, J., Stoeck, T., 2010. Spatio-temporal variations in protistan communities along an O_2 /H_2S gradient in the anoxic Framvaren Fjord (Norway). FEMS Microbiol. Ecol. 72, 89–102. https://doi.org/10.1111/j.1574-6941.2010.00836.x

Bekker, A., Holland, H.D., 2012. Oxygen overshoot and recovery during the early Paleoproterozoic. Earth Planet. Sci. Lett. 317–318, 295–304. https://doi.org/10.1016/j.epsl.2011.12.012

Bennett, W.W., Canfield, D.E., 2020. Redox-sensitive trace metals as paleoredox proxies: A review and analysis of data from modern sediments. Earth-Sci. Rev. 204, 103175. https://doi.org/10.1016/j.earscirev.2020.103175

Benson, R.B.J., Campione, N.E., Carrano, M.T., Mannion, P.D., Sullivan, C., Upchurch, P., Evans, D.C., 2014. Rates of Dinosaur Body Mass Evolution Indicate 170 Million Years of Sustained Ecological Innovation on the Avian Stem Lineage. PLoS Biol. 12, e1001853. https://doi.org/10.1371/journal.pbio.1001853

Beukes, N.J., Dorland, H., Gutzmer, J., Nedachi, M., Ohmoto, H., 2002. Tropical laterites, life on land, and the history of atmospheric oxygen in the Paleoproterozoic. Geology 30, 491–494. https://doi.org/10.1130/0091-7613(2002)030<0491:TLLOLA>2.0.CO;2

Blodgett, R.H., Crabaugh, J.P., McBride, E.F., 1993. The Color of Red Beds—A Geologic Perspective, in: Soil Color. John Wiley & Sons, Ltd, pp. 127–159. https://doi.org/10.2136/sssaspecpub31.c8

Bodorkos, S., Crowley, J.L., Claoué-Long, J.C., Anderson, J.R., Jr, C.W.M., 2021. Precise U–Pb baddeleyite dating of the Derim Derim Dolerite, McArthur Basin, Northern Territory: old and new SHRIMP and ID-TIMS constraints. Aust. J. Earth Sci. 68, 36–50. https://doi.org/10.1080/08120099.2020.1749929

Boyd, G.A., Wallace, M.W., Holdgate, G.R., and Gallagher, S.J., 2004. Marine clays and porosity evolution in the Nullawarre Greensand, Otway Basin, southeastern Australia, in: Paper Presented at Petroleum Exploration Society of Australia Eastern Australian Basin Symposium II. pp. 537-552.

Brasier, M.D., 1980. The Lower Cambrian transgression and glauconite-phosphate facies in western Europe. J. Geol. Soc. 137, 695–703. https://doi.org/10.1144/gsjgs.137.6.0695

Burnett, W.C., Roe, K.K., Piper, D.Z., 1983. Upwelling and Phosphorite Formation in the Ocean, in: Suess, E., Thiede, J. (Eds.), Coastal Upwelling Its Sediment Record: Part A: Responses of the Sedimentary Regime to Present Coastal Upwelling, NATO Conference Series. Springer US,

Boston, MA, pp. 377–397. https://doi.org/10.1007/978-1-4615-6651-9_18
Caird, R.A., Pufahl, P.K., Hiatt, E.E., Abram, M.B., Rocha, A.J.D., Kyser, T.K., 2017. Ediacaran stromatolites and intertidal phosphorite of the Salitre Formation, Brazil: Phosphogenesis during the Neoproterozoic Oxygenation Event. Sediment. Geol. 350, 55–71. https://doi.org/10.1016/j.sedgeo.2017.01.005
Canfield, D.E., Bjerrum, C.J., Zhang, S., Wang, H., Wang, X., 2020. The modern phosphorus cycle informs interpretations of Mesoproterozoic Era phosphorus dynamics. Earth-Sci. Rev. 208, 103267. https://doi.org/10.1016/j.earscirev.2020.103267
Cappellen, P. Van, Ingall, E.D., 1994. Benthic phosphorus regeneration, net primary production and ocean anoxia. Paleoceanography 9, 677–692.
Caswell, B.A., Coe, A.L., 2014. The impact of anoxia on pelagic macrofauna during the Toarcian Oceanic Anoxic Event (Early Jurassic). Proc. Geol. Assoc. 125, 383–391. https://doi.org/10.1016/j.pgeola.2014.06.001
Caswell, B.A., Coe, A.L., 2013. Primary productivity controls on opportunistic bivalves during Early Jurassic oceanic deoxygenation. Geology 41, 1163–1166. https://doi.org/10.1130/G34819.1
Chafetz, H.S., Reid, A., 2000. Syndepositional shallow-water precipitation of glauconitic minerals 136, 29–42.
Chemtob, S.M., Nickerson, R.D., Morris, R.V., Agresti, D.G., Catalano, J.G., 2017. Oxidative Alteration of Ferrous Smectites and Implications for the Redox Evolution of Early Mars. J. Geophys. Res. Planets 122, 2469–2488. https://doi.org/10.1002/2017JE005331
Cohen, P.A., Macdonald, F.A., 2015. The Proterozoic Record of Eukaryotes. Paleobiology 41, 610–632. https://doi.org/10.1017/pab.2015.25
Cole, D.B., O'Connell, B., Planavsky, N.J., 2018. Authigenic chromium enrichments in Proterozoic ironstones. Sediment. Geol. 372, 25–43. https://doi.org/10.1016/j.sedgeo.2018.05.002
Corentin, P., Deconinck, J.F., Pellenard, P., Amédro, F., Bruneau, L., Chenot, E., Matrion, B., Huret, E., Landrein, P., 2020. Environmental and climatic controls of the clay mineralogy of Albian deposits in the Paris and Vocontian basins (France). Cretac. Res. 108. https://doi.org/10.1016/j.cretres.2019.104342
Cosmidis, J., Benzerara, K., Gheerbrant, E., Estève, I., Bouya, B., Amaghzaz, M., 2013. Nanometer-scale characterization of exceptionally preserved bacterial fossils in Paleocene phosphorites from Ouled Abdoun (Morocco). Geobiology 11, 139–153. https://doi.org/10.1111/gbi.12022
Cox, G.M., Jarrett, A., Edwards, D., Crockford, P.W., Halverson, G.P., Collins, A.S., Poirier, A., Li, Z.-X., 2016. Basin redox and primary productivity within the Mesoproterozoic Roper Seaway. Chem. Geol. 440, 101–114. https://doi.org/10.1016/j.chemgeo.2016.06.025
Cox, G.M., Sansjofre, P., Blades, M.L., Farkas, J., Collins, A.S., 2019. Dynamic interaction between basin redox and the biogeochemical nitrogen cycle in an unconventional Proterozoic petroleum system. Sci. Rep. 9, 5200. https://doi.org/10.1038/s41598-019-40783-4
Derry, L.A., 2015. Causes and consequences of mid-Proterozoic anoxia. Geophys. Res. Lett. 42, 8538–8546. https://doi.org/10.1002/2015GL065333
Donnelly, T.H., Crick, I.H., 1988. Depositional environment of the middle proterozoic velkerri formation in Northern Australia: Geochemical evidence. Precambrian Res. 42, 165–172. https://doi.org/10.1016/0301-9268(88)90015-0
Egger, M., Jilbert, T., Behrends, T., Rivard, C., Slomp, C.P., 2015. Vivianite is a major sink for phosphorus in methanogenic coastal surface sediments. Geochim. Cosmochim. Acta 169, 217–235. https://doi.org/10.1016/j.gca.2015.09.012
Ernst, R.E., Wingate, M.T.D., Buchan, K.L., Li, Z.X., 2008. Global record of 1600-700 Ma Large Igneous Provinces (LIPs): Implications for the reconstruction of the proposed Nuna (Columbia) and Rodinia supercontinents. Precambrian Res. 160, 159–178. https://doi.org/10.1016/j.precamres.2007.04.019
Flannery, E.N., George, S.C., 2014. Assessing the syngeneity and indigeneity of hydrocarbons in the ~1.4 Ga Velkerri Formation, McArthur Basin, using slice experiments. Org. Geochem. 77, 115–125. https://doi.org/10.1016/j.orggeochem.2014.10.008
Föllmi, K.B., 2012. Early Cretaceous life, climate and anoxia. Cretac. Res. 35, 230–257. https://doi.

org/10.1016/j.cretres.2011.12.005
Garven, G., Bull, S.W., Large, R., 2001. Hydrothermal fluid flow models of stratiform ore genesis in the McArthur Basin, Northern Territory, Australia. https://doi.org/10.1046/J.1468-8123.2001.00021.X
Gibson, T.M., Wörndle, S., Halverson, G.P., Agiæ, H., Lamothe, K.G., Rainbird, R.H., 2017. Composite stratigraphic section of exceptionally exposed middle Bylot Supergroup carbonate rocks along Tremblay Sound , northwestern Baffin Island , Nunavut 81–92.
Gomez-Saez, G.V., Dittmar, T., Holtappels, M., Pohlabeln, A.M., Lichtschlag, A., Schnetger, B., Boetius, A., Niggemann, J., 2021. Sulfurization of dissolved organic matter in the anoxic water column of the Black Sea. Sci. Adv. 7, eabf6199. https://doi.org/10.1126/sciadv.abf6199
Guan, C., Zhou, C., Wang, W., Wan, B., Yuan, X., Chen, Z., 2014. Fluctuation of shelf basin redox conditions in the early Ediacaran: Evidence from Lantian Formation black shales in South China. Precambrian Res. 245, 1–12. https://doi.org/10.1016/j.precamres.2014.01.003
Guilbaud, R., Poulton, S.W., Thompson, J., Husband, K.F., Zhu, M., Zhou, Y., Shields, G.A., Lenton, T.M., 2020. Phosphorus-limited conditions in the early Neoproterozoic ocean maintained low levels of atmospheric oxygen. Nat. Geosci. 13, 296–301. https://doi.org/10.1038/s41561-020-0548-7
Hao, J., Knoll, A.H., Huang, F., Hazen, R.M., Daniel, I., 2020a. Cycling phosphorus on the Archean Earth: Part I. Continental weathering and riverine transport of phosphorus. Geochim. Cosmochim. Acta 273, 70–84. https://doi.org/10.1016/j.gca.2020.01.027
Hao, J., Knoll, A.H., Huang, F., Schieber, J., Hazen, R.M., Daniel, I., 2020b. Cycling phosphorus on the Archean Earth: Part II. Phosphorus limitation on primary production in Archean ecosystems. Geochim. Cosmochim. Acta 280, 360–377. https://doi.org/10.1016/j.gca.2020.04.005
Harries, P.J., Little, C.T.S., 1999. The early Toarcian (Early Jurassic) and the Cenomanian–Turonian (Late Cretaceous) mass extinctions: similarities and contrasts. Palaeogeogr. Palaeoclimatol. Palaeoecol. 154, 39–66. https://doi.org/10.1016/S0031-0182(99)00086-3
Hesselbo, S.P., Jenkyns, H.C., 1995. A comparison of the Hettangian to Bajocian successions of Dorset and Yorkshire.
Hiatt, E.E., Pufahl, P.K., Guimarães da Silva, L., 2020. Iron and phosphorus biochemical systems and the Cryogenian-Ediacaran transition, Jacadigo basin, Brazil: Implications for the Neoproterozoic oxygenation event. Precambrian Res. 337, 105533. https://doi.org/10.1016/j.precamres.2019.105533
Holtermann, P., Prien, R., Naumann, M., Umlauf, L., 2020. Interleaving of oxygenized intrusions into the Baltic Sea redoxcline. Limnol. Oceanogr. 65, 482–503. https://doi.org/10.1002/lno.11317
Hunt, D., Tucker, M.E., 1992. Stranded parasequences and the forced regressive wedge systems tract: deposition during base-level'fall. Sediment. Geol. 81, 1–9. https://doi.org/10.1016/0037-0738(92)90052-S
Jackson, M.J., Muir, M.D., Plumb, K.A., 1987. Geology of the southern McArthur Basin, Northern Territory (Australia). Bull. - Bur. Miner. Resour. Geol. Geophys. Aust. 220.
Jackson, M.J.J., Raiswell, R., 1991. Sedimentology and carbon-sulphur geochemistry of the Velkerri Formation, a mid-Proterozoic potential oil source in northern Australia. Precambrian Res. 54, 81–108. https://doi.org/10.1016/0301-9268(91)90070-Q
Jarrett, A.J.M., Cox, G.M., Grosjean, E., Boreham, C.J., Edwards, D.S., 2019. Microbial assemblage and palaeoenvironmental reconstruction of the 1 . 38 Ga Velkerri Formation , McArthur Basin , northern Australia. https://doi.org/10.1111/gbi.12331
Javaux, E.J., Knoll, A.H., 2017. Micropaleontology of the lower Mesoproterozoic Roper Group, Australia, and implications for early eukaryotic evolution. J. Paleontol. 91, 199–229. https://doi.org/10.1017/jpa.2016.124
Javaux, E.J., Knoll, A.H., Walter, M.R., 2001. Morphological and ecological complexity in early eukaryotic ecosystems. Nature 412, 66–69. https://doi.org/10.1038/35083562
Johnson, B.R., Tostevin, R., Gopon, P., Wells, J., Robinson, S.A., Tosca, N.J., 2020. Phosphorus burial in ferruginous SiO_2-rich Mesoproterozoic sediments. Geology 48, 92–96. https://doi.org/10.1130/G46824.1

Johnston, D.T., Farquhar, J., Summons, R.E., Shen, Y., Kaufman, A.J., Masterson, A.L., Canfield, D.E., 2008. Sulfur isotope biogeochemistry of the Proterozoic McArthur Basin. Geochim. Cosmochim. Acta 72, 4278–4290. https://doi.org/10.1016/j.gca.2008.06.004

Keighley, D., Boonsue, S., Hall, D., 2018. Phosphatized tungsten-metabolizing coccoid microbes interpreted from oil shale of an Eocene lake, Green River Formation, Utah, USA. Geobiology 16, 610–627. https://doi.org/10.1111/gbi.12310

Keller, W.D., 1968. Flint C L a Y a N D a Flint-Clay 16, 113–128. https://doi.org/10.1093/nar/gks1169

Khan, K.F., Dar, S.A., Khan, S.A., 2012. Rare earth element (REE) geochemistry of phosphorites of the Sonrai area of Paleoproterozoic Bijawar basin, Uttar Pradesh, India. J. Rare Earths 30, 507–514. https://doi.org/10.1016/S1002-0721(12)60081-7

Kidder, D.L., Worsley, T.R., 2010. Phanerozoic Large Igneous Provinces (LIPs), HEATT (Haline Euxinic Acidic Thermal Transgression) episodes, and mass extinctions. Palaeogeogr. Palaeoclimatol. Palaeoecol. 295, 162–191. https://doi.org/10.1016/j.palaeo.2010.05.036

Kirscher, U., Mitchell, R.N., Liu, Y., Nordsvan, A.R., Cox, G.M., Pisarevsky, S.A., Wang, C., Wu, L., Murphy, J.B., Li, Z.-X., 2020. Paleomagnetic constraints on the duration of the Australia-Laurentia connection in the core of the Nuna supercontinent. Geology 49, 174–179. https://doi.org/10.1130/G47823.1

Knoll, A.H., 2014. Paleobiological perspectives on early eukaryotic evolution. Cold Spring Harb. Perspect. Biol. 6, a016121. https://doi.org/10.1101/cshperspect.a016121

Knoll, A.H., 1996. Breathing room for early animals. Nature 382, 111–112. https://doi.org/10.1038/382111a0

Koehler, M.C., Stüeken, E.E., Kipp, M.A., Buick, R., Knoll, A.H., 2017. Spatial and temporal trends in Precambrian nitrogen cycling: A Mesoproterozoic offshore nitrate minimum. Geochim. Cosmochim. Acta 198, 315–337. https://doi.org/10.1016/j.gca.2016.10.050

Konhauser, K.O., Lalonde, S.V., Amskold, L., Holland, H.D., 2007. Was There Really an Archean Phosphate Crisis? Science 315, 1234–1234. https://doi.org/10.1126/science.1136328

Kuliński, K., Rehder, G., Asmala, E., Bartosova, A., Carstensen, J., Gustafsson, B., Hall, P.O.J., Humborg, C., Jilbert, T., Jürgens, K., Meier, M., Müller-Karulis, B., Naumann, M., Olesen, J.E., Savchuk, O., Schramm, A., Slomp, C.P., Sofiev, M., Sobek, A., Szymczycha, B., Undeman, E., 2021. Baltic Earth Assessment Report on the biogeochemistry of the Baltic Sea. Earth Syst. Dyn. Discuss. 1–93. https://doi.org/10.5194/esd-2021-33

Laakso, T.A., Schrag, D.P., 2018. A small marine biosphere in the Proterozoic. Geobiology 1–11. https://doi.org/10.1111/gbi.12323

Laakso, T.A., Schrag, D.P., 2014. Regulation of atmospheric oxygen during the Proterozoic. Earth Planet. Sci. Lett. 388, 81–91. https://doi.org/10.1016/j.epsl.2013.11.049

Large, R.R., Mukherjee, I., Gregory, D., Steadman, J., Corkrey, R., Danyushevsky, L. V., 2019. Atmosphere oxygen cycling through the proterozoic and phanerozoic. Miner. Deposita 54, 485–506. https://doi.org/10.1007/s00126-019-00873-9

Lloyd, D., Harris, J.C., Biagini, G.A., Hughes, M.R., Maroulis, S., Bernard, C., Wadley, R.B., Edwards, M.R., 2004. The plasma membrane of microaerophilic protitsts: Oxidative and nitrosative stress. Microbiology 150, 1183–1190. https://doi.org/10.1099/mic.0.26834-0

Mack, G.H., Cole, D.R., 2005. Geochemical model of δ18O of pedogenic calcite versus latitude and its application to Cretaceous palaeoclimate. Sediment. Geol. 174, 115–122. https://doi.org/10.1016/j.sedgeo.2004.12.002

Martin, R.E., Servais, T., 2020. Did the evolution of the phytoplankton fuel the diversification of the marine biosphere? Lethaia 53, 5–31. https://doi.org/10.1111/let.12343

Michiels, C.C., Darchambeau, F., Roland, F.A.E., Morana, C., Llirós, M., García-Armisen, T., Thamdrup, B., Borges, A.V., Canfield, D.E., Servais, P., Descy, J.-P., Crowe, S.A., 2017. Iron-dependent nitrogen cycling in a ferruginous lake and the nutrient status of Proterozoic oceans. Nat. Geosci. 10, 6.

Mingxiang, M.E.I., Fengjie, Y., Jinhan, G.A.O., Qingfen, M., 2008. Glauconites Formed in the High-energy Shallow-Marine Environment of the Late Mesoproterozoic : Case Study from Tieling Formation at Jixian Section in Tianjin , North China 15.

Mitchell, R.N., Kirscher, U., Kunzmann, M., Liu, Y., Cox, G.M., 2020. Gulf of Nuna: Astrochronologic correlation of a Mesoproterozoic oceanic euxinic event. Geology 49, 25–29. https://doi.org/10.1130/G47587.1

Mukherjee, I., Large, R.R., 2016. Pyrite trace element chemistry of the Velkerri Formation, Roper Group, McArthur Basin: Evidence for atmospheric oxygenation during the Boring Billion. Precambrian Res. 281, 13–26. https://doi.org/10.1016/j.precamres.2016.05.003

Mukherjee, I., Large, R.R., Bull, S., Gregory, D.G., Stepanov, A.S., Ávila, J., Ireland, T.R., Corkrey, R., 2019. Pyrite trace-element and sulfur isotope geochemistry of paleo-mesoproterozoic McArthur Basin: Proxy for oxidative weathering. Am. Mineral. 104, 1256–1272. https://doi.org/10.2138/am-2019-6873

Müller, J., Reisz, R.R., 2006. The Phylogeny of Early Eureptiles: Comparing Parsimony and Bayesian Approaches in the Investigation of a Basal Fossil Clade. Syst. Biol. 55, 503–511. https://doi.org/10.1080/10635150600755396

Munson, T.J., 2016. Sedimentary characterisation of the Wilton package, greater MacArthur Basin, Northern Territory. Northern Territory Geological Survey.

Nelson, G.J., Pufahl, P.K., Hiatt, E.E., 2010. Paleoceanographic constraints on Precambrian phosphorite accumulation, Baraga Group, Michigan, USA. Sediment. Geol. 226, 9–21. https://doi.org/10.1016/j.sedgeo.2010.02.001

Nguyen, K., Love, G.D., Lyons, T.W., Zumberge, J.A., Kelly, A.E., Owens, J.D., Rohrssen, M.K., Bates, S.M., Cai, C., 2019. Absence of biomarker evidence for early eukaryotic life from the Mesoproterozoic Roper Group : Searching across a marine redox gradient in mid- Proterozoic habitability 247–260. https://doi.org/10.1111/gbi.12329

Ohfuji, H., Rickard, D., 2005. Experimental syntheses of framboids - A review. Earth-Sci. Rev. 71, 147–170. https://doi.org/10.1016/j.earscirev.2005.02.001

Özsoy, E., Ünlüata, Ü., 1997. Oceanography of the Black Sea: A review of some recent results. Earth-Sci. Rev. 42, 231–272. https://doi.org/10.1016/S0012-8252(97)81859-4

Pahlow, M., Riebesell, U., 2000. Temporal trends in deep ocean Redfield ratios. Science 287, 831–833. https://doi.org/10.1126/science.287.5454.831

Piane, C.D., Uysal, I.T., Pan, Z., Bourdet, J., Li, Z., Raven, M.D., 2019. A multidisciplinary evaluation of the Velkerri Formation in the Beetaloo Sub- Basin : Implications for geological history and reservoir quality Beetaloo Sub-Basin.

Planavsky, N.J., 2014. The elements of marine life. Nat. Geosci. 7, 855–856. https://doi.org/10.1038/ngeo2307

Planavsky, N.J., Cole, D.B., Isson, T.T., Reinhard, C.T., Crockford, P.W., Sheldon, N.D., Lyons, T.W., 2018. A case for low atmospheric oxygen levels during Earth's middle history. Emerg. Top. Life Sci. 2, 149–159. https://doi.org/10.1042/ETLS20170161

Planavsky, N.J., Rouxel, O.J., Bekker, A., Lalonde, S. V., Konhauser, K.O., Reinhard, C.T., Lyons, T.W., 2010. The evolution of the marine phosphate reservoir. Nature 467, 1088–1090. https://doi.org/10.1038/nature09485

Porter, S.M., Agić, H., Riedman, L.A., 2018. Anoxic ecosystems and early eukaryotes. Emerg. Top. Life Sci. ETLS20170162. https://doi.org/10.1042/ETLS20170162

Pörtner, H., 2001. Climate change and temperature-dependent biogeography: Oxygen limitation of thermal tolerance in animals. Naturwissenschaften 88, 137–146. https://doi.org/10.1007/s001140100216

Poulton, S.W., Canfeld, D.E., 2011. Ferruginous conditions: A dominant feature of the ocean through Earth's history. Elements 7, 107–112. https://doi.org/10.2113/gselements.7.2.107

Powell, J.H., 2010. Jurassic sedimentation in the Cleveland Basin: a review. Proc. Yorks. Geol. Soc. 58, 21–72. https://doi.org/10.1144/pygs.58.1.278

Pufahl, P.K., Hiatt, E.E., 2012. Oxygenation of the Earth's atmosphere–ocean system: A review of physical and chemical sedimentologic responses. Mar. Pet. Geol. 32, 1–20. https://doi.org/10.1016/j.marpetgeo.2011.12.002

Raiswell, R., Berner, R.A., 1985. Pyrite formation in euxinic and semi-euxinic sediments. Am. J. Sci. 285, 710–724. https://doi.org/10.2475/ajs.285.8.710

Rasmussen, B., Muhling, J.R., Suvorova, A., Fischer, W.W., 2021. Apatite nanoparticles in 3.46–2.46 Ga iron formations: Evidence for phosphorus-rich hydrothermal plumes on early Earth. Geology 49, 647–651. https://doi.org/10.1130/G48374.1

Rasmussen, B., Muhling, J.R., Zi, J.W., Tsikos, H., Fischer, W.W., 2020. A 1.25 ga depositional age for the "Paleoproterozoic" mapedi red beds, kalahari manganese field, South africa: New constraints on the timing of oxidative weathering and hematite mineralization. Geology 48, 44–48. https://doi.org/10.1130/G46707.1

Reinhard, C.T., Planavsky, N.J., Gill, B.C., Ozaki, K., Robbins, L.J., Lyons, T.W., Fischer, W.W., Wang, C., Cole, D.B., Konhauser, K.O., 2017. Evolution of the global phosphorus cycle. Nature 541, 386–389. https://doi.org/10.1038/nature20772

Reinhard, C.T., Planavsky, N.J., Ward, B.A., Love, G.D., Le Hir, G., Ridgwell, A., 2020. The impact of marine nutrient abundance on early eukaryotic ecosystems. Geobiology gbi.12384. https://doi.org/10.1111/gbi.12384

Retallack, G.J., 2005. Pedogenic carbonate proxies for amount and seasonality of precipitation in paleosols. Geology 33, 333–336. https://doi.org/10.1130/G21263.1

Retallack, G.J., 1997. Colour guide to paleosols. Colour Guide Paleosols.

Rickaby, R.E.M., Eason Hubbard, M.R., 2019. Upper ocean oxygenation, evolution of RuBisCO and the Phanerozoic succession of phytoplankton. Free Radic. Biol. Med. https://doi.org/10.1016/j.freeradbiomed.2019.05.006

Rickard, D., 2012. Sedimentary Pyrite, Developments in Sedimentology. https://doi.org/10.1016/B978-0-444-52989-3.00006-4

Rudmin, M., Banerjee, S., Abdullayev, E., Ruban, A., Filimonenko, E., Lyapina, E., Kashapov, R., Mazurov, A., 2020. Ooidal ironstones in the Meso-Cenozoic sequences in western Siberia: assessment of formation processes and relationship with regional and global earth processes. J. Palaeogeogr. 9, 1–21. https://doi.org/10.1186/s42501-019-0049-z

Ruttenberg, K.C., 2003. 8.13 The Global Phosphorus Cycle 59.

Schenau, S.J., Passier, H.F., Reichart, G.J., de Lange, G.J., 2002. Sedimentary pyrite formation in the Arabian Sea. Mar. Geol. 185, 393–402. https://doi.org/10.1016/S0025-3227(02)00183-4

Schieber, J., 1986. The possible role of benthic microbial mats during the formation of carbonaceous shales in shallow Mid-Proterozoic basins. Sedimentology 33, 521–536. https://doi.org/10.1111/j.1365-3091.1986.tb00758.x

Schieber, J., Bose, P., Eriksson, P.G., Banerjee, S., Sarkar, S.A., Wladyslaw Catuneanu, O., 2007. Atlas of Microbial Mat Features Preserved within the Siliciclastic Rock Record, 2nd ed. Elsevier.

Schulz, H.N., Schulz, H.D., 2005. Large sulfur bacteria and the formation of phosphorite. Science 307, 416–418. https://doi.org/10.1126/science.1103096

Shen, Y., Canfield, D.E., Knoll, A.H., 2002. Middle proterozoic ocean chemistry: Evidence from the McArthur Basin, Northern Australia. Am. J. Sci. 302, 81–109. https://doi.org/10.2475/ajs.302.2.81

Shen, Y., Thiel, V., Suarez-Gonzalez, P., W Rampen, S., Reitner, J., 2020. Sterol preservation in hypersaline microbial mats. Biogeosciences 17, 649–666. https://doi.org/10.5194/bg-17-649-2020

Sood, A., Tellis, G.J., 2005. Technological Evolution and Radical Innovation. J. Mark. 69, 152–168. https://doi.org/10.1509/jmkg.69.3.152.66361

Sperling, E.A., Rooney, A.D., Hays, L., Sergeev, V.N., Vorob'eva, N.G., Sergeeva, N.D., Selby, D., Johnston, D.T., Knoll, A.H., 2014. Redox heterogeneity of subsurface waters in the Mesoproterozoic ocean. Geobiology 12, 373–386. https://doi.org/10.1111/gbi.12091

Stüeken, E.E., 2013. A test of the nitrogen-limitation hypothesis for retarded eukaryote radiation: Nitrogen isotopes across a Mesoproterozoic basinal profile. Geochim. Cosmochim. Acta 120, 121–139. https://doi.org/10.1016/j.gca.2013.06.002

Suits, N.S., Wilkin, R.T., 1998. Pyrite formation in the water column and sediments of a meromictic lake. Geology 26, 1099–1102. https://doi.org/10.1130/0091-7613(1998)026<1099:PFITWC>2.3.CO;2

Swanner, E.D., Lambrecht, N., Wittkop, C., Harding, C., Katsev, S., Torgeson, J., Poulton, S.W., 2020. The biogeochemistry of ferruginous lakes and past ferruginous oceans. Earth-Sci. Rev. 211, 103430. https://doi.org/10.1016/j.earscirev.2020.103430

Tuğrul, S., Murray, J.W., Friederich, G.E., Salihoğlu, İ., 2014. Spatial and temporal variability in the chemical properties of the oxic and suboxic layers of the Black Sea. J. Mar. Syst., Assessing and modelling ecosystem changes in the Mediterranean and the Black Sea pelagic ecosystem - SESAME 135, 29–43. https://doi.org/10.1016/j.jmarsys.2013.09.008

Walker, T.R., 1976. Diagenetic Origin of Continental Red Beds, in: Falke, H. (Ed.), The Continental Permain in Central, West, and South Europe, Nato Advanced Study Institutes Series. Springer Netherlands, Dordrecht, pp. 240–282. https://doi.org/10.1007/978-94-010-1461-8_20

Warren, J.K., George, S.C., Hamilton, P.J., Tingate, P., 1998. Proterozoic source rocks: sedimentology and organic characteristics of the Velkerri Formation, Northern Territory, Australia. AAPG Bull. 82, 442–463. https://doi.org/10.1306/1d9bc435-172d-11d7-8645000102c1865d

Wignall, P.B., 1994. Black shales. Oxford University Press, USA.

Wilkin, R.T., Barnes, H.L., 1997. Formation processes of framboidal pyrite. Geochim. Cosmochim. Acta 61, 323–339. https://doi.org/10.1016/S0016-7037(96)00320-1

Williams, G.E., 1968. Torridonian weathering, and its bearing on Torridonian palaeoclimate and source. Scott. J. Geol. 4, 164–184. https://doi.org/10.1144/sjg04020164

Wylezich, C., Jürgens, K., 2011. Protist diversity in suboxic and sulfidic waters of the Black Sea. Environ. Microbiol. 13, 2939–2956. https://doi.org/10.1111/j.1462-2920.2011.02569.x

Yamaguchi, K.E., Oguri, K., Ogawa, N.O., Sakai, S., Hirano, S., Kitazato, H., Ohkouchi, N., 2010. Geochemistry of modern carbonaceous sediments overlain by a water mass showing photic zone anoxia in the saline meromictic Lake Kai-ike, southwest Japan: I. Early diagenesis of organic carbon, nitrogen, and phosphorus. Palaeogeogr. Palaeoclimatol. Palaeoecol. 294, 72–82. https://doi.org/10.1016/j.palaeo.2009.10.024

Yang, B., Collins, A.S., Cox, G.M., Jarrett, A.J.M., Denyszyn, S., Blades, M.L., Farkaš, J., Glorie, S., 2020. Using Mesoproterozoic sedimentary geochemistry to reconstruct basin tectonic geography and link organic carbon productivity to nutrient flux from a Northern Australian large igneous Province. Basin Res. bre.12450. https://doi.org/10.1111/bre.12450

Yang, S., Kendall, B., Lu, X., Zhang, F., Zheng, W., 2017. Uranium isotope compositions of mid-Proterozoic black shales: Evidence for an episode of increased ocean oxygenation at 1.36 Ga and evaluation of the effect of post-depositional hydrothermal fluid flow. Precambrian Res. 298, 187–201. https://doi.org/10.1016/J.PRECAMRES.2017.06.016

Zhang, S.H., Zhao, Y., Li, X.H., Ernst, R.E., Yang, Z.Y., 2017. The 1.33–1.30 Ga Yanliao large igneous province in the North China Craton: Implications for reconstruction of the Nuna (Columbia) supercontinent, and specifically with the North Australian Craton. Earth Planet. Sci. Lett. 465, 112–125. https://doi.org/10.1016/j.epsl.2017.02.034

Zhang, Y., Pufahl, P.K., Du, Y., Chen, G., Liu, J., Chen, Q., Wang, Z., Yu, W., 2019. Economic phosphorite from the Ediacaran Doushantuo Formation, South China, and the Neoproterozoic-Cambrian Phosphogenic Event. Sediment. Geol. 388, 1–19. https://doi.org/10.1016/j.sedgeo.2019.05.004

6. Core Logs

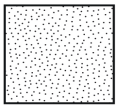
Sandstone

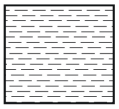
silty claystone
-claystone

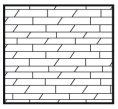
Interlaminated Fe-clay
and limestone


siltstone
-clayey siltstone


Organic-rich
sediment

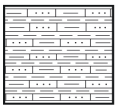
Interlaminated silty Fe-clay
and limestone

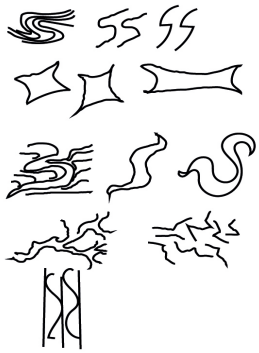

Convoluted bedding/soft sediment disruption/dewatering structures

Pseudomorphs

Sub-aqueous cracks

Pervasive veins/hydrothermal breccia

Tilted bedding

Laminated rip ups isolated/imbrecated

Unlaminated rip ups isolated/imbrecated

Brecciated bedding (post lithification, no obvious source)

OM-rich winkly laminations

Flattened wrinkly/filamentous crypto-microbial bedding surface
(OM not always present)

crypto-microbial Shreds and blobs on bedding surface

Domal stromatolites, either clay or carbonate

Coated grains (Fe-clay or Fe-clay and sand)

Crypto-microbial 'stylolights' on bedding surface

Rhomboidal crystals

Euhedral pyrite

Nodular pyrite

Bedding paralell mineralisation/mineralised sand-silt scours

Flaser bedding/mud drapes

Erosive scours with coarser grains than host bedding

Synsedimentary faulting

Postlithification faulting

Scour geometry (when visible)

12BCNTGS001

Deapths refer to the base of the core section in that particular tray without decimal readings could not be read directly from the core or tray and are taken from my measurements. Unit boundaries set by me as the top of the last 'Red rubble clay', core report (EL27475_2013_AS_01) places unit boundary at 320m but no explanation as to why this horizon was picked, I presume it is because it's the highest observed OM rich sediment and gamma peak? Numbers in text refer to bed number, bed divisions set by me on the basis of erosional contacts, and shared characteristics between adjacent bed sets visible at log scale. Sedimentary structures are 'as seen' and not to vertical scale.

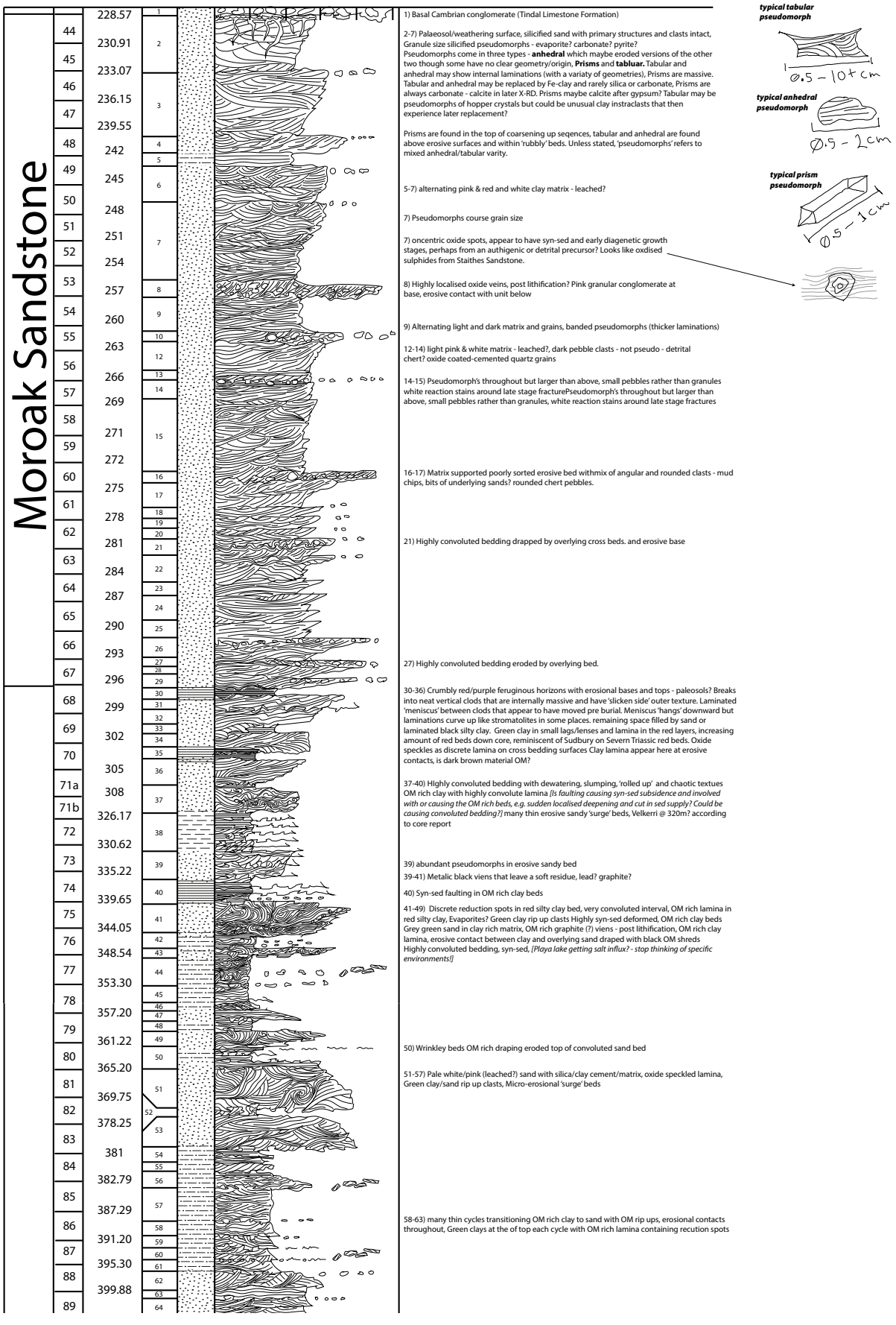

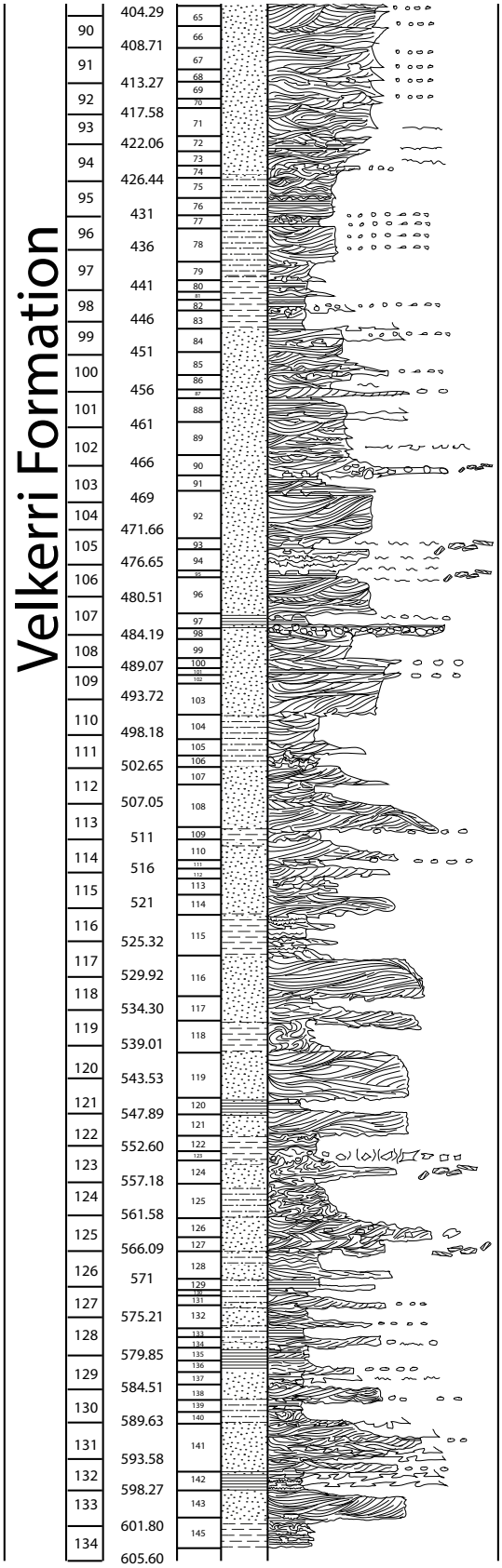

63-70) orange metalic oxide(?) granules-fine pebbles, subrounded, restricted to erosion surfaces and adjacent few cm

71-73) Concentrated tabular and anhedral pseudomorph bands, abundant OM-rich wrinkle lamina

77-78) abundant green clay rip up clasts

82) Pseudomorphs and green clay above a red clay horizon

85) Pseudomorphs at erosional surfaces

87-89) Pseudomorphs throughout, interbedded with green clay cemented sand, black OM-ruch bedd with wrinkled lamina at teh base of bed 89

90-91) Green rip up clasts in sands that top red rubble clay and fine up to green silty clay
Chicken wire texture with intra clast and chert pebble/silicified conglomerate
2-5mm rounded oxidised glauconite grains in cross bedded - laminated sands

92-95) Interbedded sand and mud horizons with turbid appearence *[looks like Carboniferous deltaic seds from Howick].* Pale green waxy platy clay with 'slicken lines' at erosional contacts, pale green clay rip ups *[standing water body?]* interbedded with red rubbly clay that has reduction spots red mud rip ups, OM-rich black wrinkly clays at the top of red rubble beds

97-98) green clay draping granule to gravel angular conglomerate that erodes into cross bedded - laminated sand with glauc grains

100-107) Red clay with rubble texture, very fine clay with chaotic chunks of coarser clay jumbled up or micro faulted

palaeopod soil? has same features as red clod horizons above Red rubble clay often has marbled swirly chaotic "gas giant" texture - lighter bands could be carbonate or evaporite? - weak reaction with 10%HCl]

Red rubble clay topping highly convoluted sand unit with slity clay draping and infilling in the convolutions

108-114) Pale pink sand - green sand bands, green beds have smaller grain size
green beds are quartz sand glauconite grains and powdery pale green cement

113-114) sand is sparkly - muscovite rich in the green bands

115) Highly convoluted clay beds

117) Green clay at bed contact eroded by overlying sand

118) alternating red rubble clay and green clays that show soft sed deformation highly convoluted interval

120-122) Interbedded red rubble and green laminated clay

123-127) interbedded Red rubble and green laminated clay - planar to convoluted lamination
Pseudomorph layers with convoluted lamina and erosional contacts and dewatering structures, oxide grains along sand lamina, Clay rip ups, Grey green laminated silt, 5mm sub-angular pebbled in sand/clay, green clay lamina between layers of clasts, some clasts are green clay ripups but most are quartz/chert

128- 142) Green clay interbeds areprevailant and highly convoluted, fines up from erosive sand in the lower part of each bed, some basal sands feature Glauconitic 'agglomerate' - chunks of reworked cemented glauconitc sandstone, black OM-rich wrinkly clays interlaminated with green clays near the top of each bed, common fractures and breccaited clay filled faults that are restricted to individual beds or laminae - not obvious if its syn sed or syn-diagenetic fracturing/faulting? many thin Green lamina with pseudomorphs and syn-sed deformation, sets of thin alternating green laminated and red rubble beds, with planar erosional (?) contacts, common syn-sed faulting, deformation and dewatering in sandy layers convoluted green layers with turbid contacts with adjacent beds (can't remember name for the 'turbid' texture) Pseudomorph beds that appear reworked and eroded out rather than dissolved thin green sands - green cement and glauconite grains - throughout core glauc grains are fine - medium grained.

143-145) Pink silicified sand overlying red silty clay, green red clay cycles and red rubble clay with marble 'gas giant' texture, contact with overlying sand is highly convoluted. *[Pink colour appears to be staining from overlying red rubble, are pink/white sands leached?]*

END OF CORE

Urapunga - 4

Formation boundaries placed by me and addpted from core report **URAPUNGA456_WCR-REC1986_019**. *Velkerri member boundaries asigned by Munson and Revie 2018 on the basis of wireline data indicating organic enrichment. Colours represent the dominant colour of that particular.*

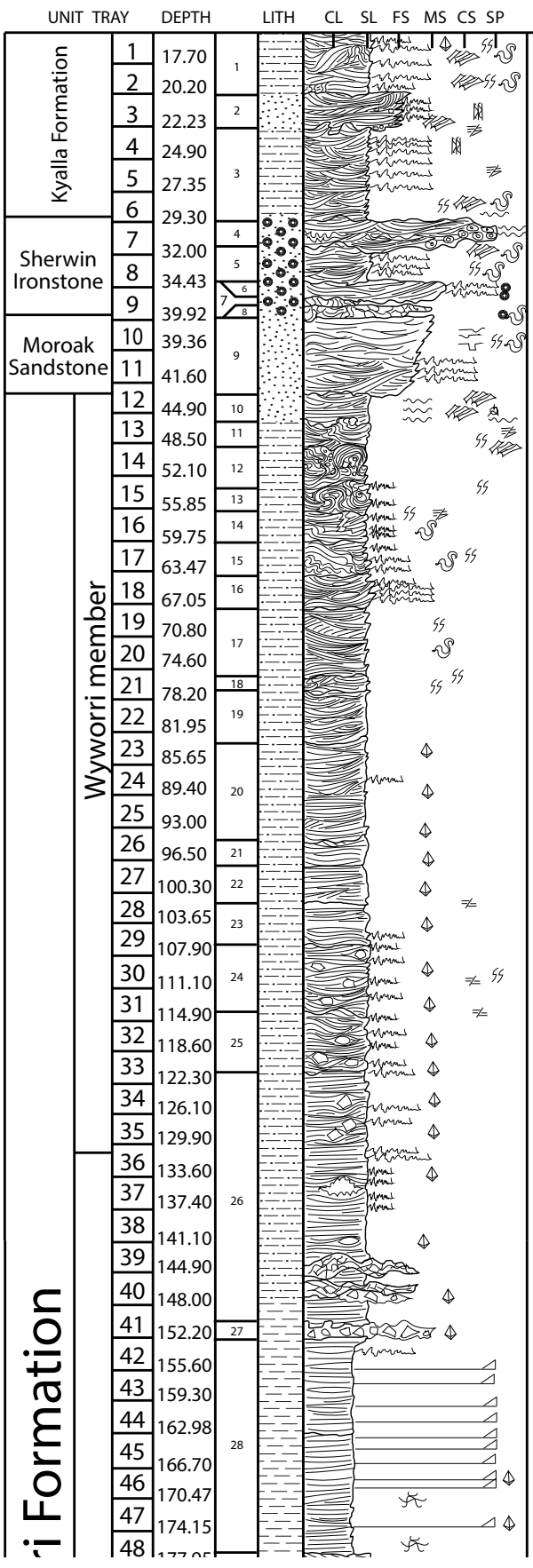

Notes

1)Light grey silt with cross beds and many minor coarsening up cycles from clay to silt topped with erosively based fine to medium sand scours. Sub-aqueous cracks, convoluted bedding and dewatering structures are all abundant. Rip up clasts of green and black silty clay are found at the top of coarsening up cycles and appear to have been pliable during reworking. Pyrite is common as mm scale lamina destructive and displasive euhedral crystals. Tetrahedra are the most common habit but pyritohedral, cuboidal and dodecahedral are also present. Sediments of bed 1 drape the erosive contact with underlying bed 2.

2) Green clay cemented cross bedded fine sand with many minor cycles of coarsening up topped by erosively based glauconitic medium sand scours. Convoluted bedding is common including a steeply dipping erosively based beds, small scale syn-sedimentary faulting also present. Rare thin beds of sugary textured sparkly red weathering sand. Imbricated rip up clasts of green and black silty clay common at the top of coarsening cycles along with less common s-sub sounded pebbles of chert (?) and rare green clay coated grains. Lower surface is an irregular erosive boundary were overlying sediments drape and then infill topography. Isolated OM-rich lamina can be found in the lower most part of the bed.

3) Cross bedded silt with many minor cycles that coarsen up to erosively based glauconitic medium sand scours. Convoluted and tilted bedding are foundin the upper part of the bed, middle part of the bed features small scale syn-sedimentary faulting. Some sandy beds have a sugary texture and a sparkly metallic sheen. *[looks like pyrite cement under binoscope]* Lower most part of the bed features black and green imbrecated silty clay rip ups, and sub-aqueous cracks. Green clay coated grains become common towards the base of the bed. Sediments of this bed drape the underlying bed with OM-rcih wrinkly lamina common at and adjacent to the contact. Contact with the underlying bed is sharp and undulose.

4-8) The Sherwin Ironstone, cross bedded fine to medium sand cemented by green clay and with green clay coated grains that superficially resemble ooids and oncoids. Sand and coated grain beds are interbedded with cyclic green clay cemented clay beds as per bed 3 but with additional green clay intervals that have convoluted to stromatolitic laminations. See Sherwin log for detailed descriptions of the unit. Lower most sandstone beds have sugary texture and metallic sparkly cement. Contact with underlying bed 9 is sharp and planar.

9) Crossbedded fine to medium sand that coarsens upwards through several smaller cycles. Some cycles are topped with erosive coarse sands with less abundant granular size grains. Upper surface of the bed is erosively truncated with red and yellow oxide staining that seeps down core so that the whole bed is pale pink. Many beds have the same sugary texture as sand beds above, though the metallic cement is rare. A white powdery to waxy cement is also common. The contact also contains cracks that are filled with fine to medium micaceous sand that is distinct from the host bed and overlying sediments. The upper part of the bed also contains horizons with possible desication and sub-aqueous crack, some are too compacted to ID for sure. Convoluted bedding and dewatering structures are common in the lower part of the bed.

10-11) interlaminated green clay cemented silts and dark green clays with abundant OM-rich wrinkled laminations, deposited in alternating sets from here termed 'green rhythmites'. Upper surface and contact is erosively truncated, features sand filled cracks, and heavilly oxidsed with oxidation waning over a short interval. Convoluted and cross bedding and lamination common, small scale syn-sedimentary faulting in lower part. Green and black rip up clasts are common locally in both imbrecated stacks and as isolated chips. Contact between bed 10 and 11 is erosive and convoluted. Base of bed 11 drapes undlying bed with a sharp contact that does not appear to be erosional.

12-18) green cemented silts and green clays in minor coarsening up cycles from clay to fine - medium sand ersoively based glauconitic scours. Conovluted and cross bedding are common, the bed 13-14 contact features small scale syn-sedimentary faulting, bed 14 features unusal 'rubble' of host sediment that is draped by overlying sediments. Sub-aqueous cracks are common in descrete intervals in the middle and lower part of ther interval. Convoluted bedding and laminations have an unusual 'stromatolitic' appearence in beds 12-13, including pustular and domal forms that consist of interlaminated green clay and black wrinkly laminae, and appear to show reworking and 'healing' or 're-growth' of damange. Pyrite is disseminated through some silty laminae as a fine grained cement, some examples from cm scale nodular shaped 'clouds' Green clay cement appears has a 'feathered' texture in some silty cross beds so that is grades into mid-grey silt. The base of bed 18 sharply drapes the eroded top of the underlying bed.

19-25) Interbedded silts and silty clays with erosively based glauconitic fine sand scours in the lower part of the interval. Convolute bedding is rare and restricted to the upper and lower most parts of the interval. Wrinkly OM-rich laminations are common throughout in packages of planar to undulose laminated silty and silty clay similar to the green rhythmite sediments above. Clay fraction begins as dark green waxy clay at the sharp contact with the overlying bed and gradually lightens down core with less abundant thin dark red platy to shaley clay bed. The contact between red and green clay beds is sharp and undulose but does not appear to be erosional. Fabric displacive and destructive euhedral pyrite is present through out. This interval of core is cut in three locations by post-lithification faulting.

26) Planar and undulose laminations dominate this bed, though some are gently tilted relative to adjacent sets. The top of the bed is eroded by bed 25 and there is a sharp change to the green ryhythmite sediment type. Halfway down the bed there is a sharp change to a dark blue grey colour that is independent of any change to the depositional lithology. Ovoid cm scale nodular pyrite is present, some of which appears to have been syn-sedimentary or pre-compaction, while others are clearly later and fabrice displacive and destructive. Euhedral pyrite grains are also common and locally aggregate into euhedral pyrite beds where the crystals are packed tightly but do not intergrow. The lower part of the bed hosts a complex set of quartz, carbonate and metalice sulphide viens that both destroy and follow fabric.

27) Fine to medium sand bed whos original textures and bed contacts have been destroyed by pervasive metallic sulphide mineralisation. Metallic sulphides consist of mm scale euhedra similar to the pyrite in adjacent beds, and a pervasive cement cement of accicular, finely granular and massive metallic sulphides that appears to post date the pyrite euhedra.

28) dark blue grey shaley silty mud stone dominated by planar and undulose lamination, and with rare low angle cross beds. Upper to middle part of bed is pervasively threaded by a wed of bedding parralel and cross cutting quartz-carbonate-metallic sulphide viens, Euhedral pyrite is only present towards the base of the vien zone. Lowermost part of bed hosts OM-rich laminations some of which feature a 'flattened' wrinkle texture on their bedding planes. Sediments of bed 28 drap a sharp contact with bed 29.

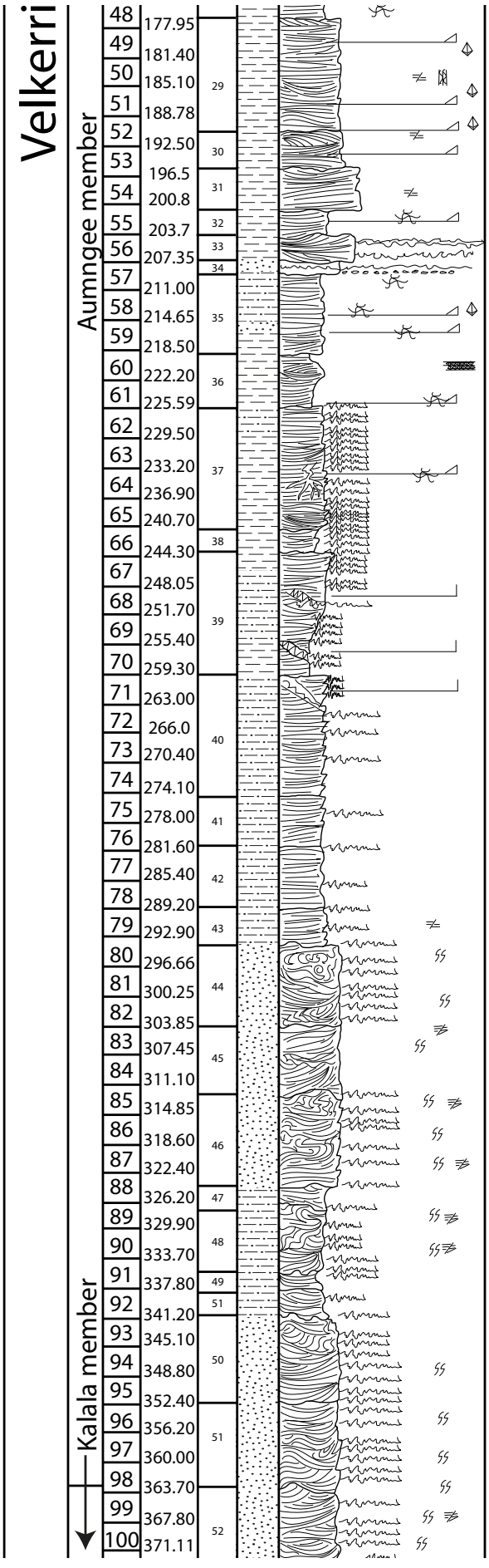

29-35) Return of green rhythmite, and green cemented silts and and dark green clays similar in character to beds 19-25. Cross bedding is common and features higher angles that in bed 28. Post-lithification faulting cuts core in three intervals and some bed packages appear to have been tiled post-lithification. Vein webbing is present and not as prevailent and euhedral pyrite is only locally common in some beds and one pyrite cemented bed. There are many OM-rich beds that feature the wrinkled surface texture and wrinkly laminae. Bed 33 features prominent glauconite granule-rich horiozons which increase in abundance and thickness down core. The contact between glauconite-bearing and adjacent horizons is sharp and undulose but not erosive, grains appear to rest on the underlying surface. Bed 35 is a distinct bed with glauconite grains mixed with unusual blue coarse sand sized grains in a laminated matrix of silica and carbonate that has texture like collapsed honeycomb. the contact with adjacent beds is sharp and undulose but does not appear to be erosive, grains appear to rest on the underlying surface. Bed 35 features a bed of black granular-crystaline material that may be OM that has been 'cooked' by an adjacent mineral vien.

36-39) Interbedded silts and silty clays with minor coarsening up sequences topped by erosively based glauconitic fine sand scours. Sediments grade from pale grey at the top of the interval to dark blue grey down core. cross-bedding is common near the top of each cycle and passes down into planar and undulose laminatsion in thin packages that may be horizontal or gently dipping. Alternating cycles of OM-rich and OM-poor cycles are common. OM-rich beds increase in thickness and abundance down core in two broad cycles that feature black silts and silty clays at the base. The two black silts and silty clays may correspond to two of the basin wide OM-rich beds known from the middle Velkerri. This interval features several large mineralised faults which cut the core. These are adjacent to thin veins that host pink quartz and carbonate and rare mm to cm pink to white tabular crystal masses. The base of bed 39 drapes the undlying bed in a sharp undulose contact that does not appear to be erosive. The organic enrichment in this interval appears to be independant of grain size or lithology.

40-43) Green rhythmites with planar to undulose laminations and low angle cross bedding. There are distrete thin packages of wrinkly OM-rich lamainae through out. The ~1m of bed 40 is OM-rich and produced a conspicuous HC smell and may correspond to one of the HC rich intervals of middle Velkerri. The contact between the OM-rich, and green rhythmite portion of the bed is sharp and undulose. A mineralised fault cuts the core in the upper most part of bed 40. The lower most part of bed 40 hosts a distinct dark red clay bed that contains glauconite greens and similar blue granules to bed 34 diseminated through out and concentrated near the top. The red bed has sharp undulose contacts with adjacent beds and the dark red clay has a play-blocky texture. The base of bed 43 hosts a glauconitic erosively based fine sand scour that cuts into the uncerlying bed.

44-46) Green rhythmite silty clays and silts, but the green clay is darker green than the overlying beds with rare blue-blue green to blue-grey clay intervals. Erosively based fine to medium sand scours are common. Cross bedding and convolute bedding are common. The blue-green/grey clay beds appear massive and have concoidal feacture but cross bedding is picked out in places by shreds of OM that may appear folded or twisted and rare thin silt laminae. Small scale synsedimentary faulting is common in the beds adjacent to sand scours, and convoluted bedding. OM-rich wrinkly lamina are locally common and may host mm scale anhedral 'lumpy' pyrite nodules that are fabric concordant.

47-52) Lithologically simialr to the overlying beds with the main difference being a change from green clay cement to a mid grey clay cement with subordinate green clay laminations that drape the surface of cross beds and convoluted bed sets. Fine to medium erosively based sand scours increase in abundance and regularity down core. OM-rich beds and lamina are common and occur as three broad cycles that decrease in OM up core and that start with very OM-rich beds at bed boundaries. The lower part of bed 51 is very OM-rich with OM enrichment having a sharp conract with the over and underlying sediments.

52) Typical green rhythmite that draps the underlying Bessie Creek Sanstone with a sharp undulose contact.

Scarborough-1

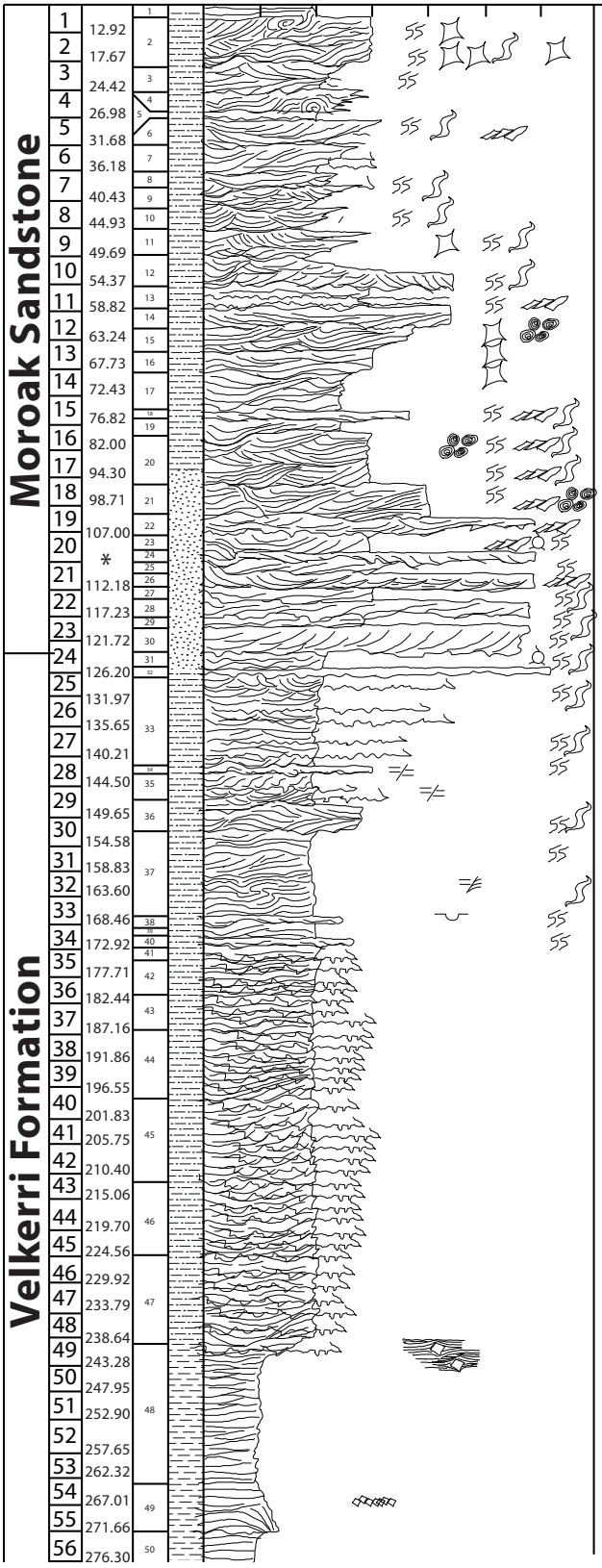

1) dark grey-black silty cross laminated clay that passes upwards into heavilly weathered rock overlain by modern soil, started logging and sampling at the base of tray 1 where there is no obvious recent weathering. Sand- black silty mud transition is labled as contact with Kyalla Mudstone in the core report.

2-12) Interlaminated pale green silt and silty clay with less abundant dark green waxy clay laminations, and red platy to rubbly beds, sharp planar to undulose lamination and bed contacts throughout, abundant tabular pseudomorphs at bed contacts, sigmoidal to convoluted cracks throughout, some appear to be desication, some appear to be sub-aqueous, some are unable to be identified due to convoluted nature of folding from compaction (?), cracks are filled by plae grey fine to medium sand and fragments of overlying beds, there are no corresponding pale grey sand beds in this part of the core. Cross bedding and cross lamination throughout. Many thin coarsening up cycles imprinted on larger bed scale cycles, thin beds of wrinkle laminated black silty clay at the base of each finning up cycle. Imbrecated rip up clasts abundant in upper parts of each cycle with one horizon at the base of bed 2 hosting unusual 'vermiculate' rip ups. Bed 6 features thin beds that fine up from fine glauconitic sand into blue grey missive clay with concoidal fracture that reacts weakly with HCl. The base of bed 9 features a prominent erosive surface with interlaminated brown, black, green and white sands and silts that have 'turbulent' contacts. Dewatering structures are common throughout. Bed 12 hosts a prominent erosive surface at the base with black and green clay rip up clasts/pebble bed overlain by cross laminated sands that fine up to a thin blue clay bed. The base of bed 12 and top of bed 13 have a rubbly texture and dark red-purple colour that 'seeps' ten or so cm into the underlying bed.

13) thin interbeds of black and green sand and clay in thin beds, contacts are erosive through out and the base of each bed contains rip ups of (presumably) underlying beds of this type. rip ups are in imbrecated sub-horizontal to vertical stacks. Coarser beds contain glauconite granules that appear to have been partially pyritised then partially oxidised.

14) cross laminated to cross bedded alternating red and green sands - colour changes but sand grain size does not(!?) Sands are cemented by green clay so could be syn-depo oxidation? Bed surfaces feature same oxide grains as bed 13 and rare isolated partially oxidised and pyritised green clay sphearoidal coated grains in the basal erosive contact with underlying bed.

15-21) Cross bedded sands with thin interbeds of alternating blue clay, black wrinkly clay and sands with alternating green and red bands (as in bed 13), some beds are rich in coated grains as per the type described above, but with additional elipsoid, bacillus (?!), 'oncoidal' and compound/multicore morphologies. Coated grain sizes range from 5 - 20 mm, internal structures consist of detrital core and green clay concentric corticies, internal lamination varies with morphology, Oncoidal have internal discontinuities and overlap, bacillus and sphearoidal have equant internal lamina, and elipsoid have lamina that thin along the long axis. Superficially similar to the coated grains of the Sherwin Ironstone. Coated grains appear to have been transported as some are broken and do not show 'regrowth' like Sherwin Grains. Coated grains beds also contain flat eliptical structures that have been fully to partially replaced by pyrite and then oxide, the least alteres structures appear to be syn-depositional - lenticular gypsum pseudomorphs? The fully altered example have a cross section like mushroom - looks like pyrite seeping up from down core through porous beds, cracks and bed contacts? Some black beds feature an unusual granular texture in the OM and have interlaminated bright yellow-green-white powdery-'fluffy' crystaline (under hand lens) material - superficially like the 'Sulphur Band' in the Lias back home. Bed 18 contains coated grains in the black granular material at the top which grades down core into familar red and green alteranations - back ground sed texture remains consisten across colour changes. Bed 21 rests on a prominent erosion surface and is rich in coated grains. base of bed - top of underlying bed is heavyllity oxidised, oxidation fades quickly up core.

21-30) Cross bedded to laminated sands interbedded with silts and sandy clays with erosive contacts throughout. Sands host evaporite pseudomorphs - ranging from lenticular to hopper crustal in shape, imbrecated sub-orizontal to vertical stacks of intraclasts from underlying units. Sands are grey-green and cemented by green clay, some beds and lamina, e.g. upper surfaces of cross bedding have been oxdised and host oxidised glauconite. Soft sediment deformation is common in some beds and desication and sub-aqueous cracks are abundant throughout. Finer grained beds have the same features but are planar to cross laminated and some red beds are platy-rubbly. *[It appears that there is a back ground sedimentation of green clay and that coarse clastic input is fluctuating?]* Bed 22 is thickest in the interval and features a prominent erosive surface at the base which hosts oxidised reworked glauconite -grains are broken and in lithified 'agglomerates' and oxidised black shale (retains original colour and texture interntally). Heavilly oxidised along the basal bed contact with oxidation fading over ~20 cm. I have placed the boundary for the Moroak Sandstone at the base of bed 30 as it makes more sense than in bed 39 where is was placed in the log report.

31-40) cross bedded and cross laminated interbedded silt and silty clay with thin sand filled scours and erosivelly based sand beds, that increase up core to the eroded weathered contact with bed 30. Soft sediment deformation and sub-aqueous cracks throughout syn sedimentary faulting in beds 33, 34 and 36. Post lithification fault cuts this interval and contains a mix of massive carbonate, quartz, sulphides and graphitic carbon. Silt and silty-clay beds alternately black to mid-grey and weathers to rusty orange-yellow green on the outer surface of core. Black OM-rich wrinkly laminations are common through out. From bed 37 Silt and silty clay beds transition down core into alternating red and green beds and then black into grey and then to black at the base of bed 37. Black planar laminated silt and silty clay beds may be completely consumed by a white-orange-yellow powder y-fluffy crystaline material here termed 'gypsum rot' *[looks like the yorkshire lias sulphur bands].* Contacts between silts and silty clays are erosive, in beds 31, 35 and 37 the surface of the contact is heavilly oxidesed and oxide staining appears to 'seep' down core for several tens of cm. Sand beds are cemented with green clay and contain glauconite, some internal bedding surfaces within sand beds are oxidised. Upper surface of sand beds appears to be weakly erosional and overlying silts and silty clays drape the surface. Base of sand bands contains rare oxidised rip ups of black and grey silt and silty clay. Multiple small coarsening up cycles are contained in each silt and silty clay bed with one final longer coarsening up into the erosive contact with the overlying sand bed. Each sand bed appears to represent a single minor internal coarsening up cycle.

41-47) Large parts of this interval are what the core store workers call 'kitty litter'. This consists of light to mid blue grey claystone that has dissagregated into small pebble to granule sized chips apparently after hydration induced expansion. The kitty litter clay has a soft soapy texture and reacts weakly to HCl, contacts between kitty litter and adjacent beds appears to be sharp. The section of core between the lower part of bed 46 and the upper part of bed 47 has been completely disagreggated by kitty litter, only the sand scours, and a prominant gypsum rot band in the lower part of 47 remain. In some places the orignal core shape and thus sedimentary textures are retained because the expansion has wedged sections into place. In other intervals entire core sections have disintergrated leaving only cemented beds in place. As such the beds in this interval are reconstructed what I was able to piece together. In addition to kitty litter, each bed also contains the same silt and silty clay beds, and scour based thin sands as above. The scour sands are semented with pale green clay and cross laminated with oxidised granules along the top of some cross beds. Sand scours are also topped with dark red silty clay and clay beds which maybe massive, platy or rubbly. The thickness of and frequence of the dark red clay beds increases up core. Silt and silty clay beds are normally mid grey with increasing frequency of OM rich beds with wrinkly black lamina down core. There is a prominent gypsum rot band in the lower part of bed 45 that has an unusal yellow green colour and is platy rather than fluffy *[looks like oxidised paper shale from the jet rock back home but the colour is wrong]* The lower most part of bed 47 hosts red brown weathering silts and slity clays that are blue grey to green when fresh. The upper surface of each bedset hosts a sharp planar to undulose erosive contact that features a thin sand bed with granular chips of underlying material, shreds of organic matter and glauconite granules. Cross bedding in the silts and silty clays is longer than the core width and ranges from a few cm to a few tens of cm, due to this it is not possible to assign the type of cross bedding, but the contacts of cross bedding sets are angled against each other and appear to be erosional. There are many minor coarsening up cycles within in each bed.

48-50) Interbedded to interlaminated clay and silty clay with thin silt beds and very thin rare sand scours. Uppermost part of bed 48 grades up to silt over ~ 25 cm and is then truncated by a sand scour. Contact with overlying bed is oxidised and the red - brown oxidation appears to 'seep' down core. Under oxidation sediments are mid blue grey to green, sand scour is cemented by green clay and contains glauconite grains. Down core the sediment is alternately mid grey, black and pale green with changes between colours appearing as sharp contacts but occasionally grading from green to grey over a few cm. Wrinkly black lamina are common through out but most abundant int he green and black beds. Blue grey beds increase in abundance and green beds decrease down core to the base of bed 49 where there is a silt and glauconite rich erosive contact. below which the cycle repeats down to the base of bed 50. Visible sulphide grains become abundant in bed 48 and increase in size and abundance down core. Some appear to be syn-sedimentary pyrite framboids between 2-5 mm that are draped by overlying lamina. Other sulphides are large single euhedral tetrahedra, pyritohedra and dodecahedra between 5=15mm and nodular aggregates of tetrahedra between 5-25 mm, the single crystals and aggregates are fabric destructive and appear to have formed after lithification. I call these 'sulphides' as the crystaline forms show a number of different colours and variations on the described crystal habits that could be other sulphides like galena or sphalerite etc.

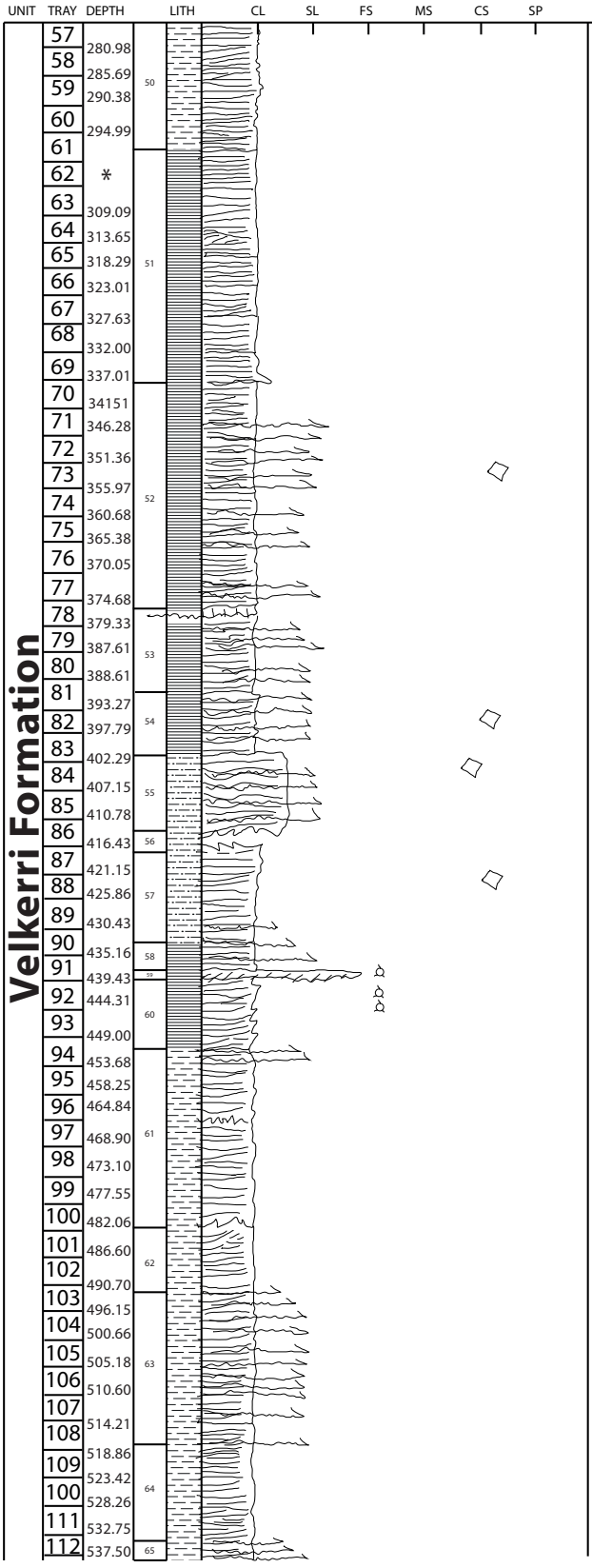

NOTES

48-50) *continued* near the middle of bed 50 there is a massive to platy red clay bed, below this there are no more framboids in this bed, though sulphide crystals remain abundant. those smaller and with no large crystaline aggregate nodules. In the lower part of bed 50 there is a distinct hard horizon ~2m thick that appears to be brecciated silty clay that has been cemented by rusty brown weathering carbonates. The surface of this horizon bears many ~5 mm pustular disks that superficially resemble Ediacaran medusoid disks. This horizon has destructive contacts with adjacent horizons so is probably diagenetic? Below this horizon there are mm scale angular pits with a rusty brown residue, there are also rusty brown weathering mm scale carbonate rhombs which may have left the pits when dissolved (?). The lower most meter of bed 50 increases in OM abundance down core and features bands of prominent gypsum rot. Sedimentary structures in this interval range from the large scale cross bedding described above to thinner cross bedding and laminations that are still longer than co width and undulose, wrinkly and planar laminations which increas in abundance down core with OM abundanc

51-54) the lithology of this interval is similar to the overlying interval but with a reduced number of silt beds, silt beds are still present as a silt free beds, bed 51 is also devoid of any observed sandscours. Sedimentary structure this interval is dominated by undulose, wrinkly and planar laminations with less instances of low angle cross be in bed 51 and the upper part of bed 52. Organic matter is enriched in this interval to the degree that original sediment colours are obscured and sedimentary structures are obscured so that beds may appear massive, or fi planar laminated where drilling marks score the core surface (aka 'core score'). Gypsum rot helps pick out beddi lamination in some places, in others, structure can only be seen then the core is sectioned and cleaned and held the correct angle to light. Bed 52 is particularly rich in OM and live oil was released from some of the silt and san beds when cut. The oil smells strongly of sulphur and tar and this interval is probably equivalent to the "C" and " bands of hydrocarbon rich sediments found throughout the Velkerri Formation. There is a beds of blue-grey kitt with sharp contacts on either side near the base of bed 51. The underlying part of bed 51 coarsens down core in erosively based siltstone. The contact between bed 51 and 52 hosts a thin carbonate cemented beccia that cont black mud stone chunks, bellow this there is another interval of blue-grey kitty litter hosting a band of gypsum with sharp contacts between the carbonate breccia and the underlying silt scour. Bed 52 hosts a metalic sulphic cemented silt scour and the clay beds adjacent to this scour are unsually dense, have weathered to rusty orange brown, internally, the organic matter is mottled and there is a sparkling metallic yellow dust permeating the sec which forms descrete metallic sulphide laminations and hair thin diagonal to vertical metallic sulphide viens ne silt scour. The contact between bed 52 and 53 hosts an intrusion of crystaline material that appears to be a mix quartz and carbonate (HCl reaction) but also small tabular crystals suggestive of plagioclase, the contact with surrounding sediments is 'turbulent' and ductile, with a cement of black glassy meterial and metallic sulphides, granule sized sphearules of hollow glassy material is also present and the adjacent sediments are pock marked these are missing. Metalllic sulphides permeate the adjacent sediments as this laminae, veins, and dust. The res bed 52 - 54 consists of OM rich clays and silty clays in minor coarsening upward cycles topped with a glauconiti erosivelly based silt scour. The frequency and abundance of silt scours increases towards the base of bed 54. Col beds lightens down core, possibly as OM content decreases.

55-56) Bed 55 consists of silty clay and many slit scours in thin ersoively based fining up packages. Clay rich bed feature undulose, wrinkly and gently dipping cross laminated planar laminates. Silt rich beds feature gentle dip cross bedding that is longer than core width. silty beds are rich in glauconite, clays range from mid grey to pale Pyrite is abundant through out as mm scale lamination destructive crystals . Bed 56 consits of a chaotic breccia metallic sulphides, silt and green, mid grey and black clay chips. The contact with adhacent beds is shows inclin 'ragged' fractures *[as though the breccia was injected with force from one side?]*

57) Repeats the lithology of seen in beds 54 and 55. Near the top is a platy layer that has been destroyed by the yellow-green variety of gypsum rot. The middle of the bed hosts fabric destructive euhedral pyrite crystal as abo rare cm scale bedding destructive nodules of accular mettalic sulphides. The metallic sulphide layer is connecte base of the bed by a network of thin horizontal and vertical metallic sulphide veins which extend up from the b bed *[they look just like a tiny dyke and sill network]* Towards the base of the bed there are several thick laminae of matte-vitreous 0.5 -1 mm long crystals that appear as losenge or rhombus shaped.

58-60) This intervalfeatures similar levels of organic enrichment to beds 51-54 and probably is equivalent to the band of organic enrichment in the Velkerri formation. Organic enrichment occurs over only a few tens of cm at t of the interval, at the base, OM enrichment occurs sharply at the base of bed 60. The lithology of this interval co many cycles of coarsening up from clay to thin erosively based glauconitic silt scours which contain increasing amounts of fine sand down core. Bed 59 is an erosively based glauconitic fine sand that hosts uni directional cro bedding and possible hummocks but the latter are longer than core width. Upper surfaces of cross beds host glauconitic and oxide granules and laminated shreds of OM that drape the cross bed surface. Hydrocarbons in t fill voids as amorphous blobs and may have migrated from adjacent beds. The base of bed 59 also contains rip u underlying material that appears to have been ridgid when eroded and incorporated. Bed 60 continues the tren bed 58 and hosts an orange-white-yellow gypsum fluffy and powder gypsum rot bed near the base and many t erosively based glauconitic fine sand scours.

61-65) Are similar to beds 58-60 but with out the organic enrichment. Beds consist of ligh blue, and green grey l undulose, wrinkled, gently dipping planar and longer than core width cross laminated clays and silty clays. Erosi glauconitc silt scours are present in beds 63 and 65 but are draped by overlying clays and silty clays without any fining or coarsening cycles. The scoursin both beds become less abundant and thinner up core. Clay rich beds h 'soapy' or waxy appearence when fresh and concoidal fracture in some beds and waxy slicken sides in others g weather to dark teal green colour, blue beds weather to mid grey. The blue-green colour banding does not appe correspond to silty content and contacts between the two colours apear sharp and planar to undulose. The gree abundance and thickness of green bands increases down core. OM is present as thin wrinkled lamina in green b flecks and shreds that drape bedding planes and may ppear folded and twisted. the lower part of bed 62 hosts blue kitty litter underlain by a thin hydrocrabon rich clay that rests with a sharp draping base on the silt scour at the bed. Near the top of bed 64 there are several thin dark blue to purple planar laminated clay beds that smell sulphur and bitumen but hold no obvious OM or HC. Green beds adjacent to the blue and purple beds weather descrete bands. There are two thin quartz-carbonate breccias in this interval, one in bed 61 and another at the b beds 61 and 62. Breccia contacts are ragged and fractured indicatinc intrusion after lithification.

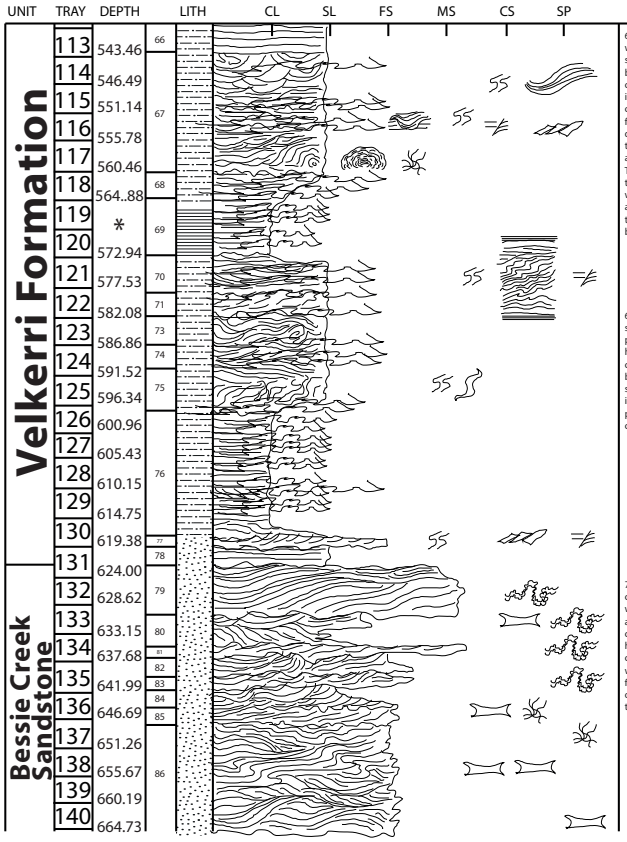

66-67) bed 66 coarsens from clay to silt over the top ~10 cm. the bed consits of thinly bedded green clay cemented silt with intervening green clay laminations that drape underlying silt beds. Beds are gently undulose which may be cross statification that is longer than core width. The contact with the underlying bed 67 is sharp planar erosive and marked by a glauconitic fine sand that is in turn erosively overlain by the first silt bed of bed 66. Bed 67 consistes of highly convoluted green clay cemented silt with thin erosively based scours of glauconitic fine sand that also contain imbrecated fragments of sub-horizontal to vertical stacked green and black clay. Soft sediment deformation is common as folds of what appear to be cohesive sediemt, convoluted bedding and dewatering structures. These features are draped by overlying sediments. There are a number of steep sided flat based scours that are infilled and draped by underlying seddiments. Syn-sed faulting is found in the lower pard of bed 67 with the fault cutting across the width of the core over ~1.5 m. Throughout bed 67green clays that immediately overly scours and silt rich beds have a soft waxy massive texture distinct from the matte-earthy texture of the laminated green clays n the rest of the bed. The lower most part of the bed consts of unusual green clay and silt mounds blisters and pustules that rest directly on teh fine glauconitic erosively based scour at the base of the bed. The green clay mounds etc are internallly laminated with OM in wrinkled, convulted and discontinuous laminations, mounds appear to overgrow each other. The surfaces and bedding planes that hold the mounds have a texture like flattened wrinkles. Most mounds etc are 0.5 - 10mm but the largest is ~100 mm high and ~ 250 mm wide. The mound bed is draped by an unsual 'carbonate sand/granule/pebble bed with unidirectional cross beds which is cut by an erosive sand scour.

68--78) range from clays throung to silts with many minor coarsening up cylces topped by erosive glauconitic fine sand or silt scours. The colour of clay cementing silt beds and in the clay beds themselves alternates between black, pale green, mid green and dark green independent of lithology. Several of the black clay beds have a HC odor and host yellow-green sulphur bands. Syn sed folds, dewatering structures, flame structures and convoluted bedding are common in the silt rich interval between beds 70 and 75 as is syn sed faulting. Sub-aqueous cracks are abundant in bed 75 and are overlain by several beds with unidirectional cross beds. Mound etc structures are present resting on some sand scours but are not as well developed as above. bed 77 contains small scale synsed faulting and imbrecated sub-horizontal intraclasts of blue and green clay. Bed 78 is erosively truncated by bed 77 and is a white planar to undulose laminated silt interlaminated with thin white platy brittle clays, and waxy pale green massive clays. The white silts and clays have a powdery residue and appear leached.

79-86) This is probably the Bessie creek sandstone rather than the lower Velkerri. The BCS consists of fine to medium cross-bedded sandstones interbedded with thin silt and silty clay horizons that dominantly feature pale green waxy clay with no obvious internal structure. Convoluted bedding and dewatering structures are common. The green clay weathers to a white powdering substance and the sands weather to pale pink. Tabular, lenticular and hopper pseudomorphs are common, tabular are replaced by green clay, showing a 'collapsed' internal structure, lenticular are replaced by silica and hopper maybe either. Some of the silt and clay bedding surfaces feature the flattened wrinkle texture as seen above and contain rare 'crystalised' HC. Clay, and silt stone rip ups are common at the base of coarse beds and on erosive surfaces along with rare rounded chert pebbles. Bedding planes also feature dessication cracks and rare structures that look like stylolites filled with OM, but appear to only intercept within a few cm of the palaeo surface. Several erosion surfaces are oxide stained or oxidised, while some of the erosional surfaces appear to have undergone dissolution and look almost karstic, and have then been infilled by overlying sediment.

99VRNTGSDD2

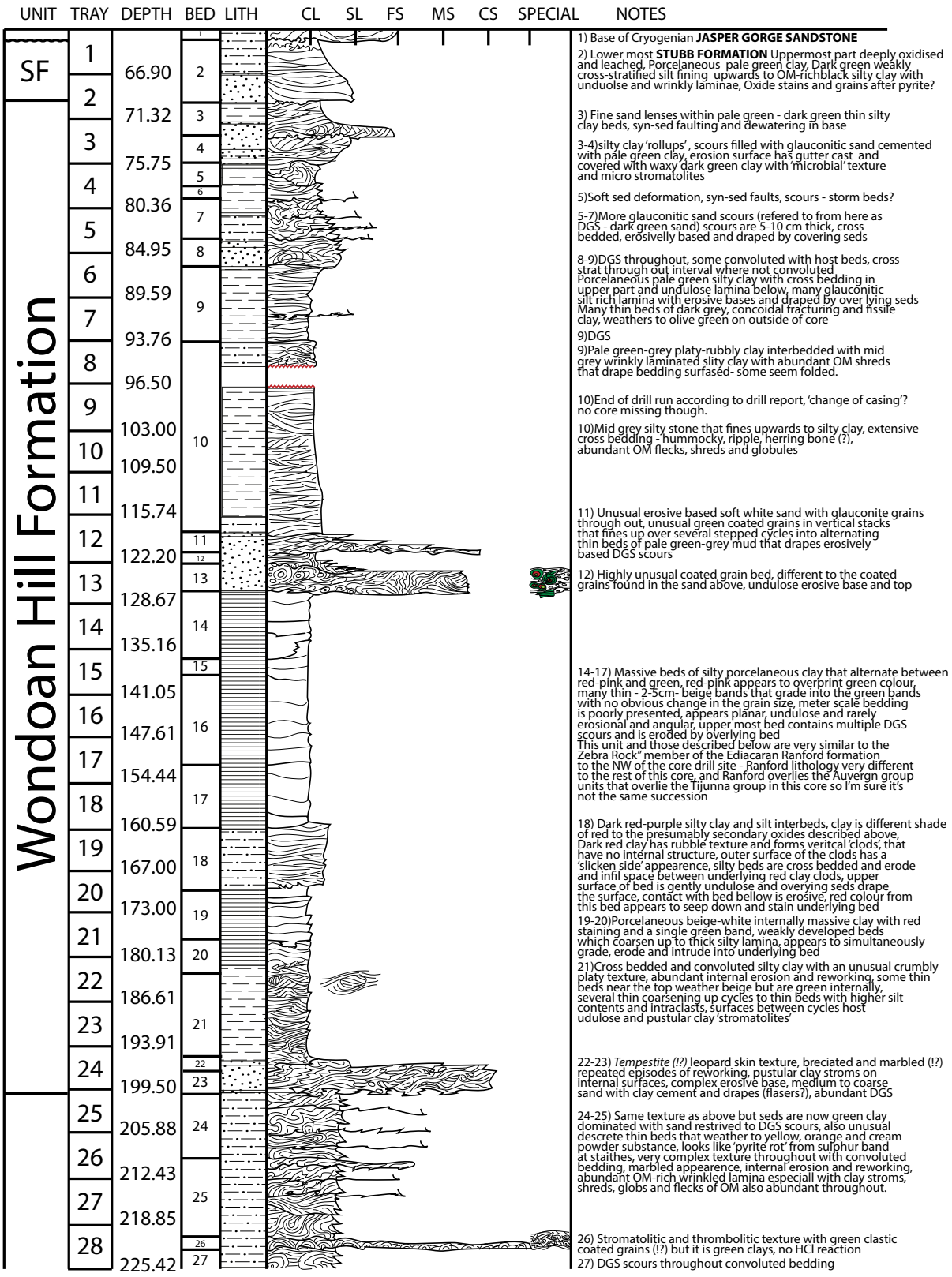

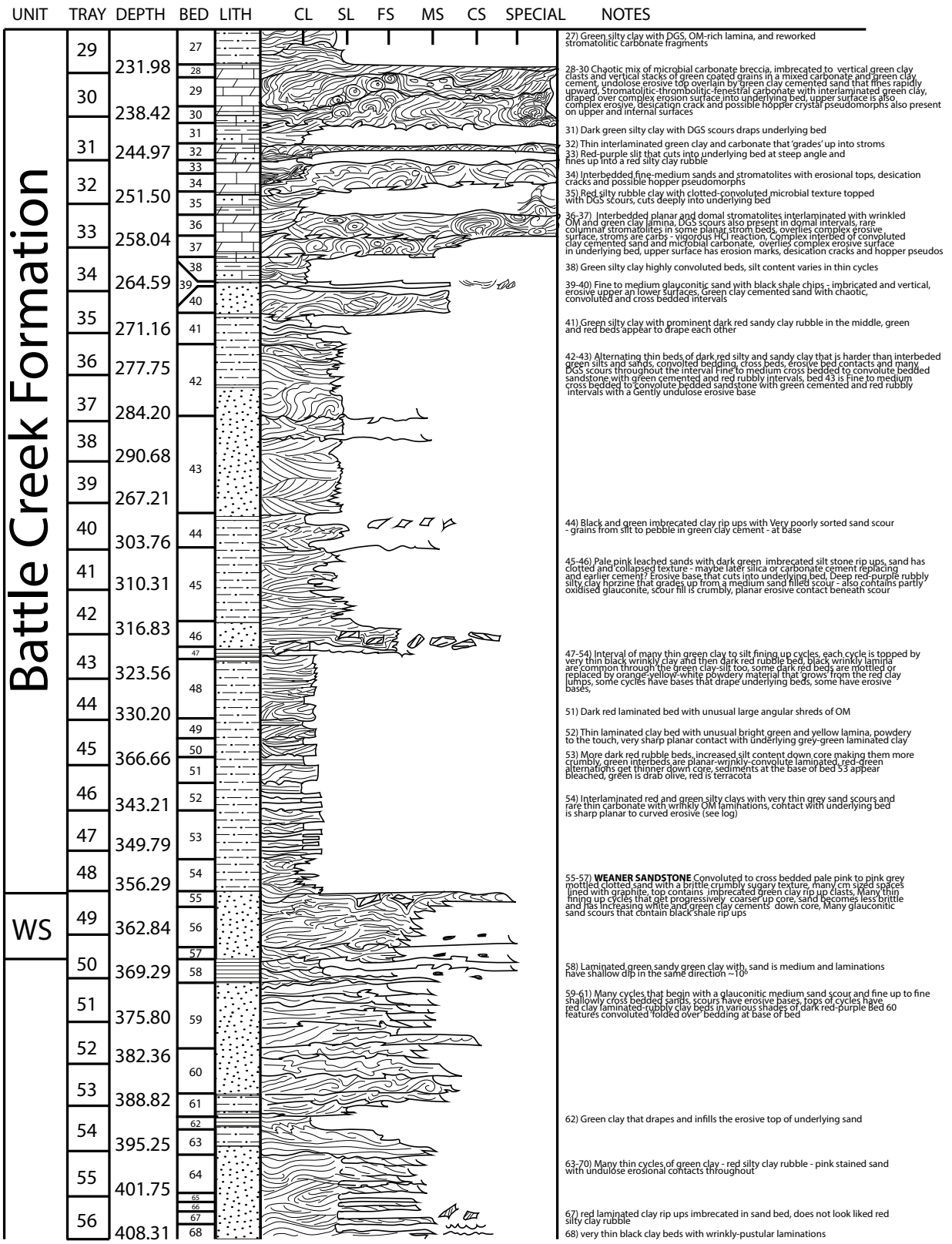
UNIT
TRAY
DEPTH
BED
LITH
CL
SL
FS
MS
CS
SPECIAL
NOTES
Battle Creek Formation
WS
29
231.98
30
238.42
31
244.97
32
251.50
33
258.04
34
264.59
35
271.16
36
277.75
37
284.20
38
290.68
39
267.21
40
303.76
41
310.31
42
316.83
43
323.56
44
330.20
45
366.66
46
343.21
47
349.79
48
356.29
49
362.84
50
369.29
51
375.80
52
382.36
53
388.82
54
395.25
55
401.75
56
408.31
27
28
29
30
31
32
33
34
35
36
37
38
39
40
41
42
43
44
45
46
47
48
49
50
51
52
53
54
55
56
57
58
59
60
61
62
63
64
65
66
67
68
27) Green silty clay with DGS, OM-rich lamina, and reworked stromatolitic carbonate fragments
28-30 Chaotic mix of microbial carbonate breccia, imbrecated to vertical green clay clasts and vertical stacks of green coated grains in a mixed carbonate and green clay cement, undolose erosive top overlain by green clay cemented sand that fines rapidly upward, Stromatolitic-thrombolitic-fenestral carbonate with interlaminated green clay, draped over complex erosion surface into underlying bed, upper surface is also complex erosive, desication crack and possible hopper crystal pseudomorphs also present on upper and internal surfaces
31) Dark green silty clay with DGS scours draps underlying bed
32) Thin interlaminated green clay and carbonate that 'grades' up into stroms
33) Red-purple slit that cuts into underlying bed at steep angle and fines up into a red silty clay rubble
34) Interbedded fine-medium sands and stromatolites with erosional tops, desication cracks and possible hopper pseudomorphs
35) Red silty rubble clay with clotted-convoluted microbial texture topped with DGS scours, cuts deeply into underlying bed
36-37) Interbedded planar and domal stromatolites interlaminated with wrinkled OM and green clay lamina, DGS scours also present in domal intervals, rare columnar stromatolites in some planar stromb beds, overlies complex erosive surface, stroms are carbs - vigorous HCl reaction, Complex interbed of convoluted clay cemented sand and microbial carbonate, overlies complex erosive surface in underlying bed, upper surface has erosion marks, desication cracks and hopper pseudos
38) Green silty clay highly convoluted beds, silt content varies in thin cycles
39-40) Fine to medium glauconitic sand with black shale chips - imbricated and vertical, erosive upper an lower surfaces, Green clay cemented sand with chaotic, convoluted and cross bedded intervals
41) Green silty clay with prominent dark red sandy clay rubble in the middle, green and red beds appear to drape each other
42-43) Alternating thin beds of dark red silty and sandy clay that is harder than interbeded green silts and sands, convolted bedding, cross beds, erosive bed contacts and many DGS scours throughout the interval Fine to medium cross bedded to convolute bedded sandstone with green cemented and red rubbly intervals, bed 43 is Fine to medium cross bedded to convolute bedded sandstone with green cemented and red rubbly intervals with a Gently undulose erosive base
44) Black and green imbrecated clay rip ups with Very poorly sorted sand scour - grains from silt to pebble in green clay cement - at base
45-46) Pale pink leached sands with dark green imbrecated silt stone rip ups, sand has clotted and collapsed texture - maybe later silica or carbonate cement replacing and earlier cement? Erosive base that cuts into underlying bed, Deep red-purple rubbly silty clay horzine that grades up from a medium sand filled scour - also contains partly oxidised glauconite, scour fill is crumbly, planar erosive contact beneath scour
47-54) Interval of many thin green clay to silt fining up cycles, each cycle is topped by very thin black wrinkly clay and then dark red rubble bed, black wrinkly lamina are common through the green clay-silt too, some dark red beds are mottled or replaced by orange-yellow-white powdery material that 'grows' from the red clay lumps, some cycles have bases that drape underlying beds, some have erosive bases,
51) Dark red laminated bed with unusual large angular shreds of OM
52) Thin laminated clay bed with unusual bright green and yellow lamina, powdery to the touch, very sharp planar contact with underlying grey-green laminated clay
53) More dark red rubble beds, increased silt content down core making them more crumbly, green interbeds are planar-wrinkly-convolute laminated, red-green alternations get thinner down core, sediments at the base of bed 53 appear bleached, green is drab olive, red is terracota
54) Interlaminated red and green silty clays with very thin grey sand scours and rare thin carbonate with wrinkly OM laminations, contact with underlying bed is sharp planar to curved erosive (see log)
55-57) **WEANER SANDSTONE** Convoluted to cross bedded pale pink to pink grey mottled clotted sand with a brittle crumbly sugary texture, many cm sized spaces lined with graphite, top contains imbrecated green clay rip up clasts, Many thin fining up cycles that get progressively coarser up core, sand becomes less brittle and has increasing white and green clay cements down core, Many glauconitic sand scours that contain black shale rip ups
58) Laminated green sandy green clay with, sand is medium and laminations have shallow dip in the same direction ~10°
59-61) Many cycles that begin with a glauconitic medium sand scour and fine up to fine shallowly cross bedded sands, scours have erosive bases, tops of cycles have red clay laminated-rubbly clay beds in various shades of dark red-purple Bed 60 features convoluted 'folded over' bedding at base of bed
62) Green clay that drapes and infills the erosive top of underlying sand
63-70) Many thin cycles of green clay - red silty clay rubble - pink stained sand with undulose erosional contacts throughout
67) red laminated clay rip ups imbrecated in sand bed, does not look liked red silty clay rubble
68) very thin black clay beds with wrinkly-pustular laminations

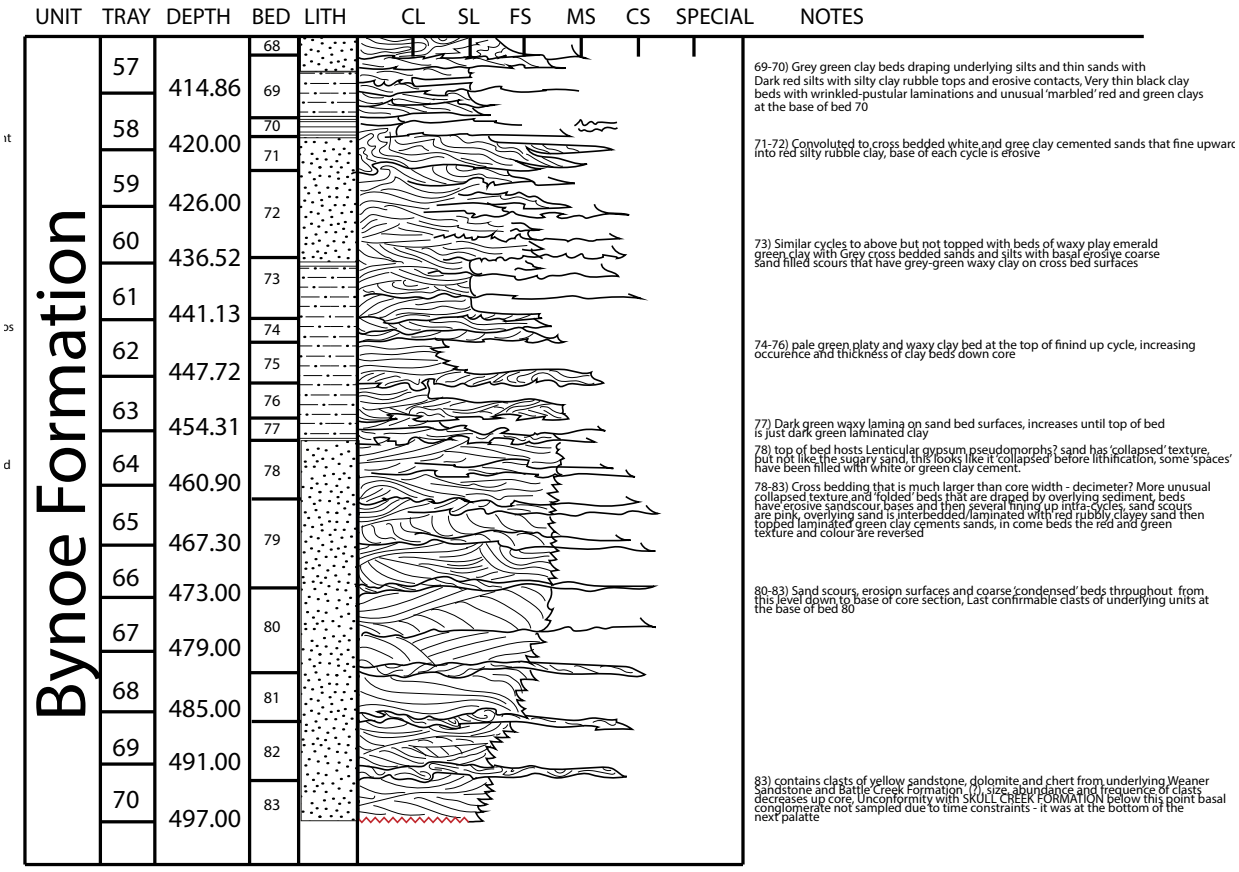

Unit boundaries set by me on the basis of major lithological changes e.g. appearence of the first authigenic carbonate beds , signaling a major change in depositional environment. Boundaries in drilling report were based on projected unit thickness from outcrop studies adjacent areas. Underlying untis match descriptions from other drill cores and outcrop. The Wondoan HIll and Stubb Formation in this hole mostly match outcrop and descriptions from other drill cores. The carbonate and coated grain beds have not been observed or described from the limited outcrop and drill core study. A potential explanation is that this core intercepted a package of sediments bound by faults thought to be active during deposition and so may have represented a lowland area prone to flooding. No further drill cores have been sunk, and no outcrop is available in this area to test this hypothesis. Beds were set by me on the basis of erosional boundaries and shared characteristics with adjacent beds.

McManus-1

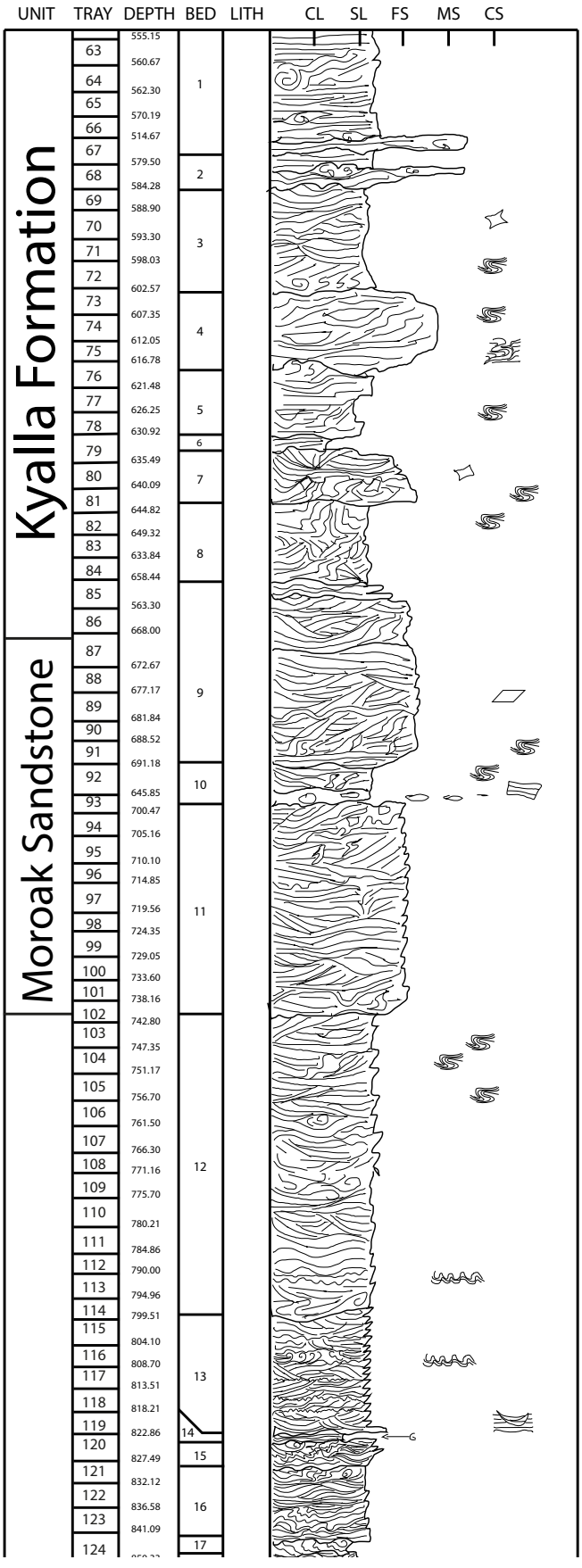

1-3) Green and grey clay cemented silts and sands with common cross and convoluted bedding. Pale waxy green clay lamina drape cross and convoluted bedding surfaces. Two thin pink medium to coarse sand beds contain abundant glauconite and red earthy granules. Winkly OM-rich lamina are common through out the interval. Upper surface of bed 1 is erosively truncated and oxidised with silica cemented sand filled cracks at the upper contact. Base of bed 3 contains many alternating thin beds of laminated to massive waxy to earthy green clay, and red rubbly clay infilled with pale grey silt. base of bed 3 is an undulose planar contact that does not appear to be erosional.

4-8) Bed 4 is a pink to pale yellow cross and convolute bedded medium sand with common silt filled scours. The upper surface is erosionally truncated and oxidised with a leached sugary texture. Dewatering structures are common throughout. Contains several thin red platy clay beds. Bed 4 may correspond to the 'Elliot Sandstone' member of some workers. Bed 5 is similar but features and extensive green clay cement and is silt to fine sand grade and is underlain by a thin silty OM rich clay (bed 6). Bed 7 is similar to bed 4 and features a well oxidised upper part and surface that hosts green clay rip up clasts and hopper (?!) pseudomorphs filled with laminated pale green clay. Below the oxidation the sand cemented by pale green and green grey clay and hosts internal erosion surfaces rich in glauconite granules and dewatering structures. Bed 8 is another green clay cemented fine sand to silt stone with common wrinkly OM-rich lamina, the upper few meters of the bed below the contact are especially ferruginous with glauconite grains alonger cross bedding surfaces and a mix of pale green powdery and dark green waxy cements and thin beds that drape cross beds and convolutions. This bed is extremely convoluted - core report describes this texture as 'chaotic'.

9-11) This interval is dominated by fine to medium cross and convolute bedded sands with common dewatering structures and internal erosion surfaces. The top of bed 9 hosts an unsual bright yellow-green silty clay bed that is finely laminated and drapes the underlying sand. The upper surface of the sand is erosively truncated and oxidised but there are pale grey-green reduced areas where it contacts the yellow-green bed. Bed 9 is also cemented by green clay and features waxy pale to dark green clay thin beds that drape bedding surfaces. in the middle of bed 9 there is a prominent internal erosion surface which hosts mm scale red-orange translucent rhombohedral crystals, overlain by a thin dark red rubbly clay bed. Bed ten also features a red rubbly clay layer which overlies an ersional surface at the top of bed 11 and hosts green and black silty clay rip ups and hopper pseudomorphs filled with laminated green clay. Bed 11 is also features green clay cements and bed coatings. The upper surface of bed 11 is oxidised with the red staining fading down core. Several of the internal erosion surfaces are also oxidised in the same way. The lower part of bed 11 features scours filled with black and green clay chips and beds of larger imbrecated rip up clasts of black and green clay. *[The green sands here are the ferruginous sands of Lanagan - could be the basinal regions equivalent of the Sherwin Ironston as it occurs in the correct stratigraphic positions.]*

12-15) The Velkerri Formation is erosionally truncated by the overlying Moroak Sandstone. The contact shows evidence of oxidation, sub-aerial weathering and evaporite "chicken wire" like texture. Bed 12 consists of many coarsening up cycles of silty mudstone to fine sandstone, dewatering structures, convoluted bedding, trough, uni directional, and bi directional crossbedding are common. Inclined, planar and wrinkled laminations are common down core. Ferruginous green intervals are common as are sulphide rich intervals with intense gypsum rot. Rare thin massive to rubbly and planar laminated red clay beds interspersed through out. Unusual pink quartzite bed at ~790 m - possibly hydrothermal? Scours and internal erosion with green clay rip up clasts common throughout interval. Glauconite lag laminations common throughout. Alternating red and green waxy and platy thin clay beds in lower part of interval.

16-19) Black silty mudstone that coarsens to black siltstone up section. Sedimentary structures as above. Many small decimeter coarsening upcycles topped by glauconitic lags. Organic matter disseminated throughout and strong hydrocarbon smell. Rare red clay beds at the top of some coarsening cycles. Unusually highly deformed organic rich bed at ~845m.

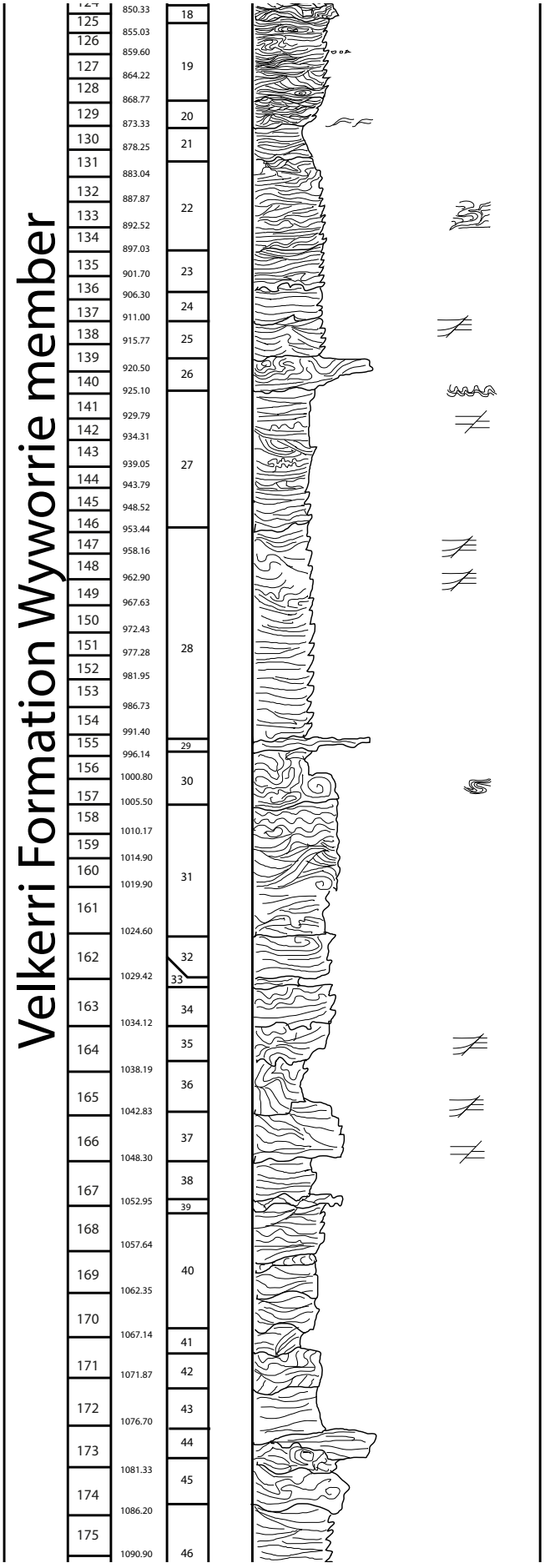

20) Pale green platy and waxy silty mud stone that fines to clay then coarsening back up to silty mud across the bed. Many glauconitic lags. Trough and unidirectional cross beds common along with convoluted bedding. Cross bed foresets commonly draped with red clay in the silt rich intervals. Rare yellow-green 'fluffy' and rubbly clay bands dispersed through out interval. Red crystaline mm spots throughout - siderite?

21-28) Black organic rich interval with many decimeter mudstone to siltstone coarsening up cycles topped with glauconitic lags. Unidirectional and trough cross bedding and lamination common. Intense convoluted bedding in localised intervals around possible syn-sedimentary faults. Sulphides present as cm scale fabric disruptive nodules and vein networks. Frequence erosive scourse and erosive contacts between beds. OM and sulphides destroyed by intense localised gypsum rot on outer surface. Many 'rotten' beds are green internally when cut. Rare bands of platy to massive red clay throughout. Amplitude, frequency and intensity of cross and convoluted bedding increases up section.

29-48) Thin glauconitic sand bed that erosively truncates the underlying unit at the top of the interval. Sedimentary structres as above, many intervals of intense concovoluted bedding. Interval dominantly black silty and sandy mudstone with thin clay beds, erosive contacts through out. Alternating black and red clay bands in the upper part interval. Post sed faulting at 1048m possible syn sed faulting at 1034m and 1042m. Rare thin beds of purple-blue clay stone in lower part of interval. Extensive gypsum rot in OM rich areas. Glauconitc lags common at the top/base of beds and thin ferruginous clay beds throughout. Some parts of this interval have many mud - silt coarsening up cycles but overal this interval has no obvious grain size or sed structures trend and is chaotic. Imbrecated and jumbled rip up clasts locally common.

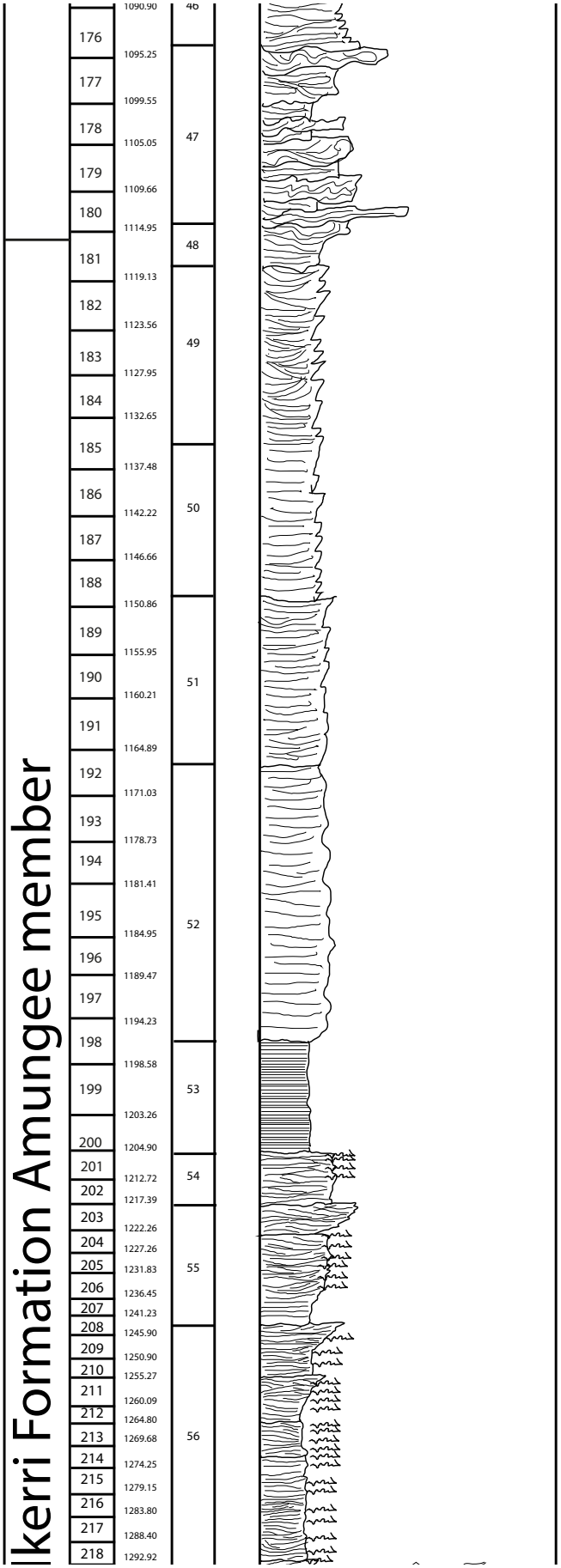

49-52) Variably slit rich mudstone with many coarsening up cycles of claystone to siltstone. Planar, inclined and wrinkly cross lamination common throughout interval. Trough, unidirection and bidirectional cross bedding locally common. Alternately black, dark grey, pale green and red bands that are conformable with bedding and sed structures. common thick laminae of waxy laminated to play yellow green to dark green clay throughout. OM rich laminae, and OM flecks and shreds common through out. Many thin erosively based silt stone and fine sandstone scours through out. Glauconitic lags common at the top of coarsening upcycles (or base of overlying cycle?)

53) Finely laminated OM rich mudstone consisting of alternating variable OM rich and poor clay and silt laminae. Laminae at mm thickness but there appears to be poorly developed unidirectional cross lamination within each lamination. Fine glauconite granuals through out. Silt laminations are erosively based and some form mm to cm scale channels. Bed 53 draps a glauconitic erosive surface at the top of bed 54.

54-56) Interval coarsens from claystone to sandy mudstone at the top. Composed of several meter scale coarsening up cycles, that are in turn composed of many cm scale coarsening up cycles. Erosicely based fine sand beds are found through out and appear to be independant of any of the coarsening cycles. OM rich laminae common through out with extensive gypsum rot. Meter scale cycles are erosively based. Trough, uni and bidirectional cross bedding and laminations common throughout and increase in frequency and amplitude upsection. Glauconitic lags through out. Black OM-rich wrinkly laminations are common in the lower part of the interval e.g., sample 1279.15m. Base of intveral drapes erosive surface at the top of the underlying bed.

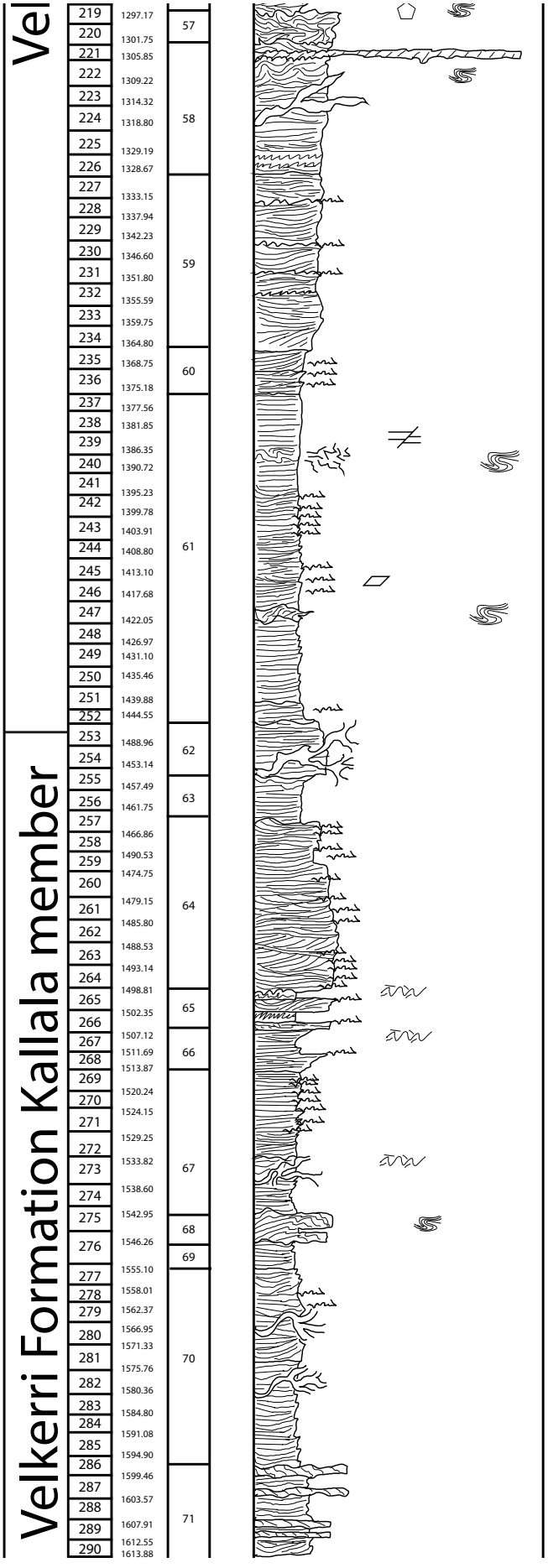

57-60) Silty mudstone to muddy siltstone that coarsens over the intervals with many cm scale cycles. Sedimentary structures as above, aslo many fine erosive thin fine sand beds. Interval is OM-rich both as OM beds and beds with disseminated OM flecks and shreds. Rare olive green waxy massive thick laminations. Upper part of interval has been intruded by dolerite at several depths and features extensive hydrothermal veins of quartz, carbonate and sulphides. Some dolerite appears to be post sedimentary e.g., 1306m and has breciated the host rock, some appears to have a peperite texture e.g., 1301m and may be syn- or shortly post sed.

61-63) thick bed of variably silt-rich mudstone with planar, inclined and wrinkly laminations and many erosively based silt scours. Localised unidicertional cross lamination and convoluted laminations. Possible pepperite at 1390m, 1422m and 1453m as well as carbonate and sulphide veins throughout. Wrinkled possible microbial laminae locally common. Extensive gypsum rot in OM rich intervals.

64) Thick erosively based bed of siltstone that fines upward to silty mudstone. Trough, uni- and bidirectional cross beds and laminations common throughout along with thin erosively based fine sand beds. Basal contact contains rip up clasts and material reworked from underlying intervals of the Velkerri Formation. Is dark grey and green grey in the lower half and changes abruptly to light grey upsection.

65) Highly convoluted erosively based bed with rip up clasts and many erosively based fine sand scours. Trough, uni- and bidirectional cross beds common where the bed is not convoluted. Locally pervasive quartz, carbonate and sulphide mineralisation that permeates the coarser grained beds and cuts clay rich laminations.

66-67) Claystone that coarsens up to silty mudstone in many cm scale coarsening cycles. Interlaminated with many silt and fine sand erosive scours. Planar and inclined laminations common through out with bidirectional cross lamination in the upper part of the interval. Many thin OM-rich laminae throughout. Grey coloured in lower part with OM-rich bands that are independent of lithology. Increasingly green coloured upsection with glauconitic lags at the top(base?) of some cm coarsening cycles. Rare intervals of rip up clasts and convoluted beds that appear to have been laterally 'injected' into the host rock. Lower part of intervals hosts a large quartz, carbonate, sulphide vein network that has brecciated the host rock. OM adjecent to the veins is graphitised to fluids must have been hot >200 degrees C?

68) Convoluted to folded (slumped?) sandy siltstone that is eroded by the overlying bed and erodes the underlying bed. Unusual internal stratigraphy (see diagram below)



69-71) Blue grey variably silt-rich claystone with rare erosively based silt and fine sands scours. Inclined, undulose, and wrinkly laminations common. Trough, uni- and bidirectional cross laminations locally common. Many cm scale clay to silt coarsening up cycles but there is no overall grain size change up section. Bed 70 hosts two quartz, carbonate, sulphide vein networks as above. OM present as flecks and shreds disseminated through out and as rare wrinkled laminations. Bed 71hosts several erosively based of unidirectional crossbedded fine sandstone - poorly sorted and many angular clasts. Bed 71 is green with the colour grading to blue grey upsection with no obvious change in lithology. Glauconitic lags throughout at the top (base?) of coarsening up cycles.

Sherwin Ironstone as intercepted in Urapunga 4

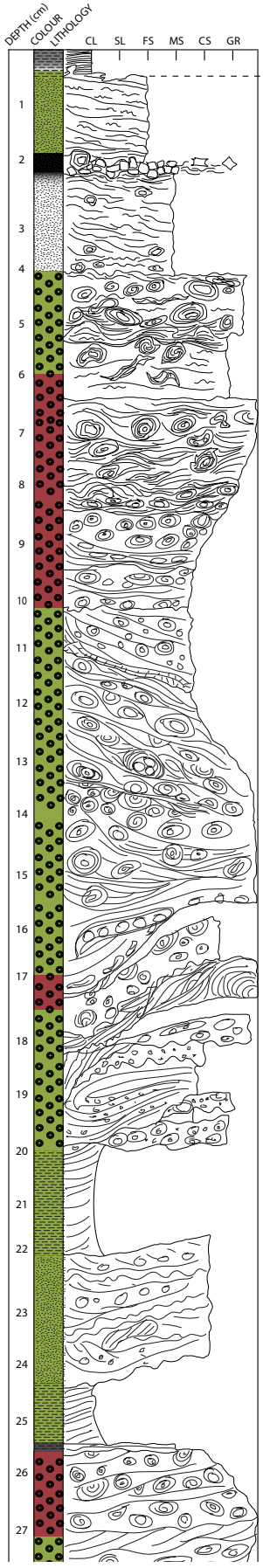

Kyalla Mudstone Formation Green grading into dark grey finely laminated mudstone that drapes topography in the underlying erosional contact

Sherwin Ironstone/Moroak Formation

Cross bedded, green, thinly bedded alternating sandy and OM-rich layers. OM-rich layers have wrinkled, microbial appearance.

Thick highly OM rich lamina which drapes onto the underlying silica-rich bed. Possible evaporite bed composed of blue-green silicified grains in a carbonate and silt matrix that has a collapsed mesh-like texture. Blue-Green grains are composed of ferro-aluminous chert in SEM-EDS.

Laminated to weakly cross bedded pink-grey sand dominated by quartz and microcline, common glauconite and less common pyrite grains. Eroded and reworked green Fe-silicate ooids present and increase in abundance down section. Appearance suggests ooids were transported and eroded after lithification. Base of the bed consists of dark green sandy clay which contains poorly developed ooids and lighter green and green-yellow stromatolitic layers, and grades conformably into the overlying sand. The base drapes the minor erosional surface in the underlying bed, and which is OM-rich. Ooids at the upper contact are truncated.

Large ooids and cm scale oncoids in a cross bedded matrix of sand, green clay and broken reworked ooids and oncoids. Many oncoids and ooids are elongated and display a sinusoidal form. Clay rich lamina appear stromatolitic and some have OM -rich wrinkled lamina. Lower part of bed is rich in OM and green clay lamina which drape the underlying erosional contact filling the hollows with 'inverse' stromatolites.

Possible hiatus surface, green clay stromatolites with OM-rich wrinkled lamina form 1-3 cm mounds with a sharp undulating basal contact on the underlying bed

Dark green irregular elongate oncoids and spastolithic ooids which show plastic deformation and shearing in a low angle cross bedded matrix of sand, green clay, and secondary carbonate. Wrinkled OM-rich lamina abundant throughout and abundant at the top and base of the bed. Oncoids and ooids at the top of the bed are truncated by the bed contact. Matrix becomes increasingly oxidised down core, oxidation emanates from, and through, sand rich lamina. Base of bed has a sharp erosional contact and drapes the underlying bed.

Original green lithology has been heavily oxidised which in turn is overprinted by siderite and calcite, and finally pyrite. Oxide and carbonate/pyrite all cross cut primary sedimentary structures. Cores of some ooids and oncoids retain partially oxidised green clays, pyrite cores of coated grains also shows oxidation indicating pyrite cores are a primary feature. Oxidation emanates along, and from, sand-rich lamina and in places is arrested by OM or clay-rich lamina. Primary lithology is hummocky and swaley sands with clay and OM-rich lamina between sand packages . Coated grains are large and split evenly between post-lithification reworking, and spastolithic reworking. Structures and coated grains in the upper surface of the bed are truncated. The lower contact is sharp and undulose with the common OM-rich stromatolitic clay.

Thin bed of compacted and spastolithically deformed oncoids in a sandy clay matrix. Upper surface is composed of green stromatolitic clay forming 1-2 cm domes which show signs of reworking and regrowth. Matrix is heavily infused with pyrite which cross cuts lamina. Lower surface is low undulose and erosive.

Cross bedded ooid and oncoid packed bed with partial oxidation along sandy lamina. Coated grains in the upper surface are truncated. Lower quarter abruptly changes to cross bedded to stromatolitic green clay with spastolithic green ooids and partially pyritized organic lamina. Matrix of upper part contains sand and diagenetic carbonates. Some larger oncoids host yellow euhedral siderite layers. Lower contact is low angle undulose and erosional.

Similar to the overlying bed but is more clay dominated and oxidation lessens down core. Coated grains in the upper contact are truncated while those on the lower contact 'collect' into shallow depressions in the underlying bed. Top and base third hold cross bedded coated grains, middle third is stromatolitic green clay. Oxidation is restricted to sandy matrix, interior of coated grains and clay lamina retain green mineralogy.

Oxidation ends abruptly at a thin OM and green clay-rich stromatolitic lamina at the top of the bed. Cross bedded , green clay cemented sands containing abundant post lithification reworked coated grains, dominates the core. Upper OM lamina partially truncates and overgrows coated grains and cross beds. Base of the bed is a stromatolitic green clay that is composed of spastolithically deformed and overgrown coated grains which drapes the underlying undulose erosional surface.

Complex bed containing cross bedded and hummocky stratification in discrete packages bound by erosional surfaces. Matrix is quartz and feldspar sand cemented by green clay. Coated grains are common throughout in both post lithification and spastolithic forms. Coated grains at internal surface boundaries show erosionally truncation and some are partially exhumed and reworked into overlying layers. Upper surfaces of erosional packages contain thin stromatolitic green clay lamina. Basal layers contain unusual 'pea pod' shaped oncoids composed of strings of ooids in an irregular wrinkly lamina green clay coating. Below the pea pod layer, is a thin bed of spastolithic green ooids in a partially oxidised sand matrix. Coated grains in this bed include composite grains of up to three separate ooids combined and forming a core for larger oncoids. Many coated grains have a core formed from broken and partially eroded ooids and often feature spastolithically deformed cortices. Lower bed surface is erosional and forms a large high angle cross bed that is larger than the width of the core.

Thin bed of laminated OM and green clay-rich stromatolitic mudstone. Lamina show a sharp erosional contact with the underlying bed that drapes underlying topography at an angle suggesting the mudstone was infilling an erosional structure that was larger than the width of the core.

Large scale cross bedded sandstone that is green clay cemented and contains abundant post lithification reworked green coated grains. The upper part of the bed is partially oxidised by a sharp reaction front that cross cuts primary sedimentary structures and the internal lamina of coated grains. Both upper and lower contacts are sharply erosional. The upper surface is smoothed and contains erosionally truncated coated grains. The lower surface also follows cross bedding that is wider than the core, but has a highly irregular erosional contact with the underlying bed. Lowermost surface contains rip up clasts of the underlying bed.

Microbialite composed of inter-laminated green clay and OM. Dominated by domal stromatolites that show signs of erosion, reworking and regrowth. Upper surface is heavily eroded and incised by overlying layer. Lower most laminae drape the erosional surface in the underlying bed at an angle that suggests growth on a curved or tilted surface.

Spastolithic ooids in cross bedded sand cemented by green clay that grades laterally into stromatolitic green clay. Minor oxidation of the sand matrix in the lower surface. Upper contact lightly undulose and erosional, lower contact highly convolute and draping underlying bed. Angles suggest deposition on a slope.

Thin pod of cross bedded coarse sand with highly convoluted upper and lower erosional contacts, heavy oxidation which has been overprinted by pyrite.

Cross bedded to highly convoluted and slump folded sand with a green clay matrix and partially infused by secondary pyrite. Upper surface is eroded by overlying bed, lower surface erodes and incises into underlying bed. Lower part of bed is incised/intruded laterally by a pod of coarse sand and post lithification reworked ooids.

Cross bedded sand lens that laterally incises/intrudes adjacent beds, contains reworked spastolithic coated grains that show signs of compaction and post burial regrowth.

Laminated to shallowly cross bedded green clay with alternating lighter and darker bands. Lower contact is sharply undulose and lamina drape the underlying bed.

High and low angled cross bedded packages of green clay cemented sand and coated grains that are bound by minor erosional surfaces. Upper surface shows erosional truncation of sedimentary structure and coated grains. Lower surface is convoluted, contains rip up clasts and incises the underlying bed.

Laminated to shallowly cross bedded green clay with alternating lighter and darker bands. Lower contact is sharply undulose and lamina drape the underlying bed.

Thin laminated grey sand stone than incises the underlying beds

Complex bed containing cross bedded and hummocky stratification in discrete packages bound by erosional surfaces. Matrix is quartz and feldspar sand cemented by green clay. Upper half of bed is partially oxidised while lower half is pristine. Oxidation boundary is very sharp and cuts primary sedimentary structures and coated grain lamina. Coated grains appear preferentially oxidised in the upper half while the green clay matrix is less oxidised. Oxidation can be seen moving from the outside of coated grains inward and replacing a primary green mineralogy. Coated grains are both spastolithic and post lithification with spastolithic more common towards the base of the bed. Upper contact is erosional and structures and coated grains are truncated. Lower surface is low angle undulose to planar and erodes the underlying bed.

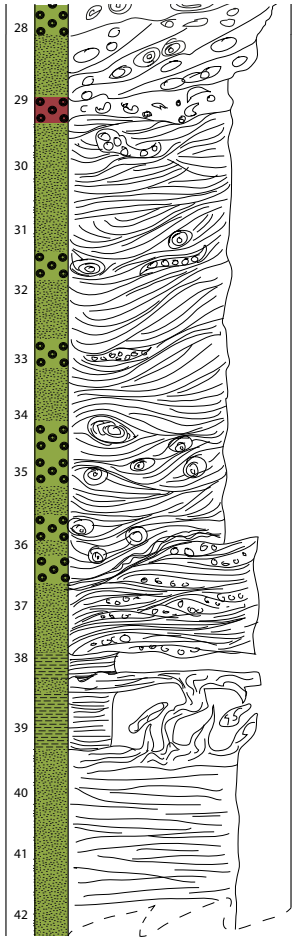

Highly convoluted bed of green clay cemented quartz sand. Contains abundant oncoidal and oolitic debris, erosively truncated by the overlying bed. Lower contact with underlying unit appears to be planar conformable and is possibly a non-erosive hiatus surface. Some of the coated grains are partially oxidised.

Cross stratified and hummocky quartz sandstone with green clay cement over printed in patches by several generations of oxidation. Secondary pyrite and carbonates are disseminated through out the matrix. Rare large red ooids and oncoids and pea-pod oncoids but also rare vertical ooid trains/stacks that cross cut sedimentary features. Several erosive hiatus surfaces that contain mixed carbonate and green clay stromatolites. Most grains are post lithification. but very little reworking damage. Coated grain abundance increases down core to a basal dark green clay horizon with stromatolitic lamina. Basal layer drapes underlying bed features suggesting deposition on a slope with some erosional truncation.

Cross bedded and hummocky quartz sandstone with a green clay cement and ooid debris. Common ooid-rich horizons with abundant spastolithic ooids. Erosively truncated by overlying layer, and incises underlying bed.

Dark green laminated to stromatolitic clay stone with minor silt and silty to fine sand lamina with scoured contacts. Apprently intruded by underlying sandstone.

Convoluted and cross bedded quartz sandstone with a green clay cement. Abundant ooid debris and patches of secondary carbonate. Appear to intrude the overlying bed with both sill and dyke geometries, the latter intrude from both above and below. 'Actual' contact with overlying bed appears to be abruptly planar and non-erosive.

Cross bedded and hummocky quartz sand beds with silica and/or kaolinitic cement. Inter-bedded with thinly bedded blue-grey illitic silty mudstones with abundant large flecks of organic matter and thin organic-rich lamina. No Fe-facies features are present in this interval.

200cm of sand and clay ommited

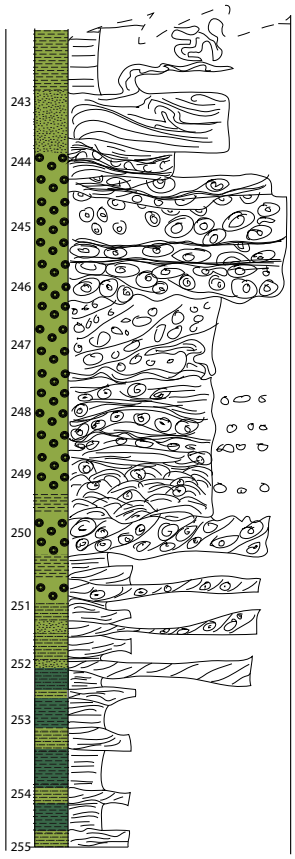

Rapid change to green silty clay, lithology remains consistent, only colour and mineralogy change from illitic to berthierine/chloritic clay. Intruded from above and below by underlying bed.

Convolute, slumped, cross bedded and hummocky quartz sandstone with a green clay cement, inter-bedded with a mix of silt/green clay and green clay rich bed. Abundant secondary carbonate cement that follows and emanates from sandy beds.

Cross bedded and hummocky quartz sandstone with green clay cement and thin glauconitic horizons. Erosive undulose contact with overlying and underlying beds

Cross bedded quartz sandstone with green clay cement and abundant ooid debris. middle of this bed hosts a stromatolitic green clay horizon interpreted to represenent a hiatus in detrital depositional , which also erosively truncates the underlying structures.

High angle cross bedded green clay oolite with interstitial quartz sand cemented by additional green clay. Abundant coated grains with spastolithic texture. Abundant coated grains with partially lithified sheared and compacted morphology. Internal erosive hiatus surfaces composed of stromatolitic green clay. Patches of secondary carbonate and pyrite cement. Erosively truncated by overlying bed, 'fills in' highly irregular underlying contact surface.

High angle cross bedded quartz sandstone with green clay cement and tightly packed ooids and oolitic debris. Abundant examples of ooids in various stages of formation. Upper surface is highly eroded semi lithified irregular erosional surface. Lower surface obscured by syn-sedimentary intergrowth of underlying bed.

Stromatolitic green clay horizon with minor silt that appears to intergrow into overlying bed, and drapes features in the bed below.

Cross bedded and hummocky quartz sandstone with abundant ooids and glauconitic horizons. Arranged in packages bound by dark green stromatolitic clay but with no apparent erosion and minor relief. Stromatolitic and clotted microbial textures increase in size and abundance down core. Base of unit contains cm scale green clay domal stromatolites and abundant clotted texture.

High angle cross bedded quartz sandstone with green clay cement and tightly packed ooids and oolitic debris. Abundant examples of ooids in various stages of formation. Upper surface is highly eroded semi lithified irregular erosional surface. Lower surface incises underlying bed.

Alternating beds of high angle cross bedded quartz sand with ooids and laminated dark green clay. Size and abundance of ooids and size of sand grains decreases down core.

Below this point sediment rapidly transitions from green clay and green cemented sands to blue-gray clay and kaolinite/silica cemented medium to fine sands. Followed by a rapid transition in to the regular facies of the Upper Velkerri Formation.

7. Acknowledgements

The following eukaryotes are thanked in no particular order, for their help, assistance and general support during the agglutination of this project and thesis.To be fair, none of us knew what were getting into at the time. A more comprehesive, and decidedly better written list will be prepared for the physical submission.

Dr's Nick Tosca, Rosalie Tostevin, and Stuart Robinson for all the help advice support and for generally being exemplary advisors from the start. Extra special shout out to Rosalie for organising the sampling trips and putting up with me on long haul flights and during a cyclone. On the subject of Australia, thanks to Dr Amber Jarrett for sending Nick that box of rocks and all the help and discussion since. Shout out to the lads at the NTGS corestore Darwin for lugging crates and keeping up with my requests. Darryll, I promise I will get you that report and data asap. Thanks go as well to Brutus, one eyed king of the river, spiritual mascot of the project. Sara Middleton is specially thanked for being super supportive ove the last year and especially the last three months of writing. Prof Bruce Levell and Prof Peir Pufhal are thanked for their sound advice and assistance during the correction of this work. My sinscere apologies to both of you for having to read this ~~twice~~ *three* times.

I really will do a better list for the final *final* thing....

8. Honesty Declaration

I declare on my honour that what is written in this work has been written exclusively by me and that,excluding quotations, no part has been copied from scientific publications, Internet (any type of programs,set of tools and others included) or research works - or, more generally, any other source - already presented in the academic field (but not only) by me, other students or third parties.In the case of parts taken from scientific publications, the Internet or any other document, I have expressly and directly indicated the source at the end of the quotation or at the foot of the page as well as having duly marked them in the text by quotation marks where indicated verbatim.

Brooke Robert Johnson 05/09/2021